Space-time Coded Systems with Continuous Phase Modulation

A thesis submitted in fulfillment

of the requirements for the Degree of

Doctor of Philosophy

in Electrical and Computer Engineering

from the University of Canterbury,

Christchurch, New Zealand.

Rachel L. Maw

B.E. (Hons 1)

March 2007

Abstract

Space-time coded systems developed in the last ten years have been designed primarily using linear modulation. Non-linear continuous phase modulation has desirable constant envelope properties and considerable potential in space-time coded systems.

The work in this thesis is focussed on developing and analysing an integrated space-time coded continuous phase modulated (STC-CPM) system. The coding of the space-time encoder and the modulation is incorporated into a single trellis encoder. This allows state combining, which leads to complexity reduction due to the reduced number of states.

Design criteria for STC-CPM are summarized and the Euclidean distance is shown to be important for code design. The integrated STC-CPM system design enables systematic space-time code searches that find optimal space-time codes, to be easily implemented. Optimal rate-$\frac{1}{2}$ and rate-$\frac{2}{3}$ space-time codes are found by maximizing the system's minimum squared Euclidean distance. These codes can provide high throughput and good coding gains over un-optimized full rank codes, such as delay diversity, in a quasi-static flat fading environment.

Performance bounds are developed using a union bound argument and the pairwise error probability. Approximations of the bounds are evaluated. These truncated upper bounds predict the slopes of the simulated performance curves at low error rates.

Acknowledgements

I would like to acknowledge those who have helped me during my PhD research.

I would like to thank Professor Des Taylor, my supervisor, for his invaluable support and direction during this research. I appreciate the countless hours spent reviewing conference and journal papers, and this thesis. Also, I would like to thank Des for his financial support, partly funding my conference travel and later with a scholarship to see me through to the end.

My studies were also supported by the New Zealand Government Tertiary Education Commission with a Bright Futures Scholarship.

I would also like to thank my past and present colleagues in the Comms Lab, for their friendship and conversation.

Finally, many thanks to my friends and family for their support and love, especially to Greg whose patience and kindness I could not be without.

The University of Canterbury *Rachel Maw*
March 2007

Contents

List of Tables

List of Figures

Glossary

APCO	association of public-safety communications officials
AWGN	additive white Gaussian noise
BER	bit error rate
BLAST	Bell-labs layered space-time
BPSK	binary phase shift keying
CPE	continuous phase encoder
CPFSK	continuous phase frequency shift keying
CPM	continuous phase modulation
FER	frame error rate
FF-CPE	feedback-free continuous phase encoder
ISED	incremental squared Euclidean distance
LPF	low pass filter
LRC	CPM with a raised cosine frequency pulse with pulse duration LT
LREC	CPM with a rectangular frequency pulse with pulse duration LT
MAP	maximum a posteriori probability
M-CPFSK	M-ary continuous phase frequency shift keying with $h = \frac{1}{M}$
MIMO	multiple input multiple output
MSED	minimum squared Euclidean distance
MSK	minimum shift keying
PSK	phase shift keying
PEP	pairwise error probability
QPSK	quadrature phase shift keying
SED	squared Euclidean distance
SER	symbol error rate

SNR	signal to noise ratio
STBC	space-time block code
STC	space-time coding
STC-CPM	space-time coded continuous phase modulation
STTC	space-time trellis code

Chapter 1

Introduction

In today's "knowledge society" there is an insatiable desire for communication systems that are smaller, cheaper, faster and of higher quality. The proliferation of wireless communication services for voice, video and data, has necessitated a growth of research into systems that have greater capacity and can operate over the often hostile wireless channel. In order to achieve greater capacity, larger channel bandwidth and transmit power can be employed and/or more spectrally efficient methods for transferring information are required. Due to limited spectrum and regulatory restrictions, the latter is often the more viable and cost effective option.

Significant improvement in spectral efficiency is attainable by increasing the number of antennas used at the transmitter and the receiver [1, 2, 3]. A technique that employs coding across multiple transmit antennas is space-time coding (STC) [4]. STC utilizes spatial and temporal diversity to exploit the multipath fading channel to improve performance without sacrificing bandwidth. To date STC has improved quality but not spectral efficiency. Recent work by Cavers [5, 6] has demonstrated that minimum shift keying (MSK), a particular form of continuous phase modulation (CPM) [7], is an excellent signalling format for use in space-time coded systems. Moreover, Zhang and Fitz [8] have shown that more general forms of CPM are good alternatives to linear modulation in such schemes.

CPM has advantages over linear modulation, such as its ability to use low cost and efficient non-linear power amplifiers. However, not using amplitude to communicate information causes it to exhibit low bandwidth efficiency, and this has prevented its widespread use. The use of multiple antennas can compensate for CPM's relatively low bandwidth efficiency and

result in a system that maintains power efficiency, with a high data rate and high performance in wireless environments.

The work in this thesis is aimed at designing and analysing an emerging format for digital wireless communications. The design consists of a space-time trellis coded system based on continuous phase modulation. An integrated structure that reduces implementation complexity and allows for systematic code design is formed.

1.1 Literature Review

Transmit diversity schemes with continuous phase modulation (CPM) are not a recent phenomenon. An early minimum shift keyed (MSK) transmit diversity scheme developed by Ogose et al. [9] reduced signal degradation due to multipath fading; however, it required increased bandwidth. More recently, space-time coding techniques with CPM that do not require additional bandwidth have been developed. Cavers presents a simple space-time coded scheme using MSK in [5, 6]. The scheme takes advantage of the properties of both CPM and offset linear modulation; MSK is a special case of both. Code design for more general space-time CPM has been investigated in [10, 11, 12, 13]. Zhang and Fitz [11] derive design rules for space-time codes using CPM in quasi-static fading, for a small number of parallel spatial channels. Cheng and Lu [12] expand on these design rules by considering code design in fast fading channels. Ahmadi and Rao [14] use the rank (spatial diversity) and product distance criteria derived in [11] to find feedforward space-time trellis codes for particular binary CPM schemes. Zajić and Stüber [15] investigate the product distance criterion for space-time code design with full response CPM.

The search for good space-time codes with continuous phase modulation is more difficult and more computationally intensive than for linearly modulated space-time codes. This is due to the inherent memory and nonlinearity of CPM. In [11] linear decompositions of CPM signals relate the rank criterion for phase shift keyed (PSK) space-time coded systems [16] to various space-time coded continuous phase modulated (STC-CPM) systems. These general code constructions guarantee full spatial diversity for specific forms of CPM. If the number of receive antennas multiplied by the spatial diversity exceeds three, maximizing the spatial diversity becomes less relevant in code design and is superseded by the requirement to maximize the minimum squared Euclidean distance. This is illustrated in Chapter 4.

Further work on space-time coded CPM has led to interleaved, externally encoded, STC-CPM systems, which have been developed in [17, 12]. This type of scheme, with offset carrier frequencies, is investigated in [18]. However, this system requires an expanded bandwidth. A soft-output algorithm is necessary for iterative detection in concatenated systems. The STC-CPM schemes developed in this thesis may be used as the inner code of an interleaved, iteratively decoded system.

An orthogonal STC-CPM system based on Alamouti's linearly modulated design [19] reduces joint maximum-likelihood decoding to subset index searching and symbol by symbol searching on each branch from a state [20]. However, the difficulty of obtaining the orthogonal design with CPM and the large bandwidth required, limits the usefulness of this scheme. The orthogonal STC-CPM design has been extended to allow non-coherent detection of a two-transmit antenna, full response CPM scheme [21].

Differential space-time coding [22, 23] for linear modulation formats is applied to CPM in [24]. No channel state information is required at the receiver. However, to achieve orthogonality only one transmit antenna is allowed to operate during a given signalling interval. This results in a low transmission rate of $\frac{\log_2(M)}{L_t}$ bits per symbol period, where L_t is the number of transmit antennas and M is the cardinality of the modulation alphabet. A reduced complexity receiver for layered space-time schemes with MSK-like modulations is presented in [25]. For this scheme, the number of receive antennas must be greater than or equal to the number of transmit antennas.

1.2 Scope

In this thesis, a generalized space-time coded continuous phase modulated (STC-CPM) framework is developed. It allows for a wide variety of space-time trellis codes, including high-rate codes. An integrated design is obtained by defining all code structures on the same integer ring. This integrated design enables performance measures to be readily evaluated. This work is an extension of the ideas in [26, 27, 28, 29] and [30], where integrated ring convolutional code designs are implemented for various single thread CPM systems. Yang and Taylor [26, 27] investigate ring convolutional code design for a subset of CPM called continuous phase frequency shift keying (CPFSK), and Rimoldi and Liu [28] extend this concept to more general CPM. In [29, 30], Griffin and Taylor use a ring convolutional code to differentially

encode CPFSK, and investigate ring convolutional code design for differentially demodulated CPFSK. The examples and performance results presented in this thesis are primarily focused on CPFSK modulated space-time codes.

A Rayleigh fading channel model with additive white Gaussian noise (AWGN) is assumed. The proposed STC-CPM schemes are narrowband. Therefore, we assume the Rayleigh fading to be non-frequency selective (flat-fading). At the receiver, we assume there is ideal knowledge of channel information and transmitter parameters, such as, symbol timing and carrier frequency. In real-world systems, estimates of such parameters are required and obtaining these can involve much work. This is beyond the scope of this thesis. Also, the effects of inter-symbol interference are not considered.

The new STC-CPM design will be implementable in real world wireless communication systems at affordable costs and has considerable potential for commercial development in the area of rapidly deployable wireless data networks. The scheme could be developed to operate within the APCO 25 Standard [31], which is a voluntary standard for narrowband public safety digital radio.

1.3 Thesis Overview

Chapter 2 begins by introducing the wireless channel, which is the environment in which the space-time coded systems will be transmitting. Continuous phase modulation is then reviewed. In particular, the Rimoldi decomposition of CPM [32] is described. It separates CPM into a ring convolutional encoder that represents its inherent coding and a memoryless modulator. The decomposition is used in the STC-CPM system model developed in this thesis. Multi-antenna communication systems are discussed, with a focus on space-time trellis codes (STTC). Current literature on STTC CPM is then reviewed. Possible areas where this research can be extended and improved are discussed. This discussion provides motivation for the work in this thesis.

In Chapter 3, a transmitter with multiple antennas is constructed. Each antenna transmits a continuous phase modulated signal and the CPM modulators are modelled using the Rimoldi decomposition. The fading and the noise processes that the combined CPM signals experience are described, and the coherent receiver that decodes the combined signal is detailed. The focus then returns to the transmitter. A feedback-free, multi-CPM transmitter model is formed

and then extended by the concatenation of a STTC. A ring convolutional encoder is used to implement the space-time trellis coding. The space-time encoder is combined with the inherent coding of the CPM, which is explicitly defined as a ring convolutional encoder using the Rimoldi decomposition, to form a single ring convolutional encoder. The combined encoder structure enables state reduction and allows space-time code searches to be implemented more easily. Viterbi decoding is performed on the combined encoder's trellis.

A pairwise error probability (PEP) bound for space-time coded CPM is derived in Chapter 4. The derivation is based on the method used for linearly modulated space-time coded systems [3]. The PEP is then used to determine design criteria for STC-CPM. The Euclidean distance criterion developed is used to search for optimal space-time codes, for CPFSK modulated schemes. These codes offer the best performance when there is a large number of parallel spatial channels. The optimized codes will also perform well in a system with a small number of parallel spatial channels, that is, a system with few receive antennas and low transmit diversity, if the transmit diversity is maximized.

In Chapter 5, performance bounds are formed for STC-CPM systems. The bounds incorporate the PEP bound derived in the previous chapter. Performance bounds that utilize the PEP bound developed in [33] are also considered. A method to evaluate the rank and the product distance of the signal distance matrix is developed. Approximate performance bounds for various STC-CPM schemes are then evaluated and plotted. These truncated bounds are compared to the corresponding simulated performance curves.

Finally, the pertinent results of the thesis are summarized and some ideas for future research related to the work completed in this thesis are presented.

1.4 Thesis Contributions

The original work in this thesis is formed by Chapters 3, 4 and 5, and includes:

- A reduced-state ring convolutional trellis encoder that incorporates the continuous phase coding of the modulation and the space-time coding.

- A search for optimal rate-$\frac{1}{2}$ and rate-$\frac{2}{3}$ space-time codes for M-ary CPFSK modulated schemes based on the Euclidean distance criterion for $M = \{2, 4, 8\}$.

- Development and simulation of optimized high rate space-time coded CPM with receive diversity.

- Performance bounds for space-time coded CPM schemes that are evaluated in truncated form using the product distance, the rank and the trace of the signal distance matrices.

1.5 Publications

The following papers are written on the research presented in this thesis.

R. L. Maw and D. P. Taylor, "Externally encoded space-time coded systems with continuous phase frequency shift keying," in *Proc. Int. Conf. on Wireless Networks, Commun. and Mobile Computing*, vol. 2, June 2005, pp. 1597–1602.

R. L. Maw and D. P. Taylor, "Space-time coded systems with continuous phase frequency shift keying," in *Proc. Global Telecommun. Conf.*, vol. 3, Nov. 2005, pp. 1581–1586.

R. L. Maw and D. P. Taylor, "Space-time coded systems using continuous phase modulation," accepted for publication in *IEEE Trans. Commun.*.

R. L. Maw and D. P. Taylor, "High rate CPFSK space-time trellis codes," submitted to *IEEE Trans. Commun.*.

Chapter 2

Background

2.1 Introduction

In this chapter, we present the relevant background information for the space-time coded continuous phase modulated (STC-CPM) schemes developed in this thesis. First, we describe the wireless channel and the fading environment. A fading channel can have devastating effects on the performance of communications systems and it is important to know its characteristics.

We then describe continuous phase modulation (CPM). We pay particular attention to the Rimoldi model [32] of CPM, which separates the modulation into an encoder and a memoryless modulator. It will be utilized in Chapter 3 when defining the STC-CPM system model. We define convolutional encoders on integer rings, and show that the encoder of the modulation decomposition can be viewed as such an encoder. Ring convolutional encoders have been used to great effect in combination with single thread CPM modulators [27, 28]. We also describe a particular subset of CPM known as continuous phase frequency shift keying (CPFSK). We later use CPFSK in simulation examples due to its simplicity.

The following section introduces space-time coding (STC), which is a multi-transmit antenna scheme used to overcome the fading effects of the wireless channel. We describe the two main forms of STC, they are space-time block codes and space-time trellis codes (STTC). The majority of the literature on space-time codes is based on linear modulations. STTC provide a good fit for combination with CPM. Both, CPM and STTC can be described, in part, by ring convolutional encoders. We present STTC design criteria for linearly modulated systems that

are found in the literature. The criteria are based on minimizing the worst case pairwise error probability. These design criteria are extended to space-time coded CPM in Chapter 4.

We then summarize space-time trellis coded CPM systems and code design criteria found in the literature. We discuss possible extensions to this work and provide motivation for the original research presented in this thesis. We conclude the chapter with a summary of the information presented.

2.2 Wireless Channel

The performance attainable by wireless communication systems is limited by the effects of the radio channel. The channel has a time-varying nature, and hence transmission and analysis is more difficult than for fixed wired channels [34]. Transmission paths may be obstructed by natural and man-made objects such as hills, buildings and trees. Large scale fading over long distances causes the strength of the transmitted signal to reduce at a rate proportional to $\left(\frac{d_s}{d_0}\right)^n$ [34], where d_s is the distance between the transmitter and the receiver, d_0 is the close-in reference distance determined by measurement close to the transmitter and n is the path loss exponent. The value of the path loss exponent depends on the propagation environment [34]. For example, in free space $n = 2$, in a largely obstructed environment $n > 2$, and for a line of sight or guided wave environment, such as urban streets, n may be less than 2.

Obstructions in the environment cause multiple reflections of the transmitted signal to be received from different directions and with different propagation delays. Interaction between the waves causes a phenomenon known as multipath fading. Multipath fading can cause severe and rapidly fluctuating attenuation of the transmitted signal, which may result in an inability to reliably transfer information. Small scale fading models are used to describe this process. In the following we discuss possible forms of the multipath fading channel.

2.2.1 Time Selective Fading

Relative motion between the transmitter and the receiver causes a transmitted signal and its reflections to undergo different frequency shifts, which are known as Doppler shifts. A received tone transmitted at frequency f_c will experience a Doppler shift given by

$$f_d = \frac{f_c v_m}{c} \cos\theta, \tag{2.1}$$

where θ is the incident angle of the received signal with respect to the direction of the receiver's motion, v_m is the velocity of the receiver towards the transmitter and c is the speed of light. In a multipath channel the signal is spread over the frequency range

$$f_c \pm f_{d_{\max}}, \tag{2.2}$$

where $f_{d_{\max}}$ is the maximum Doppler shift

$$f_{d_{\max}} = \frac{f_c v_m}{c}. \tag{2.3}$$

This is known as frequency dispersion or time selective fading.

A channel is classed as a slow fading channel if the channel impulse response changes at a much slower rate than the transmitted baseband signal [34]. In this case, the channel can be assumed to be static over one or more symbol intervals. Equivalently, the Doppler spread, which is a measure of the frequencies over which the Doppler spectrum is large enough to cause frequency dispersion, is much less than the bandwidth of the transmitted signal.

Conversely, for a fast fading channel, the Doppler spread is comparable to or larger than the bandwidth of the transmitted signal. In the time domain, the coherence time of the channel, which is approximately equal to the reciprocal of the Doppler spread [34], is less than the transmitted signal's symbol period, T. Fast fading occurs at very low data rates or at high vehicle velocity.

In the following, we assume a quasi-static fading model in which the fading parameters are constant over a data frame and vary from frame to frame, where a frame is a grouping of data symbols to be transmitted. We assume that the fading is uncorrelated between frames.

2.2.2 Frequency Flat and Frequency Selective Fading

Time dispersion causes received signals to overlap, which results in frequency flat or frequency selective fading [34] of the transmitted signal. If all of the spectral components are similarly affected, the fading is frequency non-selective or flat. Conversely, if distinct spectral components experience different magnitudes of fading, the fading is frequency selective. The coherence bandwidth is a statistical measure of the range of frequencies over which the fading may be considered flat. Spectral components within the band are passed with approximately the same gain and change in phase [34].

Frequency selective fading occurs when the bandwidth of the transmitted signal is greater than the coherence bandwidth of the channel. Different gains are experienced over the transmitted signal band resulting in a variable frequency response. This is characteristic of wideband systems. Frequency selective fading induces inter-symbol interference.

Flat fading occurs if the symbol period is much greater than the multipath delay spread of the channel. The multipath delay spread is proportional to the reciprocal of the coherence bandwidth. In a flat fading environment, channel fading causes negligible inter-symbol interference because the signal bandwidth is narrow relative to the coherence bandwidth of the channel. Flat fading channels often experience deep fades. Flat fading is characteristic of narrowband systems. The systems presented in this thesis are usually narrowband. Therefore, we use a frequency flat fading model.

2.2.3 Rician and Rayleigh Fading Channel

Rician and Rayleigh fading channels are commonly used to model land mobile radio channels. In urban environments, where there are a large number of scatterers affecting propagation and there is a dominant stationary (non-fading) signal component, such as a line of sight propagation, the Rician fading channel is an appropriate model [34]. If there is no line of sight between the transmitter and the receiver, the Rayleigh fading channel, which is a special case of the Rician fading channel, may be used.

Proakis describes the fading channel in the following manner [35]. The equivalent low-pass received signal, without additive white Gaussian noise, is given by

$$r_l(t) = \int_{-\infty}^{\infty} c(\tau; t) s_l(t - \tau) d\tau, \tag{2.4}$$

where $c(\tau; t)$ represents the response of the channel at time t, due to an impulse applied at time $t - \tau$, and $s_l(t)$ is the equivalent low-pass transmitted signal. We let $S_l(f)$ denote the transmitted signal's frequency content. Then the received signal may also be written as

$$r_l(t) = \int_{-\infty}^{\infty} C(f; t) S_l(f) e^{j2\pi f t} df, \tag{2.5}$$

where $C(f; t)$ is the Fourier transform of $c(\tau; t)$ given by

$$C(f; t) = \int_{-\infty}^{\infty} c(\tau; t) e^{-j2\pi f \tau} d\tau. \tag{2.6}$$

If we assume that the channel is non-frequency selective, then due to the frequency content of $S_l(f)$ being concentrated about $f = 0$, we may let $C(f;t) = C(0;t)$ and

$$\begin{aligned} r_l(t) &= C(0;t)\int_{-\infty}^{\infty} S_l(f)e^{j2\pi ft}df \\ &= C(0;t)s_l(t) \\ &= \alpha(t)e^{-j\phi(t)}s_l(t), \end{aligned} \tag{2.7}$$

where $\alpha(t)$ represents the envelope and $\phi(t)$ represents the phase, of the equivalent low-pass channel response, respectively. The Rice distribution may used to model the behaviour of the envelope of these channels [35]. A Rician distributed random variable, Z, has the probability density function

$$p_Z(z) = \begin{cases} \frac{z}{\sigma^2}\exp\left(-\frac{(z^2+A^2)}{2\sigma^2}\right)\mathbf{I}_0\left(\frac{Az}{\sigma^2}\right), & A \geq 0, z \geq 0 \\ 0, & z < 0 \end{cases}, \tag{2.8}$$

where $2\sigma^2$ is the average power in the non-line of sight multipath components, A^2 is the power in the line of sight component and $\mathbf{I}_0(x)$ is the modified Bessel function of the first kind of order zero.

If a single tone with a constant amplitude is transmitted, such that the direct path of the wave is obstructed and the mobile unit receives a large number of reflected waves, then by the central limit theorem, the two quadratic components of the received signal are uncorrelated Gaussian processes with zero mean. Thus, the envelope of the received signal, $\alpha(t)$, varies in time according to the Rayleigh distribution and the change in phase, $\phi(t)$, is uniformly distributed over the interval $(-\pi, \pi)$. If the fading is assumed to sufficiently slow, the phase can be estimated from the received signal and coherent detection may be used.

The Rayleigh fading channel is a special case of the Rician channel with no line of sight component. For this model, the received envelope is Rayleigh distributed for any fixed value of t. We substitute $A = 0$ into the probability density function of Equation (2.8), to find the Rayleigh probability density function as

$$p_Z(z) = \begin{cases} \frac{z}{\sigma^2}\exp\left(-\frac{z^2}{2\sigma^2}\right), & z \geq 0 \\ 0, & z < 0 \end{cases}. \tag{2.9}$$

If the Rayleigh fading channel has a maximum Doppler shift of $f_{d_{\max}}$, then the autocorrelation of the fading is given by [36]

$$R(\tau) = J_0(2\pi f_{d_{\max}}\tau), \tag{2.10}$$

where J_0 is the zero order Bessel function of the first kind. Jakes' presents a method to generate Rayleigh fading for simulation purposes [37] based on summing sinusoids.

2.3 Continuous Phase Modulation

Continuous Phase Modulation (CPM) is a non-linear, constant-envelope modulation [7, 38]. CPM is well suited to transmission of digital signals over power and bandwidth limited channels, such as mobile land and satellite, radio channels [38].

The phase continuity of CPM that results from the modulation's memory improves its spectral efficiency [38] by maintaining smooth phase transitions, rather than the abrupt phase transitions exhibited by modulations without phase continuity. The instantaneous phase of CPM can be described by a phase trellis. This trellis structure can be exploited by concatenating convolutional codes with CPM to form trellis coded modulations that have improved performance [7, 26, 27, 28].

CPM is a true constant envelope modulation, which allows the use of low cost, power efficient, non-linear power amplifiers without introducing distortion. Conversely, if a modulation's envelope varies with time and it is transmitted using a non-linear amplifier, there will be non-linear distortion. To reduce the distortion, expensive linearized amplifiers can be used, or the output power must be significantly reduced, which will mean the amplifier cannot operate at its peak efficiency [39]. Thus in practice, CPM can provide an energy advantage over non-constant envelope modulations.

The general form of a CPM signal [40] is given by

$$s(t, \boldsymbol{\alpha}) = \sqrt{\frac{2E_s}{T}} \cos\left(2\pi f_c t + \phi(t, \boldsymbol{\alpha}) + \phi_0\right), \quad t \geq 0, \tag{2.11}$$

where E_s is the symbol energy, T is the symbol period, f_c is the carrier frequency, ϕ_0 is the initial phase offset and $\boldsymbol{\alpha}$ is a sequence of M-ary data symbols such that

$$\boldsymbol{\alpha} = (\alpha_0, \alpha_1, \ldots), \quad \alpha_i \in \{\pm 1, \pm 3 \ldots \pm (M-1)\}, \quad i \geq 0, \tag{2.12}$$

for M even. The information carrying phase, $\phi(t, \boldsymbol{\alpha})$, during the n-th symbol interval is given by

$$\phi(t, \boldsymbol{\alpha}) = 2\pi h \sum_{i=0}^{n} \alpha_i q(t - iT), \qquad nT \leq t \leq (n+1)T, \tag{2.13}$$

where $q(t)$ is the phase function and h is the modulation index. The phase function is defined as the integral of an instantaneous frequency pulse and has the properties

$$q(t) = \begin{cases} 0 & t \leq 0 \\ \frac{1}{2} & t > LT \end{cases}, \tag{2.14}$$

where L is the frequency response pulse length. The frequency pulse length dictates the time interval over which a single input data symbol can affect the instantaneous frequency. A full response CPM has $L = 1$ and a partial response CPM has $L > 1$. Continuous phase frequency shift keying (CPFSK), which is also known as 1REC, has a rectangular frequency pulse and is full response.

The phase of CPM can be represented by a tree structure. The tree structure is found by manipulating the information carrying phase of Equation (2.13) during the n-th symbol interval to give

$$\phi(t, \boldsymbol{\alpha}) = 2\pi h \sum_{i=n-L+1}^{n} \alpha_i q(t - iT) + \theta_n, \qquad nT \leq t \leq (n+1)T, \tag{2.15}$$

where θ_n is the $phase\ state$

$$\theta_n = \pi h \sum_{i=0}^{n-L} \alpha_i, \qquad nT \leq t \leq (n+1)T. \tag{2.16}$$

For example, the phase tree for 4-ary CPFSK is shown in Figure 2.1.

The tree will reduce to a trellis structure if the modulation index, h, is set to a ratio of two relatively prime integers, such that $h = \frac{v}{p}$. The trellis structure is obtained by reducing the phase modulo-2π. The phase reduced modulo-2π is termed the $physical\ phase$ [32] and we denote it as $\tilde{\phi}(t, \boldsymbol{\alpha})$. It is impossible to distinguish between two phases that differ by 2π, and thus, the physical phase is the phase that is observable.

During the n-th symbol interval, $\tilde{\phi}(t, \boldsymbol{\alpha})$ is given by

$$\begin{aligned} \tilde{\phi}(t, \boldsymbol{\alpha}) &= [\phi(t, \boldsymbol{\alpha})] \mod 2\pi \\ &= \left[2\pi h \sum_{i=n-L+1}^{n} \alpha_i q(t - iT) + \theta_n \right] \mod 2\pi \\ &= \left[2\pi h \sum_{i=n-L+1}^{n} \alpha_i q(t - iT) + [\theta_n] \mod 2\pi \right] \mod 2\pi \\ &= \left[2\pi h \sum_{i=n-L+1}^{n} \alpha_i q(t - iT) + \tilde{\theta}_n \right] \mod 2\pi, \qquad nT \leq t \leq (n+1)T. \end{aligned} \tag{2.17}$$

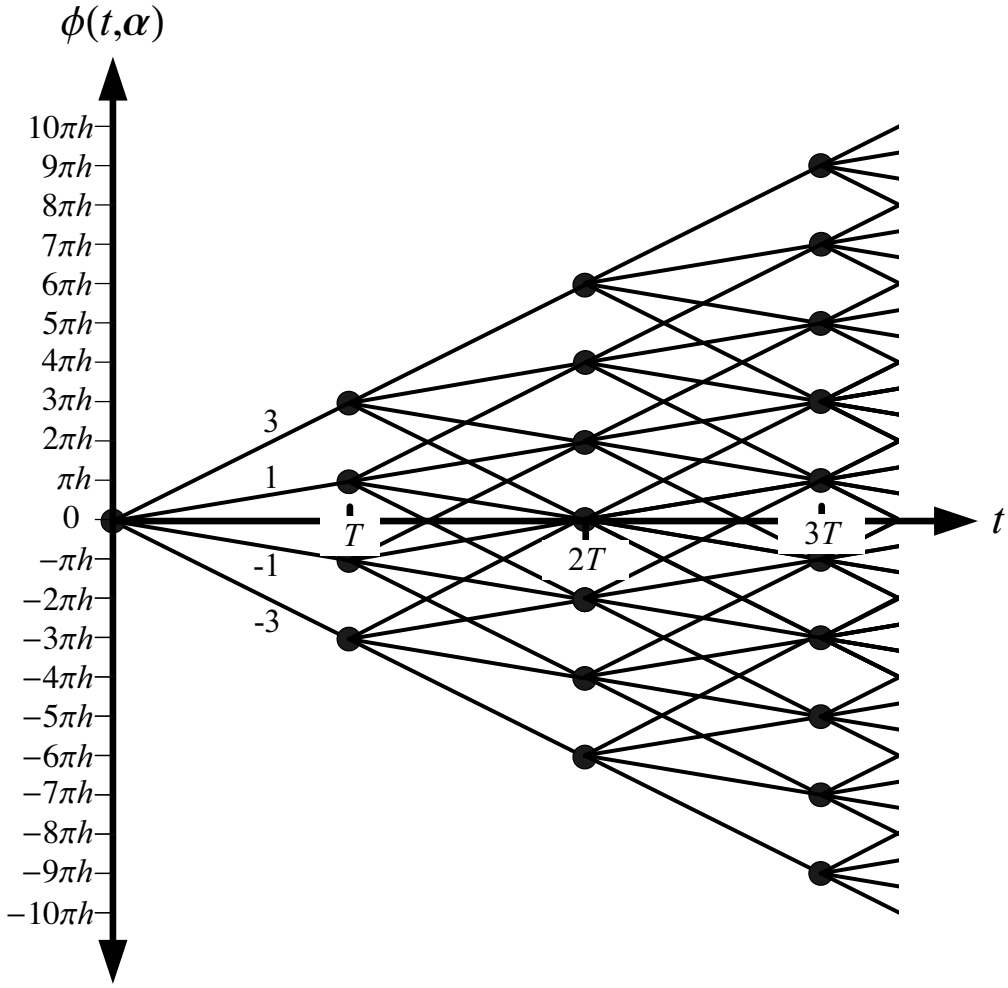

Figure 2.1: Phase tree for 4-ary CPFSK.

The $physical\,phase\,state$, $\tilde{\theta}_n$, can take on $2p$ values and is given by

$$\begin{aligned}\tilde{\theta}_n &= [\theta_n] \mod 2\pi \\ &= \left[\pi h \sum_{i=0}^{n-L} \alpha_i\right] \mod 2\pi.\end{aligned} \tag{2.18}$$

The first term of Equation (2.17), $2\pi h \sum_{i=n-L+1}^{n} \alpha_i q(t-iT)$, is dependent on the sequence of $L-1$ past input data symbols, $(\alpha_{n-L+1}, \ldots, \alpha_{n-1})$, and is called the $correlative\,state$ [41]. There are M^{L-1} possible correlative states. The total number of states in the CPM phase trellis is the number of correlative states multiplied by the number of physical phase states, and is given by $2pM^{L-1}$. This CPM phase trellis is time varying, in that it differs at even and odd symbol times, such that during any given symbol interval only pM^{L-1} states are used and the

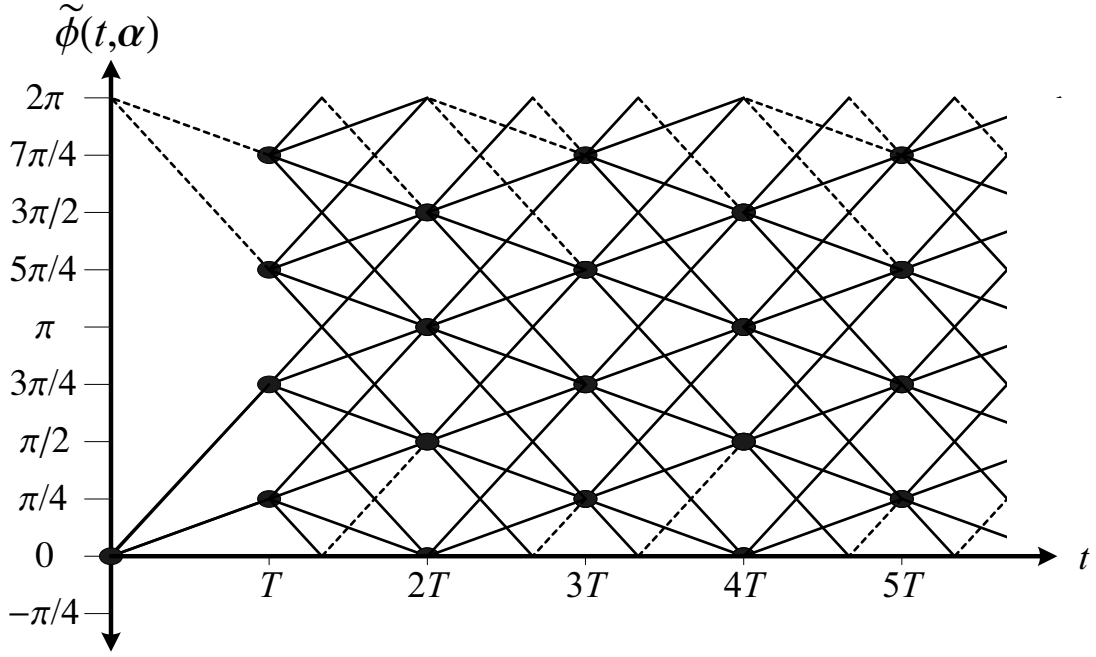

Figure 2.2: Phase trellis for 4-CPFSK.

phase alternates between two such sets of states. If the phase shifts are viewed as positive, rather than balanced about zero, the trellis is reduced to pM^{L-1} states [42]. We expand on this in Section 2.3.2.

Performing a modulo-2π operation on the phase tree of 4-ary CPFSK, with $h = \frac{1}{4}$ (4-CPFSK), results in the phase trellis of Figure 2.2. The phase can be pictured as wrapping around at 2π. The dotted lines represent the changes in phase, where the phase has wrapped around.

2.3.1 Ring Convolutional Codes

Massey and Mittelholzer showed that convolutional codes over rings [43, 44, 45] are $natural$ codes for M-ary phase modulation in [43]. The codes are defined over the ring of integers modulo-M instead of the binary field. Convolutional codes on rings have thus far produced the best codes for concatenation with single antenna CPM systems [27, 28]. We use the standard notation and properties of *linear multi-valued sequential coding networks* to describe ring encoders and their input and output sequences. The theory of coding networks can be found, for example, in [46], which we summarize in Appendix B.

We follow [44] and let $R = \mathbb{Z}_p$ denote a finite commutative ring with multiplicative identity 1, where $\mathbb{Z}_p$ is the ring of integers modulo-p. We let $\boldsymbol{R}(D)$ denote the ring of rational functions over R, where a rational function is the ratio of two polynomials that have coefficients in R, and the trailing coefficient of the denominator is a unit of R. The trailing coefficient is the smallest power of D, whose coefficient is not equal to zero. The trailing coefficient of the denominator of a causal and realizable rational function is the coefficient of D^0.

Every rate-$\frac{k}{l}$ convolutional code over R can be generated by a $(k \times l)$-dimensional encoding matrix, $\boldsymbol{G}(D) \in \boldsymbol{R}(D)^{k \times l}$, where the rows of $\boldsymbol{G}(D)$ are linearly independent. The elements of $\boldsymbol{G}(D)$, which are denoted

$$\{\boldsymbol{G}^{i,j}(D)\} \in \boldsymbol{R}(D), \quad 1 \leq i \leq k, \quad 1 \leq j \leq l, \tag{2.19}$$

are rational functions over R. The input data sequence

$$\boldsymbol{a}(D) = [\boldsymbol{a}^1(D) \;\; \boldsymbol{a}^2(D) \quad \ldots \quad \boldsymbol{a}^k(D)] \tag{2.20}$$

produces the output data sequence

$$\boldsymbol{b}(D) = [\boldsymbol{b}^1(D) \;\; \boldsymbol{b}^2(D) \quad \ldots \quad \boldsymbol{b}^l(D)]. \tag{2.21}$$

The output sequence is related to the input by

$$\boldsymbol{b}^j(D) = \sum_{i=1}^{k} \boldsymbol{a}^i(D)\boldsymbol{G}^{i,j}(D), \quad 1 \leq j \leq l, \tag{2.22}$$

and we may write

$$\boldsymbol{b}(D) = \boldsymbol{a}(D)\boldsymbol{G}(D). \tag{2.23}$$

2.3.2 CPM Decomposition

In [32], Rimoldi developed a model of CPM that separates the modulation into two components; one component has memory and the other does not. The model allows the inherent coding associated with the phase continuity constraint, and the modulation operation of CPM to be considered independently. The memory component is modelled as a linear convolutional encoder on the ring of integers modulo-p ($\mathbb{Z}_p$), where p is the denominator of the modulation index. This encoder is termed the *continuous phase encoder* (CPE) and it can be represented by a time-invariant trellis. The memoryless component receives information

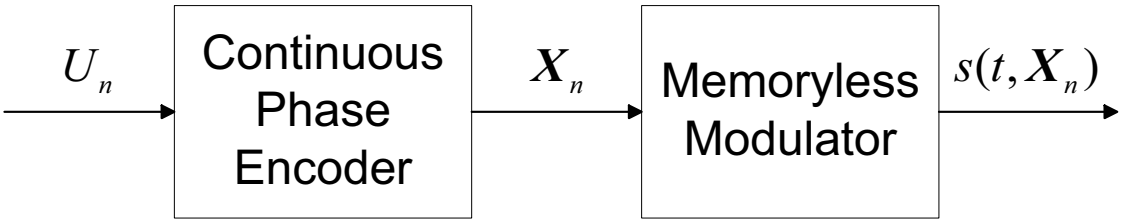

Figure 2.3: Rimoldi decomposition of CPM.

from the CPE that determines which modulated output sequence to transmit. It is termed the $memoryless\,modulator$. The memoryless modulator is time-invariant and requires no knowledge of previously transmitted information. A diagram of the Rimoldi decomposition is shown in Figure 2.3 [32]. The forms of the memoryless modulator and the continuous phase encoder are derived in the following sections, based on Rimoldi's work in [32].

Offset Time Invariant Phase Trellis

As noted previously, the number of states in the CPM phase trellis can be reduced to pM^{L-1}. This is achieved by measuring the phase relative to the lowest phase trajectory [32]. For example, for 4-ary CPFSK the lowest phase trajectory shown in Figure 2.1 is generated by the input data sequence, $\boldsymbol{\alpha} = (-3, -3, \ldots)$. Measuring the phase in this manner is equivalent to offsetting the traditional information carrying phase, $\phi(t, \boldsymbol{\alpha})$ of Equation (2.15), by $\frac{\pi h(M-1)t}{T}$. This new offset phase is called the $tilted\,phase$, and when reduced modulo-2π is termed the $physical\,tilted\,phase$. The tilted phase is given by

$$\begin{aligned}\psi(t, \boldsymbol{\alpha}) &= \phi(t, \boldsymbol{\alpha}) + \frac{\pi h(M-1)t}{T} \\ &= 2\pi h \sum_{i=n-L+1}^{n} \alpha_i q(t - iT) + \pi h \sum_{i=0}^{n-L} \alpha_i + \frac{\pi h(M-1)t}{T}, \qquad nT \leq t \leq (n+1)T\end{aligned} \tag{2.24}$$

and the physical tilted phase is given by

$$\tilde{\psi}(t, \boldsymbol{\alpha}) = [\psi(t, \boldsymbol{\alpha})] \mod 2\pi. \tag{2.25}$$

We let $\boldsymbol{U} = (U_0, U_1, \ldots)$ denote a modified data sequence. The i-th M-ary data symbol, U_i, is calculated from the bipolar data symbol, α_i, as

$$U_i = \left(\frac{\alpha_i + (M-1)}{2} \right) \in \{0, 1, \ldots, (M-1)\}. \tag{2.26}$$

The tilted phase can then be written as a function of $\boldsymbol{U}$ by substituting Equation (2.26) into Equation (2.24), to obtain

$$\psi(t,\boldsymbol{U}) = 4\pi h \sum_{i=n-L+1}^{n} U_i q(t-iT) - (M-1)2\pi h \sum_{i=n-L+1}^{n} q(t-iT) + 2\pi h \sum_{i=0}^{n-L} U_i - (M-1)\pi h(n-L+1) + \frac{\pi h(M-1)t}{T}, \quad nT \le t \le (n+1)T. \quad (2.27)$$

The trellis derived from the physical tilted phase is time-invariant. To illustrate this we let $t = \tau + nT$. The tilted phase of Equation (2.27), is then

$$\begin{aligned}\psi(\tau+nT,\boldsymbol{U}) &= 4\pi h \sum_{i=n-L+1}^{n} U_i q(\tau+nT-iT) - (M-1)2\pi h \sum_{i=n-L+1}^{n} q(\tau+nT-iT) \\ &+2\pi h \sum_{i=0}^{n-L} U_i - (M-1)\pi h(n-L+1) + \frac{\pi h(M-1)(\tau+nT)}{T}, \quad nT \le \tau+nT \le (n+1)T \\ &= 4\pi h \sum_{i=0}^{L-1} U_{n-i} q(\tau+iT) - (M-1)2\pi h \sum_{i=0}^{L-1} q(\tau+iT) \\ &+ 2\pi h \sum_{i=0}^{n-L} U_i + (M-1)\pi h(L-1) + \frac{\pi h(M-1)\tau}{T}, \quad 0 \le \tau \le T.\end{aligned} \quad (2.28)$$

We observe that the time dependent terms of the tilted phase of Equation (2.28) only depend on the translated time variable $\tau = t - nT$. Using the modulo operation identity

$$\left[x\ \frac{y}{z}\right] \mod A = \left[([x] \mod z)\ \frac{y}{z}\right] \mod A \quad (2.29)$$

the time independent, data dependent terms reduced modulo-2π can be written as

$$\begin{aligned}\tilde{\delta}_n &= \left[2\pi h \sum_{i=0}^{n-L} U_i\right] \mod 2\pi \\ &= \left[\frac{2\pi}{p} v \sum_{i=0}^{n-L} U_i\right] \mod 2\pi \\ &= \left[\frac{2\pi}{p}\left[v \sum_{i=0}^{n-L} U_i\right] \mod p\right] \mod 2\pi \\ &= \frac{2\pi}{p}\left[v \sum_{i=0}^{n-L} U_i\right] \mod p.\end{aligned} \quad (2.30)$$

It is observed that $\tilde{\delta}_n$ can take only the same p possible values during each symbol interval. It is possible for $\tilde{\delta}_n$ to equal any of these values after an initial transient that allows the expression,

$\left[v\sum_{i=0}^{n-L} U_i\right] \mod p$, to equal any value of the set, $\{0, 1, \ldots, p-1\}$. This transient lasts until the n-th symbol interval, when n satisfies the inequality

$$v(n-L+1)(M-1) \geq p-1. \tag{2.31}$$

Therefore, the physical tilted phase and its trellis are indeed time-invariant.

Memoryless Modulator

To determine the form of the CPE and the memoryless modulator, the CPM signal of Equation (2.11) is written as

$$s(t, \boldsymbol{U}) = \sqrt{\frac{2E_s}{T}} \cos\left(2\pi f_1 t + \tilde{\psi}(t, \boldsymbol{U}) + \psi_0\right), \quad t \geq 0, \tag{2.32}$$

where f_1 is the offset carrier frequency and ψ_0 is the initial phase offset. The frequency, f_1, compensates for the difference between $\psi(t, \boldsymbol{U})$ and $\phi(t, \boldsymbol{U})$, and is defined as

$$f_1 = f_c - \frac{h(M-1)}{2T}. \tag{2.33}$$

The initial phase offset, ψ_0, can be set to zero without loss of generality. The physical tilted phase may be written as

$$\begin{aligned}
\tilde{\psi}(t, \boldsymbol{U}) &= [\psi(t, \boldsymbol{U})] \mod 2\pi \\
&= \left[2\pi h \sum_{i=0}^{n-L} U_i + 4\pi h \sum_{i=n-L+1}^{n} U_i q(t-iT) + W(t)\right] \mod 2\pi \\
&= \left[2\pi h \left[\sum_{i=0}^{n-L} U_i\right] \mod p + 4\pi h \sum_{i=n-L+1}^{n} U_i q(t-iT) + W(t)\right] \mod 2\pi, \\
&\qquad\qquad nT \leq t \leq (n+1)T,
\end{aligned} \tag{2.34}$$

where $W(t)$ is the sum of the data independent terms of the physical tilted phase and is given by

$$\begin{aligned}
W(t) = \frac{\pi h(M-1)t}{T} - (M-1)2\pi h \sum_{i=n-L+1}^{n} q(t-iT) - (M-1)\pi h(n-L+1), \\
nT \leq t \leq (n+1)T.
\end{aligned} \tag{2.35}$$

The tilted phase trellis for 4-CPFSK is shown in Figure 2.4. The trellis is time-invariant after a transient of one symbol interval and periodic over one symbol interval.

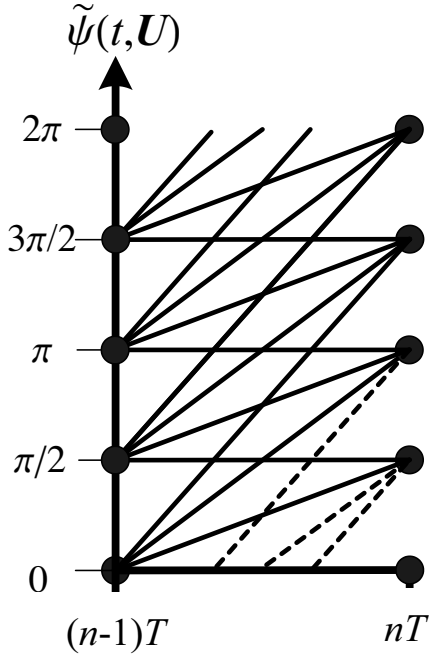

Figure 2.4: Tilted phase trellis for 4-CPFSK.

The data dependent output phase, $\tilde{\psi}(t, \boldsymbol{U})$, of the modulator, and hence the output of the memoryless modulator, are completely specified by the vector $\boldsymbol{X}_n$, which is defined as

$$\begin{aligned} \boldsymbol{X}_n &\triangleq [U_n, \ldots, U_{n-L+1}, V_n] \\ &= \left[X_n^1, \ldots, X_n^L, X_n^{L+1}\right], \end{aligned} \tag{2.36}$$

where

$$\begin{aligned} X_n^i &= U_{n-i+1}, \qquad 1 \le i \le L, \\ X_n^{L+1} &= V_n = \left[\sum_{i=0}^{n-L} U_i\right] \mod p. \end{aligned} \tag{2.37}$$

The vector, $\boldsymbol{X}_n$, is the input to the memoryless modulator; it is the information required to specify which physical phase trajectory the memoryless modulator should output in the current symbol interval. There are pM^L possible values of the $(L+1)$-dimensional vector $\boldsymbol{X}_n$. The

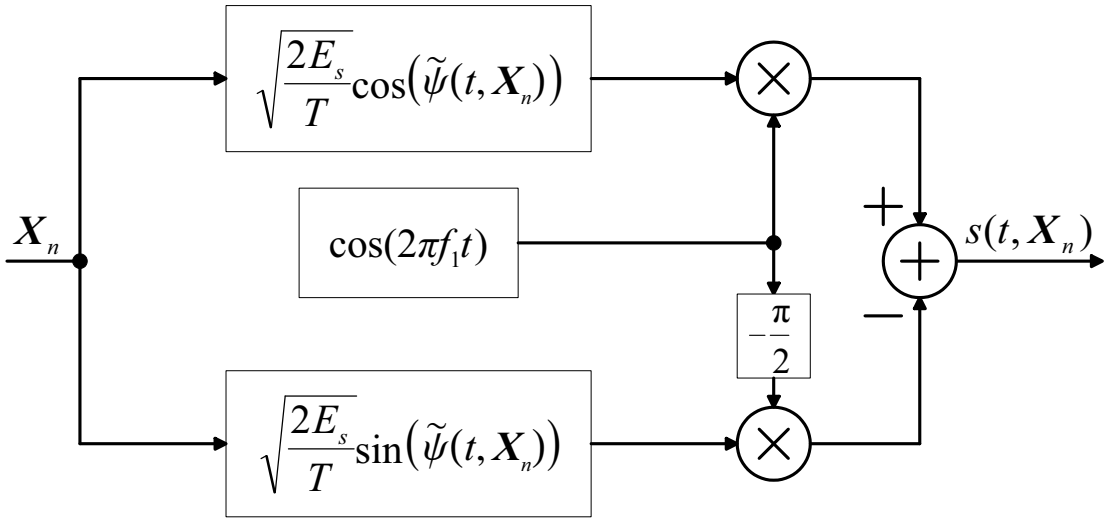

Figure 2.5: Memoryless modulator.

value of V_n can be found using the recursive equation,

$$\begin{aligned} V_{n+1} &= \left[\sum_{i=0}^{n-L+1} U_i\right] \mod p \\ &= \left[\sum_{i=0}^{n-L} U_i + U_{n-L+1}\right] \mod p \\ &= \left[\left[\sum_{i=0}^{n-L} U_i\right] \mod p + U_{n-L+1}\right] \mod p \\ &= [V_n + U_{n-L+1}] \mod p, \end{aligned} \tag{2.38}$$

so that

$$V_n = [V_{n-1} + U_{n-L}] \mod p. \tag{2.39}$$

Figure 2.5 shows the memoryless modulator in block diagram form. The output of the memoryless modulator in terms of in-phase and quadrature components is given by

$$s(t,\boldsymbol{X}_n) = s_I(t,\boldsymbol{X}_n)\cos(2\pi f_1 t) - s_Q(t,\boldsymbol{X}_n)\sin(2\pi f_1 t), \quad nT \le t \le (n+1)T, \tag{2.40}$$

where $s_I(t,\boldsymbol{X}_n)$ is the in-phase component given by

$$s_I(t,\boldsymbol{X}_n) \triangleq \sqrt{\frac{2E_s}{T}}\cos\left(\tilde{\psi}(t,\boldsymbol{X}_n)\right), \quad nT \le t \le (n+1)T, \tag{2.41}$$

and $s_Q(t,\boldsymbol{X}_n)$ is the quadrature component given by

$$s_Q(t,\boldsymbol{X}_n) \triangleq \sqrt{\frac{2E_s}{T}}\sin\left(\tilde{\psi}(t,\boldsymbol{X}_n)\right), \quad nT \le t \le (n+1)T. \tag{2.42}$$

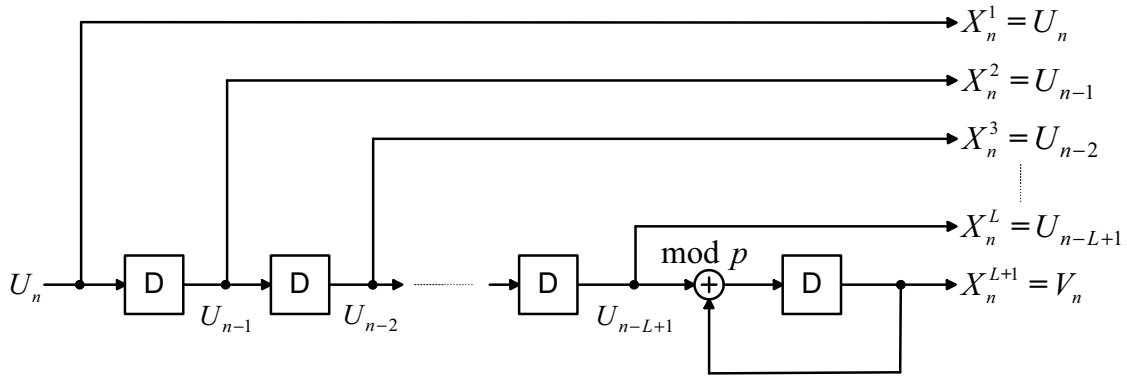

Figure 2.6: Continuous phase encoder.

Continuous Phase Encoder

The continuous phase encoder (CPE) generates the memoryless modulator input sequence, $\boldsymbol{X} = (\boldsymbol{X}_0, \boldsymbol{X}_1, \ldots)$, from the modified data stream, $\boldsymbol{U}$. The CPE calculates the vector $\boldsymbol{X}_n$ using Equation (2.36) and the recursion of Equation (2.39). An implementation of a generic CPM CPE is shown in Figure 2.6. It consists of delay elements and a modulo-p adder. The CPE can be interpreted as a linear convolutional encoder over the ring of integers modulo-p ($\mathbb{Z}_p$). The CPE can then be represented by a time-invariant trellis with pM^{L-1} states.

We let the M-ary data symbols have the property, $M = p^{k_m}$, where k_m is an integer and the modulation index is $h = \frac{v}{p}$. The data symbols may then be represented in radix-p form as

$$U_n = \sum_{j=1}^{k_m} U_n^j p^{k_m - j}, \quad nT \leq t \leq (n+1)T, \tag{2.43}$$

where each sub-symbol, U_n^j, for $n \geq 0$ and $1 \leq j \leq k_m$, is an element of the integer ring $\mathbb{Z}_p$. Each sub-symbol sequence

$$\boldsymbol{U}^j(D) = U_0^j + U_1^j D + U_2^j D^2 \ldots, \quad 1 \leq j < k_m \tag{2.44}$$

is encoded by the polynomial

$$\boldsymbol{C}^{j,j}(D) = \begin{cases} \begin{bmatrix} 1 & D & D^2 & \ldots & D^{L-1} \end{bmatrix} & 1 \leq j < k_m \\ \begin{bmatrix} 1 & D & D^2 & \ldots & D^{L-1} & \frac{D^L}{1-D} \end{bmatrix} & j = k_m \end{cases}. \tag{2.45}$$

The resulting $(k_m \times (k_m L + 1))$-dimensional generator matrix of the CPE on $\mathbb{Z}_p$ is

$$\boldsymbol{C}(D) = \begin{bmatrix} 1 & D & D^2 & \dots & D^{L-1} & \mathbf{0}_{1,L} & \cdots & \mathbf{0}_{1,L+1} \\ \mathbf{0}_{1,L} & & & \ddots & & \mathbf{0}_{1,L} & & \vdots \\ \mathbf{0}_{1,L} & & & \mathbf{0}_{1,L} & 1 & D & D^2 & \dots & D^{L-1} & \mathbf{0}_{1,L+1} \\ \mathbf{0}_{1,L} & & & \cdots & & \mathbf{0}_{1,L} & 1 & D & D^2 & \dots & D^{L-1} & \frac{D^L}{1-D} \end{bmatrix}, \tag{2.46}$$

where $\mathbf{0}_{i,j}$ represents an $(i \times j)$-dimensional matrix of zeroes.

The input and output sequences of the CPE can be represented in delay polynomial form. The input sequence is given by

$$\begin{aligned} \boldsymbol{U}(D) &= \boldsymbol{U}_0 + \boldsymbol{U}_1 D + \boldsymbol{U}_2 D^2 \dots \\ &= \left[\boldsymbol{U}^1(D) \;\; \boldsymbol{U}^2(D) \;\; \dots \;\; \boldsymbol{U}^{k_m}(D)\right], \end{aligned} \tag{2.47}$$

where

$$\boldsymbol{U}_n = \left[U_n^1 \;\; U_n^2 \;\; \dots \;\; U_n^{k_m}\right], \quad n = 0, 1, \dots, \tag{2.48}$$

and $\boldsymbol{U}^j(D)$ for $1 \leq j \leq k_m$ is given by Equation (2.44). The output sequence is given by

$$\boldsymbol{X}(D) = \boldsymbol{X}_0 + \boldsymbol{X}_1 D + \boldsymbol{X}_2 D^2 \dots, \tag{2.49}$$

where

$$\boldsymbol{X}_n = \left[X_n^{1,1} \quad \dots \quad X_n^{L,1} \quad X_n^{1,2} \quad \dots \quad X_n^{L,k_m} \quad X_n^{L+1,1}\right], \quad n = 0, 1, \dots. \tag{2.50}$$

The relationship between the input and output sequences of the CPE is then

$$\boldsymbol{X}(D) = \boldsymbol{C}(D)\boldsymbol{U}(D). \tag{2.51}$$

2.3.3 Continuous Phase Frequency Shift Keying

Continuous phase frequency shift keying (CPFSK) is a subset of CPM with a full response $(L = 1)$ rectangular frequency pulse. The phase response of CPFSK is given by

$$q(t) = \begin{cases} 0 & t \leq 0 \\ \frac{t}{2T} & 0 < t \leq T \\ \frac{1}{2} & t > T \end{cases}. \tag{2.52}$$

The data independent term, $W(t)$, of the physical tilted phase is equal to zero for CPFSK. This is illustrated using Equations (2.35) and (2.52)

$$\begin{aligned} W(t) &= \frac{\pi h(M-1)t}{T} - (M-1)2\pi h \sum_{i=n-L+1}^{n} q(t-iT) - (M-1)\pi h(n-L+1) \\ &= \frac{\pi h(M-1)t}{T} - (M-1)2\pi h q(t-nT) - (M-1)\pi hn \\ &= \frac{\pi h(M-1)t}{T} - (M-1)2\pi h \frac{t-nT}{2T} - (M-1)\pi hn \\ &= 0, \qquad\qquad nT \le t \le (n+1)T. \end{aligned} \tag{2.53}$$

Substituting Equations (2.36), (2.37) and (2.53) into Equation (2.34), we find that the physical tilted phase for CPFSK is given by

$$\begin{aligned} \tilde{\psi}(t, \boldsymbol{X}_n) &= \left[2\pi h \left[\sum_{i=0}^{n-1} U_i\right] \mod p + 4\pi h \sum_{i=n-1+1}^{n} U_i q(t-iT) + W(t)\right] \mod 2\pi \\ &= \left[2\pi h \left[\sum_{i=0}^{n-1} U_i\right] \mod p + 2\pi h U_n \frac{t-nT}{T}\right] \mod 2\pi \\ &= \left[2\pi h \left(V_n + U_n \frac{t-nT}{T}\right)\right] \mod 2\pi \\ &= \left[2\pi h \left(X_n^2 + X_n^1 \frac{t-nT}{T}\right)\right] \mod 2\pi, \quad nT \le t \le (n+1)T. \end{aligned} \tag{2.54}$$

The memoryless modulator output during the n-th symbol interval then becomes

$$\begin{aligned} s(t, \boldsymbol{X}_n) &= \sqrt{\frac{2E_s}{T}} \cos(2\pi f_1 t + \tilde{\psi}(t, \boldsymbol{X}_n)) \\ &= \sqrt{\frac{2E_s}{T}} \cos\left(2\pi f_1 t + 2\pi h \left(X_n^2 + X_n^1 \frac{t-nT}{T}\right)\right), \quad nT \le t \le (n+1)T. \end{aligned} \tag{2.55}$$

From Equation (2.36) we see that the input to the memoryless modulator during the n-th symbol interval for CPFSK is

$$\boldsymbol{X}_n = [X_n^1 \quad X_n^2] = [U_n \quad V_n], \tag{2.56}$$

where

$$V_n = [V_{n-1} + U_{n-1}] \mod p. \tag{2.57}$$

If we consider the radix-p form of the data symbols described by Equation (2.43), then

$$V_n = \left[V_{n-1} + U_{n-1}^{k_m}\right] \mod p. \tag{2.58}$$

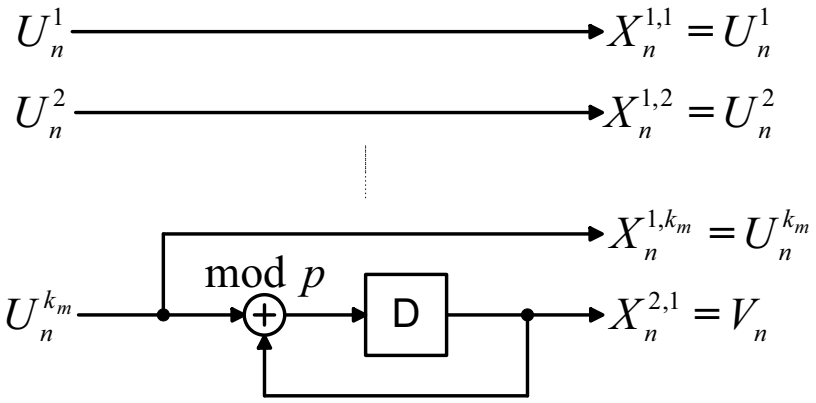

Figure 2.7: Continuous phase encoder for CPFSK.

The CPE sub-encoders of Equation (2.45) for CPFSK with $h = \frac{v}{p}$ and $M = p^{k_m}$ reduce to

$$\boldsymbol{C}^{j,j}(D) = \begin{cases} [1] & 1 \leq j < k_m \\ \begin{bmatrix} 1 & \frac{D}{1-D} \end{bmatrix} & j = k_m \end{cases} . \tag{2.59}$$

The overall generator matrix is then

$$\boldsymbol{C}(D) = \begin{bmatrix} \boldsymbol{I}_{k_m-1} & 0 & 0 \\ 0 & 1 & \frac{D}{1-D} \end{bmatrix}, \tag{2.60}$$

where $\boldsymbol{I}_i$ is the $(i \times i)$ identity matrix. An implementation of the CPE for CPFSK on $\mathbb{Z}_p$ is illustrated by Figure 2.7. Note that this CPE is inherently systematic.

For the common case of $p = M$ $(k_m = 1)$, the CPE is linear over the integer ring $\mathbb{Z}_M$. The CPE generator matrix of Equation (2.60), for M-ary CPFSK with $h = \frac{v}{M}$ then becomes

$$\boldsymbol{C}(D) = \begin{bmatrix} 1 & \frac{D}{1-D} \end{bmatrix}. \tag{2.61}$$

In this work, M-ary CPFSK with $h = \frac{1}{M}$ $(p = M)$ is used in the examples and is denoted as M-CPFSK. Minimum shift keying (MSK) is a special case of M-CPFSK that has $h = \frac{1}{2}$ and a binary alphabet. The value of h changes the balance between the bandwidth and the energy required by the modulation. Large values of h cause bandwidth expansion. Letting $h = \frac{1}{M}$ is a good tradeoff [7].

2.4 Space-Time Coding

A common method to combat multipath fading effects, is to use diversity techniques, which provide replicas of the information signal in various forms to the receiver. One such technique that uses spatial and temporal diversity is called space-time coding. Spectral efficiency can be significantly improved by using multiple antennas at both the transmitter and the receiver. Multiple-input multiple-output (MIMO) systems consist of a transmitter with $L_t > 1$ antennas and a receiver with $L_r > 1$ antennas. Telatar [2], and Foschini and Gans [1] developed theoretical results for the capacity of a MIMO system. They showed that MIMO system capacity is linearly proportional to the minimum of L_r and L_t and illustrated the potential spectral efficiency of such schemes [3].

Two forms of MIMO communication techniques have developed. Layered or threaded architectures that incorporate traditional coding schemes were introduced by Foschini [47] and are known as BLAST techniques. Spatial multiplexing is used to transmit independent data streams from different transmit antennas and in general requires that $L_r \geq L_t$. These schemes utilize signal processing to reduce decoding complexity and allow for high throughput and spectral efficiencies. The condition for L_r to be greater than or equal to L_t can be relaxed through the use of more advanced detection/decoding [3].

The second technique is space-time coding (STC) [48]. It employs multiple transmit antennas and requires one or more receive antenna, which can result in cheaper receivers than for BLAST techniques. STC introduces spatial and temporal correlation to the transmitted signals without increasing the total transmit power or bandwidth [48]. Both diversity and coding gains can be realized. However, in general space-time coded systems suffer a throughput loss. Space-time coded systems can be divided into two distinct forms, space-time block codes and space-time trellis codes.

2.4.1 Space-Time Block Codes

The Alamouti transmit diversity scheme [19] achieves full spatial diversity using two transmit antennas. Generalizing this scheme to any number of transmit antennas resulted in orthogonal space-time block codes (STBC), which are designed to achieve full transmit diversity equal to the number of transmit antennas. Orthogonal STBC can have simple maximum likelihood decoding structures that only require linear processing at the receiver [19, 49]. However, the

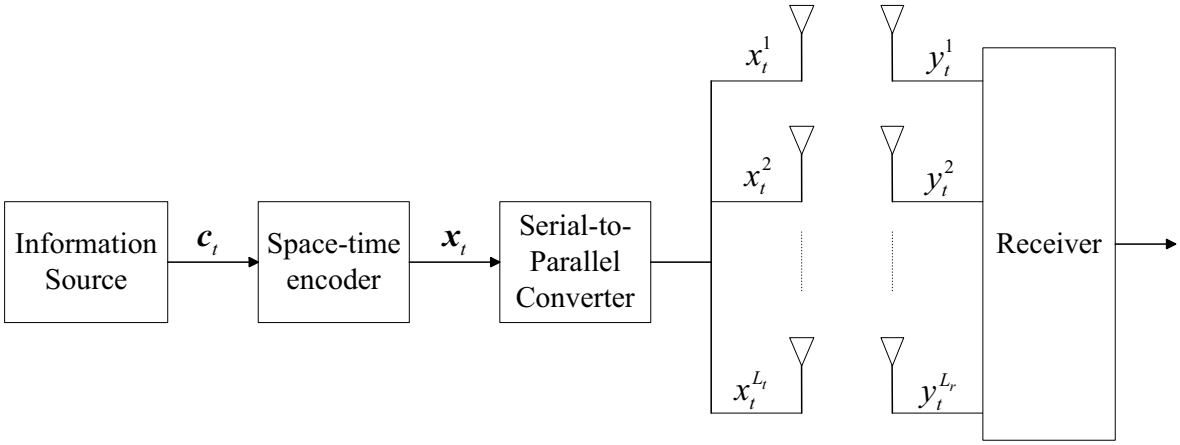

Figure 2.8: Baseband space-time coded system.

rate of orthogonal STBC suffers as the number of transmit antennas is increased and they do not yield coding gain. More recent quasi-orthogonal STBC designs [50] have enabled better data rates, at the cost of greater decoding complexity. There is a trade-off with performance at high signal to noise ratio due the inferior diversity of the quasi-orthogonal systems. The use of signal constellation rotations [51, 52] can be used to inhibit the diversity loss to some extent.

2.4.2 Space-Time Trellis Codes

Space-time trellis codes (STTC) can achieve coding gain, spectral efficiency and diversity advantage on frequency flat fading channels. In general, the error rate performance of STTC is superior to STBC, but the decoding is more complex. The encoder maps binary data to modulation symbols according to a mapping function. This mapping may be described by a trellis diagram. In this section, we summarize the theory of space-time code design and analysis presented in [3]. We consider the baseband space-time coded system with L_t transmit antennas and L_r receive antennas shown in Figure 2.8.

The input to the space-time encoder at each time instant t is a block of $\log_2 M$ binary information symbols. We denote the block as

$$\boldsymbol{c}_t = \left[c_t^1,\ c_t^2,\ \ldots, c_t^{\log_2 M}\right]. \tag{2.62}$$

The space-time encoder maps the data to L_t modulation symbols drawn from a set of M

points. These modulated symbols are fed to a serial-to-parallel converter, which forms the vector

$$\boldsymbol{x}_t = \left[x_t^1,\ x_t^2,\ \ldots, x_t^{L_t}\right]^T, \tag{2.63}$$

where ^{T} denotes the transpose of a vector or matrix. The modulation symbol, x_t^i, for $1 \leq i \leq L_t$, is transmitted from the i-th transmit antenna at time instant t.

The received signal on the j-th antenna at time t is then given by

$$y_t^j = \sum_{i=1}^{L_t} \tilde{m}_{j,i}^t x_t^i + n_j^t, \quad 1 \leq j \leq L_r, \tag{2.64}$$

where n_j^t represents AWGN and $\tilde{m}_{j,i}^t$ is the fading coefficient representing the fading channel between transmit antenna i and receive antenna j. The fading coefficients form the matrix

$$\tilde{\boldsymbol{m}}^t = \begin{bmatrix} \tilde{m}_{1,1}^t & \tilde{m}_{1,2}^t & \ldots & \tilde{m}_{1,L_t}^t \\ \tilde{m}_{2,1}^t & \tilde{m}_{2,2}^t & \ldots & \tilde{m}_{2,L_t}^t \\ \tilde{m}_{3,1}^t & \tilde{m}_{3,2}^t & \ldots & \tilde{m}_{3,L_t}^t \\ \vdots & \vdots & \ddots & \ldots \\ \tilde{m}_{L_r,1}^t & \tilde{m}_{L_r,2}^t & \ldots & \tilde{m}_{L_r,L_t}^t \end{bmatrix}. \tag{2.65}$$

In a slow fading channel the fading coefficients are assumed to be constant during a frame and vary from one frame to the next, we call this quasi-static fading [4]. Therefore, during a frame $\tilde{\boldsymbol{m}} = \tilde{\boldsymbol{m}}^t$ and the quasi-static channel coefficients are then given by $\tilde{m}_{j,i} = \tilde{m}_{j,i}^t$ for $1 \leq i \leq L_t$ and $1 \leq i \leq L_r$. The coefficients are assumed to be independent complex Gaussian random variables with 0 mean and variance $\frac{1}{2}$ per dimension, which represents a Rayleigh fading channel. The decoder selects the hypothesized received sequence having the minimum Euclidean distance from the actual received sequence. The metric is given by

$$\sum_t \sum_{j=1}^{L_r} \left| y_t^j - \sum_{i=1}^{L_t} \tilde{m}_{j,i}^t x_t^i \right|^2. \tag{2.66}$$

As an example, we consider a STTC with 4-ary phase shift keying (QPSK) and 2 transmit antennas. A generic encoder for a 2 transmit antenna, QPSK scheme is shown in Figure 2.9 [3]. The binary input stream to the k-th shift register, for $1 \leq k \leq \log_2 M$, is denoted $\boldsymbol{c}^k(D)$ and is given by

$$\boldsymbol{c}^k(D) = c_0^k + c_1^k D + c_2^k D^2 +, \ldots, \quad c_t^k \in \{0, 1\}, \quad k = 1, 2, \quad t = 0, 1, 2, \ldots. \tag{2.67}$$

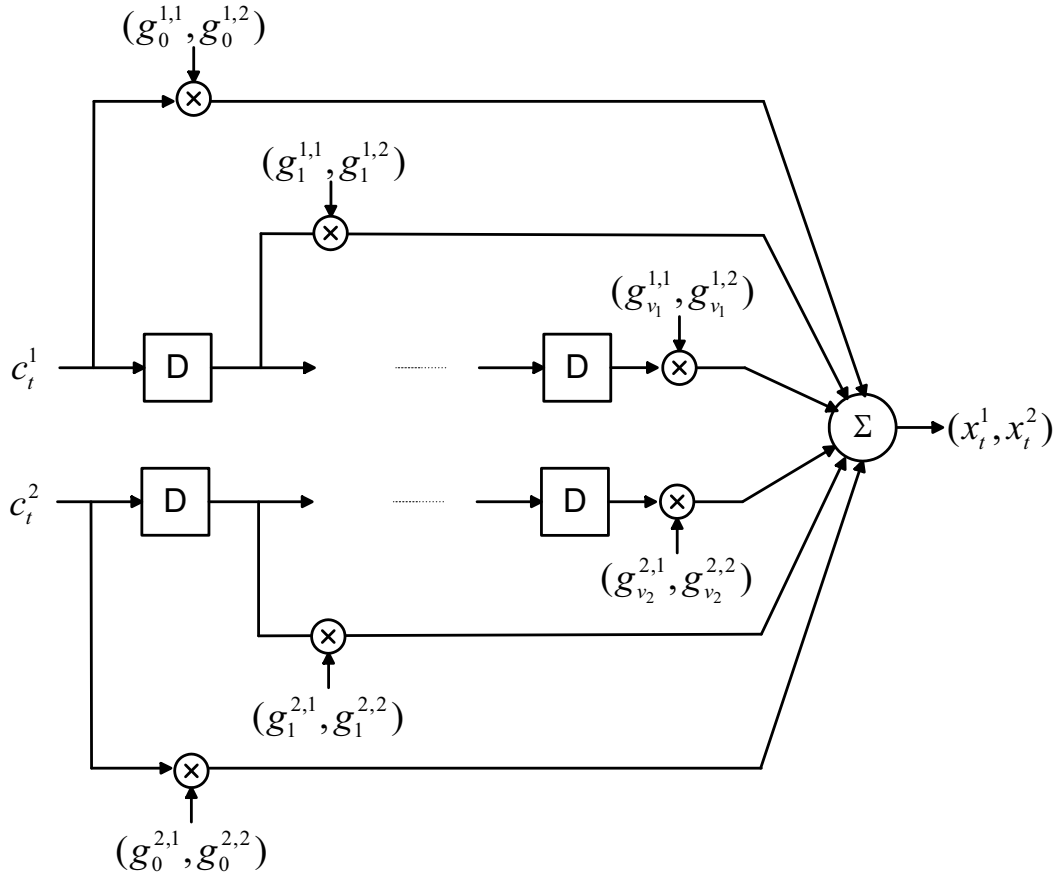

Figure 2.9: Encoder for space-time coded QPSK with 2 transmit antennas.

The generator polynomials of the STTC corresponding to the i-th transmit antenna are given by

$$\boldsymbol{G}^{1,i}(D) = g_0^{1,i} + g_1^{1,i}D + g_2^{1,i}D^2 + , \ldots + g_{\nu_1}^{1,i}D^{\nu_1}, \quad g_\nu^{1,i} \in \{0,1,2,3\}, \quad i = 1,2, \quad \nu = 0,1,2,\ldots,\nu_1, \tag{2.68}$$

and

$$\boldsymbol{G}^{2,i}(D) = g_0^{2,i} + g_1^{2,i}D + g_2^{2,i}D^2 + , \ldots + g_{\nu_2}^{2,i}D^{\nu_2}, \quad g_\nu^{2,i} \in \{0,1,2,3\}, \quad i = 1,2, \quad \nu = 0,1,2,\ldots,\nu_2. \tag{2.69}$$

The sequence transmitted from antenna i is given by

$$\boldsymbol{x}^i(D) = \left[\boldsymbol{c}^1(D)\ \boldsymbol{c}^2(D)\right] \begin{bmatrix} \boldsymbol{G}^{1,i}(D) \\ \boldsymbol{G}^{2,i}(D) \end{bmatrix} \mod 4, \quad 1 \le i \le L_t = 2. \tag{2.70}$$

If we set $\begin{bmatrix} \boldsymbol{G}^{1,i}(D) \\ \boldsymbol{G}^{2,i}(D) \end{bmatrix} = \begin{bmatrix} 2 \\ 1 \end{bmatrix}$, for any i, where $1 \le i \le L_t$, then the space-time trellis code

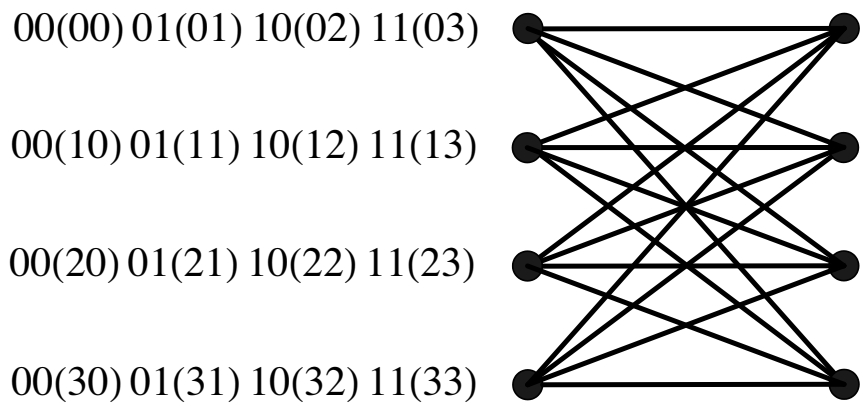

Figure 2.10: Trellis structure for space-time coded QPSK with 2 transmit antennas.

will be systematic; the encoder maps the binary information to a QPSK sequence to transmit from the i-th antenna.

An example of a QPSK STTC, is the systematic delay diversity scheme that has the generator polynomials

$$\begin{aligned} \boldsymbol{G}^{1,1}(D) &= 2D, \\ \boldsymbol{G}^{1,2}(D) &= 2, \\ \boldsymbol{G}^{2,1}(D) &= D, \\ \boldsymbol{G}^{2,2}(D) &= 1. \end{aligned} \tag{2.71}$$

The trellis of the encoder is shown in Figure 2.10. The branches are labelled with the input and output symbols, $c_t^1 c_t^2 (x_t^1 x_t^2)$.

2.4.3 Space-Time Code Design

Design criteria for linearly modulated space-time coded systems, transmitted over a quasi-static fading channel, are presented by Guey et al. in [53] and Tarokh et al. in [4]. The criteria were derived by optimizing the worst case pairwise error probability (PEP) at high signal to noise ratio (SNR). In this section, we summarize the derivation of the design criteria following [3].

The probability that the decoder selects an incorrect sequence

$$\check{\boldsymbol{x}} = (\check{\boldsymbol{x}}_1,\ \check{\boldsymbol{x}}_2,\ \ldots), \tag{2.72}$$

instead of the correct sequence

$$\boldsymbol{x} = (\boldsymbol{x}_1,\ \boldsymbol{x}_2,\ \ldots), \tag{2.73}$$

is the pairwise error probability $P(\boldsymbol{x} \rightarrow \check{\boldsymbol{x}})$. A pairwise error occurs when

$$\sum_{j=1}^{L_r} \sum_{t} \left| \sum_{i=1}^{L_t} \tilde{m}_{j,i} \left[\check{x}_t^i - x_t^i \right] \right|^2 \leq \sum_{j=1}^{L_r} \sum_{t} 2\mathbb{R} \left\{ (n_j^t)^* \sum_{i=1}^{L_t} \tilde{m}_{j,i} \left[\check{x}_t^i - x_t^i \right] \right\}. \tag{2.74}$$

Assuming that ideal channel state information is available at the receiver, the left hand side of the inequality of Equation (2.74) is a constant equal to

$$\begin{aligned} d_m^2(\boldsymbol{x}, \check{\boldsymbol{x}}) &= ||\tilde{\boldsymbol{m}} \cdot (\check{\boldsymbol{x}} - \boldsymbol{x})||^2 \\ &= \sum_{j=1}^{L_r} \sum_{t} \left| \sum_{i=1}^{L_t} \tilde{m}_{j,i} \left[\check{x}_t^i - x_t^i \right] \right|^2 . \end{aligned} \tag{2.75}$$

The right hand side of the inequality of Equation (2.74) is a zero mean Gaussian random variable. The pairwise error probability conditioned on the fading matrix, $\tilde{\boldsymbol{m}}$, is then

$$P(\boldsymbol{x} \rightarrow \check{\boldsymbol{x}} | \tilde{\boldsymbol{m}}) = Q\left(\sqrt{\frac{E_s}{2N_0} d_m^2(\boldsymbol{x}, \check{\boldsymbol{x}})} \right), \tag{2.76}$$

where E_s is the energy per symbol on each transmit antenna and $Q(x)$ is the Gaussian Q function defined by

$$Q(x) = \frac{1}{\sqrt{2\pi}} \int_x^\infty \exp\left(\frac{-u^2}{2} \right) du. \tag{2.77}$$

Using the inequality

$$Q(x) \leq \frac{1}{2} \exp\left(-\frac{x^2}{2} \right), \quad x \geq 0, \tag{2.78}$$

the conditional pairwise error probability of Equation (2.76) can be upper bounded by

$$P(\boldsymbol{x} \rightarrow \check{\boldsymbol{x}} | \tilde{\boldsymbol{m}}) \leq \frac{1}{2} \exp\left(-\frac{E_s}{4N_0} d_m^2(\boldsymbol{x}, \check{\boldsymbol{x}}) \right). \tag{2.79}$$

In order to evaluate the unconditional pairwise error probability, a codeword distance matrix is constructed from the differences between pairs of distinct code sequences. We define the codeword difference matrix, for the sequences $\boldsymbol{x}$ and $\check{\boldsymbol{x}}$, as

$$\boldsymbol{B}(\boldsymbol{x}, \check{\boldsymbol{x}}) = \boldsymbol{x} - \check{\boldsymbol{x}}, \tag{2.80}$$

and the codeword distance matrix, for the sequences $\boldsymbol{x}$ and $\check{\boldsymbol{x}}$, as

$$\boldsymbol{A}(\boldsymbol{x}, \check{\boldsymbol{x}}) = \boldsymbol{B}(\boldsymbol{x}, \check{\boldsymbol{x}}) \cdot \boldsymbol{B}^H(\boldsymbol{x}, \check{\boldsymbol{x}}), \tag{2.81}$$

where ^{H} denotes the Hermitian or transpose conjugate of a matrix.

The matrix $\boldsymbol{A}(\boldsymbol{x}, \check{\boldsymbol{x}})$ is non-negative definite Hermitian, and hence its eigenvalues are non-negative definite [54]. Therefore, there is a unitary matrix $\boldsymbol{V}$ and a diagonal matrix $\boldsymbol{D}$ such that

$$\boldsymbol{D} = \boldsymbol{V}\boldsymbol{A}(\boldsymbol{x}, \check{\boldsymbol{x}})\boldsymbol{V}^H. \tag{2.82}$$

The diagonal elements of $\boldsymbol{D}$ are the eigenvalues of $\boldsymbol{A}(\boldsymbol{x}, \check{\boldsymbol{x}})$, which we denote $\lambda_i \geq 0$ for $1 \leq i \leq L_t$. Assuming quasi-static fading, we let $\tilde{\boldsymbol{m}}_j = [\tilde{m}_{j,1}, \tilde{m}_{j,2}, \ldots, \tilde{m}_{j,L_t}]$ denote the array of fading coefficients that affect the signal on the j-th receive antenna. Then, manipulating Equation (2.75) we find

$$\begin{aligned} d_m^2(\boldsymbol{x}, \check{\boldsymbol{x}}) &= \sum_{j=1}^{L_r} \tilde{\boldsymbol{m}}_j \boldsymbol{A}(\boldsymbol{x}, \check{\boldsymbol{x}}) \tilde{\boldsymbol{m}}_j^H \\ &= \sum_{j=1}^{L_r} \tilde{\boldsymbol{m}}_j \boldsymbol{V}^H \boldsymbol{D} \boldsymbol{V} \tilde{\boldsymbol{m}}_j^H \\ &= \sum_{j=1}^{L_r} \sum_{i=1}^{L_t} \lambda_i \left|\beta_{i,j}\right|^2, \end{aligned} \tag{2.83}$$

where $\beta_{i,j} = \tilde{\boldsymbol{m}}_j {\boldsymbol{v}_i}^H$ and $\boldsymbol{v}_i$ is the i-th row of $\boldsymbol{V}$. Then, substituting Equation (2.83) into the inequality of Equation (2.79), the conditional pairwise error probability is bounded by

$$P(\boldsymbol{x} \to \check{\boldsymbol{x}} | \tilde{\boldsymbol{m}}) \leq \frac{1}{2} \exp\left(-\frac{E_s}{4N_0} \sum_{j=1}^{L_r} \sum_{i=1}^{L_t} \lambda_i \left|\beta_{i,j}\right|^2 \right). \tag{2.84}$$

To find a bound on the unconditional pairwise error probability, the inequality of Equation (2.84) is averaged with respect to the random variables, $\beta_{i,j}$ for $1 \leq i \leq L_t$ and $1 \leq j \leq L_r$. Further detail of this process is given in Section 4.2. Assuming a small number of parallel spatial channels, the fundamental design parameters are the diversity gain and the coding gain. These parameters are found respectively from the minimum rank, and the minimum product of the nonzero eigenvalues, of $\boldsymbol{A}(\boldsymbol{x}, \check{\boldsymbol{x}})$, over all pairwise error events. We call the coding gain the product distance. The diversity gain is the more important parameter; it determines the asymptotic slope of the system's error rate performance curves. The diversity gain is upper bounded by the number of transmit antennas multiplied by the number of receive antennas. In general, when designing space-time codes using the rank and product distance criteria, the transmit diversity is maximized first and the coding gain is a secondary consideration. Obtaining full transmit diversity with a linear modulation implies a restriction on the rate and code complexity [4].

The early focus of STC design was on maximizing the transmit diversity and maximizing the coding gain. However, the performance of a STC is also dependent on its product distance spectrum [55]. The product distance spectrum is the enumeration of the product distance measures of important pairwise error events. It provides a more complete performance characterization and thus, is a more accurate criterion for STC design. However, its computation is more complex.

If there is a large number of parallel spatial channels, the bound on the PEP can be approximated using the trace of the codeword distance matrices, or equivalently, the Euclidean distance between codewords [56, 57]. The bound is valid when there is a large number of independent sub-channels. This is assumed to be the case when the transmit diversity multiplied by the number of receive antennas exceeds three. Maximizing the minimum trace of the signal distance matrices over all distinct transmitted codeword pairs can then be used as a STTC design criterion. The Euclidean distance spectrum can provide a more complete performance characterization of a STC system, with a large number of independent sub-channels.

Thus, for linear modulations the design criteria [56, 57] for optimal space-time codes depends on the value of $\rho_{\min} L_r$, where $\rho_{\min}$ is the minimum rank of the codeword distance matrices over all pairs of distinct codewords, and $\rho_{\min} \leq L_t$. If $\rho_{\min} L_r \leq 3$, then $\rho_{\min}$ and the minimum product distance [4] of the codeword distance matrices over all pairs of distinct codewords, are the important parameters for code design. If $\rho_{\min} L_r > 3$, then maximizing the minimum trace of the codeword distance matrices over all pairs of distinct codewords, or equivalently the minimum squared Euclidean distance, should be used as the design criterion.

In [4], some simple phase shift keyed (PSK) space-time codes were found by hand design; these codes have maximum diversity gain, but not necessarily maximum coding gain. Using extensive computer searches Grimm [58] and Baro et al. [59] independently found STTC with improved coding gain. Traditional code design for single antenna systems is performed over finite fields or rings. STTC design using the rank and the product distance criteria defined over codeword distance matrices can be more difficult. Hammons and Gamal [16] derived general code constructions for binary PSK and QPSK with an arbitrary number of transmit antennas that guarantee full spatial diversity. The design techniques specify criteria on the generator matrix relating to the unmodulated code-words over finite fields or rings. This can simplify the search for good STTC. These code constructions are used by Zhang and Fitz to create full diversity design criteria for STTC CPM schemes [11]. These criteria are described in the next

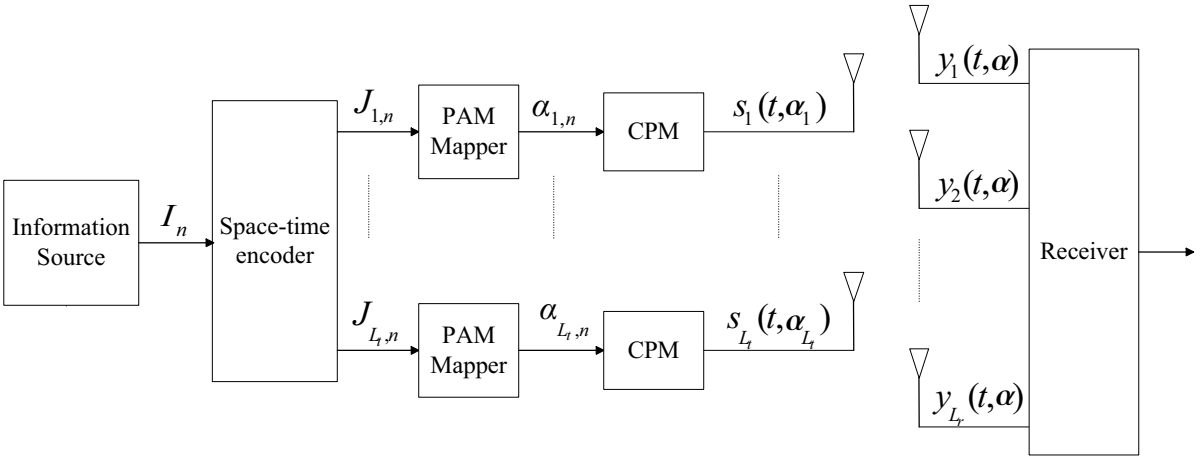

Figure 2.11: Space-time coded CPM system.

section.

2.5 Space-Time Trellis Coding with CPM

A summary of research on MIMO and space-time coded continuous phase modulation (CPM) is presented in Section 1.1. In this section, we present an in depth review of the current state of space-time trellis coded CPM research. We then identify possible areas for further research and provide motivation for the original research presented in the following chapters of this thesis.

The promise of good performance by space-time trellis coded CPM systems is illustrated by Cavers in [5] and [6]. Cavers presents space-time coded schemes using minimum shift keying (MSK). The decoding complexity of the MSK schemes is shown to be lower than that of QPSK (linearly modulated) space-time coded schemes by a ratio that increases exponentially with the number of transmit antennas. The simple delay diversity space-time code is shown to have better performance with MSK than with QPSK, for systems with 2 and 3 transmit antennas. There are a number of ways to extend the design presented by Cavers, such as more powerful space-time codes, different CPM formats and receive diversity.

Zhang and Fitz have investigated more general space-time coded CPM. The space-time coded CPM system presented by Zhang and Fitz in [11] is shown in Figure 2.11. A CPM modulated signal is transmitted from each transmit antenna. The traditional representation of

the CPM modulator, which is described in Section 2.3, is used. Therefore, following the space-time encoder, pulse amplitude mappers (PAM) are required to map the space-time encoded data $J_{i,n} \in \{0, 1, \ldots, M-1\}$ to the channel symbols $\alpha_{i,n} \in \{-(M-1), -(M-3), \ldots, M-1\}$ for $1 \leq i \leq L_t$.

The modulation index is set to $h = \frac{v}{p}$ where v and p are relatively prime integers. Then, the physical phase is constrained to lie on a trellis. The state of the phase at the i-th transmit antenna is dependent on the vector

$$S_{i,n} = \left[\tilde{\theta}_{i,n}, \alpha_{i,n-1}, \ldots, \alpha_{i,n-L+1}\right], \quad 1 \leq i \leq L_t, \tag{2.85}$$

where $\tilde{\theta}_{i,n}$ is defined by Equation (2.18) as

$$\tilde{\theta}_{i,n} = \left[\pi h \sum_{j=0}^{n-L} \alpha_{i,j}\right] \mod 2\pi. \tag{2.86}$$

Each vector described by Equation (2.85) for $1 \leq i \leq L_t$, has $2pM^{L-1}$ possible states.

Zhang and Fitz assume that the space-time encoder is feedforward, has constraint length ν, and is defined over a finite field. The overall transmitter may be represented by a supertrellis and the state of the trellis at time nT is

$$S_n = \left[\tilde{\theta}_{1,n}, \ldots, \tilde{\theta}_{L_t,n}, I_{n-1}, \ldots, I_{n-L-\nu+1}\right], \tag{2.87}$$

where the information symbols, I_n, are binary. This supertrellis has $(2p)^{L_t}2^{\nu+L-1}$ states and may take on $p^{L_t}2^{\nu+L-1}$ of these during any given interval. For example, consider M-ary CPFSK with $h = \frac{1}{M}$, which we denote as M-CPFSK, used with the delay diversity space-time code. Delay diversity with L_t transmit antennas has a constraint length of $L_t - 1$. CPFSK is full response, that is, $L = 1$ and with $h = \frac{1}{M}$, variable $p = M$. The number of states in the supertrellis for this system using the space-time coded CPM scheme proposed in [11] is

$$S_T = (2p)^{L_t}2^{\nu+L-1} = (2M)^{L_t}2^{L_t-1} = M^{L_t}2^{2L_t-1}. \tag{2.88}$$

We note that the supertrellis of this system is time-varying (and can take on one of $M^{L_t}2^{L_t-1}$ states during a given interval) because the traditional phase model, described by Equation (2.17), is used to represent the modulation.

In [11], design criteria are presented for space-time coded CPM in quasi-static fading, for a small number of parallel spatial channels. The PEP is shown to have an upper bound

analogous to that derived for linearly modulated space-time codes, with a different distance matrix. The signal distance matrix for space-time coded CPM is defined as

$$\boldsymbol{S}=\begin{bmatrix} \int_0^{N_cT} |\triangle_1(t)|^2 dt & \cdots & \int_0^{N_cT} \triangle_1(t)\triangle_{L_t}^*(t)dt \\ \vdots & \vdots & \vdots \\ \int_0^{N_cT} \triangle_{L_t}(t)\triangle_1^*(t)dt & \cdots & \int_0^{N_cT} |\triangle_{L_t}(t)|^2 dt \end{bmatrix}, \tag{2.89}$$

where $\triangle_i(t)$ is the continuous time difference between the transmitted and the decoded signal from the i-th transmit antenna. The PEP bound is derived as

$$P(\boldsymbol{\alpha} \rightarrow \breve{\boldsymbol{\alpha}}) \leq \frac{\begin{pmatrix} 2L_r\rho - 1 \\ L_r\rho - 1 \end{pmatrix} {N_0}^{L_r\rho}}{(\prod_{i=1}^{\rho} \lambda_i)^{L_r}}, \tag{2.90}$$

where λ_i are the non-zero eigenvalues of the signal distance matrix, and ρ is the number of non-zero eigenvalues or equivalently, the rank of the signal distance matrix. This bound is analogous to the PEP bound for linearly modulated space-time codes derived by Fitz et al. in [60]. From this result, Zhang and Fitz conclude that the rank and product distance design criteria found for space-time codes with linear modulation, can be applied to space-time coded CPM, as long as the appropriate distance matrix, $\boldsymbol{S}$, is taken into account.

The transmit diversity, d, of a space-time coded CPM system in quasi-static fading is limited [8, 61] by

$$d \leq 1 + \left\lfloor L_t - \frac{R_S}{\log_2(M)} \right\rfloor, \tag{2.91}$$

where M is the size of the CPM alphabet, R_S is the system throughput in bits per symbol period and L_t is the number of transmit antennas. Conditions for full spatial diversity to be achieved in space-time coded CPM systems are discussed in [11]. For the minimum rank of all signal distance matrices to equal the number of transmit antennas, such that full spatial diversity is achieved, a necessary and sufficient condition is to make all continuous time differences from all antennas linearly independent over the complex field $\mathbb{C}$. Systems that satisfy this condition and guarantee full diversity include:

- Zeros symmetry [58]. Delay diversity is a special case of zeroes symmetry.
- Using different CPM schemes on each transmit antenna. However, this method may require more bandwidth and be more complex.

- Memoryless repetition coding with different mapping rules on each antenna. The number of transmit antennas must be less than the alphabet size. This method does not work for linearly modulated space-time codes.

General code constructions that guarantee full diversity are developed in [11]. Linear decompositions of CPM signals [32, 62, 63] are used to find rank criteria for various space-time coded CPM systems. The criteria are based on the BPSK binary rank criterion and the QPSK binary rank criterion for PSK signals described in [16]. Using Rimoldi's decomposition of CPM [32] full diversity criteria were derived for full response 2^n-ary CPM, binary 2RC and binary 2REC, all with $h = 0.5$, and full response 4^n-ary CPM, with $h \in \{0.25, 0.75\}$. The modulation, 2RC, has an $L = 2$ symbol period raised cosine frequency pulse and the modulation, 2REC, has an $L = 2$ symbol period rectangular frequency pulse. Laurent's approximation of binary CPM [62] and the generalization to M-ary CPM [63], are used to derive general code constructions in a similar manner. The criteria are for the approximations of any binary CPM with $h = 0.5$, and any 4-ary CPM with $h \in \{0.25, 0.5, 0.75\}$.

Simulations presented in [11] of the frame error rate performance of rate-$\frac{1}{L_t}$ space-time codes with L_t transmit antennas and one receive antenna verify that the code constructions yield full diversity systems. A rate-$\frac{k}{m}$ code produces m coded symbols for every k input symbols. The only means of increasing the system throughput of a scheme with a rate-$\frac{1}{L_t}$ space-time code is via a higher modulation alphabet. The throughput of a system with a rate-$\frac{1}{L_t}$ space-time code is limited to $\log_2(M)$ bits per symbol period. The more general criteria to find full diversity systems, based on CPM approximations, are not valid for $M > 4$.

The design criteria presented in [11] provide means to find full diversity space-time coded systems. However, no means is provided to narrow the search once the full rank codes are identified. As we will show in Chapter 4, there can be a large performance variation between different full rank systems, especially when receive diversity is considered. The criteria derived for STTC CPM based on the QPSK binary rank criterion, are sufficient but not necessary conditions to guarantee full diversity. Thus, some full diversity codes may not be identified using this method.

In [12], Cheng and Lu derive design criteria for CPFSK modulated space-time codes. They find that the rank and product distance criteria for linear modulations are valid for CPFSK space-time code design (as is shown in [11] for more general CPM), considering a matrix that

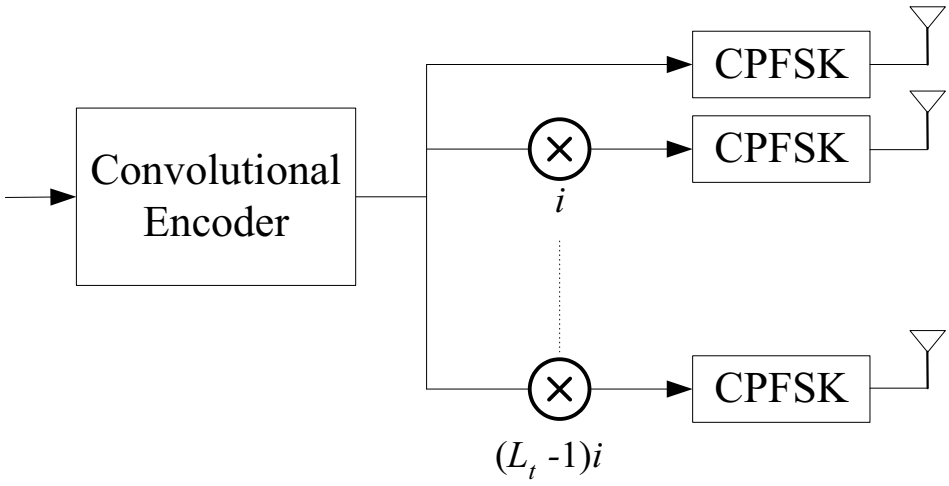

Figure 2.12: Space-time coded CPFSK transmitter.

may be interpreted as the signal distance matrix as defined by Equation (2.89). Cheng and Lu extend the space-time coded CPFSK design criteria to consider fast-fading channels. These criteria are also based on the design criteria for linearly modulated space-time codes.

A system with a ring convolutional encoder, followed by modulo-M multipliers and CPFSK modulators, is presented in [12]. The space-time coded CPFSK system is illustrated in Figure 2.12. A design criterion for the system in a fast fading channel is proposed that maximizes the pseudo-transmit diversity of the system, where the pseudo-transmit diversity is a lower bound on the true transmit diversity [12]. Cheng and Lu assert that the pseudo-transmit diversity is often equal to the system's true transmit diversity. The pseudo-transmit diversity is maximized by selecting the multiplier factor i, which is constrained by $1 \leq i < M$, to maximize the spatial diversity and by choosing a convolutional encoder that maximizes the Hamming distance. The effects of the coding inherent to the modulation are not considered.

The space-time encoder illustrated by Figure 2.13 is also discussed in [12]. The encoder consists of a ring convolutional encoder followed by a channel interleaver and then modulo-M multipliers. The receiver consists of a spatial CPFSK demodulator, a de-interleaver and a Viterbi decoder. No code design methods are given for this model. Effectively, the inner code of the system consists of the modulo-M multipliers and the continuous phase encoders of the CPFSK modulators. A trellis structure representing the CPE states of the modulators is presented. The state transitions are time-dependent.

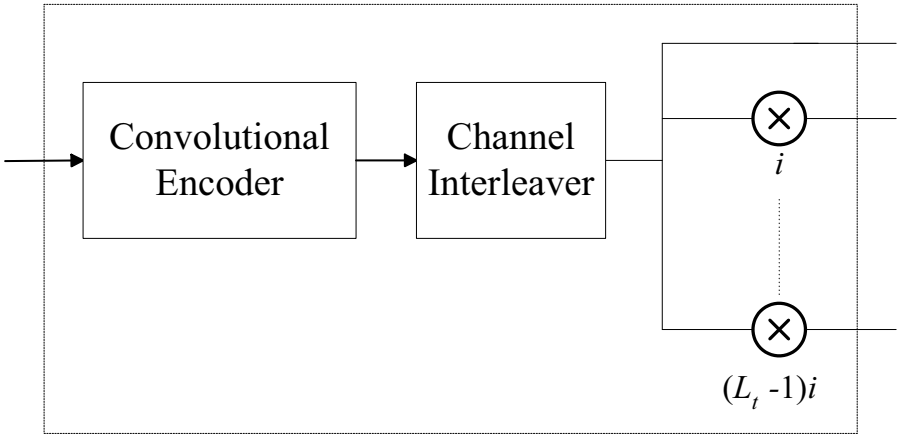

Figure 2.13: Space-time encoder.

Sykora [13] also investigates space-time code design with CPM. Sykora follows the method used to derive design criteria for linearly modulated space-time codes in [3, 4] to arrive at the conditional PEP

$$P(\boldsymbol{U} \rightarrow \check{\boldsymbol{U}}|\tilde{\boldsymbol{m}}) \leq \frac{1}{2\sqrt{\pi}} \exp\left(-\frac{1}{8N_0} d_m^2(\boldsymbol{U}, \check{\boldsymbol{U}})\right), \tag{2.92}$$

where $d_m^2(\boldsymbol{U}, \check{\boldsymbol{U}})$ is the modified Euclidean distance between the faded received signal sequences. To avoid further computation in deriving the average probability of a pairwise error, Sykora averages the modified Euclidean distance directly

$$\overline{d_m^2}(\boldsymbol{U}, \check{\boldsymbol{U}}) = E\left[d_m^2(\boldsymbol{U}, \check{\boldsymbol{U}})\right], \tag{2.93}$$

where $\overline{d_m^2}(\boldsymbol{U}, \check{\boldsymbol{U}})$ can be related to the trace of the signal distance matrix given by Equation (2.89). This reveals a design criterion based on maximizing the averaged squared distance, $\overline{d_m^2}(\boldsymbol{U}, \check{\boldsymbol{U}})$. To calculate the distance, a distance evaluation trellis is defined that has a different form to the modulator trellis. Both trellises (which are not independent) are required to evaluate the distance. This makes system design difficult. Sykora presents a simple example of a two state modulator trellis for binary modulation in [13].

Ahmadi and Rao [14] reiterate that the rank and product distance criteria derived in [11] may be used to search for space-time codes with CPM. They consider binary space-time codes, with two transmit antennas and the model of Figure 2.11. They investigate the 16 possible forms of the binary space-time code shown in Figure 2.14. For each of the three binary CPM

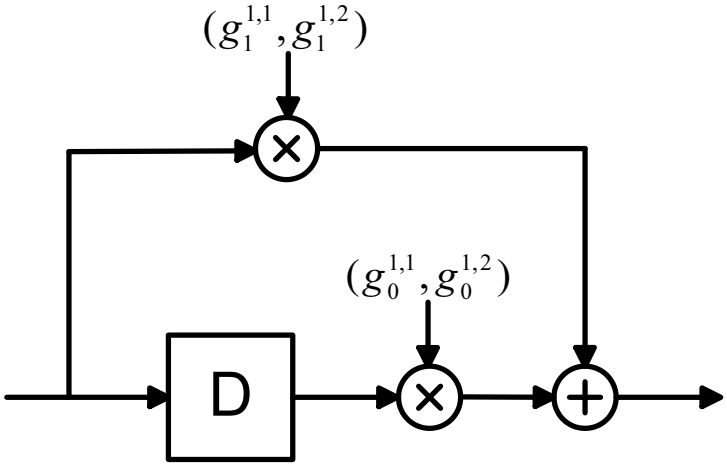

Figure 2.14: Implementation of a binary space-time encoder.

considered (rectangular, raised cosine and half cycle sinusoid), two different sets of product distances emerged for the full rank codes. Ahmadi and Rao also investigate the product distance of space-time coded schemes with binary multi-h CPFSK in [64]. The system is based on the model presented in Figure 2.11 with binary multi-h CPFSK modulators.

Zajić and Stüber [15] investigate how to maximize the product distance of space-time coded full response CPM. They consider the linear approximation of CPM developed by Mengali and Morelli [63] and the space-time coded CPM system shown in Figure 2.11. In order to maximize the product distance, they show that matrices, which are constructed from the pulse shaping functions of the modulation, must have semi-identity form. For matrix $\boldsymbol{G}$ to have semi-identity form, it must satisfy $\boldsymbol{G} = Q\boldsymbol{I}_{\rho_g}$, where Q is some constant, $\boldsymbol{I}_{\rho_g}$ is the $(\rho_g \times \rho_g)$ identity matrix and ρ_g is the rank of matrix $\boldsymbol{G}$. They show that this condition is satisfied by certain full response CPM formats, but not necessarily for CPFSK, except for the special case of MSK.

Once the semi-identity form has been established it is still difficult to maximize the exact coding gain. Therefore, the design focuses on maximizing the limit on the coding gain. Zajić and Stüber [15] show that this may be viewed as maximizing the trace of the signal distance matrix or equivalently maximizing the minimum squared Euclidean distance. Simulation results of systems are presented that are claimed to achieve full diversity and optimized coding gain. However, the slopes of the error rate curves are the same with $L_t = \{2, 3, 4\}$ transmit antennas, which is not expected with full spatial diversity.

2.6 Research Motivation

Although continuous phase modulation (CPM) has advantages such as low cost and power efficient transmitters, not using the signal amplitude to communicate information causes it to exhibit low bandwidth efficiency. This has prevented widespread use of CPM. Using multiple antennas with CPM can compensate for CPM's relatively low bandwidth efficiency and form a system with a high data rate and high performance, while maintaining the favourable properties of CPM schemes, such as power efficiency.

Space-time coded CPM schemes that use the traditional information phase representation have been developed and various methods of utilizing the rank and the product distance design criteria have been investigated. Some simple methods to obtain full transmit diversity systems are presented. There is still a lot to be gained by optimizing over these full diversity systems. However, the methods to achieve the optimization tend to be complicated, due to the two separate memory components (of the modulation and the space-time code) interacting in an uncontrolled manner. Most design examples use binary modulations and two transmit antennas. The question of finding a natural way to combine CPM with space-time codes, and utilizing the structure for code design, has not been addressed. An appropriate structure will allow the construction of more powerful space-time coded CPM systems, using systematic design techniques.

By using the Rimoldi decomposition to represent the CPM modulators the number of trellis states can be reduced by a multiple of two. We show that by then defining the space-time code over the same ring of integers as the multiple continuous phase encoders, the encoders can be combined. This results, not only in a single trellis structure, but one that is defined on a ring of integers and appears and acts as a single convolutional encoder for design purposes. No mapping is required after the space-time encoder and hence, state combining and state reduction can occur. We take advantage of the integrated encoder structure to develop simpler design methods to optimize space-time coded CPM.

STC-CPM designs, in general, have been limited to rate-$\frac{1}{L_t}$ space-time codes. We investigate higher rate space-time codes in a space-time coded CPM environment. Full spatial diversity may not always be achievable, due to the limit stated in Equation (2.91). However, we demonstrate that this is not necessarily the most important design consideration and excellent performance and throughput can be achieved by CPM systems that incorporate high rate

space-time codes.

Rank and product distance criteria have been investigated for space-time coded CPM. General code constructions for space-time codes with particular forms of CPM and design criteria for space-time codes with CPM have been developed to maximize diversity gain. It has been shown that for linearly modulated space-time codes Euclidean distance is also an important design criterion. For STC-CPM, Euclidean distance has been developed as a design criterion through approximations and upper bounds on the product distance. It has not been demonstrated that Euclidean distance is a valid criterion in its own right, for systems with a large number of parallel spatial channels, as it has been for the linearly modulated space-time codes. We show that it is indeed valid and we optimize non-trivial space-time coded CPM systems using the Euclidean distance criterion.

Performance bounds for space-time trellis coded CPM have not been presented thus far. We develop bounds for the bit, symbol and frame error rate probabilities. The rank, product distance and trace properties of the signal distance matrices of STC-CPM systems are calculated and used to evaluate approximations of the bounds. These calculations are possible due to the integrated STC-CPM design.

2.7 Summary

In this chapter, we have described the fading environment a signal transmitted over a wireless channel experiences. In this thesis, we consider narrowband systems, and thus use a frequency-flat fading model. We assume that the fading is quasi-static, such that the fading is constant during a frame and varies between frames. We have discussed continuous phase modulation (CPM) and have shown that it may be represented by a ring convolutional encoder followed by a memoryless modulator. The trellis of this encoder is time-invariant. Continuous phase frequency shift keyed signals were defined. These full response CPM signal formats will be used in the examples in the following chapters, due to their simplicity.

Space-time coding was introduced with a focus on space-time trellis codes (STTC). Design of STTC for linear modulation, based on minimizing the worst case pairwise error probability, was discussed. Important parameters are the rank, the product distance and the trace of the codeword distance matrices. The methodology used to derive these criteria will be used in Chapter 4 to develop design criteria for space-time coded CPM systems.

The current state of research on STTC combined with CPM was then summarized. STTC CPM is a promising format. However, space-time code design with CPM is shown to be difficult due to the memory inherent to continuous phase modulation. This has limited the literature to simple examples. In the next chapter, we develop an integrated system model that overcomes this difficulty by utilizing the Rimoldi decomposition of CPM and defining all encoder structures on the same ring of integers.

Chapter 3

Space-Time Coded CPM

3.1 Introduction

In this chapter, we develop a multiple transmit and multiple receive antenna scheme based on continuous phase modulation (CPM). A continuous phase modulated signal is transmitted from each antenna and each modulator is modelled using the Rimoldi decomposition. Each receive antenna receives a faded superposition of the signals simultaneously transmitted from each antenna corrupted by additive white Gaussian noise (AWGN). The fading is assumed to be frequency-flat Rayleigh fading and is assumed to be quasi-static, such that, it is constant during a frame, but varies from frame to frame. We present a coherent receiver that decodes the received signals.

We have seen in Section 2.3 that the continuous phase encoder (CPE), which represents the inherent coding of CPM, can be implemented using a linear convolutional encoder on the ring of integers modulo-p, $(\mathbb{Z}_p)$. We incorporate a space-time encoder into the multi-transmit antenna model. The space-time encoder is designed to be a convolutional encoder on the same ring as the CPEs, that is, $\mathbb{Z}_p$. We form a feedback-free version of the CPEs. By making the CPEs feedback-free they can be concatenated with any non-catastrophic space-time code to create a system that is non-catastrophic.

The encoders of the STC and the modulators are combined into a single convolutional encoder on $\mathbb{Z}_p$. Memory is introduced into the system by both the space-time encoder and the continuous phase encoders. The trellis of the combined encoder is used to decode the signal

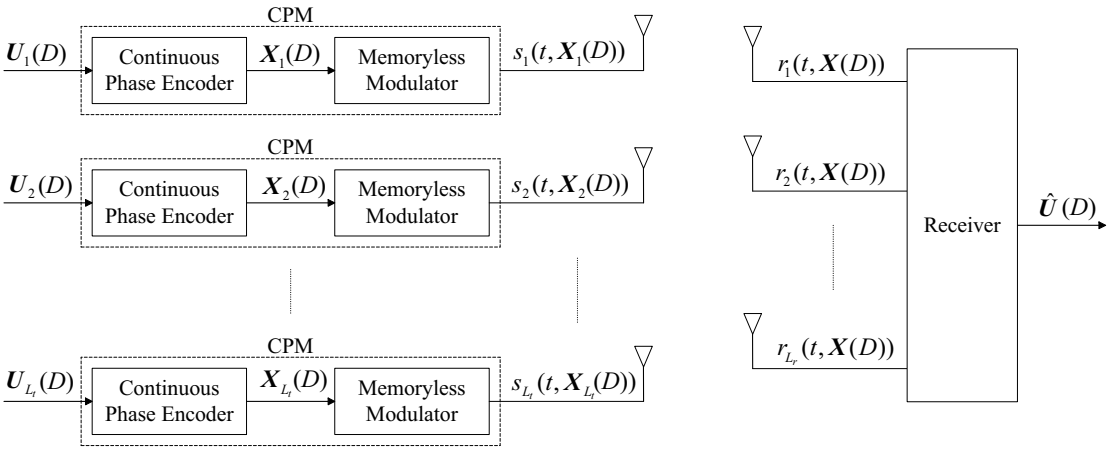

Figure 3.1: Multi-antenna CPM system.

using the Viterbi algorithm. The combined encoder makes it possible to readily calculate the Euclidean distance between the possible transmit signals, which is a function of the input to the memoryless modulators. The input to the memoryless modulators is related to the input symbols by a single convolutional encoder. Also, we may easily calculate the components of the signal distance matrices, which can be used to calculate the matrices' rank and product distance. These parameters are important for code design and are required to evaluate approximations of the performance bounds that are developed in Chapter 5. Hence, the new STC-CPM model makes code design practical and systematically implementable.

3.2 Multi-Antenna CPM Transmitter

We consider a system with L_t transmit antennas and L_r receive antennas. Each transmitter branch has a continuous phase modulator, as shown in Figure 3.1. The signal transmitted from the i-th antenna during the n-th symbol interval is given by

$$s_i(t, \boldsymbol{X}_{i,n}) = \sqrt{\frac{2E_s}{L_t T}} \cos\left(2\pi f_1 t + \tilde{\psi}(t, \boldsymbol{X}_{i,n})\right), \quad nT \le t \le (n+1)T, \tag{3.1}$$

where $\tilde{\psi}(t, \boldsymbol{X}_{i,n})$ is defined in Chapter 2 as

$$\tilde{\psi}(t, \boldsymbol{X}_{i,n}) = \left[2\pi h \left[X_{i,n}^{L+1}\right] \mod p + 4\pi h \sum_{j=1}^{L} X_{i,n}^{j} q(t - jT) + W(t)\right] \mod 2\pi, \quad nT \le t \le (n+1)T, \tag{3.2}$$

and we let

$$\boldsymbol{X}_i(D) = \boldsymbol{X}_{i,0} + \boldsymbol{X}_{i,1}D + \ldots + \boldsymbol{X}_{i,n}D^n + \ldots \tag{3.3}$$

denote the i-th data stream output from the i-th continuous phase encoder (CPE) for $1 \leq i \leq L_t$. E_s is the total transmitted energy per symbol interval and T is the symbol period. The total power transmitted from all the antennas is

$$P_t = L_t \frac{\left(\sqrt{\frac{2E_s}{L_tT}}\right)^2}{2} = \frac{E_s}{T}, \tag{3.4}$$

which we normalize to one. The transmitted signal of Equation (3.1) in canonical form with the in-phase and quadrature components referenced to the asymmetric carrier frequency, f_1, is

$$s_i(t, \boldsymbol{X}_{i,n}) = \acute{s}_{I,i}(t, \boldsymbol{X}_{i,n}) \cos(2\pi f_1 t) - \acute{s}_{Q,i}(t, \boldsymbol{X}_{i,n}) \sin(2\pi f_1 t) \ , \quad nT \leq t \leq (n+1)T, \tag{3.5}$$

where

$$\acute{s}_{I,i}(t, \boldsymbol{X}_{i,n}) = \sqrt{\frac{2E_s}{L_tT}} \cos(\tilde{\psi}(t, \boldsymbol{X}_{i,n})) \, , \quad nT \leq t \leq (n+1)T, \tag{3.6}$$

$$\acute{s}_{Q,i}(t, \boldsymbol{X}_{i,n}) = \sqrt{\frac{2E_s}{L_tT}} \sin(\tilde{\psi}(t, \boldsymbol{X}_{i,n})) \, , \quad nT \leq t \leq (n+1)T, \tag{3.7}$$

and f_1 is defined by Equation (2.33).

We may write the transmitted signal from the i-th antenna in terms of the symmetric carrier frequency, f_c, as

$$s_i(t, \boldsymbol{X}_i(D)) = s_{I,i}(t, \boldsymbol{X}_i(D)) \cos(2\pi f_c t) - s_{Q,i}(t, \boldsymbol{X}_i(D)) \sin(2\pi f_c t) \, , \tag{3.8}$$

where the in-phase and quadrature components referenced to f_c are

$$s_{I,i}(t, \boldsymbol{X}_i(D)) = \sqrt{\frac{2E_s}{L_tT}} \cos(\psi(t, \boldsymbol{X}_i(D)) - 2\pi f_0 t), \tag{3.9}$$

$$s_{Q,i}(t, \boldsymbol{X}_i(D)) = \sqrt{\frac{2E_s}{L_tT}} \sin(\psi(t, \boldsymbol{X}_i(D)) - 2\pi f_0 t), \tag{3.10}$$

and

$$f_0 = f_c - f_1 = \frac{(M-1)h}{2T}. \tag{3.11}$$

The signal can be expressed in terms of its complex envelope as

$$s_i(t, \boldsymbol{X}_i(D)) = \mathbb{R}[\tilde{s}_i(t, \boldsymbol{X}_i(D)) \exp(j2\pi f_c t)], \tag{3.12}$$

where $\tilde{s}_i(t, \boldsymbol{X}_i(D))$ denotes the complex envelope of $s_i(t, \boldsymbol{X}_i(D))$ and is given by

$$\begin{aligned}\tilde{s}_i(t, \boldsymbol{X}_i(D)) &= s_{I,i}\left(t, \boldsymbol{X}_i\left(D\right)\right) + j s_{Q,i}\left(t, \boldsymbol{X}_i\left(D\right)\right) \\ &= \sqrt{\frac{2E_s}{L_t T}} \cos\left(\psi\left(t, \boldsymbol{X}_i\left(D\right)\right) - 2\pi f_0 t\right) + j\sqrt{\frac{2E_s}{L_t T}} \sin\left(\psi\left(t, \boldsymbol{X}_i\left(D\right)\right) - 2\pi f_0 t\right) \\ &= \sqrt{\frac{2E_s}{L_t T}} \exp\left(j\left[\psi\left(t, \boldsymbol{X}_i(D)\right) - 2\pi f_0 t\right]\right).\end{aligned} \tag{3.13}$$

We let the fading experienced by the channel be Rayleigh distributed. The Rayleigh fading channel is discussed in Section 2.2.3 of Chapter 2. We describe the fading process for the sub-channel between transmit antenna i and receive antenna j as

$$m_{j,i}(t) = m_{I,j,i}(t)\cos\left(2\pi f_c t\right) - m_{Q,j,i}(t)\sin\left(2\pi f_c t\right), \tag{3.14}$$

where $m_{I,j,i}(t)$ and $m_{Q,j,i}(t)$ are zero mean Gaussian random processes with variance, $\frac{1}{2}$. Thus, the complex envelope of $m_{j,i}(t)$ is an independent complex Gaussian random process with zero mean and variance of $\frac{1}{2}$ per dimension, and is denoted

$$\tilde{m}_{j,i}(t) = m_{I,j,i}(t) + j m_{Q,j,i}(t). \tag{3.15}$$

We model the noise at the receiver as additive white Gaussian noise (AWGN). We let the AWGN component on the j-th antenna, $n_j(t)$, have two-sided power spectral density $\frac{N_0}{2}$ and be band-limited to bandwidth $f_w << f_c$, where f_c is the symmetric carrier frequency. We represent $n_j(t)$ as

$$n_j(t) = n_{I,j}(t)\cos\left(2\pi f_c t\right) - n_{Q,j}(t)\sin\left(2\pi f_c t\right), \tag{3.16}$$

where $n_{I,j}(t)$ and $n_{Q,j}(t)$ are zero mean Gaussian random processes with power spectral density N_0 for $-\frac{f_w}{2} < f < \frac{f_w}{2}$. The complex envelope of $n_j(t)$ is

$$\tilde{n}_j(t) = n_{I,j}(t) + j n_{Q,j}(t). \tag{3.17}$$

We may then write the complex envelope, $\tilde{r}_j(t, \boldsymbol{X}(D))$, of the received signal on antenna j, for $1 \leq j \leq L_r$, as

$$\tilde{r}_j(t, \boldsymbol{X}(D)) = \sum_{i=1}^{L_t} \tilde{m}_{j,i}(t)\tilde{s}_i(t, \boldsymbol{X}_i(D)) + \tilde{n}_j(t), \tag{3.18}$$

where

$$\boldsymbol{X}(D) = [\boldsymbol{X}_1(D) \quad \boldsymbol{X}_2(D) \quad \ldots \quad \boldsymbol{X}_{L_t}(D)]. \tag{3.19}$$

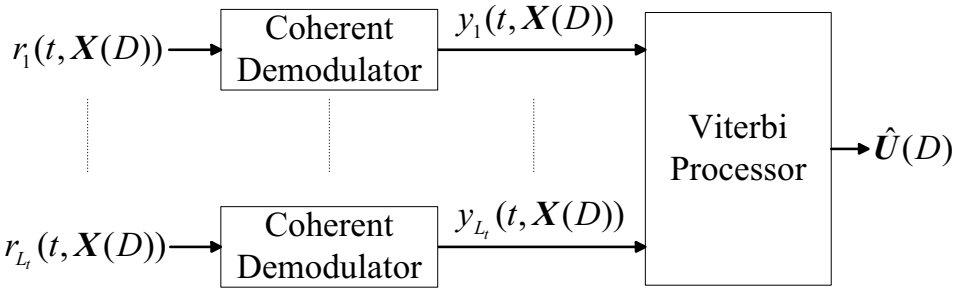

Figure 3.2: Multi-antenna coherent receiver.

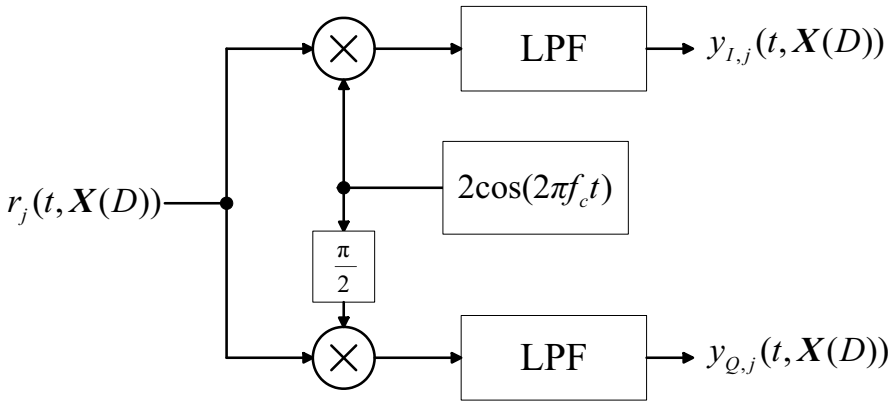

Figure 3.3: Coherent demodulator at the j-th receive antenna.

The received signal at the j-th antenna can then be expressed as

$$\begin{aligned} r_j(t, \boldsymbol{X}(D)) &= \mathbb{R}[\tilde{r}_j(t, \boldsymbol{X}(D)) \exp(j2\pi f_c t)] \\ &= \frac{1}{2}\left[\tilde{r}_j(t, \boldsymbol{X}(D)) \exp(j2\pi f_c t) + \tilde{r}_j^*(t, \boldsymbol{X}(D)) \exp(-j2\pi f_c t)\right]. \end{aligned} \tag{3.20}$$

3.3 Receiver

The received signal at each antenna is processed by a coherent demodulator. The signals from the L_r demodulators are fed to a processor, which utilizes the Viterbi algorithm to decode the information. The receiver is illustrated in block diagram form in Figure 3.2 and the form of the coherent demodulator is illustrated in Figure 3.3.

Within each demodulator, the output of the local oscillator is given by

$$2\cos(2\pi f_c t) = \left[\exp(j2\pi f_c t) + \exp(-j2\pi f_c t)\right], \tag{3.21}$$

and the $\frac{\pi}{2}$ phase shifted oscillator signal is given by

$$\begin{aligned} 2\cos\left(2\pi f_c t + \frac{\pi}{2}\right) &= -2\sin\left(2\pi f_c t\right) \\ &= \frac{1}{j}\left[\exp\left(-j2\pi f_c t\right) - \exp\left(j2\pi f_c t\right)\right]. \end{aligned} \tag{3.22}$$

The input to the in-phase low-pass filter is then

$$\begin{aligned} \acute{y}_{I,j}(t, \boldsymbol{X}(D)) &= 2r_j(t, \boldsymbol{X}(D))\cos(2\pi f_c t) \\ &= \frac{1}{2}\left[\tilde{r}_j(t, \boldsymbol{X}(D))\exp(j2\pi f_c t) + \tilde{r}_j^*(t, \boldsymbol{X}(D))\exp(-j2\pi f_c t)\right] \\ &\quad \times \left[\exp(j2\pi f_c t) + \exp(-j2\pi f_c t)\right] \\ &= \frac{1}{2}\left[\tilde{r}_j(t, \boldsymbol{X}(D))\exp(j4\pi f_c t) + \tilde{r}_j^*(t, \boldsymbol{X}(D))\right. \\ &\quad \left. + \tilde{r}_j(t, \boldsymbol{X}(D)) + \tilde{r}_j^*(t, \boldsymbol{X}(D))\exp(-j4\pi f_c t)\right]. \end{aligned} \tag{3.23}$$

After low-pass filtering the in-phase output of the demodulator is given by

$$\begin{aligned} y_{I,j}(t, \boldsymbol{X}(D)) &= \frac{1}{2}\left[\tilde{r}_j^*(t, \boldsymbol{X}(D)) + \tilde{r}_j(t, \boldsymbol{X}(D))\right] \\ &= \frac{1}{2}\left[r_{I,j}(t, \boldsymbol{X}(D)) - jr_{Q,j}(t, \boldsymbol{X}(D)) + r_{I,j}(t, \boldsymbol{X}(D)) + jr_{Q,j}(t, \boldsymbol{X}(D))\right] \\ &= \mathbb{R}\left[\tilde{r}_j(t, \boldsymbol{X}(D))\right]. \end{aligned} \tag{3.24}$$

Similarly, the input to the low-pass filter on the quadrature branch is given by

$$\begin{aligned} \acute{y}_{Q,j}(t, \boldsymbol{X}(D)) &= -2r_j(t, \boldsymbol{X}(D))\sin(2\pi f_c t) \\ &= \frac{1}{2}\left[\tilde{r}_j(t, \boldsymbol{X}(D))\exp(j2\pi f_c t) + \tilde{r}_j^*(t, \boldsymbol{X}(D))\exp(-j2\pi f_c t)\right] \\ &\quad \times \frac{1}{j}[\exp(-j2\pi f_c t) - \exp(j2\pi f_c t)] \\ &= \frac{1}{2j}\left[\tilde{r}_j(t, \boldsymbol{X}(D)) + \tilde{r}_j^*(t, \boldsymbol{X}(D))\exp(-j4\pi f_c t)\right. \\ &\quad \left. - \tilde{r}_j(t, \boldsymbol{X}(D))\exp(j4\pi f_c t) - \tilde{r}_j^*(t, \boldsymbol{X}(D))\right]. \end{aligned} \tag{3.25}$$

The low-pass filter output on the quadrature branch is then

$$\begin{aligned} y_{Q,j}(t, \boldsymbol{X}(D)) &= \frac{1}{2j}\left[\tilde{r}_j(t, \boldsymbol{X}(D)) - \tilde{r}_j^*(t, \boldsymbol{X}(D))\right] \\ &= \frac{1}{2j}\left[r_{I,j}(t, \boldsymbol{X}(D)) + jr_{Q,j}(t, \boldsymbol{X}(D)) - r_{I,j}(t, \boldsymbol{X}(D)) + jr_{Q,j}(t, \boldsymbol{X}(D))\right] \\ &= \mathbb{I}\left[\tilde{r}_j(t, \boldsymbol{X}(D))\right]. \end{aligned} \tag{3.26}$$

The complex demodulated signal received at the j-th antenna may then be written as

$$\begin{aligned} y_j(t, \boldsymbol{X}(D)) &= y_{I,j}(t, \boldsymbol{X}(D)) + j y_{Q,j}(t, \boldsymbol{X}(D)) \\ &= \mathbb{R}\left[\tilde{r}_j(t, \boldsymbol{X}(D))\right] + j\mathbb{I}\left[\tilde{r}_j(t, \boldsymbol{X}(D))\right] \\ &= \tilde{r}_j(t, \boldsymbol{X}(D) \\ &= \sum_{i=1}^{L_t} \tilde{m}_{j,i}(t)\tilde{s}_i(t, \boldsymbol{X}_i(D)) + \tilde{n}_j(t). \end{aligned} \tag{3.27}$$

3.3.1 Viterbi Processor

If we consider a data frame length of N_c symbol intervals, then the demodulated signal received on antenna j is given by

$$y_j(t, \boldsymbol{X}(D)) = \sum_{i=1}^{L_t} \tilde{m}_{j,i}\tilde{s}_i(t, \boldsymbol{X}_i(D)) + \tilde{n}_j(t), \quad 0 \leq t \leq N_c T, \quad j = 1, 2, \ldots, L_r. \tag{3.28}$$

Decoding is implemented using the Viterbi algorithm on the trellis of the combined continuous phase encoders. The Viterbi algorithm is summarized in Appendix C. The frame length, N_K, is equal to N_c plus the number of symbol intervals required to return the overall encoder to the zero state. The maximum likelihood metric [11] for the STC-CPM system assuming perfect channel state information is given by

$$M(y(t, \boldsymbol{X}(D))|\hat{\boldsymbol{X}}(D)) = -\sum_{j=1}^{L_r} \int_0^{N_K T} \left| y_j(t, \boldsymbol{X}(D)) - \sum_{i=1}^{L_t} \tilde{m}_{j,i}\tilde{s}_i(t, \hat{\boldsymbol{X}}_i(D)) \right|^2 dt, \tag{3.29}$$

where $\tilde{s}_i(t, \hat{\boldsymbol{X}}_i(D))$ is the complex envelope of the hypothesized signal transmitted from antenna i. We can rewrite the path metric of Equation (3.29), as a summation over N_K symbol intervals in the form

$$M(y(t, \boldsymbol{X}(D))|\hat{\boldsymbol{X}}(D)) = \sum_{n=0}^{N_K - 1} \lambda(\xi_n), \tag{3.30}$$

where the branch metric is

$$\lambda(\xi_n) = -\sum_{j=1}^{L_r} \int_{nT}^{(n+1)T} \left| y_j(t, \boldsymbol{X}_n) - \sum_{i=1}^{L_t} \tilde{m}_{j,i}\tilde{s}_i(t, \hat{\boldsymbol{X}}_{i,n}) \right|^2 dt, \quad n = 0, 1, \ldots, N_K - 1. \tag{3.31}$$

3.4 Feedback-Free Multi-Antenna CPM Transmitter

We now focus on the transmitter. We introduce a feedback-free continuous phase encoder model, which enables the development of a code-search model that is required to search only

over non-catastrophic space-time codes. We then form a space-time coded CPM transmission system.

3.4.1 Feedback-Free Continuous Phase Encoder

A catastrophic encoder can produce an infinite number of output errors given a finite number of input errors [65]. In order to guarantee non-catastrophic overall codes, we follow [65] and use a precoder to cancel the feedback term of the continuous phase encoder, $\boldsymbol{C}(D)$, as defined in Chapter 2, Equation (2.46). Concatenating a non-catastrophic convolutional encoder with a feedback-free encoder will result in a system that is non-catastrophic [27]. Similarly, concatenating a catastrophic encoder with a feedback-free encoder will only result in catastrophic systems. Thus, when we integrate space-time coding into the feedback-free multi-transmit antenna CPM system and search for good space-time codes, we can ignore all catastrophic codes. A precoder generator matrix that removes the feedback of the continuous phase encoder of a CPM with modulation index $h = \frac{v}{p}$ and an alphabet size of $M = p^{k_m}$, where v, p and k_m are integers, is given by

$$\boldsymbol{T}(D) = \begin{bmatrix} \boldsymbol{I}_{k_m-1} & \mathbf{0}_{k_m-1,1} \\ \mathbf{0}_{1,k_m-1} & 1-D \end{bmatrix}, \tag{3.32}$$

where $\boldsymbol{I}_i$ is the $(i \times i)$ identity matrix and $\mathbf{0}_{i,j}$ represents an $(i \times j)$-dimensional matrix of zeroes. $\boldsymbol{T}(D)$ is a scrambler [66] and its inverse is given by

$$\boldsymbol{T}'(D) = \begin{bmatrix} \boldsymbol{I}_{k_m-1} & \mathbf{0}_{k_m-1,1} \\ \mathbf{0}_{1,k_m-1} & \frac{1}{1-D} \end{bmatrix}. \tag{3.33}$$

If the input to a scrambler ranges over all possible sequences, then its output is all possible sequences in some different order, due to the existence of the scrambler's inverse. $\boldsymbol{T}(D)$ is cascaded with $\boldsymbol{C}(D)$ of Equation (2.46), to create a feedback-free CPE (FF-CPE) with the $(k_m \times (k_m L + 1))$ generator matrix

$$\boldsymbol{W}(D) = \boldsymbol{T}(D)\boldsymbol{C}(D) =$$
$$\begin{bmatrix} 1 & D & D^2 & \dots & D^{L-1} & \mathbf{0}_{1,L} & \cdots & & \mathbf{0}_{1,L+1} \\ & \mathbf{0}_{1,L} & & \ddots & & \mathbf{0}_{1,L} & & \vdots & \\ & \vdots & & \mathbf{0}_{1,L} & 1 & D & D^2 & \dots & D^{L-1} & \mathbf{0}_{1,L+1} \\ & \mathbf{0}_{1,L} & & \cdots & & \mathbf{0}_{1,L} & 1-D & D-D^2 & \dots & D^{L-1}-D^L & D^L \end{bmatrix}. \tag{3.34}$$

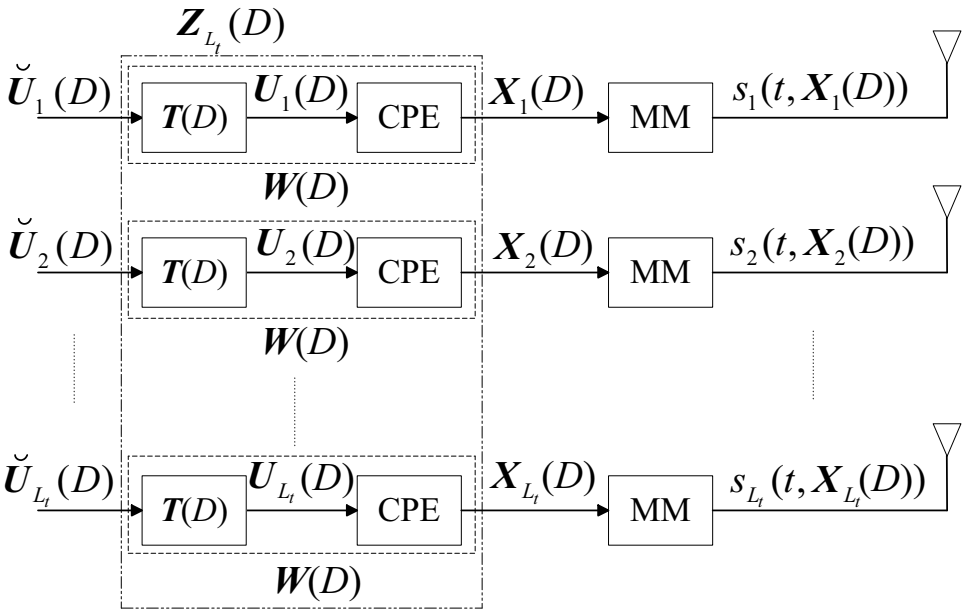

Figure 3.4: Feedback-free multi-antenna CPM transmitter.

The FF-CPE generator matrix for full response $(L = 1)$ CPM, for example CPFSK, is found by substituting $L = 1$ into Equation (3.34) and results in

$$\boldsymbol{W}(D) = \begin{bmatrix} \boldsymbol{I}_{k_m-1} & \boldsymbol{0}_{k_m-1,1} & \boldsymbol{0}_{k_m-1,1} \\ \boldsymbol{0}_{1,k_m-1} & 1-D & D \end{bmatrix}. \tag{3.35}$$

Full response M-ary CPM with $h = \frac{v}{M}$ (for example M-CPFSK) has $p = M$ and $k_m = 1$, hence the generator matrix of Equation (3.34) further reduces to

$$\boldsymbol{W}(D) = \begin{bmatrix} 1-D & D \end{bmatrix}. \tag{3.36}$$

3.4.2 Combined Feedback-Free Continuous Phase Encoders

We incorporate L_t precoders, $\boldsymbol{T}(D)$, into the multi-antenna CPM transmitter as shown in Figure 3.4. We let

$$\breve{\boldsymbol{U}}(D) = \begin{bmatrix} \breve{\boldsymbol{U}}_1(D) & \breve{\boldsymbol{U}}_2(D) & \dots & \breve{\boldsymbol{U}}_{L_t}(D) \end{bmatrix}, \tag{3.37}$$

denote the input to the multiple FF-CPE, where the i-th stream is defined as

$$\breve{\boldsymbol{U}}_i(D) = \breve{\boldsymbol{U}}_{i,0} + \breve{\boldsymbol{U}}_{i,1}D + \ldots + \breve{\boldsymbol{U}}_{i,n}D^n + \ldots, \quad i = 1, 2, \ldots, L_t. \tag{3.38}$$

The vector, $\breve{\boldsymbol{U}}_{i,n}$, consists of the k_m coefficients of the radix-p expression of Equation (2.43), which forms one M-ary channel symbol. In vector notation, we have

$$\breve{\boldsymbol{U}}_{i,n} = \begin{bmatrix} \breve{U}_{i,n}^{1} & \breve{U}_{i,n}^{2} & \dots & \breve{U}_{i,n}^{k_m} \end{bmatrix}, \quad i=1,2,\dots,L_t, \quad nT \le t \le (n+1)T. \tag{3.39}$$

The output sequence of the i-th FF-CPE may then be written as

$$\boldsymbol{X}_i(D) = \breve{\boldsymbol{U}}_i(D)\boldsymbol{W}(D), \quad i=1,2,\dots,L_t, \tag{3.40}$$

where $\boldsymbol{X}_i(D)$ is defined by Equation (3.3). The (Lk_m+1)-dimensional vector of p-ary symbols output during the n-th symbol interval is given by

$$\boldsymbol{X}_{i,n} = \begin{bmatrix} X_{i,n}^{1,1} & \dots & X_{i,n}^{L,1} & X_{i,n}^{1,2} & \dots & X_{i,n}^{L,k_m} & X_{i,n}^{L+1,1} \end{bmatrix}, \quad \begin{array}{l} nT \le t \le (n+1)T, \\ i=1,2,\dots,L_t, \end{array} \tag{3.41}$$

where

$$X_{i,n}^{j} = \begin{cases} \sum_{k=1}^{k_m} X_{i,n}^{j,k} p^{k_m-k} & j = 1,2,\dots,L \\ X_{i,n}^{L+1,1} & j = L+1 \end{cases}, \quad nT \le t \le (n+1)T, \quad i=1,2,\dots,L_t. \tag{3.42}$$

It drives the i-th memoryless modulator to generate the signal, $s_i(t, \boldsymbol{X}_i(D))$, that is transmitted from antenna i.

We can combine the L_t feedback free CPEs, $\boldsymbol{W}(D)$, into a single encoder with the $(k_mL_t \times (k_mL+1)L_t)$ generator matrix

$$\boldsymbol{Z}_{L_t}(D) = \begin{bmatrix} \boldsymbol{W}(D) & \boldsymbol{0}_{k_m,k_mL+1} & \cdots & \boldsymbol{0}_{k_m,k_mL+1} \\ \boldsymbol{0}_{k_m,k_mL+1} & \ddots & \ddots & \vdots \\ \vdots & \ddots & \boldsymbol{W}(D) & \boldsymbol{0}_{k_m,k_mL+1} \\ \boldsymbol{0}_{k_m,k_mL+1} & \cdots & \boldsymbol{0}_{k_m,k_mL+1} & \boldsymbol{W}(D) \end{bmatrix}, \tag{3.43}$$

as illustrated in Figure 3.4. During the n-th symbol interval, the input to the encoder defined by $\boldsymbol{Z}_{L_t}(D)$ is the (k_mL_t)-dimensional vector of p-ary symbols

$$\breve{\boldsymbol{U}}_n = \begin{bmatrix} \breve{\boldsymbol{U}}_{1,n} & \breve{\boldsymbol{U}}_{2,n} & \dots & \breve{\boldsymbol{U}}_{L_t,n} \end{bmatrix}, \quad nT \le t \le (n+1)T, \tag{3.44}$$

where the sub-vectors $\breve{\boldsymbol{U}}_{i,n}$ for $1 \le i \le L_t$ are given by Equation (3.39). The output of $\boldsymbol{Z}_{L_t}(D)$ during the n-th symbol interval is the $((k_mL+1)L_t)$-dimensional vector

$$\boldsymbol{X}_n = \begin{bmatrix} \boldsymbol{X}_{1,n} & \boldsymbol{X}_{2,n} & \dots & \boldsymbol{X}_{L_t,n} \end{bmatrix}, \quad nT \le t \le (n+1)T, \tag{3.45}$$

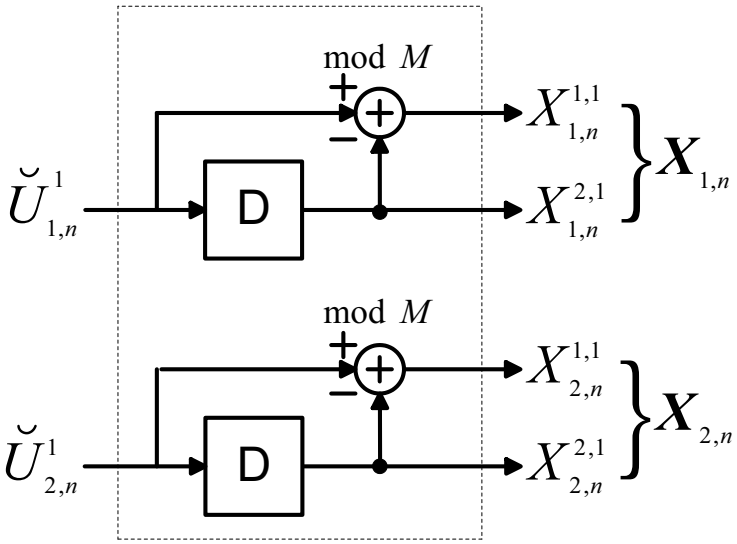

Figure 3.5: Combined feedback-free CPE, $\boldsymbol{Z}_2(D)$, for a two antenna transmitter with M-CPFSK.

where $\boldsymbol{X}_{i,n}$ is defined by Equation (3.41) for $1 \leq i \leq L_t$. The output of $\boldsymbol{Z}_{L_t}(D)$ is related to the input by

$$\boldsymbol{X}(D) = \boldsymbol{Z}_{L_t}(D)\breve{\boldsymbol{U}}(D), \tag{3.46}$$

where $\boldsymbol{X}(D)$ is defined by Equation (3.19) and $\breve{\boldsymbol{U}}(D)$ is defined by Equation (3.37).

For example, consider the L_t transmit antenna system illustrated by Figure 3.4 with M-CPFSK. Substituting Equation (3.36) into Equation (3.43), we find that the combined feedback-free CPE is represented by the $(L_t \times 2L_t)$-dimensional generator matrix

$$\boldsymbol{Z}_{L_t}(D) = \begin{bmatrix} 1-D & D & 0 & 0 & \cdots & 0 \\ 0 & 0 & 1-D & D & \ddots & \\ \vdots & \ddots & \ddots & \ddots & \ddots & \\ & & & & & 0 \\ 0 & & 0 & 0 & 1-D & D \end{bmatrix}. \tag{3.47}$$

Figure 3.5 provides an implementation of the two transmit antenna CPE structure defined by $\boldsymbol{Z}_2(D)$ for M-CPFSK.

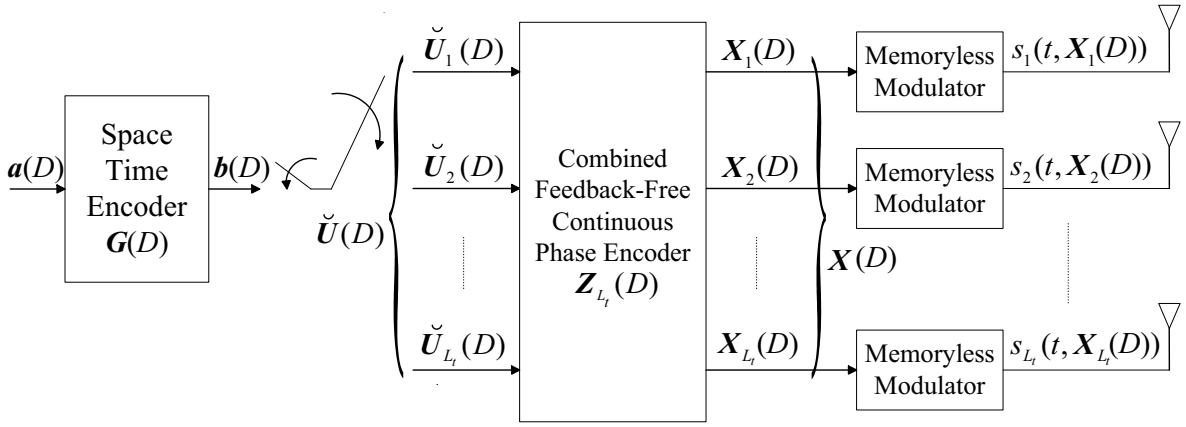

Figure 3.6: Space-time coded CPM transmitter.

3.5 Space-Time Coded CPM

We now consider a space-time coded continuous phase modulated (STC-CPM) system. The STC-CPM transmitter structure is shown in Figure 3.6. We define the space-time encoder as a linear, rate-$\frac{k}{l}$ convolutional encoder on the integer ring $\mathbb{Z}_p$, where k and l are integers and $l \geq k$. We let $\boldsymbol{G}(D)$ denote the generator matrix of the space-time encoder. It is followed by a commutator that produces the input sequences, $\breve{\boldsymbol{U}}_i(D)$ of Equation (3.38), to the L_t FF-CPEs.

The data sequence

$$\boldsymbol{a}(D) = \boldsymbol{a}_0 + \boldsymbol{a}_1 D + \ldots + \boldsymbol{a}_j D^j + \ldots \tag{3.48}$$

is input into the space-time encoder. The j-th input block, $\boldsymbol{a}_j$, consists of k p-ary symbols and is given by

$$\boldsymbol{a}_j = \begin{bmatrix} a_j^1 & a_j^2 & \ldots & a_j^k \end{bmatrix}, \quad jT_{k_v} \leq t \leq (j+1)T_{k_v}, \tag{3.49}$$

where

$$T_{k_v} = \frac{lT}{k_m L_t} \tag{3.50}$$

and T is the channel symbol interval. The space-time encoder output sequence is denoted $\boldsymbol{b}(D)$ and is given by

$$\boldsymbol{b}(D) = \boldsymbol{b}_0 + \boldsymbol{b}_1 D + \ldots + \boldsymbol{b}_j D^j + \ldots. \tag{3.51}$$

The output block, $\boldsymbol{b}_j$, has l p-ary elements and is given by

$$\boldsymbol{b}_j = \begin{bmatrix} b_j^1 & b_j^2 & \ldots & b_j^l \end{bmatrix}, \quad jT_{k_v} \leq t \leq (j+1)T_{k_v}. \tag{3.52}$$

The output sequence, $\boldsymbol{b}(D)$, is then written as a function of the input sequence, $\boldsymbol{a}(D)$, as

$$\boldsymbol{b}(D) = \boldsymbol{a}(D)\boldsymbol{G}(D). \tag{3.53}$$

The commutator groups the STC output symbols into blocks ($\breve{\boldsymbol{U}}_n$ described by Equation (3.44)) of $k_m L_t$ p-ary symbols every channel symbol interval to form the sequence $\breve{\boldsymbol{U}}(D)$ of Equation (3.37).

3.5.1 Combined STC-CPM Encoder

Both encoders of the STC-CPM system shown in Figure 3.6 are linear convolutional encoders over $\mathbb{Z}_p$. We can, with appropriate parameter definition, combine $\boldsymbol{Z}_{L_t}(D)$ with the space-time encoder, $\boldsymbol{G}(D)$, to obtain a single linear convolutional encoder over $\mathbb{Z}_p$ that incorporates the entire coding process. If the rate-$\frac{k}{l}$ space-time encoder is designed such that $l = k_m L_t$ (where $M = p^{k_m}$, $h = \frac{v}{p}$ and L_t is the number of transmit antennas), $\boldsymbol{G}(D)$ can be directly cascaded with $\boldsymbol{Z}_{L_t}(D)$. No commutator is then required, and the overall generator matrix is given by

$$\boldsymbol{J}(D) = \boldsymbol{G}(D)\boldsymbol{Z}_{L_t}(D). \tag{3.54}$$

Delay Diversity Space-Time Code Example

As an example, we examine the simple rate-$\frac{1}{L_t}$ STC known as delay diversity [4, 5, 6], with L_t transmit antennas. Delay diversity space-time codes always achieve full spatial diversity [10]. When delay diversity is combined with a continuous phase modulation with $k_m = 1$, the space-time encoder can be directly cascaded with $\boldsymbol{Z}_{L_t}(D)$. The delay diversity space-time encoder generator matrix for an L_t transmit antenna system is given by

$$\boldsymbol{G}(D) = \left[D^{(L_t-1)} \;\; D^{(L_t-2)} \;\; \cdots \;\; D \;\; 1 \right]. \tag{3.55}$$

We let $L_t = 2$, and then substitute Equations (3.47) and (3.55) into Equation (3.54) to obtain

$$\begin{aligned} \boldsymbol{J}(D) &= \boldsymbol{G}(D)\boldsymbol{Z}_2(D) \\ &= \begin{bmatrix} D & 1 \end{bmatrix} \begin{bmatrix} 1-D & D & 0 & 0 \\ 0 & 0 & 1-D & D \end{bmatrix} \\ &= \begin{bmatrix} D-D^2 & D^2 & 1-D & D \end{bmatrix}. \end{aligned} \tag{3.56}$$

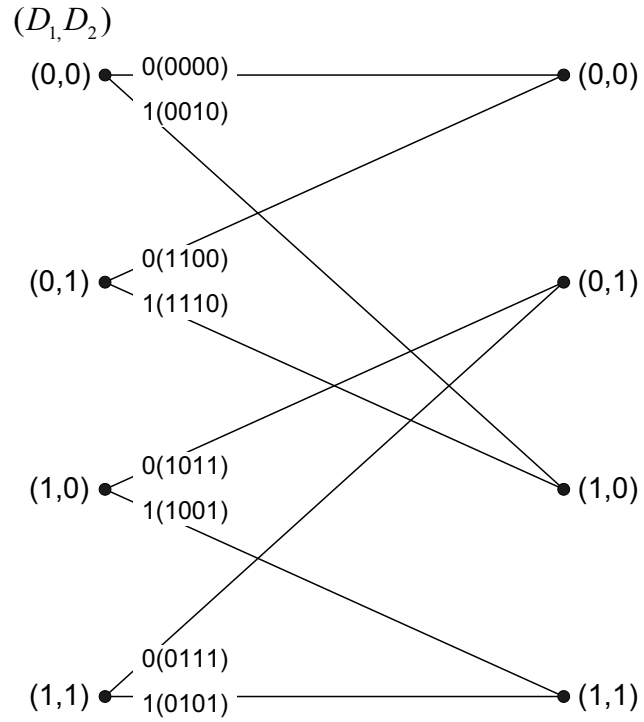

Figure 3.7: Trellis of combined encoder $\boldsymbol{J}(D) = \begin{bmatrix} D - D^2 & D^2 & 1 - D & D \end{bmatrix}$ for MSK and two transmit antennas. The space-time code is delay diversity, $\boldsymbol{G}(D) = [D \;\; 1]$.

Equation (3.56) represents the generator matrix of the overall encoder of an M-CPFSK ($h = \frac{1}{M}$), delay diversity space-time coded system, with 2 transmit antennas. An implementation of this encoder on the integer ring $\mathbb{Z}_M$ is shown in Figure 3.8. The trellis of the two transmit antenna, delay diversity space-time coded system, with MSK (2-CPFSK) is shown in Figure 3.7. The system can be implemented as in Figure 3.8 using modulo-2 adders. In Figure 3.7, the states of the delay elements of the encoder are labelled D_1 and D_2. The trellis transitions or branches are labelled with the corresponding input and output symbols, $a_n^1\big(X_{1,n}^{1,1}X_{1,n}^{2,1}\, X_{2,n}^{1,1}X_{2,n}^{2,1}\big)$, of the overall encoder, $\boldsymbol{J}(D)$.

In the following simulations we use the simulation procedure described in Appendix A. The data frame length is 130 M-ary symbols. Figure 3.9 displays the bit error rate performance of an MSK delay diversity space-time coded system with two, three and four transmit antennas. We follow [6] and use the maximum ratio combining curves for binary PSK (BPSK) as a diversity reference in Figure 3.9. Maximum ratio combining (MRC) is a diversity technique that utilizes multiple receive antennas [35]. It achieves a diversity order equal to the number of receive antennas. The bit error probability of MRC with BPSK, (which is equal to

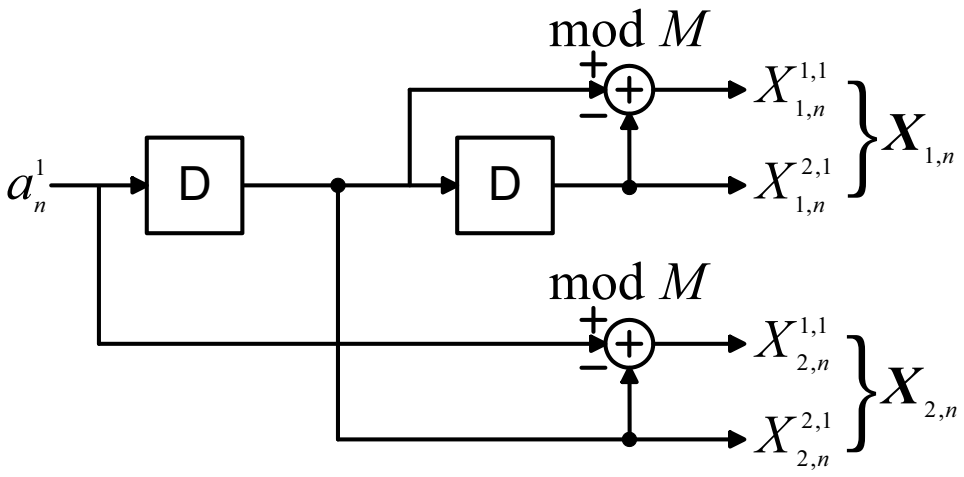

Figure 3.8: Implementation of combined encoder $\boldsymbol{J}(D) = \begin{bmatrix} D-D^2 & D^2 & 1-D & D \end{bmatrix}$ for M-CPFSK and two transmit antennas. The space-time code is delay diversity, $\boldsymbol{G}(D) = [D \;\; 1]$.

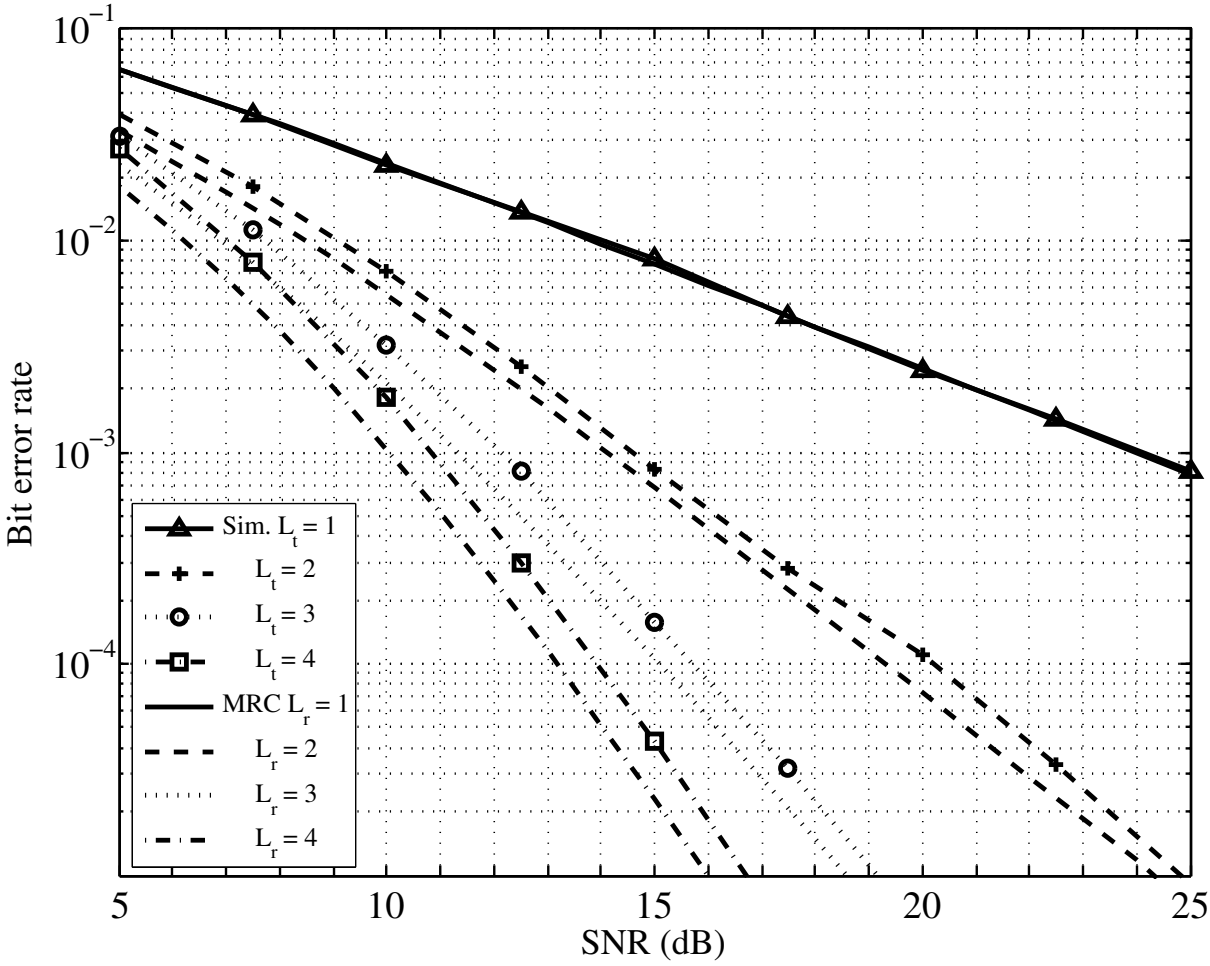

Figure 3.9: Simulated bit error rate performance of delay diversity space-time coded MSK with $L_t = \{1, 2, 3, 4\}$ and $L_r = 1$, and calculated bit error rate performance of maximum ratio combining (MRC) for BPSK with $L_t = 1$ and $L_r = \{1, 2, 3, 4\}$.

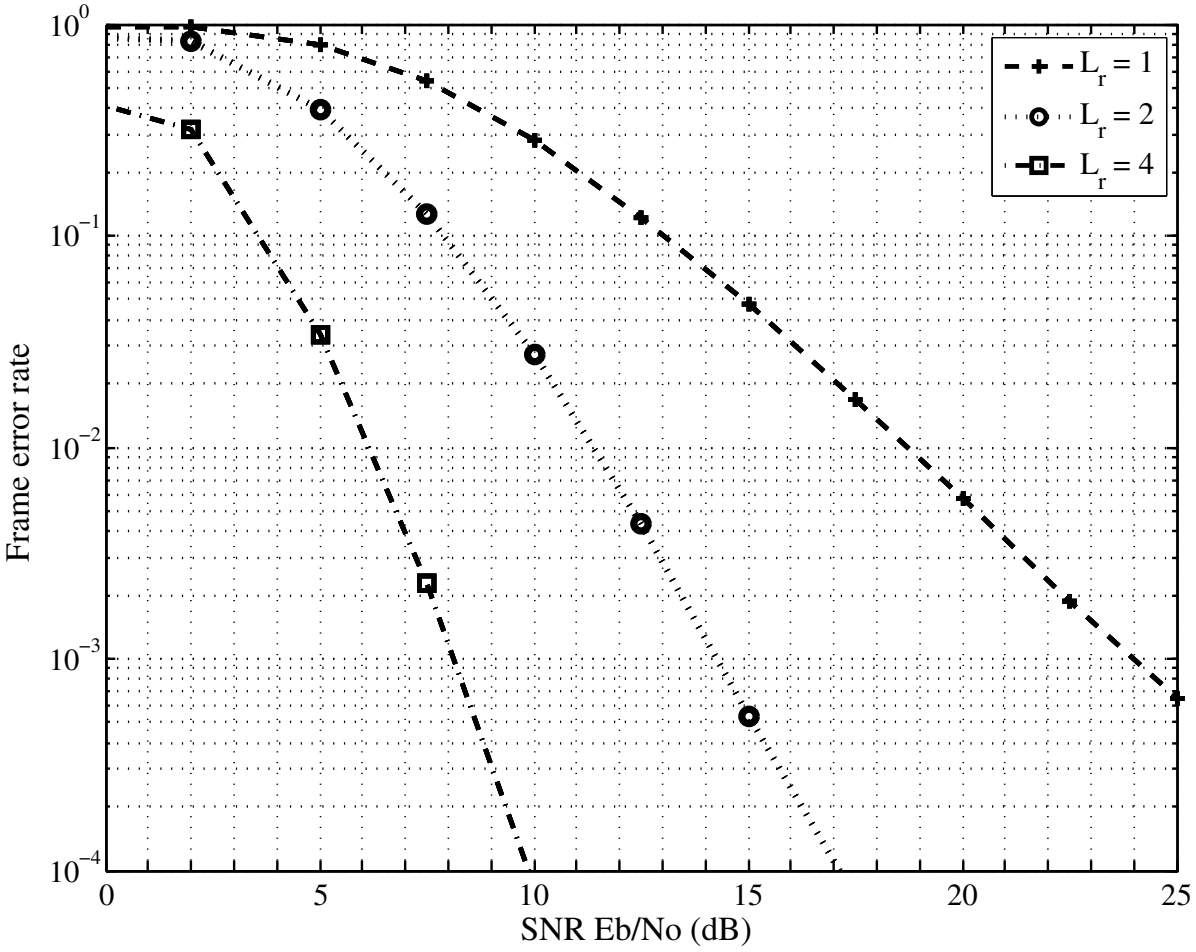

Figure 3.10: Frame error rate performance of delay diversity, $\boldsymbol{G}(D) = [D \quad 1]$, space-time coded 4-CPFSK with $L_t = 2$ and $L_r = \{1, 2, 4\}$.

the error probability for MSK [67]), 1 transmit antenna and L_r receive antennas [35] is given by

$$P_B = \left(\frac{1-\mu}{2}\right)^{L_r} \sum_{i=0}^{L_r-1} \begin{pmatrix} L_r - 1 + i \\ i \end{pmatrix} \left(\frac{1+\mu}{2}\right)^{i}, \tag{3.57}$$

where $\mu = \sqrt{\frac{\gamma}{1+\gamma}}$ and $\gamma = \frac{E_b}{N_0}$ is the average received SNR per diversity branch. To demonstrate the comparable diversity we have plotted the MRC curves against $\frac{E_b}{N_0} L_r$ and the space-time coded simulated performance curves against $\frac{E_b}{N_0}$. This removes the advantage that receive diversity has over transmit diversity in order to demonstrate the comparable diversity. The advantage occurs due to the spread of energy over the transmit antennas required for transmit diversity. The slopes of the curves in Figure 3.9 demonstrate that the space-time coded system has spatial diversity equal to the number of transmit antennas. When L_t is equal to one, there is no diversity and consequently the performance in the Rayleigh fading channel is poor.

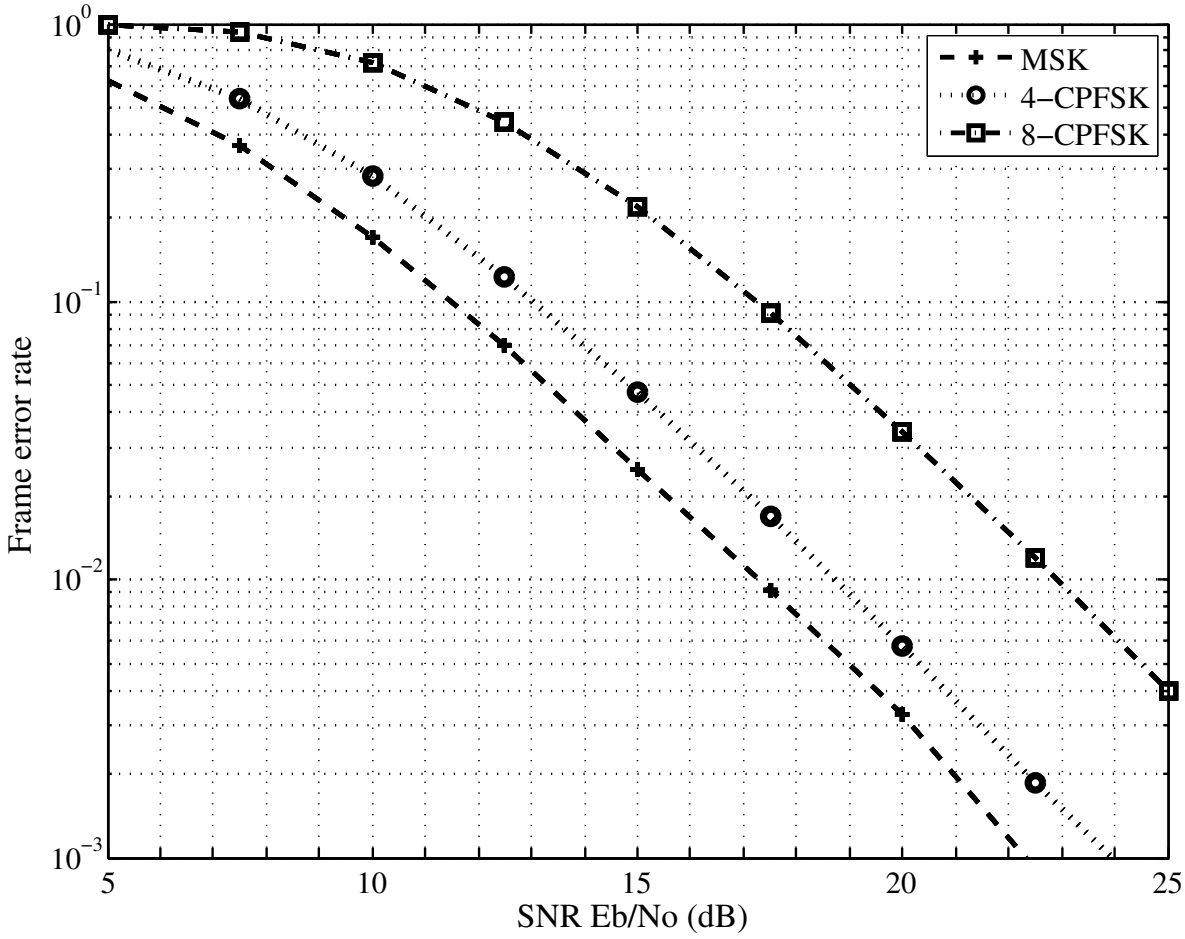

Figure 3.11: Frame error rate performance of delay diversity, $\boldsymbol{G}(D) = [D \quad 1]$, space-time coded M-CPFSK for $M = \{2, 4, 8\}$ with $L_t = 2$ and $L_r = 1$.

The encoding of a two transmit antenna, delay diversity space-time coded system with 4-CPFSK can be implemented using the encoder shown in Figure 3.8 with modulo-4 adders. The trellis for this system has 16 states. Figure 3.10 shows the frame error rate performance of delay diversity space-time coded 4-CPFSK with two transmit antennas and one, two and four receive antennas. The system diversity increases with the number of receive antennas (multiplied by the transmit diversity).

Figure 3.11 presents the frame error rate performance of delay diversity STC M-CPFSK with two transmit antennas and one receive antenna with varying modulation alphabet size, M. As the information throughput, which is equal to $\log_2 M$ for these systems, increases the performance of the systems becomes worse. The change in performance is more significant in moving from $M = 4$ to $M = 8$, than between the systems with $M = 2$ and $M = 4$. At a frame error rate of 10^{-2} the performance of the MSK modulated system is approximately

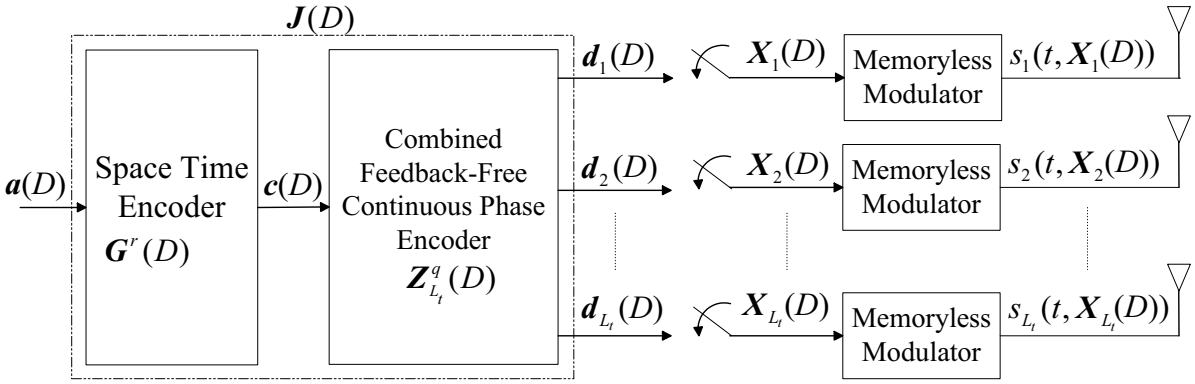

Figure 3.12: Space-time coded CPM transmitter with combined encoder.

1.5 dB better than the 4-CPFSK modulated system, and the performance of the 4-CPFSK modulated system is more than 4 dB better than the 8-CPFSK modulated system.

The total number of trellis states (denoted S_J) of the combined encoder, for the delay diversity space-time coded systems, with M-CPFSK, is

$$S_J = M^{L_t}. \tag{3.58}$$

The delay diversity space-time encoder described by Equation (3.55), has $S_G = M^{L_t-1}$ trellis states, and the combined feedback-free CPE described by Equation (3.47), has $S_Z = M^{L_t}$ trellis states. Hence, there is a significant reduction of the number of trellis states of the combined encoder, $\boldsymbol{J}(D)$, compared to the expected number, $S_G \times S_Z = M^{2L_t-1}$. The delay diversity code, in fact, adds no more complexity as $S_J = S_Z = M^{L_t}$. We compare this to the complexity of a delay diversity space-time M-CPFSK system, using the STC-CPM design presented by Zhang and Fitz in [11] and described in Section 2.5 of Chapter 2, where no state combining is possible. The number of states required by the supertrellis is $M^{L_t}2^{2L_t-1}$, as shown by Equation (2.88). This is 2^{2L_t-1} times the number of states required for our integrated design. Also, the supertrellis for Fitz and Zhang's system is time-variant.

Combined Overall Encoder for Systems with $l \neq k_m L_t$

We now consider the case where the space-time encoder and the modulation are designed such that $l \neq k_m L_t$. In order to combine $\boldsymbol{G}(D)$ and $\boldsymbol{Z}_{L_t}(D)$, we must effectively move the commutator to follow the encoding process as shown in Figure 3.12. Equivalent rate encoders

must be found for $\boldsymbol{G}(D)$ and $\boldsymbol{Z}_{L_t}(D)$, such that, at a given time the equivalent rate encoder for $\boldsymbol{G}(D)$ has the same number of output symbols, as the equivalent rate encoder for $\boldsymbol{Z}_{L_t}(D)$ has input symbols. To achieve this, we find the lowest common multiple of l and $k_m L_t$, such that $rl = qk_m L_t$, where r and q are integers. We convert, $\boldsymbol{G}(D)$ to a rate-$\frac{rk}{rl}$ encoder denoted $\boldsymbol{G}^r(D)$, and $\boldsymbol{Z}_{L_t}(D)$ to a rate-$\frac{qk_m L_t}{qL_t(k_m L+1)}$ encoder denoted $\boldsymbol{Z}^q_{L_t}(D)$. The encoders may then be directly cascaded to obtain the composite encoder

$$\boldsymbol{J}(D) = \boldsymbol{G}^r(D)\boldsymbol{Z}^q_{L_t}(D), \tag{3.59}$$

which has an $(rk \times qL_t(k_m L + 1))$-dimensional generator matrix. Only one rate conversion is required if l is a multiple of $k_m L_t$ or vice versa.

The encoder $\boldsymbol{G}^r(D)$ accepts the (rk)-symbol input vector

$$\boldsymbol{a}_m = \left[\mathrm{a}^1_m \;\; a^2_m \;\; \ldots \;\; a^{rk}_m\right], \quad mT_{k_f} \le t \le (m+1)T_{k_f}, \tag{3.60}$$

and outputs an (rl)-symbol vector every T_{k_f}-second trellis interval, where $T_{k_f} = rT_{k_v} = Tq$ and T_{k_v} is defined by Equation (3.50). The vector output from $\boldsymbol{G}^r(D)$ is denoted

$$\boldsymbol{c}_m = \left[\mathrm{c}^1_m \;\; c^2_m \;\; \ldots \;\; c^{rl}_m\right], \quad mT_{k_f} \le t \le (m+1)T_{k_f}. \tag{3.61}$$

The encoder, $\boldsymbol{Z}^q_{L_t}(D)$, accepts the $(qk_m L_t = rl)$-symbol output vector of Equation (3.61) from $\boldsymbol{G}^r(D)$ and forms the $(qL_t(k_m L + 1))$-symbol vector, $\boldsymbol{d}_m$, every T_{k_f}-second trellis interval. The vector, $\boldsymbol{d}_m$, is given by

$$\boldsymbol{d}_m = \left[\boldsymbol{d}_{1,m} \;\; \boldsymbol{d}_{2,m} \;\; \ldots \;\; \boldsymbol{d}_{L_t,m}\right], \quad mT_{k_f} \le t \le (m+1)T_{k_f}, \tag{3.62}$$

where

$$\begin{aligned}\boldsymbol{d}_{i,m} &= \left[d^1_{i,m} \;\; d^2_{i,m} \;\; \ldots \;\; d^{q(k_m L+1)}_{i,m}\right] \\ &= \left[\boldsymbol{X}_{i,mq} \;\; \boldsymbol{X}_{i,mq+1} \;\; \ldots \;\; \boldsymbol{X}_{i,(m+1)q-1}\right], \quad i = 1,2,\ldots,L_t, \quad mT_{k_f} \le t \le (m+1)T_{k_f},\end{aligned} \tag{3.63}$$

and

$$\begin{aligned}\boldsymbol{X}_{i,n} &= \left[d^{(n-mq)(k_m L+1)+1}_{i,m} \;\; d^{(n-mq)(k_m L+1)+2}_{i,m} \;\; \ldots \;\; d^{(n-mq+1)(k_m L+1)}_{i,m}\right], \\ &\quad n = mq, mq+1, \ldots, (m+1)q-1, \quad i = 1,2,\ldots,L_t, \quad mT_{k_f} \le t \le (m+1)T_{k_f}.\end{aligned} \tag{3.64}$$

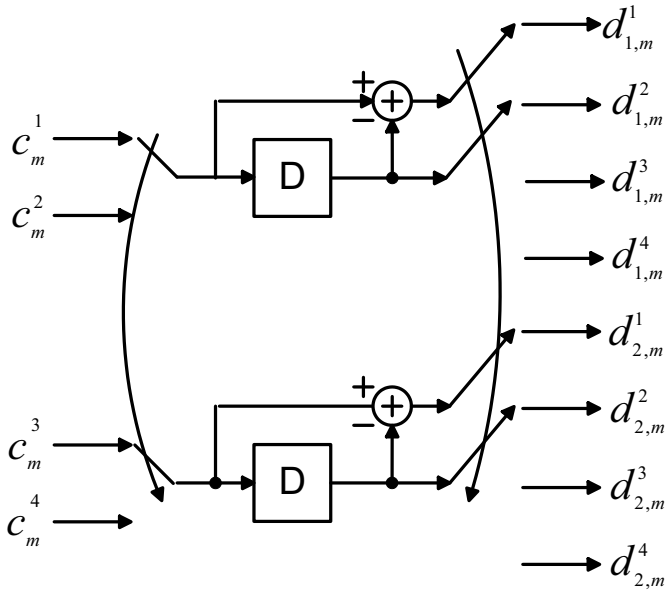

Figure 3.13: Encoder used to derive $\boldsymbol{Z}_2^2(D)$.

The input to the overall encoder, $\boldsymbol{J}(D)$ of Equation (3.59), during the trellis interval $mT_{k_f} \leq t \leq (m+1)T_{k_f}$ is $\boldsymbol{a}_m$ and the output is $\boldsymbol{d}_m$. During the n-th symbol interval, $T = \frac{T_{k_f}}{q}$, the i-th sampler selects the $(k_m L + 1)$-symbol vector $\boldsymbol{X}_{i,n}$, as input into the i-th memoryless modulator.

The equivalent rate encoders, $\boldsymbol{G}^r(D)$ and $\boldsymbol{Z}_{L_t}^q(D)$, are evaluated using the method presented in [27]. As an example, we derive the equivalent rate encoders, for a two transmit antenna $(L_t = 2)$ system. We consider an M-ary continuous phase modulation with $h = \frac{v}{p} = \frac{v}{M}$ $(k_m = 1)$, and a rate-$\frac{k}{l} = \frac{k}{4}$ space-time code. In this case

$$\begin{aligned} rl &= qk_m L_t \\ 4r &= 2q. \end{aligned} \tag{3.65}$$

Therefore, we let $r = 1$ and $q = 2$. Because $r = 1$, the space-time encoder is not required to be converted. The original generator matrix of the combined feedback-free CPE encoder, $\boldsymbol{Z}_2(D)$, is found from Equation (3.47) and is given by

$$\boldsymbol{Z}_2(D) = \begin{bmatrix} 1-D & D & 0 & 0 \\ 0 & 0 & 1-D & D \end{bmatrix}. \tag{3.66}$$

An implementation of the encoder defined by $\boldsymbol{Z}_2(D)$ is shown in Figure 3.5. To derive the equivalent encoder, $\boldsymbol{Z}_2^2(D)$, the encoder shown in Figure 3.13 is used. Each commutator in

the encoder operates simultaneously. The input and output relations of the encoder are,

$$d_{1,m}^1 = c_m^1 - D \cdot c_m^2, \tag{3.67}$$

$$d_{1,m}^2 = D \cdot c_m^2, \tag{3.68}$$

$$d_{1,m}^3 = c_m^2 - c_m^1, \tag{3.69}$$

$$d_{1,m}^4 = c_m^1, \tag{3.70}$$

$$d_{2,m}^1 = c_m^3 - D \cdot c_m^4, \tag{3.71}$$

$$d_{2,m}^2 = D \cdot c_m^4, \tag{3.72}$$

$$d_{2,m}^3 = c_m^4 - c_m^3, \tag{3.73}$$

$$d_{2,m}^4 = c_m^3. \tag{3.74}$$

The equivalent generator is derived using Equations (3.67) to (3.74) and is given by

$$\boldsymbol{Z}_2^2(D) = \begin{bmatrix} 1 & 0 & -1 & 1 & 0 & 0 & 0 & 0 \\ -D & D & 1 & 0 & 0 & 0 & 0 & 0 \\ 0 & 0 & 0 & 0 & 1 & 0 & -1 & 1 \\ 0 & 0 & 0 & 0 & -D & D & 1 & 0 \end{bmatrix}. \tag{3.75}$$

The encoder, $\boldsymbol{Z}_2^2(D)$, accepts a 4-symbol vector and outputs an 8-symbol vector during each trellis interval, $mT_{k_f} \leq t \leq (m+1)T_{k_f}$.

Example of a Rate-$\frac{1}{4}$ STC with Two Transmit Antennas

We present an example of a rate-$\frac{1}{4}$ STC in a two transmit antenna scheme with 4-CPFSK. The space-time code is constructed by combining the rate-$\frac{1}{2}$ convolutional encoder

$$\boldsymbol{F}(D) = \begin{bmatrix} 1 & \dfrac{1}{1+2D} \end{bmatrix}, \tag{3.76}$$

which was found to be optimal for single thread 4-CPFSK [29, 30], with the rate-$\frac{2}{4}$ encoder equivalent to the rate-$\frac{1}{2}$ two transmit antenna delay diversity encoder

$$\boldsymbol{G}(D) = [D \quad 1], \tag{3.77}$$

which is given by

$$\boldsymbol{G}^2(D) = \begin{bmatrix} 0 & 1 & 1 & 0 \\ D & 0 & 0 & 1 \end{bmatrix}. \tag{3.78}$$

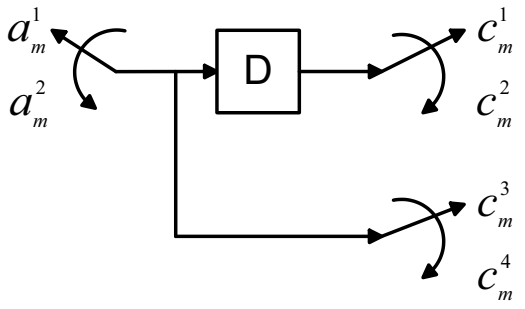

Figure 3.14: Encoder used to derive $\boldsymbol{Z}_2^2(D)$.

The encoder of Equation (3.78) is derived using Figure 3.14 and the equations

$$c_m^1 = D \cdot a_m^2, \tag{3.79}$$

$$c_m^2 = a_m^1, \tag{3.80}$$

$$c_m^3 = a_m^1, \tag{3.81}$$

$$c_m^4 = a_m^2. \tag{3.82}$$

The rate-$\frac{1}{4}$ space-time encoder generator matrix is then

$$\boldsymbol{G}(D) = \begin{bmatrix} 1 & \dfrac{1}{1+2D} \end{bmatrix} \begin{bmatrix} 0 & 1 & 1 & 0 \\ D & 0 & 0 & 1 \end{bmatrix} = \begin{bmatrix} \dfrac{D}{1+2D} & 1 & 1 & \dfrac{1}{1+2D} \end{bmatrix}. \tag{3.83}$$

This encoder can be implemented with 1 delay storage element, an adder and a scalar multiplier. Its trellis has four states and 4 branches from each state.

For this system $r = 1$ and $q = 2$, and thus we may use the encoder $\boldsymbol{Z}_2^2(D)$ of Equation (3.75), and the space-time encoder of Equation (3.83) with no rate conversion. The resulting overall generator matrix is given by

$$\begin{aligned} \boldsymbol{J}(D) &= \boldsymbol{G}(D)\boldsymbol{Z}_2^2(D) \\ &= \begin{bmatrix} \dfrac{D}{1+2D} & 1 & 1 & \dfrac{1}{1+2D} \end{bmatrix} \begin{bmatrix} 1 & 0 & -1 & 1 & 0 & 0 & 0 & 0 \\ -D & D & 1 & 0 & 0 & 0 & 0 & 0 \\ 0 & 0 & 0 & 0 & 1 & 0 & -1 & 1 \\ 0 & 0 & 0 & 0 & -D & D & 1 & 0 \end{bmatrix} \\ &= \begin{bmatrix} \frac{2D^2}{1+2D} & D & \frac{1+D}{1+2D} & \frac{D}{1+2D} & \frac{1+D}{1+2D} & \frac{D}{1+2D} & \frac{2D}{1+2D} & 1 \end{bmatrix}. \end{aligned} \tag{3.84}$$

This space-time coded system with 4-CPFSK produces an overall system with a transmission rate of 1 bit per symbol period, which is the same rate as a delay diversity system based on MSK.

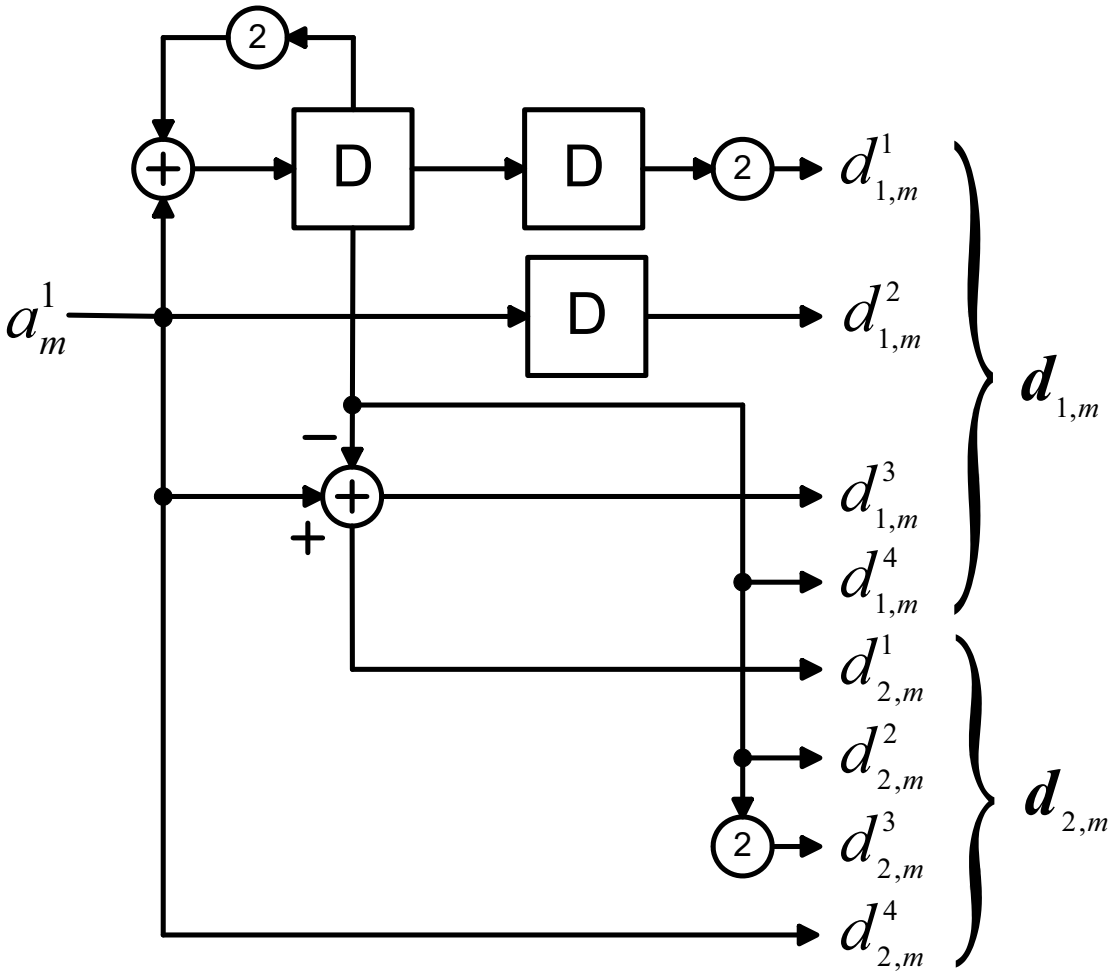

Figure 3.15: Implementation of the combined encoder
$\boldsymbol{J}(D) = \left[\frac{2D^2}{1+2D} \;\; D \;\; \frac{1+D}{1+2D} \;\; \frac{D}{1+2D} \;\; \frac{1+D}{1+2D} \;\; \frac{D}{1+2D} \;\; \frac{2D}{1+2D} \;\; 1\right]$ for 4-CPFSK and $L_t = 2$.

Figure 3.15 shows an implementation of the overall encoder given by Equation (3.84). It can be represented by an 8 state trellis with four branches originating from each state, as shown in Figure 3.16. The trellis transitions are labelled with the corresponding input and output symbols, $a_m^1\left(d_{1,m}^1 d_{1,m}^2\, d_{1,m}^3 d_{1,m}^4 \quad d_{2,m}^1 d_{2,m}^2 d_{2,m}^3 d_{2,m}^4\right)$, of the overall encoder described by Equation (3.84). The trellis states are labelled with the contents of the 3 delay elements.

Figure 3.17 shows the frame error rate performance of the rate-$\frac{1}{4}$ space-time code of Equation (3.83) with 4-CPFSK and two transmit antennas, and of the MSK delay diversity space-time coded system with two transmit antennas, for a varying number of receive antennas. Both systems have a throughput of 1 bit per symbol period. Also, both systems have full transmit diversity. The performance of the rate-$\frac{1}{4}$ space-time code with 4-CPFSK is superior for any

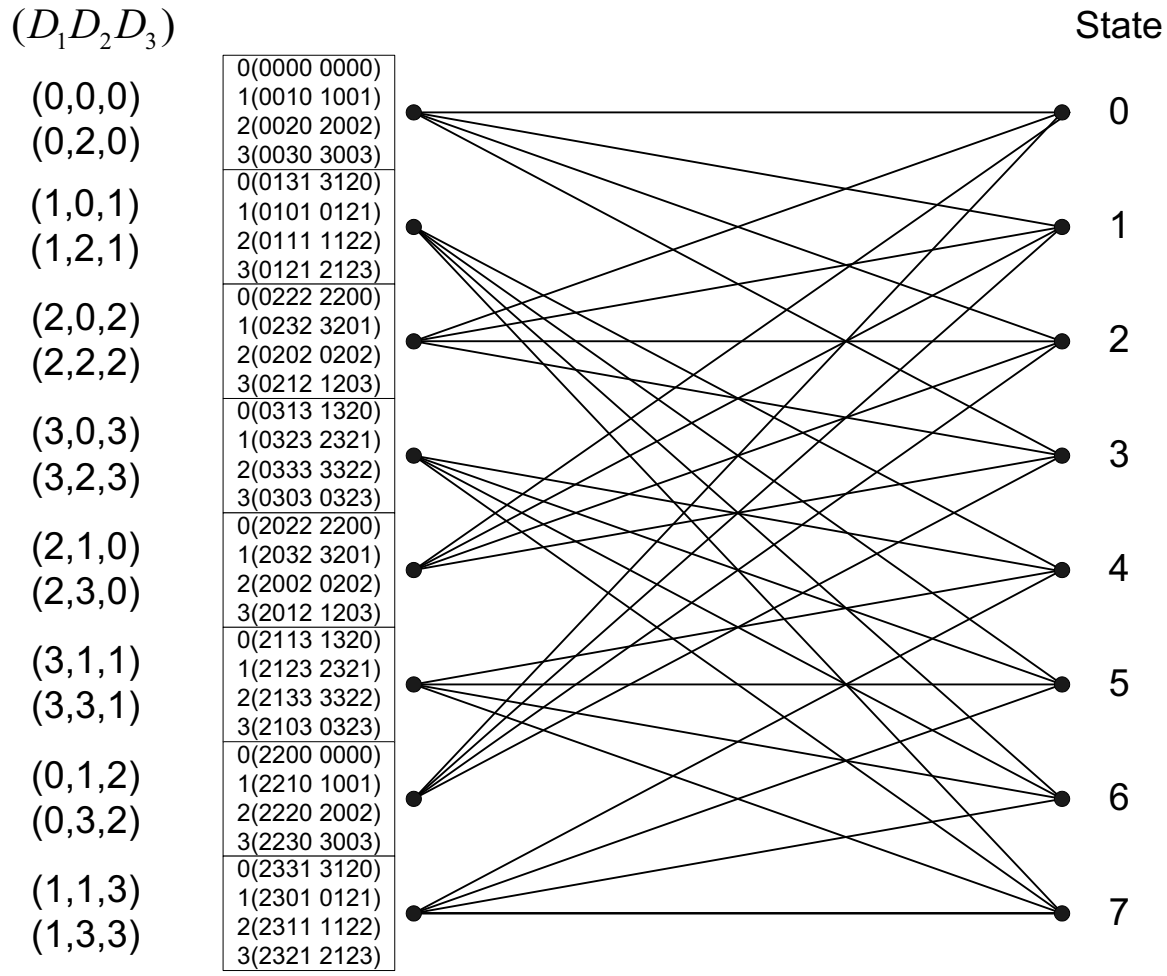

Figure 3.16: Trellis Diagram for the combined encoder
$\boldsymbol{J}(D) = \left[\frac{2D^2}{1+2D} \quad D \quad \frac{1+D}{1+2D} \quad \frac{D}{1+2D} \quad \frac{1+D}{1+2D} \quad \frac{D}{1+2D} \quad \frac{2D}{1+2D} \quad 1\right]$ for 4-CPFSK and $L_t = 2$.

number of receive antennas. This illustrates that developing a system that has full transmit diversity is only part of the overall design problem.

3.5.2 Transmission Rate of STC-CPM

The transmission rate or throughput is the information conveyed per signalling interval. The rate (bits/symbol period) of the space-time encoder is denoted R_{ST} and is given by

$$R_{ST} = \frac{rk \log_2 p}{rl \log_2 p} = \frac{k}{l} \quad \text{bits/symbol period.} \tag{3.85}$$

R_T denotes the combined scrambler transmission rate, which is given by

$$R_T = \frac{qL_t k_m \log_2 p}{qL_t k_m \log_2 p} = 1 \quad \text{bits/symbol period.} \tag{3.86}$$

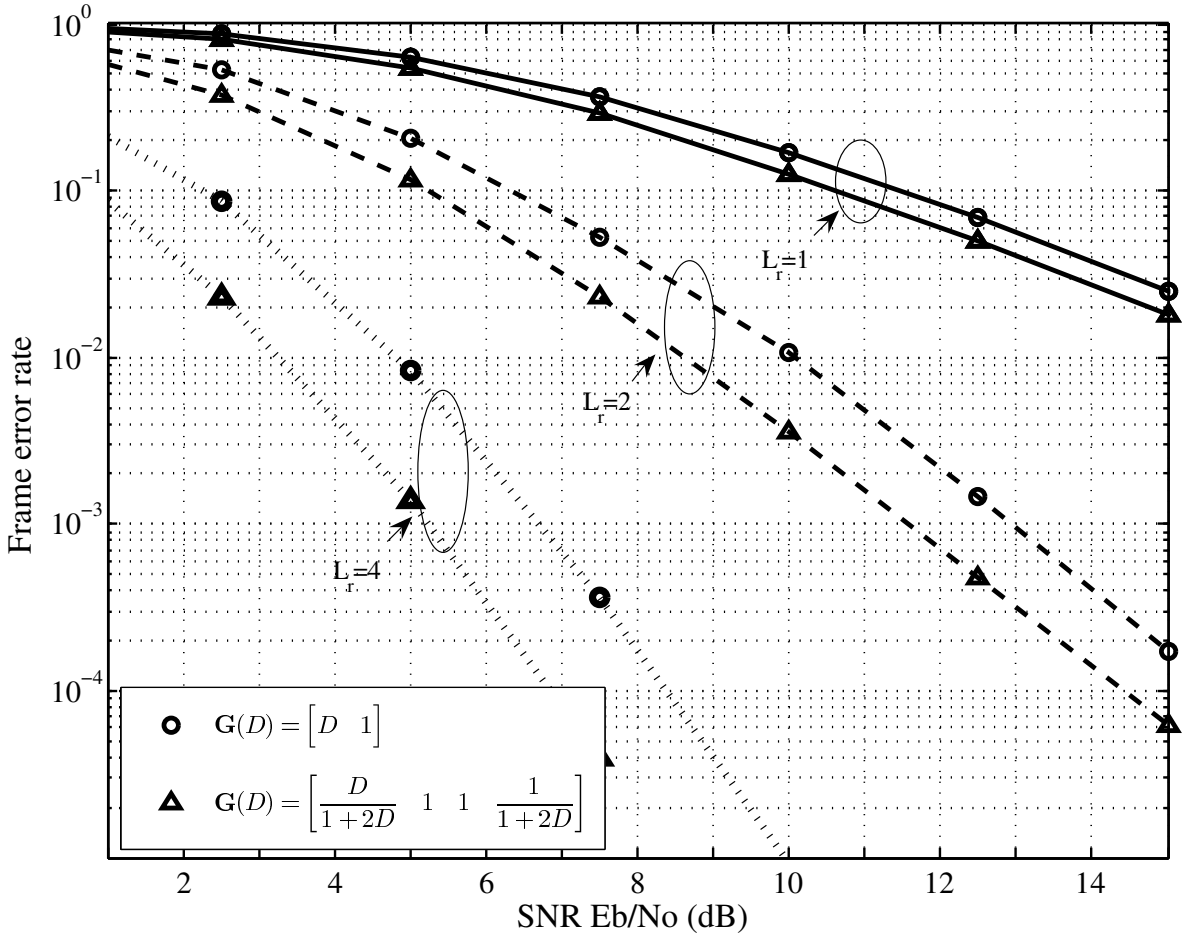

Figure 3.17: Frame error rate performance of $\boldsymbol{G}(D) = \left[\frac{D}{1+2D} \quad 1 \quad 1 \quad \frac{1}{1+2D}\right]$ with 4-CPFSK and $L_t = 2$, and $\boldsymbol{G}(D) = [D \quad 1]$ with MSK and $L_t = 2$. Both systems have the same throughput of 1 bit/symbol period.

The combined CPE throughput is denoted R_{CPE}, and is given by

$$R_{CPE} = \frac{qL_t k_m \log_2 p}{qL_t(k_m L + 1)\log_2 p} = \frac{k_m}{(k_m L + 1)} \quad \text{bits/symbol period.} \tag{3.87}$$

R_{MM} denotes the transmission rate of the memoryless modulators and

$$R_{MM} = \frac{L_t(k_m L + 1)\log_2 p}{1} = L_t(k_m L + 1)\log_2 p \quad \text{bits/symbol period.} \tag{3.88}$$

The overall rate or throughput of the STC-CPM system is then equal to

$$\begin{aligned} R_S &= R_{ST} \cdot R_T \cdot R_{CPE} \cdot R_{MM} \\ &= \frac{k}{l} \cdot 1 \cdot \frac{k_m}{(k_m L + 1)} \cdot L_t(k_m L + 1)\log_2 p \\ &= \frac{kL_t k_m \log_2 p}{l} \\ &= \frac{kL_t \log_2 M}{l} \quad \text{bits/symbol period.} \end{aligned} \tag{3.89}$$

Therefore, if a system has a rate $R_{ST} = \frac{1}{L_t}$ space-time code, its transmission rate will be $R_S = \log_2 M$ bits/symbol period. If a higher rate space-time code is used then the overall throughput will be greater than the number of bits per modulation symbol.

3.5.3 Metric for STC-CPM

In decoding, the maximum likelihood path metric of Equation (3.29) is rewritten as a sum over $N_t = \frac{N_K}{q}$ trellis intervals of duration $T_{k_f} = Tq$ as

$$M(y(t, \boldsymbol{X}(D))|\hat{\boldsymbol{X}}(D)) = \sum_{m=0}^{N_t-1} \lambda(\xi_m), \tag{3.90}$$

where

$$\lambda(\xi_m) = -\sum_{j=1}^{L_r} \sum_{n=mq}^{(m+1)q-1} \int_{nT}^{(n+1)T} \left| y_j(t, \boldsymbol{X}_n) - \sum_{i=1}^{L_t} \tilde{m}_{j,i} \tilde{s}_i(t, \hat{\boldsymbol{X}}_{i,n}) \right|^2 dt \tag{3.91}$$

is the branch metric. The Viterbi algorithm is then implemented over the trellis of the combined encoder, $\boldsymbol{J}(D)$.

3.5.4 Combined STC-CPM Encoder Complexity

The number of states in the overall encoder trellis is given by

$$S_J \leq S_G S_Z, \tag{3.92}$$

where S_G is the number of states in the trellis representing the encoder $\boldsymbol{G}^r(D)$, and S_Z is the number of states in the trellis representing the encoder $\boldsymbol{Z}^q_{L_t}(D)$ and is given by

$$S_Z = \left(pM^{L-1}\right)^{L_t} = p^{(1+k_m(L-1))L_t}. \tag{3.93}$$

The value of S_J is determined by how the states of the encoders $\boldsymbol{G}^r(D)$ and $\boldsymbol{Z}^q_{L_t}(D)$ merge in the overall trellis [65, 26, 27].

As an example, we consider the number of states in the overall encoder for the special case of full response $(L = 1)$ CPM. We assume that the space-time encoder is a rate-$\frac{k}{l}$ encoder and that l is a multiple of $k_m L_t$, such that $l = qk_m L_t$. Then number of states in the overall encoder trellis is given by

$$S_J = S_G c_s \leq S_G S_Z = S_G p^{L_t}, \tag{3.94}$$

where c_s is equal to the number of possible combinations that the L_t elements, $\{c_m^{qk_m}, c_m^{2qk_m}, \ldots, c_m^{L_t qk_m}\}$, of the space-time encoder output vector, $\boldsymbol{c}_m$ of Equation (3.61), can take on before the space-time encoder merges to the zero state.

Delay diversity with 4-CPFSK and two transmit antennas has $l = 2$, $k_m = 1$, $L_t = 2$ and $q = 1$. The space-time encoder, $\boldsymbol{G}(D) = [D \quad 1]$, has an $S_G = 4$ state trellis. The value of c_s for this system, depends on the number of combinations the elements, $\{c_m^1, c_m^2\}$, may take on before the encoder merges to the zero state. The possible combinations of $\{c_m^1, c_m^2\}$ before the space-time encoder merges to the zero state are

$$\{0,0\}, \{1,0\}, \{2,0\}, \{3,0\}. \tag{3.95}$$

Therefore, $c_s = 4$ and the number of states of the overall encoder is

$$S_J = S_G c_s = 4 \cdot 4 = 16 = M^{L_t}, \tag{3.96}$$

which as discussed previously is a significant reduction, compared to the number of states when no state combining occurs, as then, $S_G S_Z = 4 \cdot 16 = 64$.

We now consider the space-time code, $\boldsymbol{G}(D) = \left[\frac{D}{1+2D} \quad 1 \quad 1 \quad \frac{1}{1+2D}\right]$, with 4-CPFSK and 2 transmit antennas. The trellis of this space-time encoder has $S_G = 4$ states and as discussed previously, the system has $l = 4$, $k_m = 1$, $L_t = 2$ and $q = 2$. Therefore, c_s depends on the symbols, $\{c_m^2, c_m^4\}$, which may equal

$$\{0,0\}, \{2,0\}, \tag{3.97}$$

as the space-time encoder enters the zero state. Hence, the number of trellis states of the overall encoder is

$$S_J = S_G c_s = 4 \cdot 2 = 8. \tag{3.98}$$

The number of states for this system when no state combining occurs is $S_G S_Z = 4 \cdot 16 = 64$. Thus, an eightfold reduction in the number of trellis states is achieved using the integrated design.

3.5.5 STC-CPM Implementation with Feedback CPM

In order to implement the STC-CPM system using feedback CPM modulators, which are not pre-coded with $\boldsymbol{T}(D)$, we cascade the space-time code, $\boldsymbol{G}(D)$, with the L_t scramblers, $\boldsymbol{T}(D)$

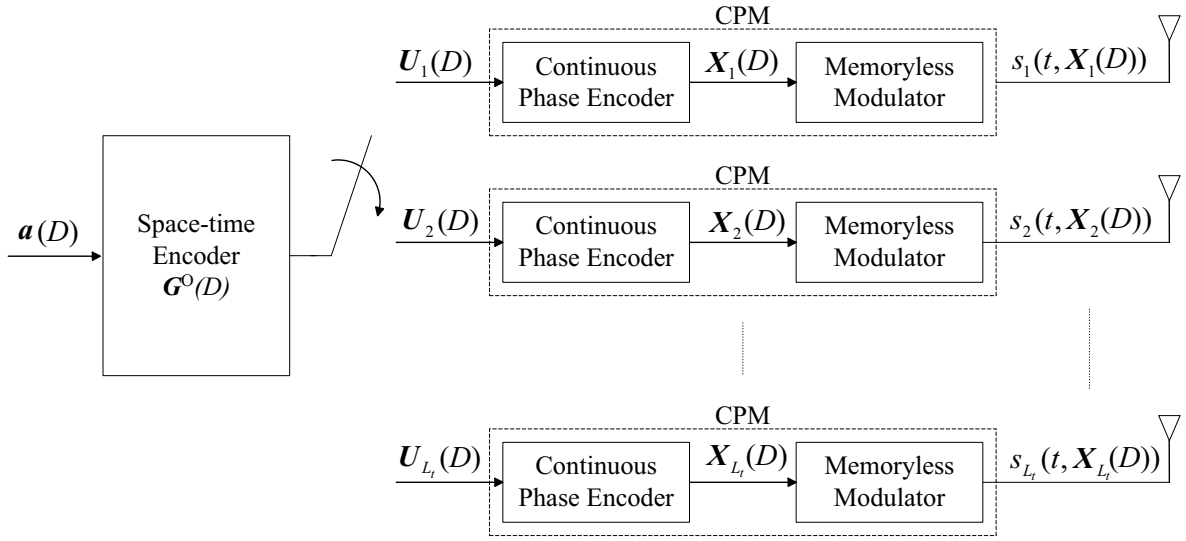

Figure 3.18: Space-time coded CPM transmitter with feedback CPM.

defined by Equation (3.32). We let $\boldsymbol{T}_{L_t}(D)$ denote a combined scrambler encoder with the generator matrix

$$\boldsymbol{T}_{L_t}(D) = \begin{bmatrix} \boldsymbol{T}(D) & \mathbf{0}_{k_m,k_m} & \cdots & \mathbf{0}_{k_m,k_m} \\ \mathbf{0}_{k_m,k_m} & \ddots & \ddots & \vdots \\ \vdots & \ddots & \boldsymbol{T}(D) & \mathbf{0}_{k_m,k_m} \\ \mathbf{0}_{k_m,k_m} & \cdots & \mathbf{0}_{k_m,k_m} & \boldsymbol{T}(D) \end{bmatrix}. \tag{3.99}$$

If $l = k_m L_t$, the new scrambled space-time encoder, denoted $\boldsymbol{G}^{\circ}(D)$, has the generator matrix

$$\boldsymbol{G}^{\circ}(D) = \boldsymbol{G}(D)\boldsymbol{T}_{L_t}(D). \tag{3.100}$$

If $l \neq k_m L_t$ then $\boldsymbol{G}(D)$ and $\boldsymbol{T}_{L_t}(D)$ must undergo the conversions as discussed in Section 3.5.1 in order to obtain the composite space-time encoder, $\boldsymbol{G}^{\circ}(D)$.

Combining $\boldsymbol{G}^{\circ}(D)$ with multiple feedback continuous phase modulators, as illustrated in Figure 3.18, results in a system with the same overall coding and performance, as a system with the space-time encoder, $\boldsymbol{G}(D)$ and feedback-free CPM, as shown in Figure 3.6. If $\boldsymbol{G}(D)$ is a systematic encoder, the encoder $\boldsymbol{G}^{\circ}(D)$ is not necessarily systematic. However, the overall system is still guaranteed to be non-catastrophic. Therefore, to find the best space-time code, $\boldsymbol{G}^{\circ}(D)$, for a STC-CPM system with the feedback CPM implementation illustrated by

Figure 3.18, first, find the best space-time code, $\boldsymbol{G}(D)$, for the feedback-free CPM model, and then scramble this space-time code to find $\boldsymbol{G}^{\circ}(D)$.

As an example, consider delay diversity, with M-ary CPM, three transmit antennas and $h = \frac{v}{M}$. The generator matrix of the space-time code is given by Equation (3.55). The new scrambled space-time code to be used with the multi-transmit antenna feedback CPM structure is then

$$\begin{aligned}\boldsymbol{G}^{\circ}(D) &= \boldsymbol{G}(D)\boldsymbol{T}_3(D) \\ &= [D^2 \quad D \quad 1]\begin{bmatrix} 1-D & 0 & 0 \\ 0 & 1-D & 0 \\ 0 & 0 & 1-D \end{bmatrix} \\ &= [D^2 - D^3 \quad D - D^2 \quad 1 - D].\end{aligned} \tag{3.101}$$

3.6 Summary

In this chapter, STC-CPM systems have been developed, in which the entire coding process including that of the modulation, may be described by a single convolutional encoder on $\mathbb{Z}_p$. The integrated structure means that performance measures can be easily evaluated and systematic design procedures can be devised. This will be demonstrated in Chapters 4 and 5.

A coherent multi-antenna receiver was described and the metric for Viterbi decoding of the STC-CPM signal was given. The decoding is implemented over the trellis of the combined encoder. Examples and properties of STC-CPM systems were presented. This included examining the trellises, the encoders, the simulated performance and the code complexity of several STC-CPM systems.

The STC-CPM system model presented allows a broad range of encoders and offers potentially high transmission rates. It was shown that there can be a substantial reduction of complexity, due to the merging trellis states of the space-time encoder and the continuous phase encoders in the combined encoder. Also, using the Rimoldi decomposition to model the CPM, results in a two-fold reduction in the number of trellis states, and allows for a time-invariant trellis representation.

Chapter 4

Space-Time Code Design

4.1 Introduction

In this chapter, we develop design criteria for space-time coded continuous phase modulated systems. We find an expression for the pairwise error probability (PEP) of space-time coded continuous phase modulation (STC-CPM) [11], which is analogous to the PEP bound for linearly modulated space-time codes presented in Section 2.4.3 of Chapter 2. The analysis used to derive design criteria for linearly modulated space-time codes is applied to STC-CPM. By considering signal distance matrices, analogous rank, determinant and Euclidean distance criteria are derived. These criteria can be used to select space-time codes for STC-CPM systems.

We first derive an expression for the normalized minimum squared Euclidean distance for STC-CPM and an exact formula for CPFSK modulated systems. We then use the Euclidean distance as the criterion to search for space-time codes with CPFSK. We consider systematic ring convolutional space-time encoders. Systematic ring encoders are always minimal, and minimal encoders are always non-catastrophic. Therefore, by using the feedback free model of the modulation, which is described in Section 3.4 of Chapter 3, non-catastrophic overall encoders are guaranteed. From the set of optimized space-time coded systems we identify the full rank schemes. These schemes will have good performance with any number of receive antennas as they are optimal in terms of both trace and rank. We present simulated performance curves of several space-time coded schemes identified by the code searches.

4.2 Pairwise Error Probability

In order to develop design criteria for space-time codes with CPM, we find now an expression for the pairwise error probability (PEP). We follow the analysis in [3] and [38], in which the pairwise error probability is derived for linearly modulated STC systems, and single thread trellis coded systems, respectively.

In a fading environment, if the complex channel coefficients are known at the receiver, the system is said to have ideal channel state information. The receiver then chooses the symbol sequence that is closest to the received signal in Euclidean distance. The receiver achieves this by maximizing the metric

$$M(y(t,\boldsymbol{X}(D))|\hat{\boldsymbol{X}}(D)) = -\sum_{j=1}^{L_r}\sum_{n=0}^{N_c-1}\int_{nT}^{(n+1)T}\left|y_j(t,\boldsymbol{X}_n) - \sum_{i=1}^{L_t}\tilde{m}_{j,i}\tilde{s}_i(t,\hat{\boldsymbol{X}}_{i,n})\right|^2 dt. \quad (4.1)$$

If an incorrect sequence, $\hat{\boldsymbol{X}}(D)$, is chosen over the correct sequence, $\boldsymbol{X}(D)$, a pairwise error has occurred. This situation will arise when

$$\begin{aligned}\sum_{j=1}^{L_r}\sum_{n=0}^{N_c-1}\int_{nT}^{(n+1)T}\left|y_j(t,\boldsymbol{X}_n) - \sum_{i=1}^{L_t}\tilde{m}_{j,i}\tilde{s}_i(t,\hat{\boldsymbol{X}}_{i,n})\right|^2 dt \leq \\ \sum_{j=1}^{L_r}\sum_{n=0}^{N_c-1}\int_{nT}^{(n+1)T}\left|y_j(t,\boldsymbol{X}_n) - \sum_{i=1}^{L_t}\tilde{m}_{j,i}\tilde{s}_i(t,\boldsymbol{X}_{i,n})\right|^2 dt,\end{aligned} \quad (4.2)$$

where N_c denotes the number of symbol intervals. In a data-transmission system that uses only a pair of sequences, $\hat{\boldsymbol{X}}(D)$ and $\boldsymbol{X}(D)$, the probability that the receiver chooses the wrong sequence is the PEP [68]. We denote the probability of a pairwise error as $P(\boldsymbol{X} \rightarrow \hat{\boldsymbol{X}})$. The PEP can be used to form expressions that bound system performance.

We now derive the PEP for a STC-CPM system. Substituting the demodulated signal

$$y_j(t,\boldsymbol{X}_n) = \sum_{i=1}^{L_t}\tilde{m}_{j,i}\tilde{s}_i(t,\boldsymbol{X}_{i,n}) + \tilde{n}_j(t), \quad 0 \leq t \leq N_cT, \quad j = 1,2,\ldots,L_r \quad (4.3)$$

into Equation (4.2), the inequality becomes

$$\sum_{j=1}^{L_r}\sum_{n=0}^{N_c-1}\int_{nT}^{(n+1)T}\left|\sum_{i=1}^{L_t}\tilde{m}_{j,i}\left[\tilde{s}_i(t,\boldsymbol{X}_{i,n}) - \tilde{s}_i(t,\hat{\boldsymbol{X}}_{i,n})\right] + \tilde{n}_j(t)\right|^2 dt \leq \sum_{j=1}^{L_r}\sum_{n=0}^{N_c-1}\int_{nT}^{(n+1)T}|\tilde{n}_j(t)|^2\,dt. \quad (4.4)$$

We manipulate the left hand side of Equation (4.4) to obtain

$$\begin{aligned}
&\sum_{j=1}^{L_r}\sum_{n=0}^{N_c-1}\int_{nT}^{(n+1)T}\left|\sum_{i=1}^{L_t}\tilde{m}_{j,i}\left[\tilde{s}_i(t,\boldsymbol{X}_{i,n})-\tilde{s}_i(t,\hat{\boldsymbol{X}}_{i,n})\right]+\tilde{n}_j(t)\right|^2 dt \\
&\quad=\sum_{j=1}^{L_r}\sum_{n=0}^{N_c-1}\int_{nT}^{(n+1)T}\left|\sum_{i=1}^{L_t}\tilde{m}_{j,i}\left[\tilde{s}_i(t,\boldsymbol{X}_{i,n})-\tilde{s}_i(t,\hat{\boldsymbol{X}}_{i,n})\right]\right|^2 dt \\
&\quad+\sum_{j=1}^{L_r}\sum_{n=0}^{N_c-1}\int_{nT}^{(n+1)T}\left(\sum_{i=1}^{L_t}\tilde{m}_{j,i}\left[\tilde{s}_i(t,\boldsymbol{X}_{i,n})-\tilde{s}_i(t,\hat{\boldsymbol{X}}_{i,n})\right]\right)^*\tilde{n}_j(t)dt \\
&\quad+\sum_{j=1}^{L_r}\sum_{n=0}^{N_c-1}\int_{nT}^{(n+1)T}\left(\sum_{i=1}^{L_t}\tilde{m}_{j,i}\left[\tilde{s}_i(t,\boldsymbol{X}_{i,n})-\tilde{s}_i(t,\hat{\boldsymbol{X}}_{i,n})\right]\right)[\tilde{n}_j(t)]^* dt \\
&\quad+\sum_{j=1}^{L_r}\sum_{n=0}^{N_c-1}\int_{nT}^{(n+1)T}|\tilde{n}_j(t)|^2 dt \\
&\quad=\sum_{j=1}^{L_r}\sum_{n=0}^{N_c-1}\int_{nT}^{(n+1)T}\left|\sum_{i=1}^{L_t}\tilde{m}_{j,i}\left[\tilde{s}_i(t,\boldsymbol{X}_{i,n})-\tilde{s}_i(t,\hat{\boldsymbol{X}}_{i,n})\right]\right|^2 dt \\
&\quad+2\mathbb{R}\left[\sum_{j=1}^{L_r}\sum_{n=0}^{N_c-1}\int_{nT}^{(n+1)T}\left(\sum_{i=1}^{L_t}\tilde{m}_{j,i}\left[\tilde{s}_i(t,\boldsymbol{X}_{i,n})-\tilde{s}_i(t,\hat{\boldsymbol{X}}_{i,n})\right]\right)[\tilde{n}_j(t)]^* dt\right] \\
&\quad+\sum_{j=1}^{L_r}\sum_{n=0}^{N_c-1}\int_{nT}^{(n+1)T}|\tilde{n}_j(t)|^2 dt.
\end{aligned} \tag{4.5}$$

Substituting Equation (4.5) into Equation (4.4) we find

$$\begin{aligned}
&2\mathbb{R}\left[\sum_{j=1}^{L_r}\sum_{n=0}^{N_c-1}\int_{nT}^{(n+1)T}\left(\sum_{i=1}^{L_t}\tilde{m}_{j,i}\left[\tilde{s}_i(t,\boldsymbol{X}_{i,n})-\tilde{s}_i(t,\hat{\boldsymbol{X}}_{i,n})\right]\right)[\tilde{n}_j(t)]^* dt\right] \\
&\quad+\sum_{j=1}^{L_r}\sum_{n=0}^{N_c-1}\int_{nT}^{(n+1)T}\left|\sum_{i=1}^{L_t}\tilde{m}_{j,i}\left[\tilde{s}_i(t,\boldsymbol{X}_{i,n})-\tilde{s}_i(t,\hat{\boldsymbol{X}}_{i,n})\right]\right|^2 dt\leq 0.
\end{aligned} \tag{4.6}$$

By substituting $-\left[\tilde{s}_i(t,\hat{\boldsymbol{X}}_{i,n})-\tilde{s}_i(t,\boldsymbol{X}_{i,n})\right]$ for $\left[\tilde{s}_i(t,\boldsymbol{X}_{i,n})-\tilde{s}_i(t,\hat{\boldsymbol{X}}_{i,n})\right]$, this can be rewritten as

$$\begin{aligned}
&\sum_{j=1}^{L_r}\sum_{n=0}^{N_c-1}\int_{nT}^{(n+1)T}\left|\sum_{i=1}^{L_t}\tilde{m}_{j,i}\left[\tilde{s}_i(t,\hat{\boldsymbol{X}}_{i,n})-\tilde{s}_i(t,\boldsymbol{X}_{i,n})\right]\right|^2 dt\leq \\
&\quad 2\mathbb{R}\left[\sum_{j=1}^{L_r}\sum_{n=0}^{N_c-1}\int_{nT}^{(n+1)T}\left(\sum_{i=1}^{L_t}\tilde{m}_{j,i}\left[\tilde{s}_i(t,\hat{\boldsymbol{X}}_{i,n})-\tilde{s}_i(t,\boldsymbol{X}_{i,n})\right]\right)[\tilde{n}_j(t)]^* dt\right].
\end{aligned} \tag{4.7}$$

We observe that the inequality of Equation (4.7) has the same form as the inequality of Equation (2.74), which describes the conditions for a pairwise error to occur in a linearly modulated STTC system. The codeword difference expression, $[\breve{x}_t^i - x_t^i]$, is replaced by the

continuous time difference between the signals, $\left[\tilde{s}_i(t, \hat{\boldsymbol{X}}_{i,n}) - \tilde{s}_i(t, \boldsymbol{X}_{i,n})\right]$, and the summations over time are replaced by sums of integrals over time in the inequality of Equation (4.7). The left hand side of the inequalities of Equations (4.7) and (2.74) are both modified Euclidean distances, for their respective continuous phase and linearly modulated STC systems. We denote the left hand side of the inequality of (4.7) as

$$d_m^2(\boldsymbol{X}, \hat{\boldsymbol{X}}) = \sum_{j=1}^{L_r} \sum_{n=0}^{N_c-1} \int_{nT}^{(n+1)T} \left| \sum_{i=1}^{L_t} \tilde{m}_{j,i} \left[\tilde{s}_i(t, \hat{\boldsymbol{X}}_{i,n}) - \tilde{s}_i(t, \boldsymbol{X}_{i,n})\right] \right|^2 dt. \tag{4.8}$$

The right hand side of Equation (4.7) is a Gaussian random variable with zero mean and variance $\sigma^2 = \sigma_n^2 d_m^2(\boldsymbol{X}, \hat{\boldsymbol{X}})$, where σ_n^2 is the noise power.

If we assume that the fading coefficients $\tilde{m}_{j,i}$ for $1 \leq i \leq L_t$ and $1 \leq j \leq L_r$ are known at the receiver, the conditional probability of a pairwise error is given by

$$\begin{aligned} &P(\boldsymbol{X} \to \hat{\boldsymbol{X}} | \tilde{\boldsymbol{m}}) \\ &\quad = \Pr\left\{ 2\mathbb{R}\left[\sum_{j=1}^{L_r} \sum_{n=0}^{N_c-1} \int_{nT}^{(n+1)T} \left(\sum_{i=1}^{L_t} \tilde{m}_{j,i} \left[\tilde{s}_i(t, \hat{\boldsymbol{X}}_{i,n}) - \tilde{s}_i(t, \boldsymbol{X}_{i,n})\right] \right) [\tilde{n}_j(t)]^* \, dt \right] \right. \\ &\quad \left. - \sum_{j=1}^{L_r} \sum_{n=0}^{N_c-1} \int_{nT}^{(n+1)T} \left| \sum_{i=1}^{L_t} \tilde{m}_{j,i} \left[\tilde{s}_i(t, \hat{\boldsymbol{X}}_{i,n}) - \tilde{s}_i(t, \boldsymbol{X}_{i,n})\right] \right|^2 dt \geq 0 \right\}, \end{aligned} \tag{4.9}$$

where $\tilde{\boldsymbol{m}}$ represents the fading coefficients, $\tilde{m}_{j,i}$ for $1 \leq i \leq L_t$ and $1 \leq j \leq L_r$. We can bound the probability of Equation (4.9) using the Chernoff bound [38], which states

$$\Pr\left\{ \sum_{i=0}^{I} z(i) \geq 0 \right\} \leq \prod_{i=0}^{I} E[\exp(\lambda z(i))], \tag{4.10}$$

where $E[\ ]$ is the expected value of the expression in the parentheses and λ is a parameter to be optimized. Using the Chernoff bound to reform Equation (4.9), and substituting from

Equation (4.8) we find the upper bound on the conditional PEP

$$
\begin{aligned}
&P(\boldsymbol{X} \to \hat{\boldsymbol{X}}|\tilde{\boldsymbol{m}}) \\
&\leq E\left[\exp\left(\lambda 2\mathbb{R}\left[\sum_{j=1}^{L_r}\sum_{n=0}^{N_c-1}\int_{nT}^{(n+1)T}\left(\sum_{i=1}^{L_t}\tilde{m}_{j,i}\left[\tilde{s}_i(t,\hat{\boldsymbol{X}}_{i,n})-\tilde{s}_i(t,\boldsymbol{X}_{i,n})\right]\right)[\tilde{n}_j(t)]^* dt\right]\right)\right] \\
&E\left[\exp\left(-\lambda\sum_{j=1}^{L_r}\sum_{n=0}^{N_c-1}\int_{nT}^{(n+1)T}\left|\sum_{i=1}^{L_t}\tilde{m}_{j,i}\left[\tilde{s}_i(t,\hat{\boldsymbol{X}}_{i,n})-\tilde{s}_i(t,\boldsymbol{X}_{i,n})\right]\right|^2 dt\right)\right] \\
&\leq \exp\left(\lambda^2\sigma_n^2 d_m^2(\boldsymbol{X},\hat{\boldsymbol{X}})\right)\exp\left(-\lambda d_m^2(\boldsymbol{X},\hat{\boldsymbol{X}})\right) \\
&\leq \exp\left(-\lambda d_m^2(\boldsymbol{X},\hat{\boldsymbol{X}})\left(1-\lambda\sigma_n^2\right)\right).
\end{aligned}
\tag{4.11}
$$

Optimizing over the Chernoff parameter gives $\lambda_{\text{opt}} = \frac{1}{2\sigma_n^2}$ [38]. Substituting λ_{opt} into the inequality of Equation (4.11) yields

$$
\begin{aligned}
P(\boldsymbol{X} \to \hat{\boldsymbol{X}}|\tilde{\boldsymbol{m}}) &\leq \exp\left(-\frac{d_m^2(\boldsymbol{X},\hat{\boldsymbol{X}})}{2\sigma_n^2}\left(1-\frac{1}{2}\right)\right) \\
&\leq \exp\left(-\frac{d_m^2(\boldsymbol{X},\hat{\boldsymbol{X}})}{4\sigma_n^2}\right).
\end{aligned}
\tag{4.12}
$$

We let the total transmit power, P_t, at each receive antenna be normalized to 1, and then

$$
\frac{P_t}{\sigma_n^2} = \frac{1}{\sigma_n^2} = \frac{E_s}{N_0}. \tag{4.13}
$$

The conditional PEP (4.12) is then bounded by

$$
P(\boldsymbol{X} \to \hat{\boldsymbol{X}}|\tilde{\boldsymbol{m}}) \leq \exp\left(-\frac{d_m^2(\boldsymbol{X},\hat{\boldsymbol{X}})E_s}{4N_0}\right). \tag{4.14}
$$

We let $\triangle_i(t) = \tilde{s}_i(t,\boldsymbol{X}_i(D)) - \tilde{s}_i(t,\hat{\boldsymbol{X}}_i(D))$ denote the continuous time difference between the transmitted and the decoded signal from the i-th transmit antenna[1]. The modified Euclidean distance of Equation (4.8) can then be written as

$$
\begin{aligned}
d_m^2(\boldsymbol{X},\hat{\boldsymbol{X}}) &= \sum_{j=1}^{L_r}\int_0^{N_cT}\left|\sum_{i=1}^{L_t}\tilde{m}_{j,i}\left[\tilde{s}_i(t,\hat{\boldsymbol{X}}_i(D))-\tilde{s}_i(t,\boldsymbol{X}_i(D))\right]\right|^2 dt \\
&= \sum_{j=1}^{L_r}\int_0^{N_cT}\left|\sum_{i=1}^{L_t}\tilde{m}_{j,i}\triangle_i(t)\right|^2 dt \\
&= \sum_{j=1}^{L_r}\sum_{i=1}^{L_t}\sum_{\acute{i}=1}^{L_t}\tilde{m}_{j,i}\int_0^{N_cT}\triangle_i(t)\triangle_{\acute{i}}^*(t)dt\;\tilde{m}_{j,\acute{i}}^*.
\end{aligned}
\tag{4.15}
$$

[1]We note that in any practical sense CPM signals and codes are indistinguishable due to the phase variation within each interval, which defines the code.

Following [11] we define the signal distance matrix as

$$\boldsymbol{S}=\begin{bmatrix} \int_0^{N_cT} |\triangle_1(t)|^2 dt & \cdots & \int_0^{N_cT} \triangle_1(t)\triangle_{L_t}^*(t)dt \\ \vdots & \vdots & \vdots \\ \int_0^{N_cT} \triangle_{L_t}(t)\triangle_1^*(t)dt & \cdots & \int_0^{N_cT} |\triangle_{L_t}(t)|^2 dt \end{bmatrix}. \tag{4.16}$$

The matrix, $\boldsymbol{S}$, is a non-negative definite Hermitian matrix. Therefore, there exists a unitary matrix, $\boldsymbol{V}$, and a real diagonal matrix, $\boldsymbol{D}$, with non-negative elements, such that

$$\boldsymbol{V}\boldsymbol{S}\boldsymbol{V}^H = \boldsymbol{D}, \tag{4.17}$$

where ^{H} denotes the Hermitian or transpose conjugate of a matrix. The rows of matrix $\boldsymbol{V}$ are the eigenvectors of $\boldsymbol{S}$, which we denote, $\boldsymbol{v}_i$ for $1 \leq i \leq L_t$. The diagonal elements of $\boldsymbol{D}$ are the eigenvalues of $\boldsymbol{S}$, which we denote, $\lambda_i \geq 0$ for $1 \leq i \leq L_t$. We let $\tilde{\boldsymbol{m}}_j = [\tilde{m}_{j,1}, \tilde{m}_{j,2}, \ldots, \tilde{m}_{j,L_t}]$ denote the array of fading coefficients that affect the signal on the j-th receive antenna. We can then write Equation (4.15) as

$$\begin{aligned} d_m^2(\boldsymbol{X}, \hat{\boldsymbol{X}}) &= \sum_{j=1}^{L_r} \tilde{\boldsymbol{m}}_j \boldsymbol{S} \tilde{\boldsymbol{m}}_j^H \\ &= \sum_{j=1}^{L_r} \tilde{\boldsymbol{m}}_j \boldsymbol{V}^H \boldsymbol{D} \boldsymbol{V} \tilde{\boldsymbol{m}}_j^H \\ &= \sum_{j=1}^{L_r} \sum_{i=1}^{L_t} \lambda_i \left|\beta_{i,j}\right|^2, \end{aligned} \tag{4.18}$$

where $\beta_{i,j} = \tilde{\boldsymbol{m}}_j {\boldsymbol{v}_i}^H$.

We substitute Equation (4.18) into the inequality of (4.14) to obtain

$$P(\boldsymbol{X} \rightarrow \hat{\boldsymbol{X}}|\tilde{\boldsymbol{m}}) \leq \exp\left(-\frac{E_s}{4N_0} \sum_{j=1}^{L_r} \sum_{i=1}^{L_t} \lambda_i \left|\beta_{i,j}\right|^2\right). \tag{4.19}$$

This bound is equivalent to the bound of Equation (2.84), which is derived for linearly modulated space-time codes. However, the eigenvalues, λ_i for $1 \leq i \leq L_t$, and eigenvectors, $\boldsymbol{v}_i$ for $1 \leq i \leq L_t$, are found from the signal distance matrix, $\boldsymbol{S}$ of Equation (4.16), instead of the codeword distance matrix, $\boldsymbol{A}(\boldsymbol{x}, \check{\boldsymbol{x}})$ of Equation (2.81). The statistical properties of $\beta_{i,j}$ are independent of the modulation. Therefore, we can utilize results derived for linearly modulated space-time codes, but consider the matrix $\boldsymbol{S}$, instead of the matrix $\boldsymbol{A}(\boldsymbol{x}, \check{\boldsymbol{x}})$. To find an unconditional PEP bound, we average the conditional PEP bound of Equation (4.19) over the variables $\beta_{i,j}$ for $1 \leq i \leq L_t$ and $1 \leq j \leq L_r$, which are dependent on the fading coefficients.

4.2.1 Large Number of Parallel Spatial Channels

In [3], it is shown that $\beta_{i,j}$ are Gaussian random variables with variance $\frac{1}{2}$ per dimension and mean, $\mu_{\beta_{i,j}} = E[\tilde{\boldsymbol{m}}_j]E[\boldsymbol{v}_i]$. In a Rayleigh fading environment $\mu_{\beta_{i,j}} = 0$. The variables $|\beta_{i,j}|^2$ are central chi squared distributed, and for a Rayleigh fading channel, they have mean $\mu_{|\beta_{i,j}|^2} = 1$ and variance $\sigma^2_{|\beta_{i,j}|^2} = 1$. The expression, $\sum_{j=1}^{L_r}\sum_{i=1}^{L_t}\lambda_i\,|\beta_{i,j}|^2$, approaches a Gaussian random variable [3], $\mathcal{D}$, according to the central limit theorem, when there is a large number of independent sub-channels (typically > 3). This occurs when $\rho_{\min}L_r > 3$, where $\rho_{\min}$ is the minimum number of non-zero eigenvalues of the signal distance matrices over all pairs of distinct signals. The random variable $\mathcal{D}$ has mean

$$\mu_{\mathcal{D}} = L_r \sum_{i=1}^{\rho} \lambda_i \tag{4.20}$$

and variance

$$\sigma^2_{\mathcal{D}} = L_r \sum_{i=1}^{\rho} \lambda_i^2, \tag{4.21}$$

where the summations are over the ρ non-zero eigenvalues and their squares. The PEP bound of Equation (4.19) then becomes [3]

$$\begin{aligned} P(\boldsymbol{X} \to \hat{\boldsymbol{X}}) &\leq \int_{\mathcal{D}=0}^{+\infty} \exp\left(-\frac{E_s}{4N_0}\mathcal{D}\right) p(\mathcal{D})d\mathcal{D} \\ &\leq \exp\left(\frac{1}{2}\left[\frac{E_s}{4N_0}\right]^2 \sigma^2_{\mathcal{D}} - \frac{E_s}{4N_0}\mu_{\mathcal{D}}\right) Q\left(\frac{E_s}{4N_0}\sigma_{\mathcal{D}} - \frac{\mu_{\mathcal{D}}}{\sigma_{\mathcal{D}}}\right) \\ &\leq \exp\left(\frac{1}{2}\left[\frac{E_s}{4N_0}\right]^2 L_r \sum_{i=1}^{\rho}\lambda_i^2 - \frac{E_s}{4N_0} L_r \sum_{i=1}^{\rho}\lambda_i\right) \times \\ &\qquad Q\left(\frac{E_s}{4N_0}\sqrt{L_r \sum_{i=1}^{\rho}\lambda_i^2} - \frac{L_r\sum_{i=1}^{\rho}\lambda_i}{\sqrt{L_r\sum_{i=1}^{\rho}\lambda_i^2}}\right), \end{aligned} \tag{4.22}$$

where $p(\mathcal{D})$ is the probability density function of the Gaussian random variable $\mathcal{D}$ and the Q function is described by

$$Q(x) = \frac{1}{\sqrt{2\pi}} \int_x^{\infty} \exp\left(\frac{-u^2}{2}\right) du. \tag{4.23}$$

It is observed in [3] that if we assume relatively high SNR such that

$$\frac{E_s}{4N_0} \geq \frac{L_r\sum_{i=1}^{\rho}\lambda_i}{\sqrt{L_r\sum_{i=1}^{\rho}\lambda_i^2}}, \tag{4.24}$$

and substitute the bound

$$Q(x) \leq \frac{1}{2}\exp\left(-\frac{x^2}{2}\right), \quad x \geq 0, \tag{4.25}$$

into Equation (4.22) we obtain the approximate PEP bound

$$\begin{aligned} P(\boldsymbol{X} \to \hat{\boldsymbol{X}}) &\leq \exp\left(\frac{1}{2}\left[\frac{E_s}{4N_0}\right]^2 L_r \sum_{i=1}^{\rho} \lambda_i^2 - \frac{E_s}{4N_0} L_r \sum_{i=1}^{\rho} \lambda_i\right) \times \\ &\quad \frac{1}{2}\exp\left(-\frac{1}{2}\left[\frac{E_s}{4N_0}\right]^2 L_r \sum_{i=1}^{\rho} \lambda_i^2\right) \\ &\leq \frac{1}{2}\exp\left(-L_r \frac{E_s}{4N_0} \sum_{i=1}^{\rho} \lambda_i\right). \end{aligned} \tag{4.26}$$

Thus, to design good space-time coded schemes based on minimizing the worst case PEP with $\rho_{\min} L_r > 3$, we need to maximize the minimum sum, $\Lambda^E_{\min}$, of the eigenvalues, $\Lambda^E = \sum_{i=1}^{\rho} \lambda_i$, over all pairs of distinct transmit signals. We can evaluate the summation, Λ^E, as the trace of the signal distance matrix

$$\begin{aligned} \Lambda^E &= \sum_{i=1}^{\rho} \lambda_i \\ &= trace(\boldsymbol{S}) \\ &= \sum_{i=1}^{L_t} S_{i,i} \\ &= \sum_{i=1}^{L_t} \int_0^{N_c T} |\triangle_i(t)|^2 dt, \end{aligned} \tag{4.27}$$

where $S_{i,i}$ for $1 \leq i \leq L_t$ are the elements of the matrix $\boldsymbol{S}$ on the diagonal. We observe that the summation of Equation (4.27) is equivalent to the squared Euclidean distance between the transmitted and the decoded signals. Thus, we may maximize the minimum squared Euclidean distance of the STC-CPM systems to find optimal schemes, when $\rho_{\min} L_r > 3$. The larger the product $\rho_{\min} L_r$ is, the more dominant the Euclidean distance is in determining the system's performance.

4.2.2 Small Number of Parallel Spatial Channels

If the number of independent sub-channels is small $(\rho_{\min} L_r < 4)$, then the Gaussian assumption is no longer valid and an upper bound on the PEP in Rayleigh fading is given by [3, 69]

$$\begin{aligned} P(\boldsymbol{X} \to \hat{\boldsymbol{X}}) &\leq \left(\prod_{i=1}^{L_t} \frac{1}{1 + \frac{E_s}{4N_0}\lambda_i}\right)^{L_r} \\ &\leq \left(1 + \frac{E_s}{4N_0} \sum_{i=1}^{\rho} \lambda_i + \left(\frac{E_s}{4N_0}\right)^{\rho} \prod_{i=1}^{\rho} \lambda_i\right)^{-L_r}. \end{aligned} \tag{4.28}$$

If the SNR is high, then the PEP bound of Equation (4.28) is dominated by the product term and we may approximate the bound by

$$P(\boldsymbol{X} \rightarrow \hat{\boldsymbol{X}}) \leq \left(\prod_{i=1}^{\rho} \lambda_i \right)^{-L_r} \left(\frac{E_s}{4N_0} \right)^{-\rho L_r}. \tag{4.29}$$

Thus, when searching for codes based on minimizing the worst case PEP in a system with a small number of parallel spatial channels, the minimum rank, $\rho_{\min}$, of the signal distance matrices over all pairs of distinct transmit signals is the most important parameter to maximize. The next most important parameter, which does not have as great an effect on the performance, is the minimum product, $\Lambda^P_{\min}$, of non-zero eigenvalues over all pairs of distinct transmit signals, where $\Lambda^P = \prod_{i=1}^{\rho} \lambda_i$ is known as the product distance.

In general, if the number of receive antennas multiplied by the rank is large (typically > 3), the system will be operating at low SNR over the error rates of interest. In this case the PEP bound of Equation (4.28) may be approximated by

$$P(\boldsymbol{X} \rightarrow \hat{\boldsymbol{X}}) \leq \left(\frac{E_s}{4N_0} \sum_{i=1}^{\rho} \lambda_i \right)^{-L_r}. \tag{4.30}$$

Then, the minimum squared Euclidean distance of the system is the parameter to maximize. This is the same criterion described in the previous section, where the PEP was approximated using the central limit theorem assuming a large number of parallel spatial channels. We note that asymptotically at high SNR the product term and hence $\rho_{\min}$ will dominate the performance.

4.2.3 Space-Time Coded CPM Design Summary

From the previous section we see that the minimum trace ($\Lambda^E_{\min}$), the minimum rank ($\rho_{\min}$) and the minimum product distance ($\Lambda^P_{\min}$), of the signal distance matrices over all pairs of distinct transmit signals are the parameters that should be used to design space-time coded CPM systems. The PEP of STC-CPM was shown to be analogous to the PEP of space-time coded linear modulation. Derivations used to find code search criteria for linearly modulated STC were applied to STC-CPM, by considering the signal distance matrix, instead of the codeword distance matrix.

Maximizing the minimum squared Euclidean distance may be used as the code search criterion when $\rho_{\min} L_r > 3$. This will hold ($\rho_{\min} L_r > 3$) for all schemes except those for which,

$\rho_{\min} = 1$ and $L_r \in \{1, 2, 3\}$, or $\rho_{\min} \in \{2, 3\}$ and $L_r = 1$. If a space-time code has full rank ($\rho_{\min} \geq 2$ for all multiple transmit antenna schemes) or is at least $\rho_{\min} = 2$, then the minimum squared Euclidean distance criterion is dominant in all cases, except when there is one receive antenna. If $\rho_{\min} L_r < 3$, maximizing the minimum rank and the minimum product distance can be used as the design criteria. In practice, we have found that the minimum product distance does not affect a system's performance noticeably if its minimum Euclidean distance is maximized. Thus, if we find the codes that maximize the minimum squared Euclidean distance, and then maximize $\rho_{\min}$, we will obtain codes that perform well, with any number of receive antennas.

4.3 Code Search Based on the Trace Criterion

We now describe the search for optimal space-time codes using the squared Euclidean distance criterion. We have shown that these codes will perform well for systems with $\rho_{\min} L_r > 3$. From the optimal space-time codes that are identified with the squared Euclidean distance criterion, we then find those that have the maximum possible transmit diversity. As discussed in the previous section, these codes will have good performance for any number of receive antennas. There may be some small loss in performance when the codes are used with one receive antenna, compared to codes that have superior minimum product distance.

4.3.1 Squared Euclidean Distance Calculation

The squared Euclidean distance (SED) between the signals, $s_i(t, \boldsymbol{X}_i(D))$ and $s_i(t, \hat{\boldsymbol{X}}_i(D))$ is defined in [7] as

$$D^2\left(\boldsymbol{X}_i(D), \hat{\boldsymbol{X}}_i(D)\right) = \int_{-\infty}^{\infty} \left| s_i(t, \boldsymbol{X}_i(D)) - s_i(t, \hat{\boldsymbol{X}}_i(D)) \right|^2 dt. \tag{4.31}$$

This can be rewritten as the sum of incremental squared Euclidean distances (ISED) in the form

$$\begin{aligned} D^2\left(\boldsymbol{X}_i(D), \hat{\boldsymbol{X}}_i(D)\right) &= \sum_n \int_{nT}^{(n+1)T} \left| s_i(t, \boldsymbol{X}_i(D)) - s_i(t, \hat{\boldsymbol{X}}_i(D)) \right|^2 \\ &= \sum_n D_n^2\left(\boldsymbol{X}_{i,n}, \hat{\boldsymbol{X}}_{i,n}\right), \end{aligned} \tag{4.32}$$

where the ISED is defined as

$$D_n^2\left(\boldsymbol{X}_{i,n}, \hat{\boldsymbol{X}}_{i,n}\right) = \int_{nT}^{(n+1)T} \left| s_i(t, \boldsymbol{X}_{i,n}) - s_i(t, \hat{\boldsymbol{X}}_{i,n}) \right|^2. \tag{4.33}$$

For the space-time coded CPM scheme the Euclidean distance between any two code segments is given by

$$D^2\left(\boldsymbol{X}(D), \hat{\boldsymbol{X}}(D)\right) = \sum_{i=1}^{L_t} \sum_{n} D_n^2\left(\boldsymbol{X}_{i,n}, \hat{\boldsymbol{X}}_{i,n}\right). \tag{4.34}$$

The minimum squared Euclidean distance (MSED) is defined as

$$D_{\min}^2\left(\boldsymbol{X}(D), \hat{\boldsymbol{X}}(D)\right) = \min_{\substack{\boldsymbol{X}(D), \hat{\boldsymbol{X}}(D) \\ \boldsymbol{X}(D) \neq \hat{\boldsymbol{X}}(D)}} D^2\left(\boldsymbol{X}(D), \hat{\boldsymbol{X}}(D)\right). \tag{4.35}$$

The normalized minimum squared Euclidean distance [7] is then

$$d_{\min}^2\left(\boldsymbol{X}(D), \hat{\boldsymbol{X}}(D)\right) = \frac{D_{\min}^2\left(\boldsymbol{X}(D), \hat{\boldsymbol{X}}(D)\right)}{2E_b}, \tag{4.36}$$

where E_b is the energy per bit, which is related to the symbol energy, E_s, by

$$E_b = \frac{E_s}{L_t \frac{k}{l} \log_2(M)}. \tag{4.37}$$

The distance of Equation (4.35) is used in combination with the trellis of a given system to find its minimum squared Euclidean distance. We describe this process in the following sections.

Squared Euclidean Distance for Space-Time Coded CPFSK Systems

It was shown in [42] and [70] that the ISED for CPFSK is defined by the input to the memoryless modulator and is given by

$$D_n^2\left(\boldsymbol{X}_{i,n}, \hat{\boldsymbol{X}}_{i,n}\right) = \begin{cases} \frac{2E_s}{L_t}\left[1 - \frac{\sin\left(2\pi h\left[X_{i,n}^1 + X_{i,n}^2 - \hat{X}_{i,n}^1 - \hat{X}_{i,n}^2\right]\right) - \sin\left(2\pi h\left[X_{i,n}^2 - \hat{X}_{i,n}^2\right]\right)}{2\pi h\left(X_{i,n}^1 - \hat{X}_{i,n}^1\right)}\right], & X_{i,n}^1 \neq \hat{X}_{i,n}^1 \\ \frac{2E_s}{L_t}\left[1 - \cos\left(2\pi h\left[X_{i,n}^2 - \hat{X}_{i,n}^2\right]\right)\right], & X_{i,n}^1 = \hat{X}_{i,n}^1 \end{cases}. \tag{4.38}$$

To find an expression for the minimum squared Euclidean distance for space-time coded CPFSK, the model of Figure 3.12 is used. During the trellis interval $mT_{k_f} \leq t \leq (m+1)T_{k_f}$ there are q vectors $\boldsymbol{X}_{i,n}$ (Equation (3.64)) that are input into each of the L_t memoryless modulators. The increment to the SED between two STC CPFSK signals generated by the data

sequences, $\boldsymbol{d}_m$ and $\hat{\boldsymbol{d}}_m$ described by Equation (3.62), over the m-th trellis interval, is the summation

$$\delta_m^2\left(\boldsymbol{d}_m, \hat{\boldsymbol{d}}_m\right) = \sum_{i=1}^{L_t}\sum_{t=0}^{q-1} D_{mq+t}^2\left(\boldsymbol{X}_{i,mq+t}, \hat{\boldsymbol{X}}_{i,mq+t}\right), \quad mT_{k_f} \leq t \leq (m+1)T_{k_f}, \quad (4.39)$$

where $D_n^2(\boldsymbol{X}_{i,n}, \hat{\boldsymbol{X}}_{i,n})$ is given by Equation (4.38). The SED over a frame of N_t trellis intervals is then

$$D^2\left(\boldsymbol{X}(D), \hat{\boldsymbol{X}}(D)\right) = \sum_{m=0}^{N_t-1} \delta_m^2\left(\boldsymbol{d}_m, \hat{\boldsymbol{d}}_m\right), \quad (4.40)$$

and $d_{\min}^2$ may be calculated using Equations (4.35) and (4.36).

Euclidean Distance Calculation Method

STC-CPM codes do not have a group property. Therefore, the minimum squared Euclidean distance cannot be calculated using the all-zero sequence as a reference. Each sequence must be compared to all other sequences. To calculate the minimum squared Euclidean distance for the space-time coded CPM systems, we use the *Viterbi algorithm in a superstate trellis* method described in [7].

Each error event can be described as a sequence of superstates. The superstate after the m-th trellis interval is denoted

$$(\sigma_m, \hat{\sigma}_m), \quad (4.41)$$

where

$$\sigma_m \in \{1, 2, \ldots, S_J\}, \quad (4.42)$$

and

$$\hat{\sigma}_m \in \{1, 2, \ldots, S_J\}, \quad (4.43)$$

are the states at the transmitter and the detector, after m trellis intervals, respectively. The sequence can start at symbol interval zero without loss of generality. Each error event sequence begins in an error free superstate. The initial superstates, $(\sigma_0, \hat{\sigma}_0)$, must therefore satisfy

$$\sigma_0 = \hat{\sigma}_0 \in \{1, 2, \ldots, S_J\}. \quad (4.44)$$

The first transition must be to an error superstate, that is, $\sigma_1 \neq \hat{\sigma}_1$. The error event ends when it next reaches an error free superstate (the sequence will include at least one error superstate).

A supertrellis with ${S_J}^2$ states can be used to describe the process. Each transition of the trellis has a SED increment, as defined by Equation (4.39), associated with it. The SED increment for transitions from error-free states to other error-free states is zero. The MSED, given by Equation (4.35), is found using the Viterbi algorithm (see Appendix C) and the supertrellis. The algorithm is stopped when all unterminated paths through the trellis have a larger distance than the minimum distance of the terminated paths.

4.3.2 Systematic Convolutional Space-Time Encoders

In this thesis, we search over rate-$\frac{l-1}{l}$ systematic convolutional encoders on the integer ring, $\mathbb{Z}_p$. Rate-$\frac{l-1}{l}$ space-time codes can form systems with good throughput [71] at the cost of achievable diversity. Systematic ring convolutional encoders are always minimal, that is, there exists a realization of the systematic encoder that uses the least number of encoder states to generate the code. Minimal encoders are always non-catastrophic [72]. Therefore, a systematic ring space-time encoder in combination with the feedback-free multi-CPM transmitter model developed in Section 3.4 will result in non-catastrophic overall encoders. For simplicity we let $l = L_t$ and use M-CPFSK as the modulation. Thus, we do not need to find equivalent rate space-time encoders or combined feedback-free CPE, as they may be directly cascaded.

The properties of the generator matrix of the space-time code, $\boldsymbol{G}(D)$, are described in Section 2.3.1 of Chapter 2. We follow [27, 29] and use the systematic feedback realization of $\boldsymbol{G}(D)$ given by

$$\boldsymbol{G}(D) = \begin{bmatrix} 1 & \dots & 0 & \frac{\boldsymbol{F}^1(D)}{\boldsymbol{F}^0(D)} \\ \vdots & \ddots & \vdots & \vdots \\ 0 & \dots & 1 & \frac{\boldsymbol{F}^{L_t-1}(D)}{\boldsymbol{F}^0(D)} \end{bmatrix}, \tag{4.45}$$

where

$$\boldsymbol{F}^i(D) = f_0^i + f_1^i D + \ldots + f_\nu^i D^\nu, \quad 0 \leq i \leq L_t - 1, \tag{4.46}$$

and ν is the number of delay cells in the encoder. The polynomial coefficients are given by

$$f_j^i \in \{0, 1, \ldots, p-1\}, \quad 0 \leq i \leq L_t - 1, \quad 0 \leq j \leq \nu. \tag{4.47}$$

Recall that M-CPFSK is M-ary CPFSK with $h = \frac{1}{M}$. For M-CPFSK the denominator of the modulation index $p = M$, and $\boldsymbol{G}(D)$ is on the integer ring $\mathbb{Z}_M$. In order for the encoder to

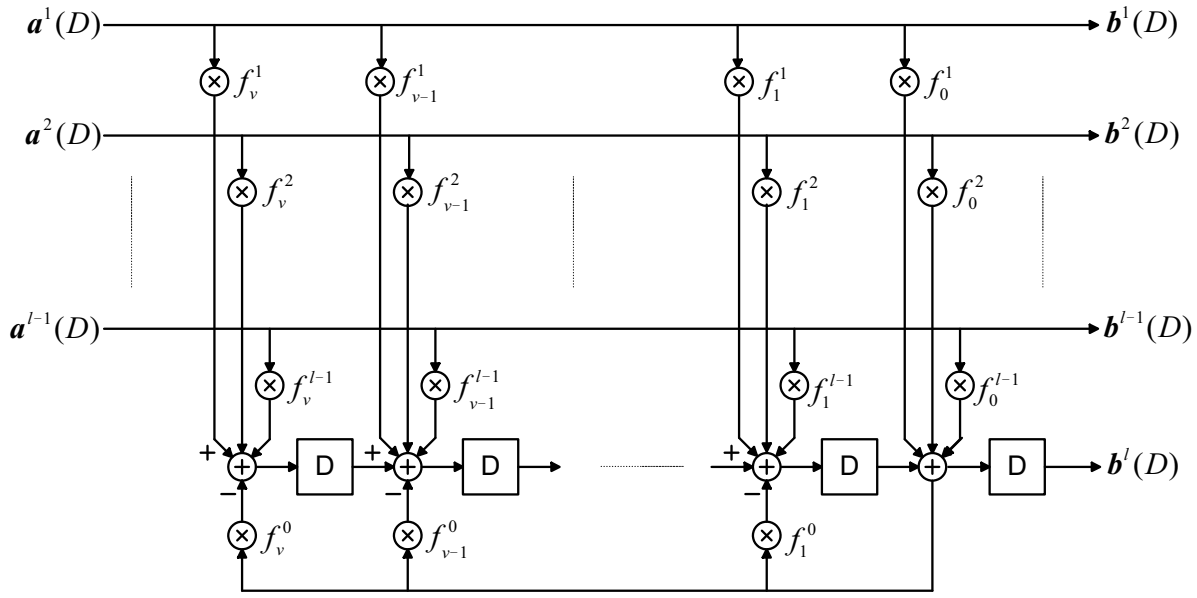

Figure 4.1: Systematic rate-$\frac{l}{l-1}$ feedback ring convolutional encoder.

be causal, realizable and thus able to be represented by adders, multipliers and delay cells, the coefficient f_0^0 must be a unit in $R = \mathbb{Z}_M$. For example, a unit in R, where $R = \mathbb{Z}_4$ is an element of the set $\{1, 3\}$; a unit multiplied by itself results in unity [45]. We limit the code search to those encoders that have $f_0^0 = 1$, which is a unit for all integer M. Note that, for example with $R = \mathbb{Z}_4$, an equivalent encoder with the coefficient $f_0^0 = 3$ is obtained by multiplying the encoder with $f_0^0 = 1$ by $\frac{3}{3} = 1$. For example,

$$\left[1 \quad \frac{3}{1+D}\right] \times \frac{3}{3} = \left[1 \quad \frac{1}{3+3D}\right]. \tag{4.48}$$

The equivalent encoders have the same minimum Euclidean distance properties. An implementation of the encoder described by Equation (4.45) with $f_0^0 = 1$ is pictured in Figure 4.1.

4.3.3 Code Search Method

The code searches were performed over the possible rate-$\frac{1}{2}$ systematic space-time encoders described by Equation (4.45) with $f_0^0 = 1$ for MSK (2-CPFSK), 4-CPFSK and 8-CPFSK with $L_t = 2$, and the corresponding rate-$\frac{2}{3}$ space-time encoders with $L_t = 3$. For each memory order, ν, of the space-time encoder, the best normalized minimum squared Euclidean distance $(d^2_{\min})$ was found for each different number of combined encoder states, S_J. The number of

states of the overall encoders was calculated using the method described in Section 3.5.4. In a given search, the same values of $d^2_{\min}$ and S_J occurred for different values of ν. The systems that required more delay elements, that is, larger ν, to implement the space-time encoder, did not provide greater transmit diversity or a larger product distance. Therefore, these systems provide no advantage over those with space-time codes of lower memory order and are not considered further.

4.3.4 Code Search Results

The following tables present the code search results. The number of delay elements of the space-time encoders is denoted ν, the number states of the combined encoder is denoted S_J, the transmit diversity is denoted $\rho_{\min}$ and the normalized minimum squared Euclidean distance is denoted $d^2_{\min}$. The code search results presented in Tables 4.1-4.3 are the optimal rate-$\frac{1}{2}$ space-time encoders with two transmit antennas and MSK, 4-CPFSK and 8-CPFSK respectively. The results presented in Tables 4.4-4.6 are the optimal rate-$\frac{2}{3}$ space-time encoders with three transmitter antennas and MSK, 4-CPFSK and 8-CPFSK respectively. Due to the large number of codes that maximize the minimum squared Euclidean distance, only one of the optimal codes for each category is presented in Tables 4.3-4.6. Full results for these code searches are presented in Appendix D.

4.3.5 Selection of the Best Codes

The space-time coded systems identified with the maximum, minimum squared Euclidean distance also maximize the minimum trace of the signal distance matrices, over all matrices formed from pairs of distinct transmit signals. If we identify those systems that have the maximum possible transmit diversity from these optimum systems, the resulting space-time coded systems will provide good performance with any number of receive antennas. Further narrowing of the search could involve searching through the full rank systems for those with the largest minimum product distance over all signal distance matrices. However, in practice we have found that there are only small gains in finding such codes. Evaluating the rank and product distance of STC-CPM is discussed in more detail in the next chapter.

Of the optimum rate-$\frac{1}{2}$ space-time codes with M-CPFSK presented in Tables 4.1-4.3, those schemes with $S_J \geq 2^{2\log_2 M}$ are full rank, except for the schemes with $M = 8$ and $S_J = 128$,

ν	S_J	$\rho_{\min}$	$d^2_{\min}$	**Space-Time Codes**
0	2	1	2.000	$[1 \;\; 1]$
1	4	2	3.000	$[1 \;\; 1+D]$, $\left[1 \;\; \frac{1}{1+D}\right]$,$\left[1 \;\; \frac{D}{1+D}\right]$
2	8	2	5.000	$\left[1 \;\; \frac{1+D+D^2}{1+D^2}\right]$, $\left[1 \;\; \frac{1+D^2}{1+D+D^2}\right]$
3	16	2	6.000	$\left[1 \;\; \frac{1+D+D^3}{1+D^2+D^3}\right]$,$\left[1 \;\; \frac{1+D+D^2+D^3}{1+D^2+D^3}\right]$, $\left[1 \;\; \frac{1+D^2+D^3}{1+D+D^3}\right]$,$\left[1 \;\; \frac{1+D^2+D^3}{1+D+D^2+D^3}\right]$, $\left[1 \;\; \frac{1+D+D^2+D^3}{1+D+D^3}\right]$ $\left[1 \;\; \frac{1+D^2+D^3}{1+D+D^2}\right]$, $\left[1 \;\; \frac{1+D+D^3}{1+D+D^2}\right]$,$\left[1 \;\; \frac{1+D+D^3}{1+D+D^2+D^3}\right]$, $\left[1 \;\; \frac{D+D^2+D^3}{1+D^2+D^3}\right]$,$\left[1 \;\; \frac{1+D+D^2+D^3}{1+D+D^3}\right]$, $\left[1 \;\; \frac{1+D+D^2}{1+D^2+D^3}\right]$,$\left[1 \;\; \frac{D+D^2+D^3}{1+D+D^3}\right]$
4	32	2	7.000	$\left[1 \;\; \frac{1+D+D^3+D^4}{1+D^3+D^4}\right]$, $\left[1 \;\; \frac{1+D+D^2+D^4}{1+D^3+D^4}\right]$, $\left[1 \;\; \frac{1+D+D^4}{1+D^2+D^3+D^4}\right]$, $\left[1 \;\; \frac{1+D^2+D^3+D^4}{1+D+D^4}\right]$, $\left[1 \;\; \frac{1+D+D^3+D^4}{1+D+D^4}\right]$, $\left[1 \;\; \frac{1+D^3+D^4}{1+D+D^3+D^4}\right]$, $\left[1 \;\; \frac{1+D+D^4}{1+D+D^3+D^4}\right]$, $\left[1 \;\; \frac{1+D^3+D^4}{1+D+D^2+D^4}\right]$, $\left[1 \;\; \frac{1+D^2+D^3+D^4}{1+D^3+D^4}\right]$, $\left[1 \;\; \frac{1+D^3+D^4}{1+D^2+D^3+D^4}\right]$, $\left[1 \;\; \frac{1+D+D^2+D^4}{1+D+D^4}\right]$, $\left[1 \;\; \frac{1+D+D^4}{1+D+D^2+D^4}\right]$

Table 4.1: Code search results for rate-$\frac{1}{2}$ STC with 2-CPFSK (MSK) and two transmit antennas. The spectral efficiency is 1 bits/s/Hz.

ν	S_J	$\rho_{\min}$	$d^2_{\min}$	**Space-Time Codes**
0	4	1	2.000	$[1 \;\; 2]$
1	8	1	2.878	$[1 \;\; 1+2D]$, $[1 \;\; 3+2D]$,$\left[1 \;\; \frac{1}{1+2D}\right]$, $\left[1 \;\; \frac{3}{1+2D}\right]$
1	16	2	4.000	$\left[1 \;\; \frac{2+D}{1+2D}\right]$,$\left[1 \;\; \frac{2+3D}{1+2D}\right]$
2	32	2	4.666	$\left[1 \;\; \frac{2+D+2D^2}{1+D}\right]$,$\left[1 \;\; \frac{2+D}{1+D+2D^2}\right]$,$\left[1 \;\; \frac{2+3D+2D^2}{1+D}\right]$,$\left[1 \;\; \frac{2+3D}{1+3D+2D^2}\right]$, $\left[1 \;\; \frac{2+3D}{1+D+2D^2}\right]$,$\left[1 \;\; \frac{2+D+2D^2}{1+3D^2}\right]$,$\left[1 \;\; \frac{2+3D+2D^2}{1+3D^2}\right]$,$\left[1 \;\; \frac{2+D}{1+3D+2D^2}\right]$
2	64	2	5.544	$\left[1 \;\; \frac{2+2D+D^2}{1+D^2}\right]$,$\left[1 \;\; \frac{2+2D+3D^2}{1+D^2}\right]$,$\left[1 \;\; \frac{2+2D+D^2}{3+D^2}\right]$,$\left[1 \;\; \frac{2+2D+3D^2}{1+3D^2}\right]$, $\left[1 \;\; \frac{2+2D+D^2}{1+2D+D^2}\right]$,$\left[1 \;\; \frac{2+2D+3D^2}{1+2D+D^2}\right]$,$\left[1 \;\; \frac{1+2D+2D^2}{1+D^2}\right]$,$\left[1 \;\; \frac{3+2D+2D^2}{1+D^2}\right]$, $\left[1 \;\; \frac{1+2D+2D^2}{1+3D^2}\right]$,$\left[1 \;\; \frac{3+2D+2D^2}{1+3D^2}\right]$,$\left[1 \;\; \frac{1+2D+2D^2}{1+2D+D^2}\right]$,$\left[1 \;\; \frac{3+2D+2D^2}{1+2D+D^2}\right]$, $\left[1 \;\; \frac{1+D^2}{1+2D+2D^2}\right]$,$\left[1 \;\; \frac{1+3D^2}{1+2D+2D^2}\right]$,$\left[1 \;\; \frac{1+2D+D^2}{1+2D+2D^2}\right]$,$\left[1 \;\; \frac{3+D^2}{1+2D+2D^2}\right]$, $\left[1 \;\; \frac{3+3D^2}{1+2D+2D^2}\right]$,$\left[1 \;\; \frac{3+2D+3D^2}{1+2D+2D^2}\right]$

Table 4.2: Code search results for rate-$\frac{1}{2}$ STC with 4-CPFSK and two transmit antennas. The spectral efficiency is 2 bits/s/Hz.

ν	S_J	$\rho_{\min}$	$d^2_{\min}$	**Space-Time Codes**
0	8	1	2.180	$[1 \;\; 3]$
1	16	1	2.374	$\left[1 \;\; \frac{2+6D}{1+D}\right]$
1	32	1	3.888	$\left[1 \;\; \frac{5+3D}{1+D}\right]$
1	64	2	4.079	$\left[1 \;\; \frac{4+3D}{1+2D}\right]$
2	64	1	4.317	$\left[1 \;\; \frac{3+2D+2D^2}{1+2D^2}\right]$
2	128	1	5.087	$\left[1 \;\; \frac{3+5D+7D^2}{1+D+3D^2}\right]$
2	256	2	5.286	$\left[1 \;\; \frac{2+D+7D^2}{1+3D+4D^2}\right]$

Table 4.3: Partial code search results for rate-$\frac{1}{2}$ STC with 8-CPFSK and two transmit antennas. The spectral efficiency is 3 bits/s/Hz.

ν	S_J	$\rho_{\min}$	$d^2_{\min}$	**Space-Time Codes**
0	4	1	2.667	$\begin{bmatrix} 1 & 0 & 1 \\ 0 & 1 & 1 \end{bmatrix}$
1	8	1	2.667	$\begin{bmatrix} 1 & 0 & 1 \\ 0 & 1 & D \end{bmatrix}$
2	16	1	4.000	$\begin{bmatrix} 1 & 0 & D+D^2 \\ 0 & 1 & 1+D+D^2 \end{bmatrix}$
2	16	2	4.000	$\begin{bmatrix} 1 & 0 & D+D^2 \\ 0 & 1 & 1+D^2 \end{bmatrix}$
3	32	2	5.333	$\begin{bmatrix} 1 & 0 & D+D^2+D^3 \\ 0 & 1 & 1+D^2+D^3 \end{bmatrix}$
4	64	2	6.667	$\begin{bmatrix} 1 & 0 & \frac{D^2+D^3+D^4}{1+D^4} \\ 0 & 1 & \frac{1+D^3+D^4}{1+D^4} \end{bmatrix}$
5	128*	2	8.000	$\begin{bmatrix} 1 & 0 & \frac{D^2+D^4+D^5}{1+D^4+D^5} \\ 0 & 1 & \frac{1+D^3+D^5}{1+D^4+D^5} \end{bmatrix}$

Table 4.4: Partial code search results for rate-$\frac{2}{3}$ STC with 2-CPFSK (MSK) and three transmit antennas. The spectral efficiency is 2 bits/s/Hz. *The search for codes with $S_J = 128$ is incomplete.

ν	S_J	$\rho_{\min}$	$d^2_{\min}$	Space-Time Codes
0	16	1	1.938	$\begin{bmatrix} 1 & 0 & 1 \\ 0 & 1 & 1 \end{bmatrix}$
1	32	1	2.667	$\begin{bmatrix} 1 & 0 & 2D \\ 0 & 1 & 1+2D \end{bmatrix}$
1	64	1	3.756	$\begin{bmatrix} 1 & 0 & \frac{1+2D}{1+D} \\ 0 & 1 & \frac{1+3D}{1+D} \end{bmatrix}$
2	128	1	4.322	$\begin{bmatrix} 1 & 0 & \frac{1+D+2D^2}{1+D^2} \\ 0 & 1 & \frac{1+2D+D^2}{1+D^2} \end{bmatrix}$
2	256	†	5.330	$\begin{bmatrix} 1 & 0 & \frac{1+3D+2D^2}{1+D+3D^2} \\ 0 & 1 & \frac{1+3D+3D^2}{1+D+3D^2} \end{bmatrix}$

Table 4.5: Partial code search results for rate-$\frac{2}{3}$ STC with 4-CPFSK and three transmit antennas. The spectral efficiency is 4 bits/s/Hz. †$\rho_{\min}$ was not calculated for the 256 state system.

ν	S_J	$\rho_{\min}$	$d^2_{\min}$	Space-Time Codes
0	64	1	1.454	$\begin{bmatrix} 1 & 0 & 2 \\ 0 & 1 & 4 \end{bmatrix}$
1	128	1	2.181	$\begin{bmatrix} 1 & 0 & \frac{2+6D}{1+D} \\ 0 & 1 & \frac{3+3D}{1+D} \end{bmatrix}$
1	256*	†	2.907	$\begin{bmatrix} 1 & 0 & 2+4D \\ 0 & 1 & 4+2D \end{bmatrix}$

Table 4.6: Partial code search results for rate-$\frac{2}{3}$ STC with 8-CPFSK and three transmit antennas. The spectral efficiency is 6 bits/s/Hz. *The search for codes with $S_J = 256$ is incomplete. †$\rho_{\min}$ was not calculated for the 256 state system.

and $M = 8$, $S_J = 64$ and $\nu = 2$, which have transmit diversity equal to 1. Any code chosen from these full rank codes will give good performance with any number of receive antennas. There is a variation in the minimum product distances between the optimum codes in each category. However, as illustrated by the simulation examples in the following section, the difference in performance is negligible between those with optimal and suboptimal minimum product distance.

The systems with the rate-$\frac{2}{3}$ space-time codes will not achieve full transmit diversity with 3 transmit antennas. The diversity/rate restriction, described by Equation (2.91) as

$$d \leq 1 + \left\lfloor L_t - \frac{R_S}{\log_2(M)} \right\rfloor, \tag{4.49}$$

means that they can have transmit diversity equal to 2 at best, as $R_S = 2\log_2(M)$. However, as we illustrate in the following section, good performance is still exhibited by these systems. We have identified some $\rho_{\min} = 2$ systems with rate-$\frac{2}{3}$ space-time codes. Over $\frac{4}{5}$ of the rate-$\frac{2}{3}$ space-time codes with MSK and $S_J = 16$ and all of the rate-$\frac{2}{3}$ space-time codes with MSK and $S_J > 32$ have $\rho_{\min} = 2$. The Euclidean distance design criterion is valid for these $\rho_{\min} = 2$ codes provided $L_r > 1$, as is the case for the full rank, two transmit antenna codes.

We have observed that for the space-time trellis coded M-CPFSK schemes we have developed, the minimum number of states of the combined encoder required to achieve transmit diversity equal to $\rho_{\min}$ is $S_J = 2^{R_s \rho_{\min}}$, where R_s is the system throughput. We may deduce from this the expected transmit diversity of the schemes for which the direct calculation of the minimum rank is too computationally intensive. For example, a 3 transmit antenna scheme with a rate-$\frac{2}{3}$ space-time code and 8-CPFSK has $R_s = 6$ and for it to have $\rho_{\min} = 2$ we require $S_J \geq 2^{6 \cdot 2} = 4096$. Thus, we do not expect $\rho_{\min} = 2$ for the 256 state code in Table 4.6. A 3 transmit antenna scheme with a rate-$\frac{2}{3}$ space-time code and 4-CPFSK requires $S_J \geq 2^{4 \cdot 2} = 256$ states for $\rho_{\min} = 2$. Thus, it is possible that the 256 state code of Table 4.5 has $\rho_{\min} = 2$.

4.3.6 Simulated Performance

In this section, simulations of the error rate performance of selected optimized space-time codes are presented. The data frame length is 130 M-ary symbols. The simulation procedure is described in Appendix A. In the following discussion the number of states in the combined

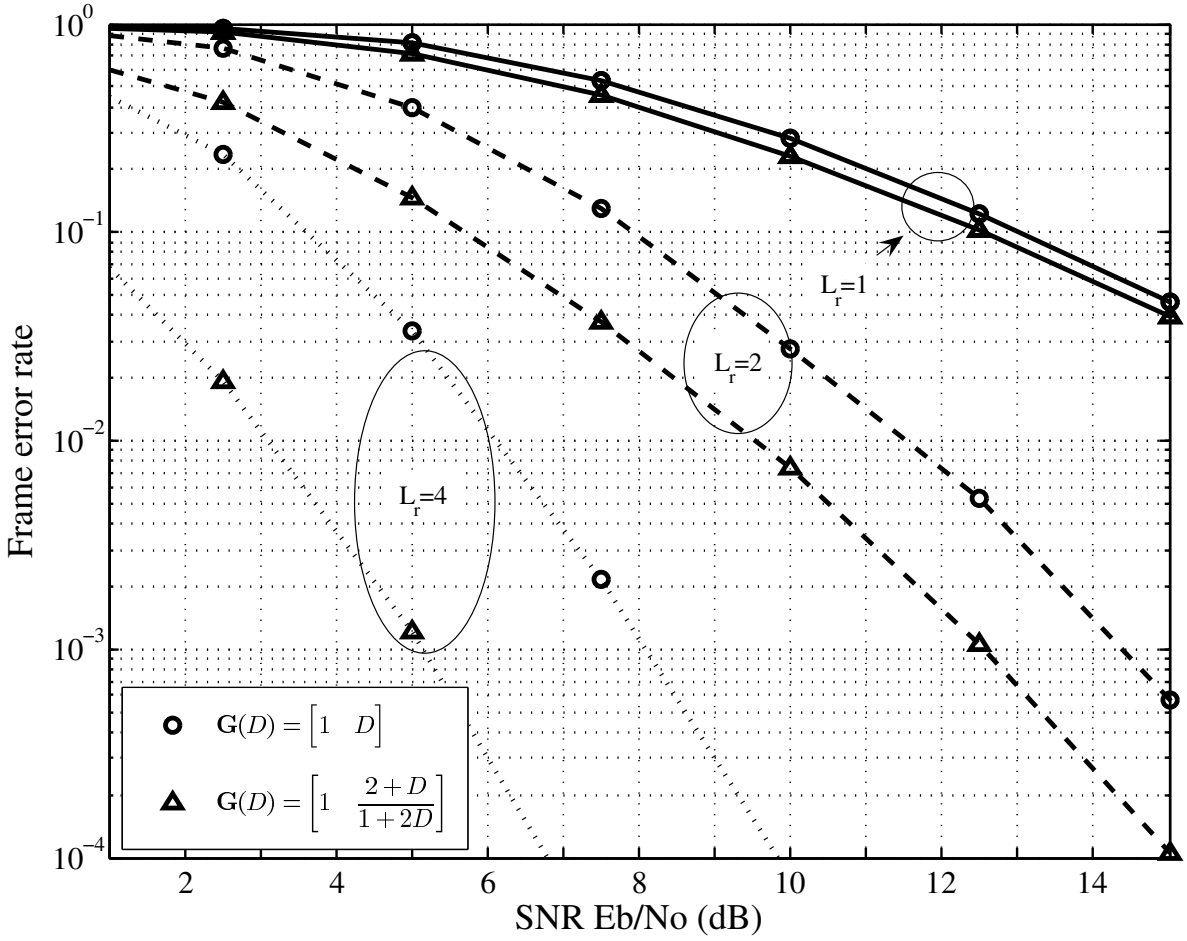

Figure 4.2: Frame error rate performance of $\boldsymbol{G}(D) = [1 \quad D]$ and $\boldsymbol{G}(D) = \left[1 \quad \frac{2+D}{1+2D}\right]$ with 4-CPFSK and $L_t = 2$.

encoder is referred to as S_J and the space-time encoder is referred to as $\boldsymbol{G}(D)$. The normalized minimum squared Euclidean distance is denoted $d^2_{\min}$, the minimum product distance is denoted $\Lambda^P_{\min}$ and the transmit diversity is denoted $\rho_{\min}$.

Rate-$\frac{1}{2}$ Space-Time Codes with 4-CPFSK

Figure 4.2 shows the frame error rate performance of one of the optimal rate-$\frac{1}{2}$ space-time codes for 4-CPFSK with $S_J = 16$ and two transmit antennas. The space-time code is $\boldsymbol{G}(D) = \left[1 \quad \frac{2+D}{1+2D}\right]$ and the normalized minimum squared Euclidean distance of the system is 4.000. The performance is shown for systems with 1, 2 and 4 receive antennas (L_r). As a comparison we have shown the performance of delay diversity with 4-CPFSK, which also has $S_J = 16$, but $d^2_{\min} = 1.454$. The generator matrix for delay diversity with two transmit antennas is $\boldsymbol{G}(D) = [1 \quad D]$. Both space-time codes form full rank systems with 4-CPFSK and $L_t = 2$.

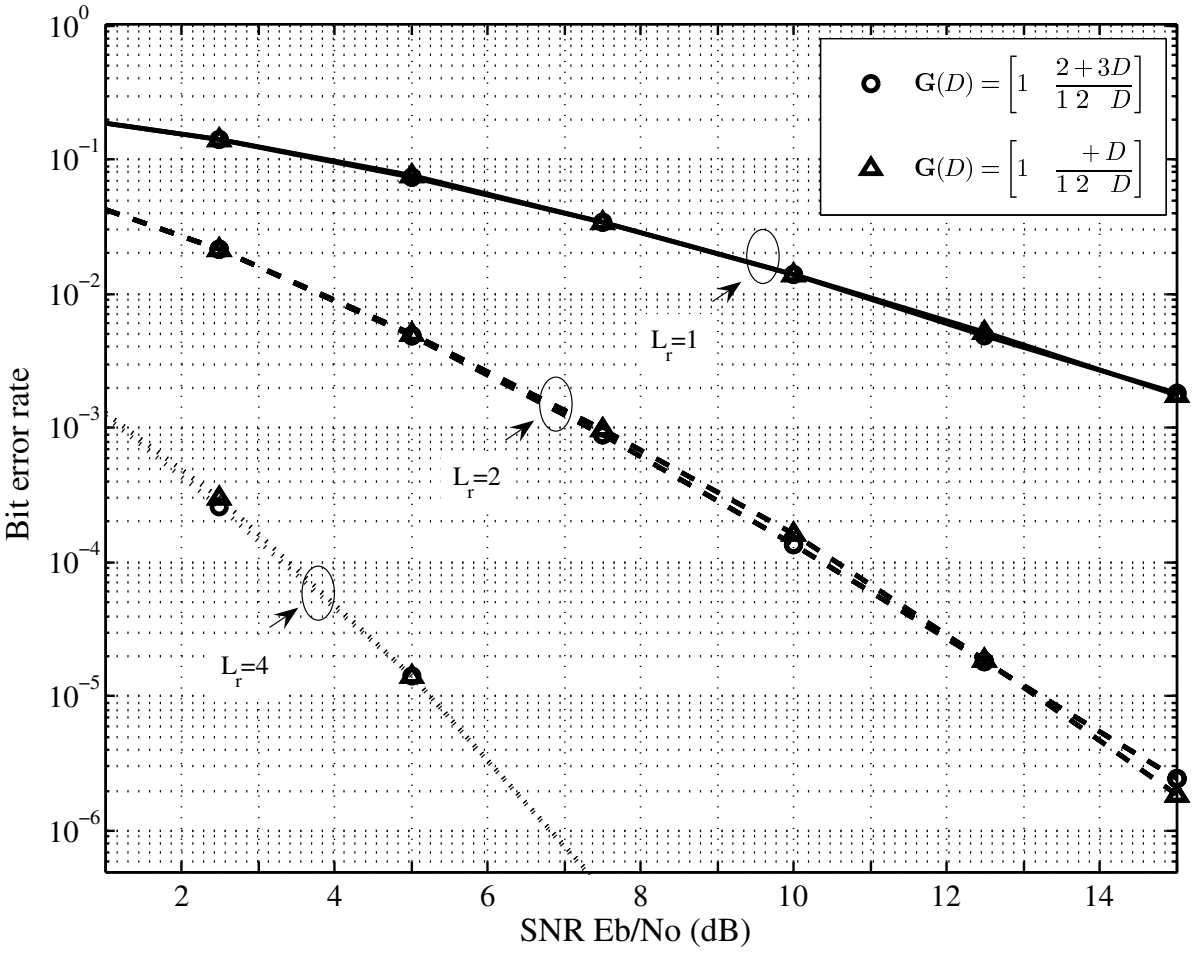

Figure 4.3: Bit error rate performance of $\boldsymbol{G}(D) = \begin{bmatrix} 1 & \frac{2+3D}{1+2D} \end{bmatrix}$ and $\boldsymbol{G}(D) = \begin{bmatrix} 1 & \frac{2+D}{1+2D} \end{bmatrix}$ with 4-CPFSK and $L_t = 2$.

We note that the optimized scheme has comparable performance to the optimal QPSK space-time trellis code with 16 states presented in [3], where both systems have spectral efficiency of 2 bits/s/Hz.

Delay diversity has inferior frame error rate performance to the STC $\boldsymbol{G}(D) = \begin{bmatrix} 1 & \frac{2+D}{1+2D} \end{bmatrix}$ with 4-CPFSK and $L_t = 2$ for any number of receive antennas. The difference in performance becomes more pronounced as the number of receive antennas is increased. At a frame error rate (FER) of 10^{-3} the performance of the space-time coded system with $\boldsymbol{G}(D) = \begin{bmatrix} 1 & \frac{2+D}{1+2D} \end{bmatrix}$ is approximately 3 dB better than the delay diversity system with $L_r = 4$, is approximately 2 dB better with $L_r = 2$ and approximately 0.5 dB better with $L_r = 1$ (not visible in Figure 4.2). This illustrates that achieving full diversity should not be the only design criterion, especially when receive diversity is employed.

The two optimum rate-$\frac{1}{2}$ STC for 4-CPFSK with $S_J = 16$ and 2 transmit antennas, which

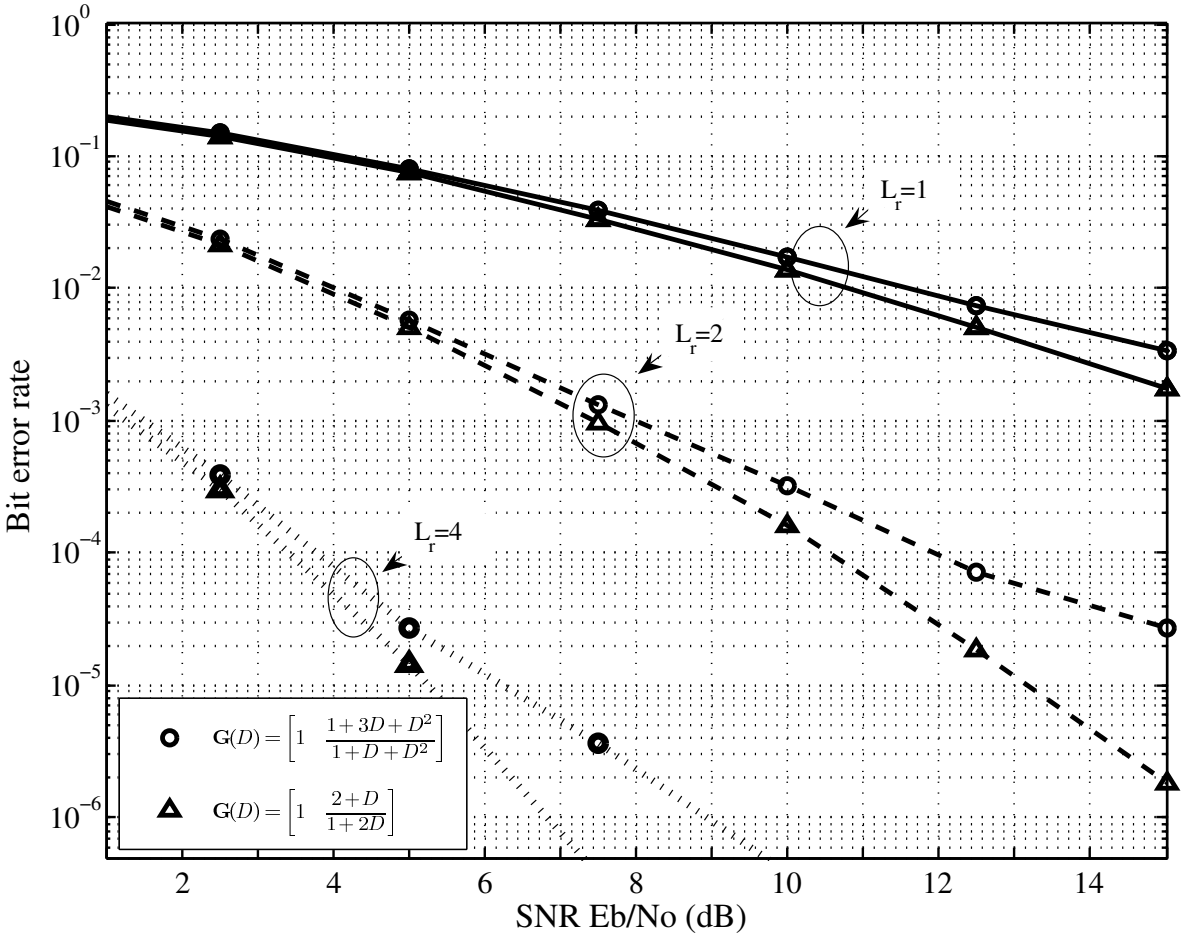

Figure 4.4: Bit error rate performance of $\boldsymbol{G}(D) = \begin{bmatrix} 1 & \frac{1+3D+D^2}{1+D+D^2} \end{bmatrix}$ and $\boldsymbol{G}(D) = \begin{bmatrix} 1 & \frac{2+D}{1+2D} \end{bmatrix}$ with 4-CPFSK and $L_t = 2$.

are shown in Table 4.2, form systems with different minimum product distance. The system with the space-time code, $\boldsymbol{G}(D) = \begin{bmatrix} 1 & \frac{2+D}{1+2D} \end{bmatrix}$, has $\Lambda^P_{\min} = 6.976$ and the system with the space-time code, $\boldsymbol{G}(D) = \begin{bmatrix} 1 & \frac{2+3D}{1+2D} \end{bmatrix}$, has $\Lambda^P_{\min} = 7.694$. We present the bit error rate performance of these two space-time codes with 4-CPFSK and $L_t = 2$ in Figure 4.3. The performance of the two schemes is shown with 1, 2 and 4 receive antennas and is almost identical in all cases. This supports the premise that the minimum product distance does not have much impact on the performance if the minimum rank and the minimum squared Euclidean distance are maximized.

The space-time code, $\boldsymbol{G}(D) = \begin{bmatrix} 1 & \frac{1+3D+D^2}{1+D+D^2} \end{bmatrix}$, has two delay elements and when combined with 4-CPFSK in a two transmit antenna scheme it results in a system with a 16 state combined trellis. The minimum Euclidean distance of this system is 4.000 and the transmit diversity is 1. We compare the performance of this space-time coded system, to the performance

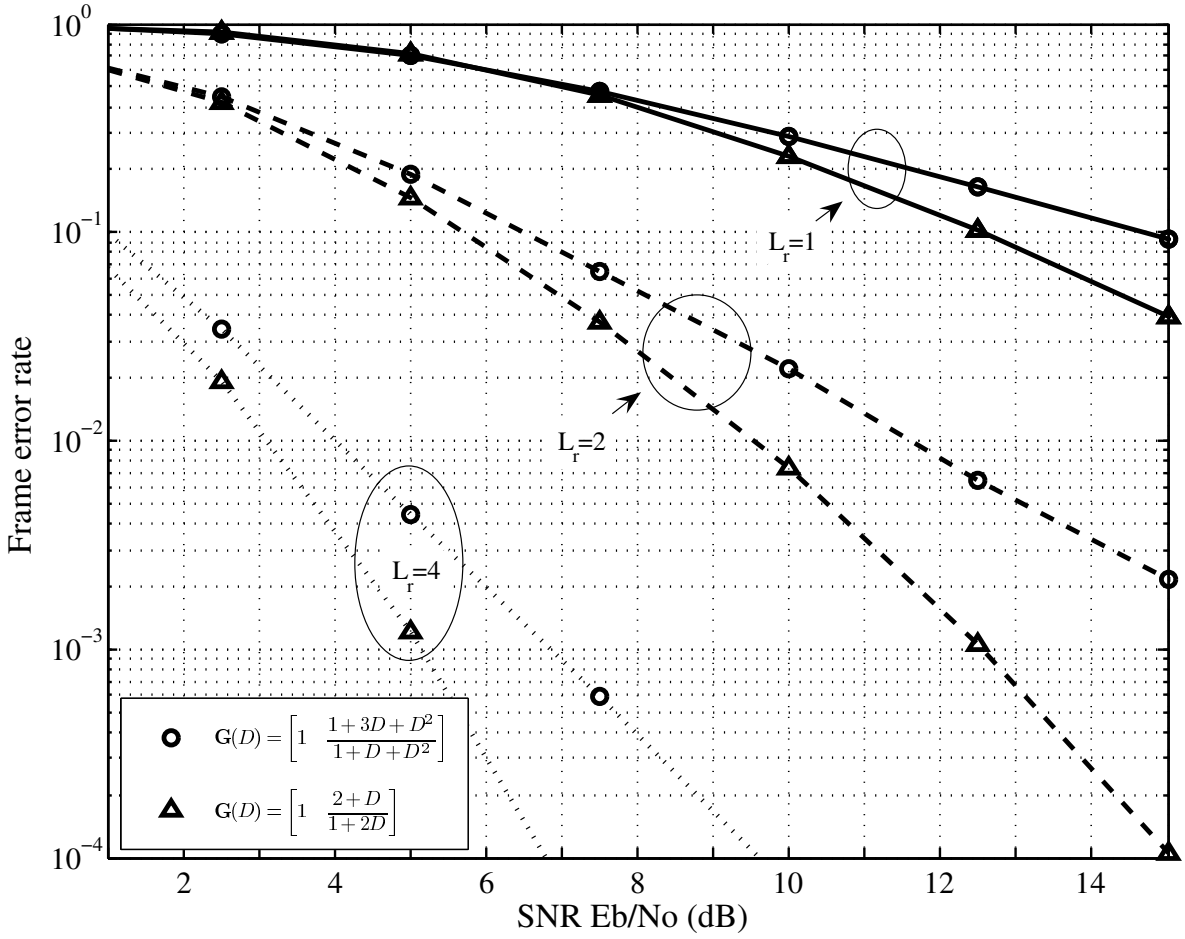

Figure 4.5: Frame error rate performance of $\boldsymbol{G}(D) = \begin{bmatrix} 1 & \frac{1+3D+D^2}{1+D+D^2} \end{bmatrix}$ and $\boldsymbol{G}(D) = \begin{bmatrix} 1 & \frac{2+D}{1+2D} \end{bmatrix}$ with 4-CPFSK and $L_t = 2$.

of the space-time coded system with $\boldsymbol{G}(D) = \begin{bmatrix} 1 & \frac{2+D}{1+2D} \end{bmatrix}$, 4-CPFSK and $L_t = 2$, which has the same number of states in the combined trellis and the same minimum squared Euclidean distance, but is full rank (and requires only one delay element to implement the space-time encoder). The bit error rate curves of these two systems with 1, 2, and 4 receive antennas are shown in Figure 4.4. The corresponding frame error rate curves are shown in Figure 4.5.

The $\rho_{\min} = 1$ system with the space-time code $\boldsymbol{G}(D) = \begin{bmatrix} 1 & \frac{1+3D+D^2}{1+D+D^2} \end{bmatrix}$, has worse performance than the $\rho_{\min} = 2$ system with the space-time code $\boldsymbol{G}(D) = \begin{bmatrix} 1 & \frac{2+D}{1+2D} \end{bmatrix}$, for any number of receive antennas. The different slopes of the curves confirm that they have different transmit diversity. We note that the bit error rate curves of the $\rho_{\min} = 1$ system are similar to the bit error rate curves of the $\rho_{\min} = 2$ system below a certain SNR for each receiver configuration. This supports the pairwise error probability (PEP) bound approximations of Equations (4.29) and (4.30), for high and low SNR respectively. At high SNR, the PEP bound

is dominated by the rank of the signal distance matrix. These two systems have different transmit diversity, which is determined by the minimum rank of the signal distance matrices, and hence their performance at high SNR diverges. At low SNR, the PEP bound is dominated by the trace of the signal distance matrix. These two systems have the same minimum Euclidean distance, and hence the same minimum trace over all signal distance matrices, and their performance is similar at lower SNR.

The frame error rate performance of the two space-time codes diverges at lower SNR than the bit error rate performance. This results in the difference in frame error rate performance between the two systems being more pronounced, than the difference in the bit error rate performance. From these performance curves, we observe that even if a 2 transmit antenna system has the optimum minimum squared Euclidean distance, it is still important to maximize the minimum rank.

Rate-$\frac{1}{2}$ Space-Time Codes with 8-CPFSK

Increasing the modulation alphabet size, M, to 8 provides an information rate of 3 bits/symbol period, with a rate-$\frac{1}{2}$ space-time code and 2 transmit antennas. Figure 4.6 displays the frame error rate performance of the system with the space-time code $\boldsymbol{G}(D) = \begin{bmatrix} 1 & \frac{2+5D}{1+4D} \end{bmatrix}$, 8-CPFSK and $L_t = 2$. This is an optimum space-time coded system with an overall encoder that has a 64 state trellis (see Table D.1). The performance of the system with the space-time code $\boldsymbol{G}(D) = [1 \quad 1]$, 8-CPFSK and $L_t = 2$ is also displayed. The scheme has $\rho_{\min} = 1$ and has a minimum squared Euclidean distance $d^2_{\min} = 0.598$, which is significantly less than the optimized code $d^2_{\min} = 4.079$. It also has a 64 state overall encoder. The latter system has a trivial space-time code that provides no coding across the transmit antennas; the same signal is transmitted simultaneously from both antennas. These frame error rate performance curves illustrate the diversity and coding gains realizable using coding across the transmit antennas. We note that the overall encoders require the same number of states.

Figure 4.7 shows the comparative frame error rate performance of the space-time codes, $\boldsymbol{G}(D) = \begin{bmatrix} 1 & \frac{2+5D}{1+4D} \end{bmatrix}$ and delay diversity, with two transmit antennas and 8-CPFSK. Both systems have overall encoders with 64 state trellises and both systems have full spatial diversity. The system with $\boldsymbol{G}(D) = \begin{bmatrix} 1 & \frac{2+5D}{1+4D} \end{bmatrix}$ has $d^2_{\min} = 4.079$ and the delay diversity system has $d^2_{\min} = 0.598$. A coding gain of more than 6 dB is realized using the space-time code

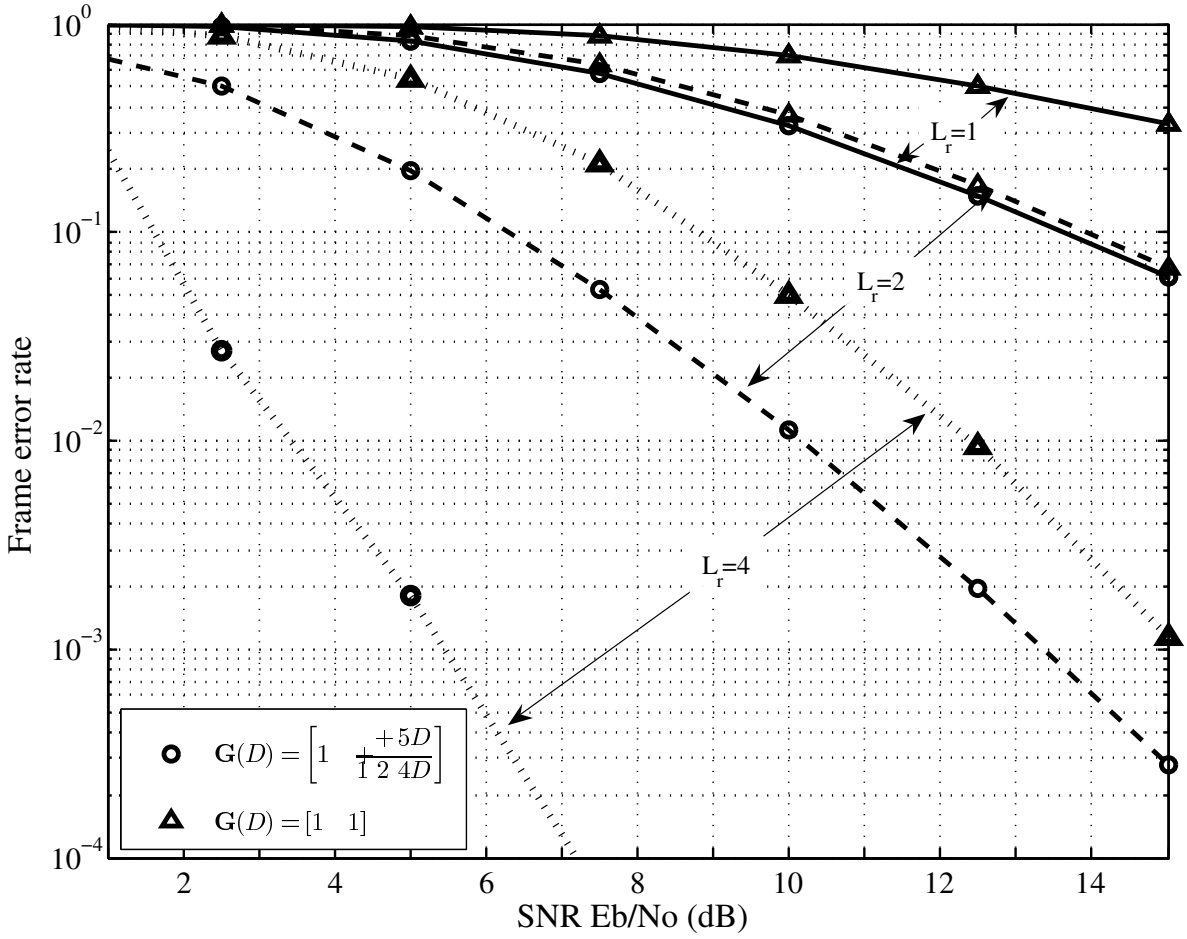

Figure 4.6: Frame error rate performance of $\boldsymbol{G}(D) = \begin{bmatrix} 1 & \frac{2+5D}{1+4D} \end{bmatrix}$ and $\boldsymbol{G}(D) = [1 \quad 1]$ with 8-CPFSK and $L_t = 2$.

$\boldsymbol{G}(D) = \begin{bmatrix} 1 & \frac{2+5D}{1+4D} \end{bmatrix}$ instead of delay diversity with four receive antennas at a frame error rate of 10^{-1}. At a frame error rate of 10^{-1}, the coding gain is more than 5.5 dB when two receive antennas are used, and with 1 receive antenna, the coding gain is more than 3 dB. The large performance gain is achieved at no extra cost in terms of encoder complexity.

Rate-$\frac{2}{3}$ Space-Time Codes

Increasing the space-time code rate to $\frac{2}{3}$ and using a three transmit antenna system yields an information rate of $2\log_2(M)$ bits/symbol period when used with M-CPFSK. For example, consider the space-time code $\boldsymbol{G}(D) = \begin{bmatrix} 1 & 0 & 2D \\ 0 & 1 & 1+2D \end{bmatrix}$ of Table 4.5 with 4-CPFSK and three transmit antennas. The system throughput is 4 bits/symbol period and the overall encoder has 32 states, with $M = 4$ branches emanating from each state. If we aim to achieve an

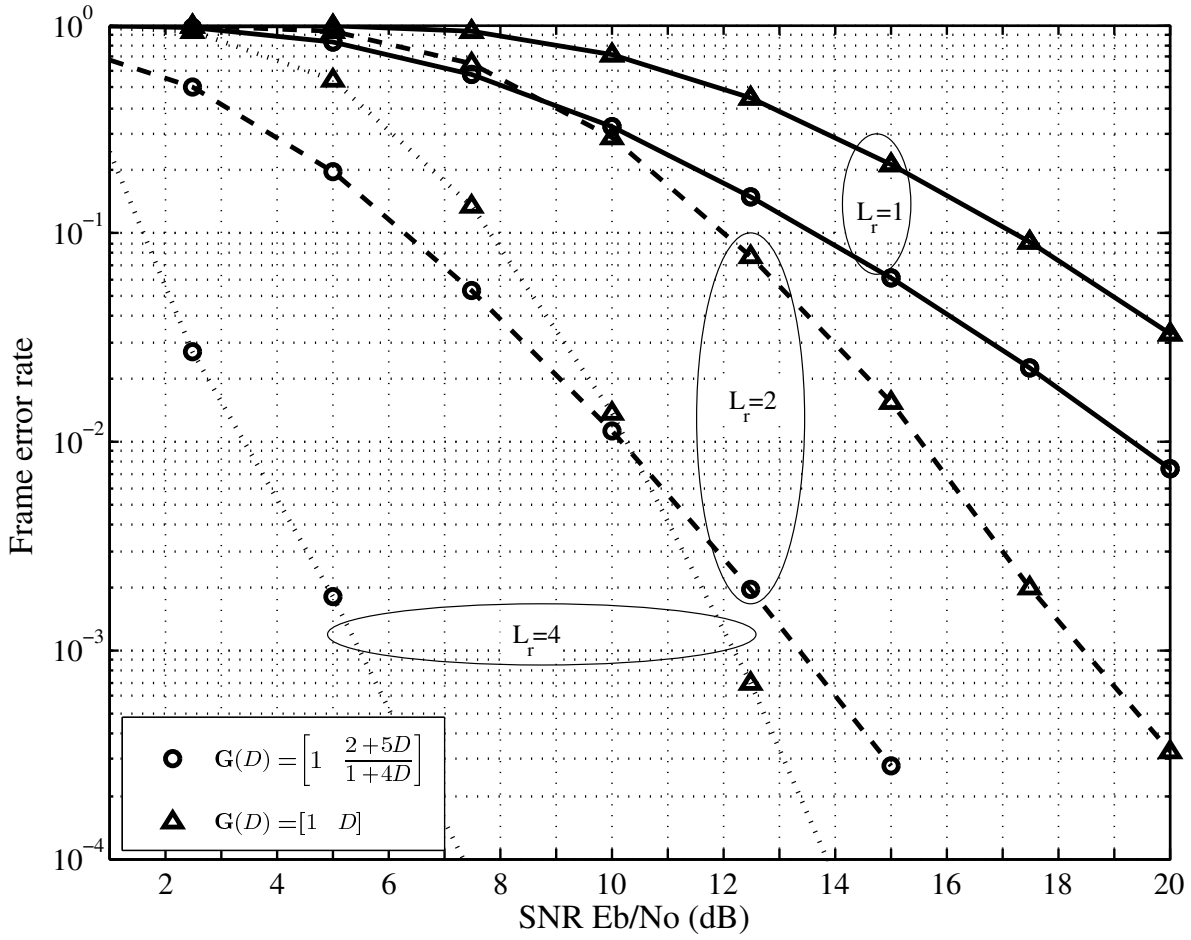

Figure 4.7: Frame error rate performance of $\boldsymbol{G}(D) = \begin{bmatrix} 1 & \frac{2+5D}{1+4D} \end{bmatrix}$ and $\boldsymbol{G}(D) = \begin{bmatrix} 1 & D \end{bmatrix}$ with 8-CPFSK and $L_t = 2$.

information rate of 4 bits/symbol period using a rate-$\frac{1}{2}$ STC with two transmit antennas, we would require $M = 16$. For example, the full rank delay diversity STC with $M = 16$ requires 256 states in the trellis of the overall encoder and 16 branches from each state in the trellis.

Figure 4.8 shows the bit error rate performance of the system with a throughput of 4 bits/symbol period and the space-time code $\boldsymbol{G}(D) = \begin{bmatrix} 1 & 0 & 2D \\ 0 & 1 & 1+2D \end{bmatrix}$. The bit error rate performance of delay diversity employing 2 transmit antennas with 16-CPFSK is shown as a reference. Despite having a trellis with 16 times fewer states and a transmit diversity of 1, the system with the rate-$\frac{2}{3}$ space-time code, $\boldsymbol{G}(D) = \begin{bmatrix} 1 & 0 & 2D \\ 0 & 1 & 1+2D \end{bmatrix}$, has superior bit error rate performance at the cost of another transmit antenna. The slopes of the $\rho_{\min} = 2$ system's bit error rate performance curves are steeper than the $\rho_{\min} = 1$ system's performance curves, at low bit error rates. At very low bit error rates the performance of the $\rho_{\min} = 2$ system

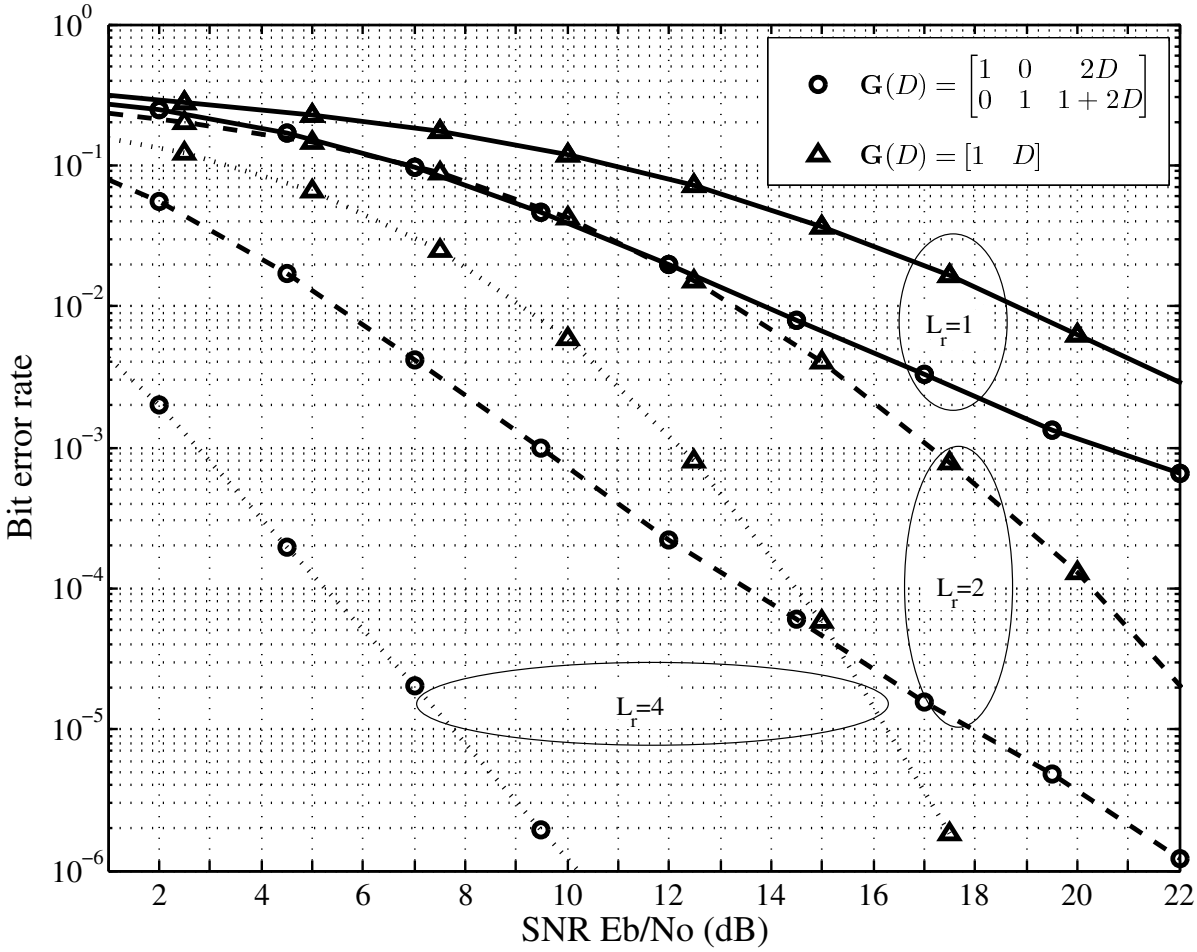

Figure 4.8: Bit error rate performance of a rate-$\frac{2}{3}$ space-time code, with 4-CPFSK, $L_t = 3$ and $S_J = 32$, and of delay diversity, with 16-CPFSK, $L_t = 2$ and $S_J = 256$. Both systems have a throughput of 4 bits/symbol period.

will be superior. However, in the range considered the optimal $\rho_{\min} = 1$ system has the best performance.

The frame error rate performance of $\boldsymbol{G}(D) = \begin{bmatrix} 1 & 0 & 2D \\ 0 & 1 & 1+2D \end{bmatrix}$ with 4-CPFSK and 3 transmit antennas and of 16-CPFSK delay diversity with 2 transmit antennas is shown in Figure 4.9. The curves exhibit similar properties to the corresponding bit error rate curves shown in Figure 4.8. At a FER of 10^{-1} the scheme with $L_t = 3$ and 1 receive antenna is 4 dB better than the corresponding delay diversity scheme, with 2 receive antennas it is 8 dB better and with 4 receive antennas it is approximately 10 dB better. The difference between the performance of the two space-time codes reduces at lower frame error rates because the slopes of the delay diversity FER curves are steeper. However, at a FER of 10^{-3} the scheme

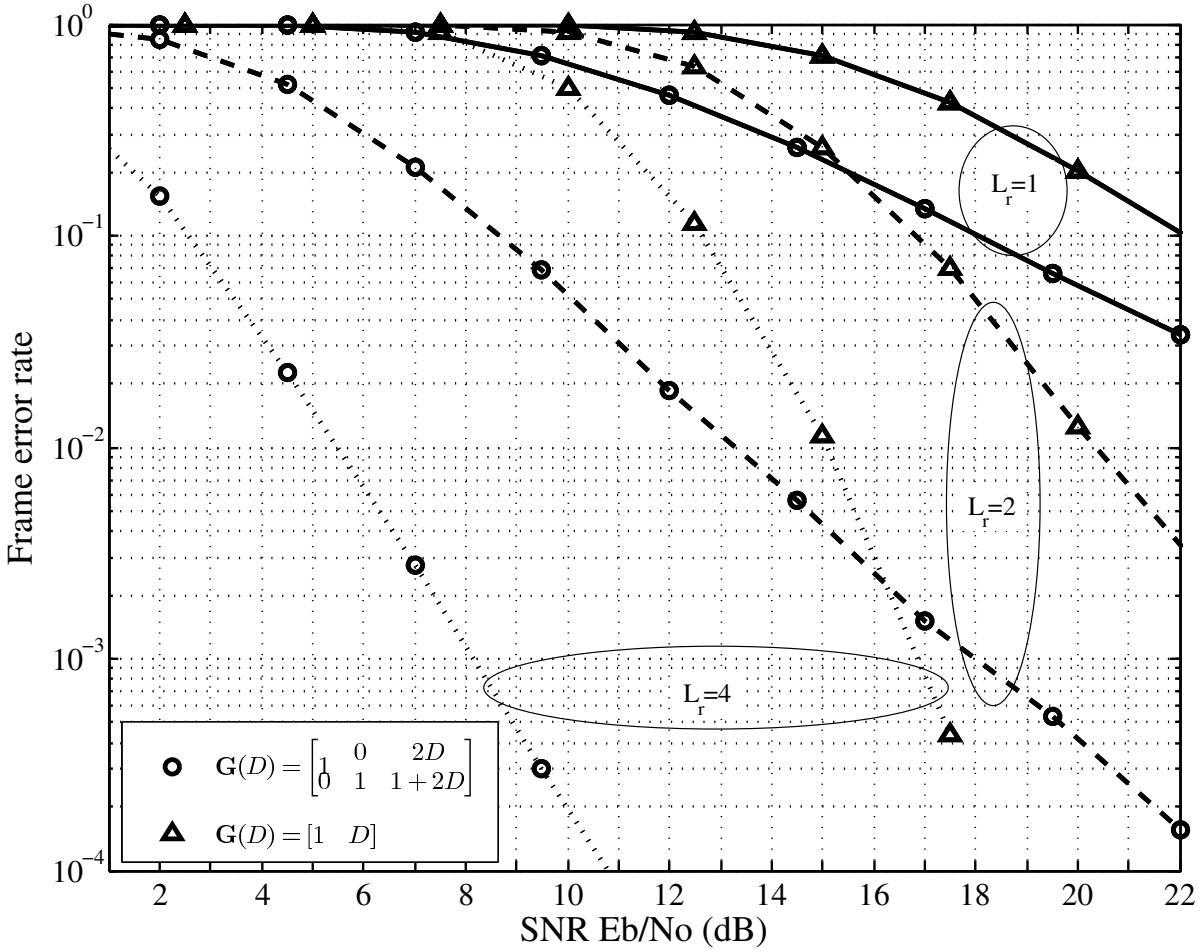

Figure 4.9: Frame error rate performance of a rate-$\frac{2}{3}$ space-time code, with 4-CPFSK, $L_t = 3$ and $S_J = 32$, and of delay diversity, with 16-CPFSK, $L_t = 2$ and $S_J = 256$. Both systems have a throughput of 4 bits/symbol period.

with $\boldsymbol{G}(D) = \begin{bmatrix} 1 & 0 & 2D \\ 0 & 1 & 1+2D \end{bmatrix}$ and 4 receive antennas is still approximately 9 dB better than the delay diversity scheme with 4 receive antennas.

We now consider the bit error rate performance of a space-time coded system with the STC $\boldsymbol{G}(D) = \begin{bmatrix} 1 & 0 & \frac{1+D+2D^2}{1+D^2} \\ 0 & 1 & \frac{1+2D+D^2}{1+D^2} \end{bmatrix}$ of Table 4.5 and 3 transmit antennas. This rate-$\frac{2}{3}$ STC with 4-CPFSK has a combined trellis with 128 states. The system throughput is 4 bits/symbol period when used with 3 transmit antennas and the scheme has $\rho_{\min} = 1$. However, as shown in Figure 4.10 the slopes of the bit error rate curves for $\boldsymbol{G}(D) = \begin{bmatrix} 1 & 0 & \frac{1+D+2D^2}{1+D^2} \\ 0 & 1 & \frac{1+2D+D^2}{1+D^2} \end{bmatrix}$ with $L_t = 3$ and 4-CPFSK are similar to or steeper than the slopes of the corresponding bit error rate curves of the $\rho_{\min} = 2$ delay diversity system with 16-CPFSK and $L_t = 2$, at bit error

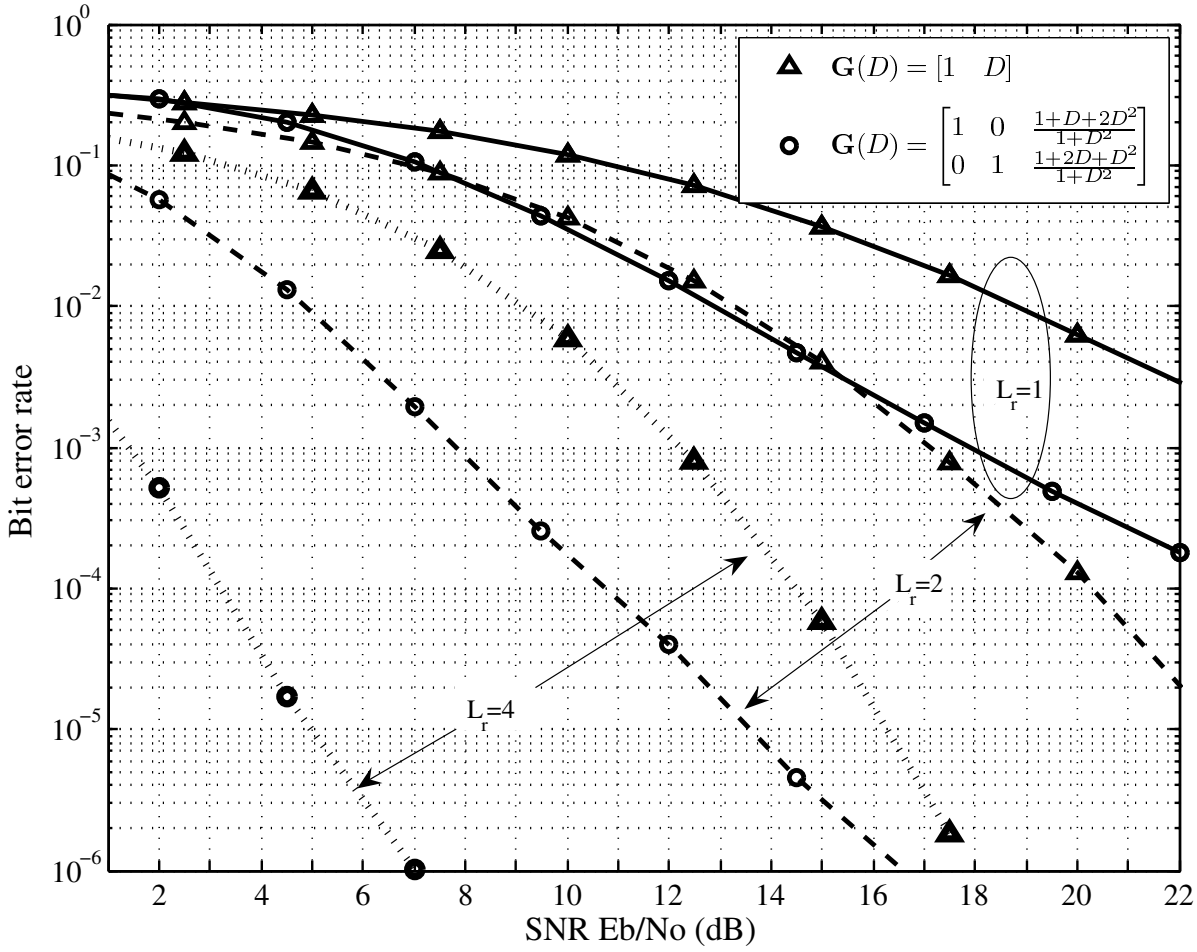

Figure 4.10: Bit error rate performance of a rate-$\frac{2}{3}$ space-time code, with 4-CPFSK, $L_t = 3$ and $S_J = 128$, and of delay diversity, with 16-CPFSK, $L_t = 2$ and $S_J = 256$. Both systems have a throughput of 4 bits/symbol period.

rates greater than 10^{-4}. The gradients of the $\rho_{\min} = 1$ system's BER curves reduce at lower bit error rates as the curves exhibit their $\rho_{\min} = 1$ asymptotic property at high SNR. Thus, the system's transmit diversity is not influencing the performance at BER $> 10^{-4}$. It is the minimum squared Euclidean distance of the system that is important. The performance of the system with $\boldsymbol{G}(D) = \begin{bmatrix} 1 & 0 & \frac{1+D+2D^2}{1+D^2} \\ 0 & 1 & \frac{1+2D+D^2}{1+D^2} \end{bmatrix}$ is more than 5 dB better than the system with $\boldsymbol{G}(D) = \begin{bmatrix} 1 & 0 & 2D \\ 0 & 1 & 1+2D \end{bmatrix}$ (shown in Figure 4.8) at a bit error rate of 10^{-6} with 2 receive antennas, and is greater than 3 dB better with 4 receive antennas, where both systems employ 3 transmit antennas and 4-CPFSK.

The frame error rate performance of $\boldsymbol{G}(D) = \begin{bmatrix} 1 & 0 & \frac{1+D+2D^2}{1+D^2} \\ 0 & 1 & \frac{1+2D+D^2}{1+D^2} \end{bmatrix}$ with 4-CPFSK and

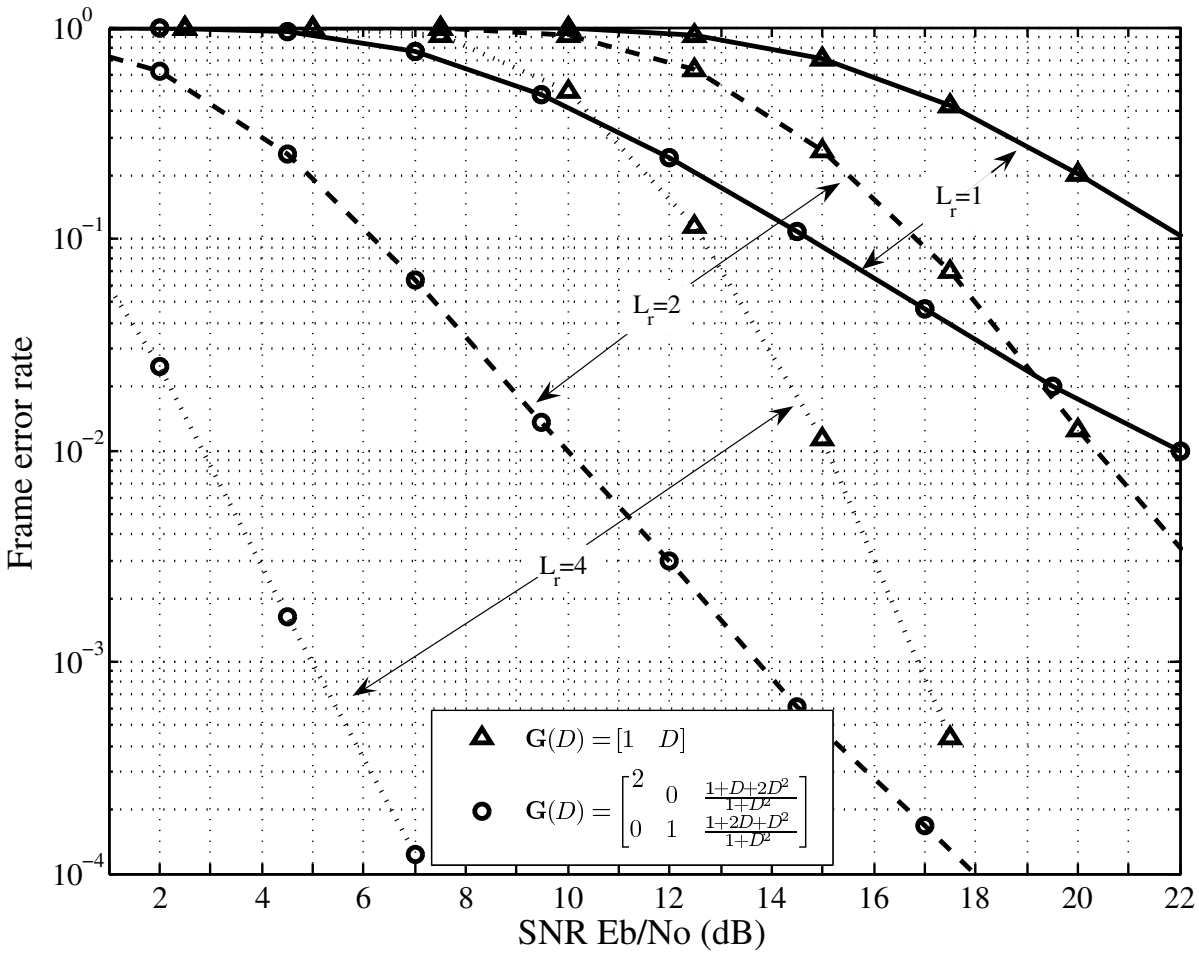

Figure 4.11: Frame error rate performance of a rate-$\frac{2}{3}$ space-time code, with 4-CPFSK, $L_t = 3$ and $S_J = 128$, and of delay diversity, with 16-CPFSK, $L_t = 2$ and $S_J = 256$. Both systems have a throughput of 4 bits/symbol period.

3 transmit antennas and of 16-CPFSK delay diversity with 2 transmit antennas is shown in Figure 4.11. Again, the curves exhibit similar properties to the corresponding bit error rate curves (Figure 4.10). By increasing the number of states of the combined encoder from 32 to 128 using the STC $\boldsymbol{G}(D) = \begin{bmatrix} 1 & 0 & \frac{1+D+2D^2}{1+D^2} \\ 0 & 1 & \frac{1+2D+D^2}{1+D^2} \end{bmatrix}$ instead of $\boldsymbol{G}(D) = \begin{bmatrix} 1 & 0 & 2D \\ 0 & 1 & 1+2D \end{bmatrix}$, gains of approximately 5 dB and 4 dB are achieved at a FER $= 10^{-4}$ for the 2 and 4 receive antenna schemes, respectively and with 1 receive antenna approximately 3 dB gain is achieved at FER $= 10^{-1}$.

4.4 Summary

The PEP of STC-CPM is shown to have an upper bound analogous to the PEP bound derived for linearly modulated STC. Therefore, the design criteria for STC with linear modulation can be applied to STC-CPM, if the signal distance matrix is considered instead of the codeword distance matrix. Due to the integrated STC-CPM design developed in Chapter 3, the minimum squared Euclidean distance is readily calculated using the overall encoder's trellis. This makes it possible to systematically search for optimal non-trivial space-time codes for STC-CPM systems. This was demonstrated by a search for optimal space-time coded CPFSK schemes. A closed form expression to evaluate the Euclidean distance for CPFSK was presented.

Code search results for rate-$\frac{1}{2}$ space-time codes and rate-$\frac{2}{3}$ space-time codes were presented. The codes were found using the minimum squared Euclidean distance as the design criterion. It was shown to be a valid criterion, due to its relationship to the trace of the signal distance matrices. In order to identify codes that have good performance with any number of receive antennas, the optimized codes were searched to find those with the best transmit diversity. It was illustrated via simulations that choosing the system with the best minimum rank over the signal distance matrices (which is the equal to the transmit diversity) amongst a given set of systems with the same Euclidean distance properties, is important. However, having the largest transmit diversity is not always the most important consideration. For example, a $\rho_{\min} = 1$ system with a rate-$\frac{2}{3}$ space-time code and 3 transmit antennas exhibiting excellent performance was presented. The system provides a throughput of 4 bits per symbol period using 4-CPFSK. The best possible transmit diversity for a throughput of 4 bits per symbol period with 3 transmit antennas and 4-CPFSK is 2. This system displayed properties that make it indistinguishable from a $\rho_{\min} = 2$ space-time coded system at BER $> 10^{-4}$.

We have shown that the optimized space-time coded CPM systems that have the same complexity as delay diversity space-time coded CPM schemes provide good coding gains. For example, a rate-$\frac{1}{2}$ space-time code identified in the code searches provides a 3.5 dB gain over delay diversity at a frame error rate of 10^{-1} with no receive diversity ($L_r = 1$). With receive diversity greater performance gains are realized. These coding gains are achieved with no extra trellis complexity. Therefore, if designing a system, for example, which requires a simple inner space-time code as part of a larger system, these optimized codes should be considered.

Chapter 5

Performance Bounds

5.1 Introduction

The error rate performance of space-time coded continuous phase modulated (STC-CPM) systems can be characterized using the union bound technique [73] that utilizes the pairwise error probability (PEP). PEP bounds are used to develop STC-CPM error probability bounds in this chapter. It was shown in Chapter 4 that an upper bound on the PEP between two signals of a STC-CPM system, can be developed using the product distance, the trace, and the rank of the corresponding signal distance matrix. To evaluate the performance bounds, knowledge of the signal distance matrix parameters for each distinct pair of transmitted and erroneously detected signals is required.

The Euclidean distance of a STC-CPM system, which is equivalent to the trace of the signal distance matrix, is described in Chapter 4. In this chapter, we present an expression to evaluate the product distance of the signal distance matrix and provide a method to determine its rank. We then derive bounds for the bit, symbol and frame error probabilities of STC-CPM systems. Approximations of these bounds are evaluated for selected schemes. The computed error performance curves are compared to the simulated error rate performance curves. We conclude the chapter with a discussion of the validity and tightness of the approximated bounds.

5.2 Product Distance and Rank Calculation

The pairwise error probability may be used to form bounds on the probability of bit, symbol and frame errors. In order to evaluate the bound on the PEP derived in Chapter 4 given by

$$P(\boldsymbol{X} \rightarrow \hat{\boldsymbol{X}}) \leq \left(1 + \frac{E_s}{4N_0} \sum_{i=1}^{\rho} \lambda_i + \left(\frac{E_s}{4N_0}\right)^{\rho} \prod_{i=1}^{\rho} \lambda_i\right)^{-L_r}, \tag{5.1}$$

the product distance, $\Lambda^P = \prod_{i=1}^{\rho} \lambda_i$, of the corresponding signal distance matrix, $\boldsymbol{S}$ of Equation (4.16), must be evaluated, where ρ is the rank of $\boldsymbol{S}$ and the variables λ_i, for $1 \leq i \leq \rho$, are the non-zero eigenvalues of $\boldsymbol{S}$. If the signal distance matrix is full rank, the product distance is equal to the determinant of $\boldsymbol{S}$.

It is well known that the product distance, Λ^P, of a matrix may be evaluated as the sum of the $\begin{pmatrix} L_t \\ \rho \end{pmatrix}$ determinants that are its $(\rho \times \rho)$ principal minors [4]. We let $\boldsymbol{A}$ denote an $(m \times n)$-dimensional matrix, and let k be a positive integer not larger than m and n. A $(k \times k)$ minor of $\boldsymbol{A}$, is the determinant of a $(k \times k)$-dimensional matrix obtained from $\boldsymbol{A}$, by deleting $m - k$ rows and $n - k$ columns [54]. We let $\boldsymbol{A}^n$ denote a $(n \times n)$-dimensional matrix and denote the $((n-1) \times (n-1))$ minors of $\boldsymbol{A}^n$ as $M_{i,j}$, for $1 \leq i, j \leq n$. The minor $M_{i,j}$ is the determinant of the sub-matrix obtained from $\boldsymbol{A}^n$ by deleting its i-th row and j-th column [54]. For example, for the (3×3)-dimensional matrix

$$\boldsymbol{A}^3 = \begin{bmatrix} A_{1,1} & A_{1,2} & A_{1,3} \\ A_{2,1} & A_{2,2} & A_{2,3} \\ A_{3,1} & A_{3,2} & A_{3,3} \end{bmatrix}, \tag{5.2}$$

the minor $M_{1,2}$ is given by

$$M_{1,2} = \det\left(\begin{bmatrix} A_{2,1} & A_{2,3} \\ A_{3,1} & A_{3,3} \end{bmatrix}\right) = A_{2,1}A_{3,3} - A_{2,3}A_{3,1}. \tag{5.3}$$

A principal minor, is a minor where the indices of the rows and columns struck out are the same. The principal minors are the determinants of the sub-matrices whose diagonal elements lie on the main diagonal of $\boldsymbol{A}$. For example, consider the (3×3)-dimensional matrix $\boldsymbol{A}^3$ of Equation (5.2). The minors $M_{1,1}$, $M_{2,2}$ and $M_{3,3}$ are its (2×2) principal minors, and the elements $A_{1,1}$, $A_{2,2}$ and $A_{3,3}$ are its (1×1) principal minors.

To determine the product distance, Λ^P, we consider the signal distance matrix, $\boldsymbol{S}$. Each element, $S_{i,j}$, of the matrix $\boldsymbol{S}$, for $1 \leq i, j \leq L_t$, is given by

$$\begin{aligned} S_{i,j} &= \int_0^{N_cT} \triangle_i(t)\triangle_j^*(t)dt \\ &= \int_0^{N_cT} \left[\tilde{s}_i(t, \boldsymbol{X}_i(D)) - \tilde{s}_i(t, \hat{\boldsymbol{X}}_i(D))\right] \times \left[\tilde{s}_j(t, \boldsymbol{X}_j(D)) - \tilde{s}_j(t, \hat{\boldsymbol{X}}_j(D))\right]^* dt \\ &= \int_0^{N_cT} \tilde{s}_i(t, \boldsymbol{X}_i(D))\tilde{s}_j^*(t, \boldsymbol{X}_j(D))dt - \int_0^{N_cT} \tilde{s}_i(t, \boldsymbol{X}_i(D))\tilde{s}_j^*(t, \hat{\boldsymbol{X}}_j(D))dt \\ &\quad - \int_0^{N_cT} \tilde{s}_i(t, \hat{\boldsymbol{X}}_i(D))\tilde{s}_j^*(t, \boldsymbol{X}_j(D))dt + \int_0^{N_cT} \tilde{s}_i(t, \hat{\boldsymbol{X}}_i(D))\tilde{s}_j^*(t, \hat{\boldsymbol{X}}_j(D))dt, \end{aligned} \tag{5.4}$$

where N_c is the number of channel symbol intervals. We define $\Omega(\boldsymbol{X}_a, \boldsymbol{X}_b)$ as

$$\Omega(\boldsymbol{X}_a, \boldsymbol{X}_b) \triangleq \int_0^{N_cT} \tilde{s}_a(t, \boldsymbol{X}_a(D))\tilde{s}_b^*(t, \boldsymbol{X}_b(D))dt. \tag{5.5}$$

Substituting Equation (5.5) into Equation (5.4) gives

$$S_{i,j} = \Omega(\boldsymbol{X}_i, \boldsymbol{X}_j) - \Omega(\boldsymbol{X}_i, \hat{\boldsymbol{X}}_j) - \Omega(\hat{\boldsymbol{X}}_i, \boldsymbol{X}_j) + \Omega(\hat{\boldsymbol{X}}_i, \hat{\boldsymbol{X}}_j). \tag{5.6}$$

The matrix element $S_{i,i}$, for $1 \leq i \leq L_t$, is on the main diagonal of the signal distance matrix and is given by

$$\begin{aligned} S_{i,i} &= \Omega(\boldsymbol{X}_i, \boldsymbol{X}_i) + \Omega(\hat{\boldsymbol{X}}_i, \hat{\boldsymbol{X}}_i) - 2\Omega(\boldsymbol{X}_i, \hat{\boldsymbol{X}}_i) \\ &= \frac{4E_sN_c}{L_t} - 2\Omega(\boldsymbol{X}_i, \hat{\boldsymbol{X}}_i). \end{aligned} \tag{5.7}$$

These diagonal elements may be used to calculate the trace of the signal distance matrix as

$$\begin{aligned} \Lambda^E &= \sum_{i=1}^{\rho} \lambda_i \\ &= trace(\boldsymbol{S}) \\ &= \sum_{i=1}^{L_t} S_{i,i}. \end{aligned} \tag{5.8}$$

We now have expressions to evaluate the elements of the signal distance matrix $\boldsymbol{S}$. The principal minors of $\boldsymbol{S}$ may be evaluated using standard linear algebra methods [54] for evaluating determinants. The determinant of $\boldsymbol{S}$ is given by

$$\det(\boldsymbol{S}) = \sum_{j=1}^{L_t} S_{i,j}C_{i,j}, \quad i = \text{constant}, \tag{5.9}$$

where $C_{i,j}$ is the cofactor of the element $S_{i,j}$ and is given by

$$C_{i,j} = -1^{i+j} M_{i,j}. \tag{5.10}$$

Consider a system with two transmit antennas ($L_t = 2$). In this case, $\boldsymbol{S}$ is a 2 by 2 matrix and the determinant of $\boldsymbol{S}$, which is the product distance of $\boldsymbol{S}$ when $\boldsymbol{S}$ is full rank, is given by

$$\det(\boldsymbol{S}) = S_{1,1}S_{2,2} - S_{1,2}S_{2,1}. \tag{5.11}$$

For an $L_t = 3$ system, the determinant of the (3×3) matrix $\boldsymbol{S}$ is given by

$$\begin{aligned} \det(\boldsymbol{S}) = {} & S_{1,1}S_{2,2}S_{3,3} + S_{1,2}S_{2,3}S_{3,1} + S_{1,3}S_{2,1}S_{3,2} \\ & - S_{3,1}S_{2,2}S_{1,3} - S_{3,2}S_{2,3}S_{1,1} - S_{3,3}S_{2,1}S_{1,2}. \end{aligned} \tag{5.12}$$

If the rank, ρ, of the signal distance matrix is not known before the product distance calculation, then we begin by evaluating the determinant of the signal distance matrix, assuming the matrix is full rank. If this determinant is non-zero, then the matrix is full rank, the determinant calculated is the product distance and $\rho = L_t$. However, if the determinant calculated under the full rank assumption is to equal to zero, then the number of non-zero eigenvalues, or equivalently ρ, is less than L_t, and the search for the product distance must continue.

In the latter case, when the determinant is equal to zero, we next calculate the product distance assuming that $\rho = L_t - 1$. The sum of the L_t $((L_t - 1) \times (L_t - 1))$ principal minors is evaluated. If this sum is non-zero, it is the correct product distance and $\rho = L_t - 1$. If the summation is zero, the rank must be less than $L_t - 1$. Therefore, the sum of the $\begin{pmatrix} L_t \\ L_t - 2 \end{pmatrix}$ $((L_t - 2) \times (L_t - 2))$ principal minors of the signal distance matrix is evaluated. This process is repeated until a valid product distance is found (not equal to zero). This may not occur until the principal minors are the diagonal elements of $\boldsymbol{S}$ and then, $\rho = 1$.

5.3 Performance Bounds for STC-CPM

We now develop upper bounds on the bit, symbol and frame error probabilities of STC-CPM systems based on union bound techniques. A full union bound considers the effect of all possible error events. The error event with the minimum distance dominates the error rate performance, making it useful for code design. However, other error events can have a significant impact on the performance, particularly at low SNR, and must be considered in order

to find an accurate measure of performance. Another consideration is event multiplicity. For example, there may be more than one error event that has the minimum distance.

A full union bound considers all of these possibilities, and hence knowledge of all the error event probabilities is required to calculate the bound. Due to the impossibly large number of these terms, we instead evaluate an approximation to the full union bound that is a truncated union bound, which considers only the important error events. We may, for example, use the x error events with the smallest Euclidean distances. The value of x will be determined in a tradeoff between the computational complexity and retaining the error events that have a major impact on the performance.

The union bound tends to be a loose upper bound and for systems operating in quasi-static fading channels convergence is not guaranteed even at high SNR [74, 6, 75]. Other more complex procedures for calculating performance bounds can provide bounds that are tighter [74]. However, the truncated union bound is a relatively simple analytical tool that we demonstrate to be useful in predicting the relative performance of STC-CPM schemes, especially those with large receive diversity.

Forney describes a method for calculating error probabilities in [73] based on the union bound. This method has been used in [76, 26, 29] to derive bit error probabilities for convolutionally encoded continuous phase modulated systems. We follow the methodology to derive bit, symbol and frame error probabilities for space-time coded continuous phase modulated schemes.

5.3.1 Bit Error Probability

We denote the input data sequence as

$$\boldsymbol{a}(D) = \{\boldsymbol{a}_0 + \boldsymbol{a}_1 D + \ldots\}, \tag{5.13}$$

and the decoded data sequence as

$$\hat{\boldsymbol{a}}(D) = \{\hat{\boldsymbol{a}}_0 + \hat{\boldsymbol{a}}_1 D + \ldots\}. \tag{5.14}$$

We assume that there are N_p independent and equally likely modulo-p symbols transmitted. The symbols are grouped into blocks, such that the vector

$$\boldsymbol{a}_m = [a_m^1 \quad a_m^2 \ \ldots \ a_m^{rk}] \tag{5.15}$$

is the input during the m-th trellis interval and consists of rk modulo-p symbols. Each p-ary symbol may be mapped to a binary symbol, using for example, natural mapping or Gray mapping. We consider natural mapping, where the mapping rules,

$$\begin{aligned} 0 &\rightarrow 00, \\ 1 &\rightarrow 01, \\ 2 &\rightarrow 10, \\ 3 &\rightarrow 11, \end{aligned} \tag{5.16}$$

apply to $\mathbb{Z}_4$ symbols. We let N_t denote the number of trellis intervals over which the transmission occurs.

The bit error probability is the expected number of bit errors, divided by the number of bits transmitted. The total number of bits transmitted is $n_B = N_p \log_2(p) = N_t rk \log_2(p)$. We let $e_B\left(\boldsymbol{a}(D), \hat{\boldsymbol{a}}(D)\right)$ denote the number of bits that differ between the input and the decoded sequences, $\boldsymbol{a}(D)$ and $\hat{\boldsymbol{a}}(D)$. The bit error probability is then

$$P_B = \frac{E[e_B\left(\boldsymbol{a}(D), \hat{\boldsymbol{a}}(D)\right)]}{n_B} = \frac{E[e_B\left(\boldsymbol{a}(D), \hat{\boldsymbol{a}}(D)\right)]}{N_t rk \log_2(p)}, \tag{5.17}$$

where $E[\,]$ is the expected value of the expression in the parentheses.

The number of states in the trellis representing the overall encoder ($\boldsymbol{J}(D)$ formed in Chapter 3) is denoted S_J. The sequence of trellis states at the transmitter is denoted

$$\boldsymbol{\sigma} = (\sigma_0, \sigma_1, \ldots, \sigma_{N_t-1}), \quad \sigma_m \in \{0, 1, \ldots, S_J\}, \quad 0 \leq m < N_t. \tag{5.18}$$

Similarly, at the decoder the sequence of trellis states is denoted

$$\hat{\boldsymbol{\sigma}} = (\hat{\sigma}_0, \hat{\sigma}_1, \ldots, \sigma_{N_t-1}), \quad \hat{\sigma}_m \in \{0, 1, \ldots, S_J\}, \quad 0 \leq m < N_t. \tag{5.19}$$

An error event of duration $\zeta = j - i$ occurs when,

$$\begin{aligned} \sigma_i &= \hat{\sigma}_i, \quad \boldsymbol{a}_i \neq \hat{\boldsymbol{a}}_i, \\ \sigma_m &\neq \hat{\sigma}_m, \quad i > m > j, \\ \sigma_j &= \hat{\sigma}_j. \end{aligned} \tag{5.20}$$

A given set of transmitted and decoded sequences can have a number of separate error events. This is illustrated in Fig 5.1, where two error events are shown. The first error event is three trellis intervals long and the second is two trellis intervals long.

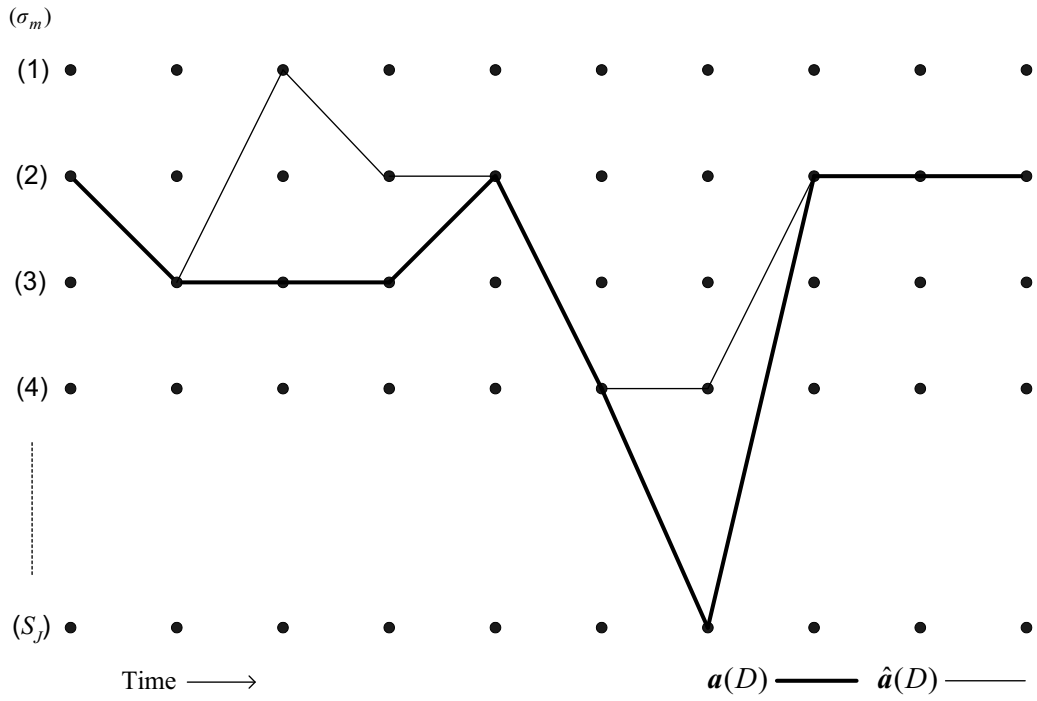

Figure 5.1: Sequence of error events between $\boldsymbol{a}(D)$ and $\hat{\boldsymbol{a}}(D)$.

We now find $E[e_B\left(\boldsymbol{a}(D), \hat{\boldsymbol{a}}(D)\right)]$ to evaluate Equation (5.17). We let W_m^B denote a random variable for $0 \leq m < N_t$, where W_m^B is defined as the number of bit errors generated by an error event that starts in the m-th trellis interval, given the sequences $\boldsymbol{a}(D)$ and $\hat{\boldsymbol{a}}(D)$. If an error event is already in progress during the m-th trellis interval, that is, it does not start in the m-th trellis interval, then $W_m^B = 0$. The total number of bit errors generated by the sequences $\boldsymbol{a}(D)$ and $\hat{\boldsymbol{a}}(D)$ is

$$e_B\left(\boldsymbol{a}(D), \hat{\boldsymbol{a}}(D)\right) = \sum_{m=0}^{N_t-1} W_m^B. \tag{5.21}$$

Strictly speaking, the number of bit errors associated with an error event that starts at a given time, is a function of the start time, unless the transmission is assumed to begin at time equal to $-\infty$ and end at time equal to ∞ [77]. We assume that the transmission period is long enough that the start time does not affect the error probability. The bit error probability of Equation (5.17) may be then written as

$$P_B = \frac{E[e_B\left(\boldsymbol{a}(D), \hat{\boldsymbol{a}}(D)\right)]}{n_B} = \frac{E\left[\sum_{m=0}^{N_t-1} W_m^B\right]}{N_t r k \log_2(p)} = \frac{\sum_{m=0}^{N_t-1} E[W_m^B]}{N_t r k \log_2(p)}, \tag{5.22}$$

assuming that N_t is large enough.

To find $E[W_m^B]$, we study the error events that start in the m-th trellis interval, that is, those events with $W_m^B > 0$. We consider an arbitrary state, $s \in \{0, 1, \ldots, S_J\}$, and label the error events that begin in this state as $F_{s,1}, F_{s,2}, F_{s,3}, \ldots$. Each error event, $F_{s,t}$ for $t = 1, 2, \ldots$ (t finite), is fully described by its starting state, s, and the pair of sequences, $(\boldsymbol{a}_{s,t}(D), \hat{\boldsymbol{a}}_{s,t}(D))$, that generate the event. The set of all error events, starting in the m-th trellis interval, is found by enumerating the lists for each of the S_J trellis states. We let $\zeta_{s,t}$ denote the length of the t-th error event starting from state-s and let $i_{s,t}^B$ denote the number of bit errors associated with this event. We let $\Lambda_{s,t}^E$, $\Lambda_{s,t}^P$ and $\rho_{s,t}$ denote the trace, the product distance and the rank of the signal distance matrix, corresponding to the error event $F_{s,t}$, respectively.

We now define the events, $f_{m,s,t}$ and $\hat{f}_{m,s,t}$ that begin in the m-th trellis interval, in state-s for $0 \leq m < N_t$, $1 \leq s \leq S_J$ and $t = 1, 2, \ldots$ (t finite). We let $f_{m,s,t}$ denote the event that $\boldsymbol{a}(D)$ is such that, $\sigma_m = s$ and

$$\boldsymbol{a}_m + \boldsymbol{a}_{m+1}D + \ldots + \boldsymbol{a}_{m+\zeta_{s,t}-1}D^{\zeta_{s,t}-1} = \boldsymbol{a}_{s,t}(D). \tag{5.23}$$

We let $\hat{f}_{m,s,t}$ denote the event that $\hat{\boldsymbol{a}}(D)$ is such that, $\hat{\sigma}_m = s$ and

$$\hat{\boldsymbol{a}}_m + \hat{\boldsymbol{a}}_{m+1}D + \ldots + \hat{\boldsymbol{a}}_{m+\zeta_{s,t}-1}D^{\zeta_{s,t}-1} = \hat{\boldsymbol{a}}_{s,t}(D). \tag{5.24}$$

The joint event $(f_{m,s,t}, \hat{f}_{m,s,t})$ describes the situation where error event $F_{s,t}$ originates in the m-th trellis interval. Using the union bound on $E[W_m^B]$ we obtain

$$\begin{aligned} E[W_m^B] &= \sum_{i^B} i^B \text{Pr}\{W_m^B = i^B\} \\ &\leq \sum_s \sum_t i_{s,t}^B \text{Pr}\{f_{m,s,t}, \hat{f}_{m,s,t}\} \\ &\leq \sum_s \sum_t i_{s,t}^B \text{Pr}\{f_{m,s,t}\} \text{Pr}\{\hat{f}_{m,s,t} | f_{m,s,t}\}, \end{aligned} \tag{5.25}$$

where i^B is the number of bit errors generated by an error event. We assume that the information sequences consist of independent and equally likely symbols, and thus we may write

$$\text{Pr}\{f_{m,s,t}\} = \text{Pr}\{\sigma_m = s\} \left(\frac{1}{p}\right)^{rk\zeta_{s,t}} = \frac{1}{S_J}\left(\frac{1}{p}\right)^{rk\zeta_{s,t}}. \tag{5.26}$$

The conditional probability, $\text{Pr}\{\hat{f}_{m,s,t} | f_{m,s,t}\}$, is equivalent to the pairwise error probability. From Equation (5.1), we know that for STC-CPM the PEP is upper bounded by

$$\text{Pr}\{\hat{f}_{m,s,t} | f_{m,s,t}\} \leq \left(1 + \Lambda_{s,t}^E \frac{E_s}{4No} + \Lambda_{s,t}^P \left(\frac{E_s}{4No}\right)^{\rho_{s,t}}\right)^{-L_r}. \tag{5.27}$$

Substituting Equations (5.27) and (5.26) into Equation (5.25) we find

$$\begin{aligned} E[W_m^B] &\leq \sum_s \sum_t i_{s,t}^B \frac{1}{S_J} \left(\frac{1}{p}\right)^{rk\zeta_{s,t}} \left(1 + \Lambda_{s,t}^E \frac{E_s}{4No} + \Lambda_{s,t}^P \left(\frac{E_s}{4No}\right)^{\rho_{s,t}}\right)^{-L_r} \\ &\leq \sum_\zeta \sum_s \sum_{i^B} \sum_{\Lambda^E} \sum_{\Lambda^P} \sum_\rho \alpha_B(s, i^B, \zeta, \Lambda^E, \Lambda^P, \rho) \times \\ &\qquad i^B \frac{1}{S_J} \left(\frac{1}{p}\right)^{rk\zeta} \left(1 + \Lambda^E \frac{E_s}{4No} + \Lambda^P \left(\frac{E_s}{4No}\right)^{\rho}\right)^{-L_r}, \end{aligned} \tag{5.28}$$

where $\alpha_B(s, i^B, \zeta, \Lambda^E, \Lambda^P, \rho)$ is the number of error events that start in state-s, have i^B bit errors, are of length ζ, and have signal distance matrices with trace, Λ^E, product distance, Λ^P, and rank, ρ.

We assume that the number of trellis intervals, N_t, is sufficiently long $(N_t \to \infty)$ that we may write [76]

$$E[W_m^B] = E[W^B], \quad 0 \leq m < N_t. \tag{5.29}$$

Then, substituting the inequality of Equation (5.28) into Equation (5.22), we find that the bit error probability is upper bounded by

$$\begin{aligned} P_B &= \frac{N_t E[W_m^B]}{N_t rk \log_2(p)} \\ &= \frac{E[W_m^B]}{rk \log_2(p)} \\ &\leq \frac{1}{rk \log_2(p)} \sum_\zeta \sum_s \sum_{i^B} \sum_{\Lambda^E} \sum_{\Lambda^P} \sum_\rho \alpha_B(s, i^B, \zeta, \Lambda^E, \Lambda^P, \rho) \times \\ &\qquad i^B \frac{1}{S_J} \left(\frac{1}{p}\right)^{rk\zeta} \left(1 + \Lambda^E \frac{E_s}{4No} + \Lambda^P \left(\frac{E_s}{4No}\right)^{\rho}\right)^{-L_r} \\ &\leq \sum_{\Lambda^E} \sum_{\Lambda^P} \sum_\rho C_B(\Lambda^E, \Lambda^P, \rho) \left(1 + \Lambda^E \frac{E_s}{4No} + \Lambda^P \left(\frac{E_s}{4No}\right)^{\rho}\right)^{-L_r}, \end{aligned} \tag{5.30}$$

where

$$C_B(\Lambda^E, \Lambda^P, \rho) = \frac{1}{rk \log_2(p) S_J} \sum_\zeta \sum_s \sum_{i^B} \alpha_B(s, i^B, \zeta, \Lambda^E, \Lambda^P, \rho) i^B \left(\frac{1}{p}\right)^{rk\zeta}. \tag{5.31}$$

If the space-time coded CPM system has full spatial diversity, every error event has a signal distance matrix with rank, $\rho = L_t$. Thus ρ may be replaced by L_t in Equation (5.30) and Equation (5.31) simplifies to

$$C_B(\Lambda^E, \Lambda^P) = \frac{1}{rk \log_2(p) S_J} \sum_\zeta \sum_s \sum_{i^B} \alpha_B(s, i^B, \zeta, \Lambda^E, \Lambda^P) i^B \left(\frac{1}{p}\right)^{rk\zeta}. \tag{5.32}$$

5.3.2 Symbol and Frame Error Probabilities

We follow the same process as above to determine the symbol error probability. We define W_m^S as a random variable that represents the number of symbol errors that are generated by an error event starting in the m-th trellis interval, given the sequences $\boldsymbol{a}(D)$ and $\hat{\boldsymbol{a}}(D)$. The symbol error probability, P_S, is defined as

$$P_S = \frac{E[e_S\left(\boldsymbol{a}(D), \hat{\boldsymbol{a}}(D)\right)]}{n_S} = \frac{E\left[\sum_{m=0}^{N_t-1} W_m^S\right]}{N_t rk} = \frac{\sum_{m=0}^{N_t-1} E[W_m^S]}{N_t rk}, \tag{5.33}$$

where $e_S\left(\boldsymbol{a}(D), \hat{\boldsymbol{a}}(D)\right)$ is the number of symbol errors associated with the sequences $\boldsymbol{a}(D)$ and $\hat{\boldsymbol{a}}(D)$, and n_S is the total number of symbols transmitted.

We find that

$$\begin{aligned} E[W_m^S] &\leq \sum_s \sum_t i_{s,t}^S \frac{1}{S_J} \left(\frac{1}{p}\right)^{rk\zeta_{s,t}} \left(1 + \Lambda_{s,t}^E \frac{E_s}{4No} + \Lambda_{s,t}^P \left(\frac{E_s}{4No}\right)^{\rho_{s,t}}\right)^{-L_r} \\ &\leq \sum_\zeta \sum_s \sum_{i^S} \sum_{\Lambda^E} \sum_{\Lambda^P} \sum_\rho \alpha_S(s, i^S, \zeta, \Lambda^E, \Lambda^P, \rho) \times \\ &\qquad i^S \frac{1}{S_J} \left(\frac{1}{p}\right)^{rk\zeta} \left(1 + \Lambda^E \frac{E_s}{4No} + \Lambda^P \left(\frac{E_s}{4No}\right)^{\rho}\right)^{-L_r}, \end{aligned} \tag{5.34}$$

where $i_{s,t}^S$ represents the number of symbol errors generated by the t-th error event, starting in state-s, during trellis interval-m and $\alpha_S(s, i^S, \zeta, \Lambda^E, \Lambda^P, \rho)$ is the number of error events that start in state-s, have i^S symbol errors, are of length ζ, and have signal distance matrices with trace, Λ^E, product distance, Λ^P, and rank, ρ. Then, the symbol error probability may be bounded by

$$\begin{aligned} P_S &= \frac{N_t E[W_m^S]}{N_t rk} \\ &= \frac{E[W_m^S]}{rk} \\ &\leq \frac{1}{rk} \sum_\zeta \sum_s \sum_{i^S} \sum_{\Lambda^E} \sum_{\Lambda^P} \sum_\rho \alpha_S(s, i^S, \zeta, \Lambda^E, \Lambda^P, \rho) \times \\ &\qquad i^S \frac{1}{S_J} \left(\frac{1}{p}\right)^{rk\zeta} \left(1 + \Lambda^E \frac{E_s}{4No} + \Lambda^P \left(\frac{E_s}{4No}\right)^{\rho}\right)^{-L_r} \\ &\leq \sum_{\Lambda^E} \sum_{\Lambda^P} \sum_\rho C_S(\Lambda^E, \Lambda^P, \rho) \left(1 + \Lambda^E \frac{E_s}{4No} + \Lambda^P \left(\frac{E_s}{4No}\right)^{\rho}\right)^{-L_r}, \end{aligned} \tag{5.35}$$

where

$$C_S(\Lambda^E, \Lambda^P, \rho) = \frac{1}{rkS_J} \sum_\zeta \sum_s \sum_{i^S} \alpha_S(s, i^S, \zeta, \Lambda^E, \Lambda^P, \rho) i^S \left(\frac{1}{p}\right)^{rk\zeta}. \tag{5.36}$$

Equation (5.36) simplifies to

$$C_S(\Lambda^E, \Lambda^P) = \frac{1}{rkS_J} \sum_{\zeta} \sum_{s} \sum_{i^S} \alpha_S(s, i^S, \zeta, \Lambda^E, \Lambda^P) i^S \left(\frac{1}{p}\right)^{rk\zeta}, \tag{5.37}$$

if the system has full transmit diversity and then ρ may be replaced by L_t in Equation (5.35).

Similarly, we find that the frame error rate probability is bounded by

$$\begin{aligned} P_F &\leq N_t \sum_{\zeta} \sum_{s} \sum_{\Lambda^E} \sum_{\Lambda^P} \sum_{\rho} \alpha_F(s, \zeta, \Lambda^E, \Lambda^P, \rho) \times \\ &\quad \frac{1}{S_J} \left(\frac{1}{p}\right)^{rk\zeta} \left(1 + \Lambda^E \frac{E_s}{4No} + \Lambda^P \left(\frac{E_s}{4No}\right)^{\rho}\right)^{-L_r} \\ &\leq \sum_{\Lambda^E} \sum_{\Lambda^P} \sum_{\rho} C_F(\Lambda^E, \Lambda^P, \rho) \left(1 + \Lambda^E \frac{E_s}{4No} + \Lambda^P \left(\frac{E_s}{4No}\right)^{\rho}\right)^{-L_r}, \end{aligned} \tag{5.38}$$

where

$$C_F(\Lambda^E, \Lambda^P, \rho) = \frac{N_t}{S_J} \sum_{\zeta} \sum_{s} \alpha_F(s, \zeta, \Lambda^E, \Lambda^P, \rho) \left(\frac{1}{p}\right)^{rk\zeta}, \tag{5.39}$$

and $\alpha_F(s, \zeta, \Lambda^E, \Lambda^P, \rho)$ is the number of error events that start in state-s, are of length ζ, and have signal distance matrices with trace, Λ^E, product distance, Λ^P, and rank, ρ. The right hand side of Equation (5.38) represents the probability of an error event originating in a trellis interval multiplied by the number of times this may occur that is the number of trellis intervals N_t. The expression $C_F(\Lambda^E, \Lambda^P, \rho)$ reduces to

$$C_F(\Lambda^E, \Lambda^P) = \frac{N_t}{S_J} \sum_{\zeta} \sum_{s} \alpha_F(s, \zeta, \Lambda^E, \Lambda^P) \left(\frac{1}{p}\right)^{rk\zeta}, \tag{5.40}$$

when the system has full transmit diversity and then ρ may be replaced by L_t in Equation (5.38).

5.3.3 Coefficient Computation

The bounds, of Equations (5.30), (5.35) and (5.38), on the error-rate probabilities can be used to plot bounds on the corresponding error-rate performance curves. These can then be used to analyse and compare space-time coded CPM systems. In this section, we present a method to evaluate approximations to the bounds. The bit, symbol and frame error probabilities may all be written in the form

$$P_E \leq \sum_{\Lambda^E} \sum_{\Lambda^P} \sum_{\rho} C_E(\Lambda^E, \Lambda^P, \rho) \left(1 + \Lambda^E \frac{E_s}{4No} + \Lambda^P \left(\frac{E_s}{4No}\right)^{\rho}\right)^{-L_r}, \tag{5.41}$$

where the error coefficient $C_E(\Lambda^E, \Lambda^P, \rho)$ is equal to $C_B(\Lambda^E, \Lambda^P, \rho)$, $C_S(\Lambda^E, \Lambda^P, \rho)$ and $C_F(\Lambda^E, \Lambda^P, \rho)$ for the bit, symbol and frame error probabilities respectively. We may search for the three error probabilities simultaneously, by evaluating each of these coefficients for the different combinations of $\{\Lambda^E, \Lambda^P, \rho\}$.

For a full union bound, we must find the error coefficient $C_E(\Lambda^E, \Lambda^P, \rho)$, corresponding to every combination of $\{\Lambda^E, \Lambda^P, \rho\}$. For full rank codes, ρ is always equal to L_t. We name each unique set of information, $\{\Lambda^E, \Lambda^P, \rho\}$, a term in the distance spectrum, where the overall distance spectrum consists of all such terms. We are not able to evaluate the coefficients of the entire distance spectrum due to the amount of computation required to evaluate such a large number of terms (which increases with the number of trellis states). Thus, we are unable to evaluate the full union bound. A truncated union bound, which is an approximation to the union bound is instead calculated. To evaluate a truncated union bound a limiting factor must be chosen. We may, for example, only evaluate the coefficients for error events that have length, ζ, less than a given number of trellis intervals, or we may limit the number of terms in the spectrum and choose those with the smallest distances, Λ^P and Λ^E. Here, we have limited the search based on the latter, because it is the events with the smallest distances that have the greatest effect on the error probability.

We define a superstate trellis, as in Section 4.3.1 of Chapter 4, with ${S_J}^2$ states. A superstate after the m-th trellis interval is denoted

$$(\sigma_m, \hat{\sigma}_m)\,, \tag{5.42}$$

where

$$\sigma_m \in \{1, 2, \ldots, S_J\} \tag{5.43}$$

and

$$\hat{\sigma}_m \in \{1, 2, \ldots, S_J\} \tag{5.44}$$

are the states at the transmitter and the detector after m trellis intervals respectively. A non-error superstate has

$$\sigma_m = \hat{\sigma}_m \tag{5.45}$$

and an error superstate has

$$\sigma_m \neq \hat{\sigma}_m. \tag{5.46}$$

An error event must start in one of the S_J error-free superstates and must finish in an error-free superstate, which is not necessarily the same superstate in which the event started. The intermediate states must include at least one error superstate and no error-free superstates, such that Equation (5.20) is true.

We let $\boldsymbol{S}(m)$ denote the signal distance matrix constructed after the m-th trellis interval, for a given path through the trellis. Due to $\boldsymbol{S}(m)$ being a real Hermitian matrix, it is only necessary to retain its lower or upper triangular elements. During each transition in the trellis there is an increment to the ${L_t}^2$ signal distance matrix elements. We denote these increments as $\Omega_{branch}(i,j)$, for $1 \leq i,j \leq L_t$. The signal distance matrix elements, after the m-th trellis interval are denoted, $S_{i,j}(m)$ and are given by

$$S_{i,j}(m) = S_{i,j}(m-1) + \Omega_{branch}(i,j), \quad 1 \leq i,j \leq L_t, \tag{5.47}$$

where $\Omega_{branch}(i,j)$ is defined as

$$\Omega_{branch}(i,j) \triangleq \Omega_U(\boldsymbol{X}_i, \boldsymbol{X}_j) - \Omega_U(\boldsymbol{X}_i, \hat{\boldsymbol{X}}_j) - \Omega_U(\hat{\boldsymbol{X}}_i, \boldsymbol{X}_j), + \Omega_U(\hat{\boldsymbol{X}}_i, \hat{\boldsymbol{X}}_j), \tag{5.48}$$

and $\Omega_U(\boldsymbol{X}_i, \hat{\boldsymbol{X}}_j)$ is given by

$$\Omega_U(\boldsymbol{X}_i, \hat{\boldsymbol{X}}_j) = \int_{mqT}^{(m+1)qT} \tilde{s}_i(t, \boldsymbol{X}_i(D)) \tilde{s}_j^*(t, \hat{\boldsymbol{X}}_j(D)) dt, \tag{5.49}$$

with q being the number of channel symbol intervals per trellis interval. We let $\Lambda^E(m)$, $\Lambda^P(m)$ and $\rho(m)$ denote the trace, the product distance and the rank of the signal distance matrix constructed after m trellis intervals, respectively.

Each transition in the trellis creates $i_{B_{branch}}$ bit errors, and $i_{S_{branch}}$ symbol errors. After m trellis intervals, the number of bit errors associated with a given path through the trellis is denoted $i^B(m)$ and is given by

$$i^B(m) = i^B(m-1) + i_{B_{branch}}. \tag{5.50}$$

Similarly, the number of symbol errors associated with a given path through the trellis after m trellis intervals is denoted $i^S(m)$ and is given by

$$i^S(m) = i^S(m-1) + i_{S_{branch}}. \tag{5.51}$$

Performance of Full Rank STC-CPM

In the following, we discuss the evaluation of the error rate performance of full rank STC-CPM. Consideration of rank deficient STC-CPM is presented in the next section. The following properties assist in the search for the product distance [74]; the rank of a signal distance matrix is a monotonically non-decreasing function of time, $\rho(m) \geq \rho(m-1)$, and if the rank of the signal distance matrix does not change, the product distance is a monotonically non-decreasing function of time. Therefore, $\Lambda^P(m) \geq \Lambda^P(m-1)$ if $\rho(m-1) = L_t$. Thus, if we search through the trellis and reach a point where the signal distance matrix of a given path is full rank, its product distance will not decrease when we extend the path through the trellis.

The product distance, $\Lambda^P(m)$, of the signal distance matrix, $\boldsymbol{S}(m)$, after m trellis intervals can be evaluated using the method described in Section 5.2. If $\rho(m-1) = L_t$, then $\rho(m) = L_t$ and $\Lambda^P(m) = \det(\boldsymbol{S}(m))$. The trace, $\Lambda^E(m)$, is a monotonically non-decreasing function of time regardless of the signal distance matrice's rank. It may be evaluated using

$$\begin{aligned} \Lambda^E(m) &= \sum_{i=1}^{L_t} S_{i,i}(m) \\ &= \sum_{i=1}^{L_t} \left(S_{i,i}(m-1) + \Omega_{branch}(i,i) \right) \\ &= \Lambda^E(m-1) + \sum_{i=1}^{L_t} \Omega_{branch}(i,i), \end{aligned} \tag{5.52}$$

where $\Omega_{branch}(i,i)$ is defined by Equation (5.48). Therefore, we do not need to retain the values of the matrix $\boldsymbol{S}(m-1)$ to evaluate $\Lambda^E(m)$, which is required to evaluate $\Lambda^P(m)$.

At each superstate, $(\sigma_m, \hat{\sigma}_m)$, after m trellis intervals, there are $\varpi_m(\sigma_m, \hat{\sigma}_m)$ sets of information to be stored. The variable $\varpi_m(\sigma_m, \hat{\sigma}_m)$ denotes the number of different combinations of $\{\Lambda^E(m), \Lambda^P(m), \rho(m), i^B(m), i^S(m)\}$ that occur at the superstate $(\sigma_m, \hat{\sigma}_m)$, after m trellis intervals. A given combination may occur more than once at each superstate, due to different paths through the superstate trellis. Therefore, the multiplicity of these events must be stored. We denote the multiplicity, of the i-th combination of $\{\Lambda^E(m), \Lambda^P(m), \rho(m), i^B(m), i^S(m)\}$ that arrives at the superstate $(\sigma_m, \hat{\sigma}_m)$, after m trellis intervals as,
$\Upsilon_{m,i}\left[(\sigma_m, \hat{\sigma}_m), \Lambda^E(m), \Lambda^P(m), \rho(m), i^B(m), i^S(m)\right]$ for $1 \leq i \leq \varpi_m(\sigma_m, \hat{\sigma}_m)$.

After the second trellis interval, error events may end. The non-error superstates, (σ_m, σ_m) for $1 \leq \sigma_m \leq S_J$, are checked for the terminated error events. There are $\varpi_m(\sigma_m, \sigma_m)$ contributions to the distance spectrum associated with each of these non-error superstates,

after the m-th ($m \geq 2$) trellis interval. The m-th partial error coefficient, $C_E^P(\Lambda^E, \Lambda^P, \rho, m)$, for the distance spectrum term, $\{\Lambda^E, \Lambda^P, \rho\}$, accounts for all error events that terminate at any state after m trellis intervals and correspond to the distance spectrum term. The sum of a distance spectrum term's partial error coefficients over all error event lengths possible for that term, is its full error coefficient, $C_E(\Lambda^E, \Lambda^P, \rho)$. The partial error coefficients that take into account the contributions of the error events terminating after the m-th trellis interval are calculated using $i^B = i^B(m)$, $i^S = i^S(m)$, $\Lambda^E = \Lambda^E(m)$, $\Lambda^P = \Lambda^P(m)$, $\rho = \rho(m)$, $\zeta = m$. For example, the bit error probability partial error coefficient, for events terminating after m trellis intervals, for the distance spectrum term, $\{\Lambda^E, \Lambda^P, \rho\}$, is given by

$$\begin{aligned} C_B^P(\Lambda^E, \Lambda^P, \rho, m) &= \frac{1}{rk \log_2(p) S_J} \sum_s \sum_{i^B} \alpha_B(s, i^B, m, \Lambda^E, \Lambda^P, \rho) i^B \left(\frac{1}{p}\right)^{rkm} \\ &= \frac{1}{rk \log_2(p) S_J} \sum_{\sigma_m=1}^{S_J} \sum_{i=1}^{\varpi_m(\sigma_m,\sigma_m)} \sum_{i^B} \sum_{i^S} \Upsilon_{m,i}\left[(\sigma_m, \sigma_m), \Lambda^E, \Lambda^P, \rho, i^B, i^S\right] i^B \left(\frac{1}{p}\right)^{rkm}, \\ & \qquad\qquad\qquad\qquad\qquad\qquad\qquad\qquad\qquad\qquad\qquad\qquad\qquad\qquad m \geq 2, \end{aligned} \tag{5.53}$$

where the full error coefficient $C_B(\Lambda^E, \Lambda^P, \rho)$ of Equation (5.31) is given by

$$C_B(\Lambda^E, \Lambda^P, \rho) = \sum_{\zeta} C_B^P(\Lambda^E, \Lambda^P, \rho, \zeta). \tag{5.54}$$

During the search, the partial error coefficients are recorded against the corresponding distance spectrum term. If the partial error coefficient corresponds to a distance spectrum term that does not already exist, a new distance spectrum term is created. Once the search has converged, the full error coefficients for each distance spectrum term evaluated are calculated. For example, Equation (5.54) is used to calculate the full coefficient of the distance spectrum term, $\{\Lambda^E, \Lambda^P, \rho\}$, for the bit error probability.

We evaluate a truncated union bound using two limiting factors, Λ^E and Λ^P. Therefore, we do not need to store information for all of the terminated error events. We set a threshold on one of the limiting factors, then search for a limited number of distance spectrum terms, with the first factor below or equal to its threshold, and with the other limiting factor minimized over all error events. For example, if we set a threshold of $\Lambda^P_{\max}$ for Λ^P, we then search for say, 1000 distance spectrum terms with $\Lambda^P \leq \Lambda^P_{\max}$ and Λ^E minimized. During the coefficient search, once 1000 distance spectrum terms (with $\Lambda^P \leq \Lambda^P_{\max}$) have been found, the largest

value of Λ^E in the spectrum is set as the threshold for Λ^E, which we label as $\Lambda^E_{\max}$. Any new distance spectrum terms that have $\Lambda^E \geq \Lambda^E_{\max}$ or $\Lambda^P > \Lambda^P_{\max}$ will be discarded. If a new distance spectrum term has $\Lambda^E < \Lambda^E_{\max}$ (and $\Lambda^P \leq \Lambda^P_{\max}$), the new term replaces one of the current terms with the largest value of Λ^E, which will equal $\Lambda^E_{\max}$. A possibly new threshold, $\Lambda^E_{\max}$, is set equal to the maximum value of Λ^E in the updated spectrum.

If the Euclidean distance of an incomplete error event, $\Lambda^E(m)$, is greater than or equal to the threshold, $\Lambda^E_{\max}$, we may discard this set of information. Similarly, if the product distance of an incomplete error event, $\Lambda^P(m)$, is greater than the threshold, $\Lambda^P_{\max}$, and the corresponding signal distance matrix is full rank, $\rho(m) = L_t$, we may discard the information for this event. If the signal distance matrix of an incomplete error event is not full rank, $\rho(m) < L_t$, the product distance may decrease in future trellis intervals. Therefore, the information for these unterminated events must be retained, even if $\Lambda^P(m) > \Lambda^P_{\max}$. This is not an issue for the Euclidean distance, which is a monotonically non-decreasing function. The overall search is terminated when all incomplete error events have either exceeded the threshold $\Lambda^E_{\max}$, or have exceeded the threshold $\Lambda^P_{\max}$ and are full rank. We say that the search has converged, when it terminates in this manner. The algorithm should always converge for full rank codes, because we have specifically designed our codes to avoid those that are catastrophic.

If it is not known if the STC-CPM scheme has full transmit diversity, all unterminated events must reach full rank before the algorithm may end. If a path (error event) terminates and its signal distance matrix rank is less than the number of transmit antennas, the code is not full rank and the search is terminated.

Performance of Rank Deficient STC-CPM

To evaluate the distance spectrum of STC-CPM systems that are not full rank, it is not possible to limit the search based on minimizing Λ^P. If there are long, unterminated error events that have $\rho < L_t$, we will not be able to end the search knowing they will not result in distance spectrum terms with $\Lambda^P < \Lambda^P_{\max}$, because $\Lambda^P(m)$ may decrease in future iterations. Therefore, the search is conducted over a fixed and limited number of iterations and/or by minimizing Λ^E.

Due to the rank of the signal distance matrices not necessarily being equal to the number of transmit antennas, the value of ρ must be noted. This is not required for the full rank codes as then $\rho = L_t$. For space-time coded systems that do not have full spatial diversity, ρ may

be less than or equal to L_t, for each error event. It only takes one error event with $\rho \neq L_t$, for a space-time code to not have full spatial diversity. In all other respects, the code search is conducted in the same manner as the full rank code search, as described in the previous section.

5.4 Numerical Results

In this section, we evaluate a truncated distance spectrum of selected STC-CPM systems. We plot truncated union bounds that are evaluated using the distance spectrum terms and Equation (5.41). The calculated performance curves are compared to the corresponding simulated results. See Appendix A for the simulation procedure. We then construct an error probability bound that uses the PEP derived in [33] instead of the PEP given by Equation (5.1).

5.4.1 Full Spatial Diversity Space-Time Code

We consider the space-time code (STC), $\boldsymbol{G}(D) = \left[1 \;\; \frac{2+D}{1+2D}\right]$, with 4-CPFSK and two transmit antennas. This STC-CPM system has full spatial diversity. Using the trace criterion, this code is optimal for $S_J = 16$ trellis states (see Table 4.2). It has a normalized, minimum squared Euclidean distance, $d^2_{\min}$, of 4.000.

The error coefficients for this STC are evaluated for 1000 distance spectrum terms. The search for the distance spectrum terms and the corresponding error coefficients was limited, such that the trace of each distance spectrum term is within 3 dB of the space-time code's minimum trace of $\Lambda^E_{\min} = 8$. That is, we set a threshold of $\Lambda^E_{\max} = 16$. We then found the 1000 distance spectrum terms with minimized product distance, Λ^P. The algorithm converged after 9 trellis intervals.

Table 5.1 presents a partial list of the error coefficients of the 1000 distance spectrum terms evaluated for the system with the space-time code, $\boldsymbol{G}(D) = \left[1 \;\; \frac{2+D}{1+2D}\right]$. Each distance spectrum term has different values of $\{\Lambda^E, \Lambda^P, \rho\}$, with $\Lambda^E \leq \Lambda^E_{\max} = 16$ and $\Lambda^P \leq 44.984$. Each distance spectrum term has full rank, $\rho = 2$, which is expected, because $\boldsymbol{G}(D) = \left[1 \;\; \frac{2+D}{1+2D}\right]$ has full spatial diversity, with 4-CPFSK and two transmit antennas. The terms in Table 5.1 are sorted by Λ^P and then by Λ^E, in ascending order.

Figure 5.2 plots truncated union bounds on the bit error rate performance of $\boldsymbol{G}(D) =$

ρ	$\mathbf{\Lambda^P}$	$\mathbf{\Lambda^E}$	$\mathbf{C_B}(\mathbf{\Lambda^E}, \mathbf{\Lambda^P}, \rho)$	$\mathbf{C_S}(\mathbf{\Lambda^E}, \mathbf{\Lambda^P}, \rho)$	$\mathbf{C_F}(\mathbf{\Lambda^E}, \mathbf{\Lambda^P}, \rho)$
2	6.976	8.605	0.07813	0.1250	8.1250
2	7.694	10.302	0.07813	0.1250	8.1250
2	8.188	8.605	0.07813	0.1250	8.1250
2	8.614	10.302	0.07813	0.1250	8.1250
2	8.862	10.302	0.07813	0.1250	8.1250
2	9.214	10.302	0.07813	0.1250	8.1250
2	9.444	10.302	0.07813	0.1250	8.1250
2	9.513	8.605	0.07813	0.1250	8.1250
2	10.063	8.605	0.07813	0.1250	8.1250
2	10.162	12.000	0.07813	0.1250	8.1250
2	10.183	10.302	0.23438	0.3750	24.3750
2	10.655	10.302	0.07813	0.1250	8.1250
⋮	⋮	⋮	⋮	⋮	⋮
2	44.984	14.663	0.00537	0.00781	0.2539

Table 5.1: Partial distance spectrum for STC $\boldsymbol{G}(D) = \left[1 \ \frac{2+D}{1+2D}\right]$ with 4-CPFSK and two transmit antennas (1000 terms).

$\left[1 \ \frac{2+D}{1+2D}\right]$, with 4-CPFSK and $L_t = 2$. The truncated union bounds are calculated using Equation (5.30) and only the 153 terms of the evaluated distance spectrum that have Λ^E within 2 dB of the minimum trace, $\Lambda^E_{\min}$, (that is, $\Lambda^E < 12.68$). We refer to these truncated union bounds as the 2 dB approximations. The simulated bit error rate performance results for the STC, with 4-CPFSK are also shown. The STC system's performance curves are presented with 1, 2 and 4 receive antennas. We observe that the approximate bit error rate bounds, for each value of L_r, follow the slope of the simulated curves at low bit error rates. Each bound approximation is offset from the simulated performance.

Figure 5.3 displays truncated frame error rate bounds calculated using Equation (5.38) and the simulated performance of $\boldsymbol{G}(D) = \left[1 \ \frac{2+D}{1+2D}\right]$ with 4-CPFSK, $L_t = 2$ and 1, 2 and 4 receive antennas. The truncated bounds are calculated using the 153 terms of the evaluated distance spectrum that have Λ^E within 2 dB of $\Lambda^E_{\min}$. The truncated frame error rate bounds are not as tight as the respective truncated bit error rate bounds, which are shown in Figure 5.2.

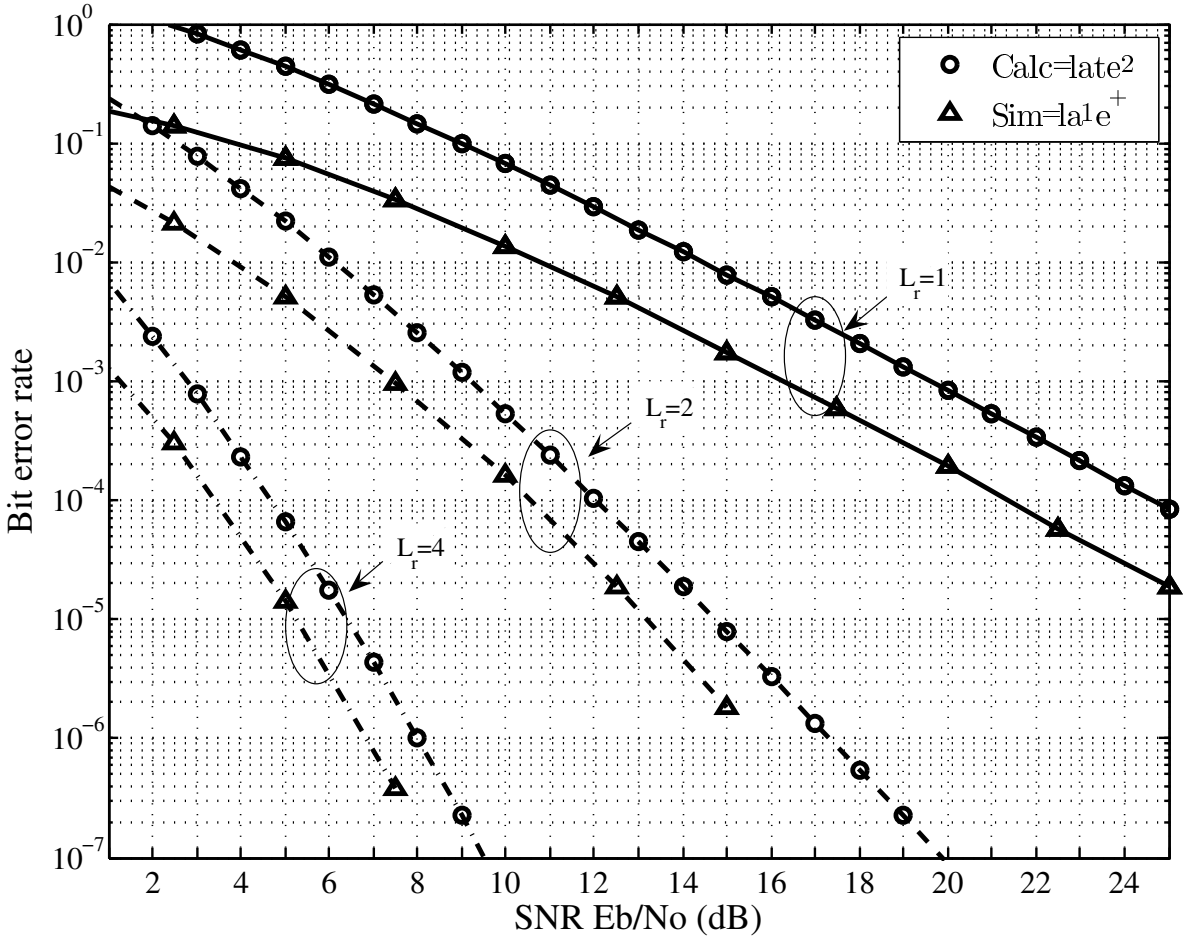

Figure 5.2: Approximate upper (2 dB) bit error rate performance bounds and simulated bit error rate performance of $\boldsymbol{G}(D) = \begin{bmatrix} 1 & \frac{2+D}{1+2D} \end{bmatrix}$ with 4-CPFSK and $L_t = 2$.

These truncated frame error rate bounds have the same slope as the simulated curves at low frame error rates. The larger the value of L_r, the tighter the truncated frame error rate bounds are to the simulated results.

Truncated bit error rate bounds are also plotted in Figure 5.4 for the space-time code $\boldsymbol{G}(D) = \begin{bmatrix} 1 & \frac{2+D}{1+2D} \end{bmatrix}$ with 4-CPFSK, $L_t = 2$ and 1, 2 and 4 receive antennas. However, the truncated bounds are calculated using all 1000 evaluated distance spectrum terms (represented by Table 5.1) and Equation (5.30). These truncated bounds are referred to as the 3 dB approximations. The calculated 3 dB bit error rate performance curve, for the system with 4 receive antennas, does not differ significantly from the calculated 2 dB bit error rate performance curve (Figure 5.2). The 3 dB approximation is calculated with the extra 847 distance spectrum terms and their coefficients that have $12.68 \leq \Lambda^E \leq 16$. The 3 dB approximation on the bit error rate performance of the system with one receive antenna is approximately 2-3 dB

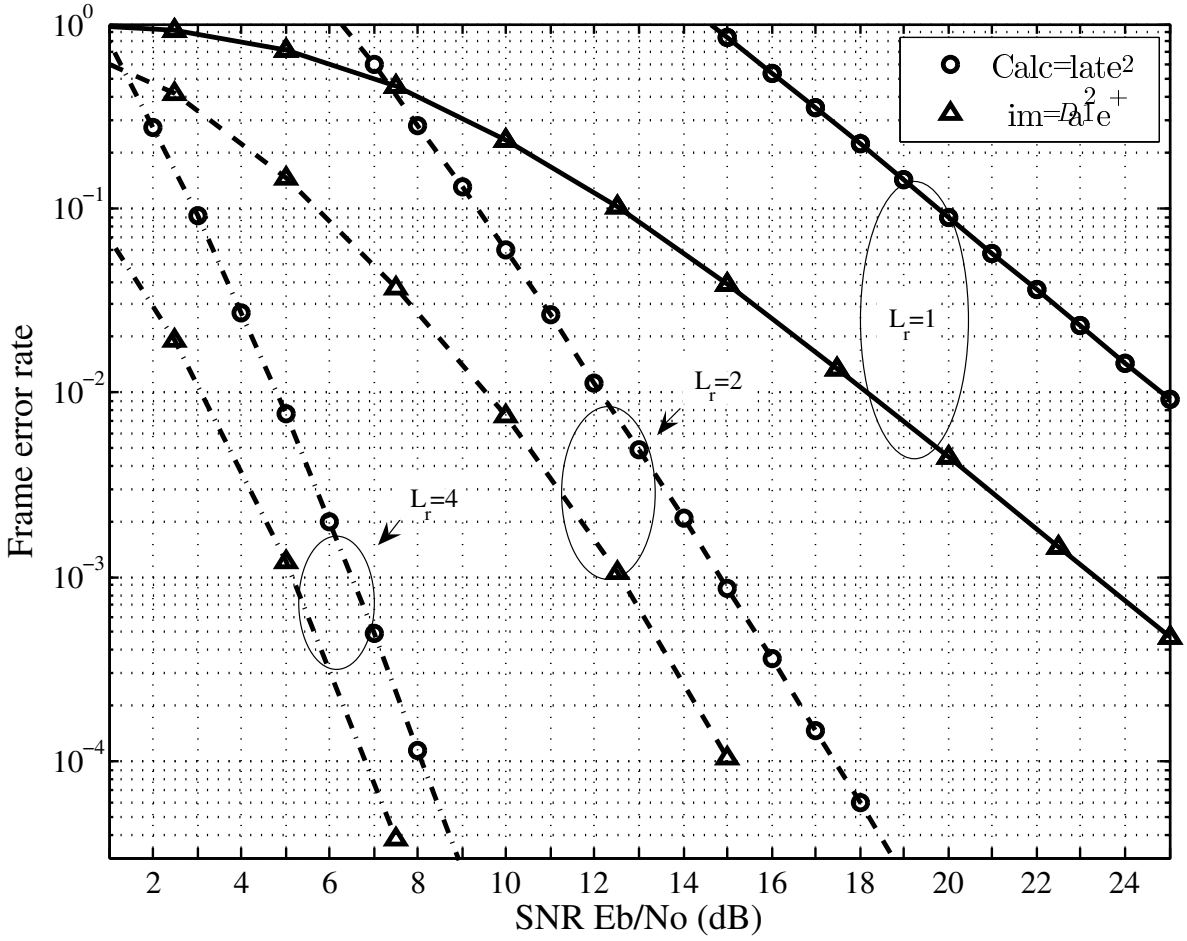

Figure 5.3: Approximate upper (2 dB) frame error rate performance bounds and simulated frame error rate performance of $\boldsymbol{G}(D) = \begin{bmatrix} 1 & \frac{2+D}{1+2D} \end{bmatrix}$ with 4-CPFSK and $L_t = 2$.

looser than the corresponding bit error rate approximation that is shown in Figure 5.2. This divergent behaviour is predicted in [6].

We have also calculated approximate frame error rate bounds for the system with the space-time code $\boldsymbol{G}(D) = \begin{bmatrix} 1 & \frac{2+D}{1+2D} \end{bmatrix}$ with 4-CPFSK, $L_t = 2$ and 1, 2 and 4 receive antennas, using all 1000 evaluated distance spectrum terms (represented by Table 5.1) and Equation (5.38). Similar to the changes in the calculated bit error rate curves, the 3 dB approximations for the frame error rate are looser than the 2 dB approximations. The 3 dB frame error rate approximation for the system with 4 receive antennas is very close to the 2 dB frame error rate approximation that is shown in Figure 5.3. While the 3 dB frame error rate approximation for the system with 1 receive antenna is more than 1 dB looser than the corresponding 2 dB frame error rate approximation.

Other bounds on the PEP may be incorporated in the union bound to obtain error rate

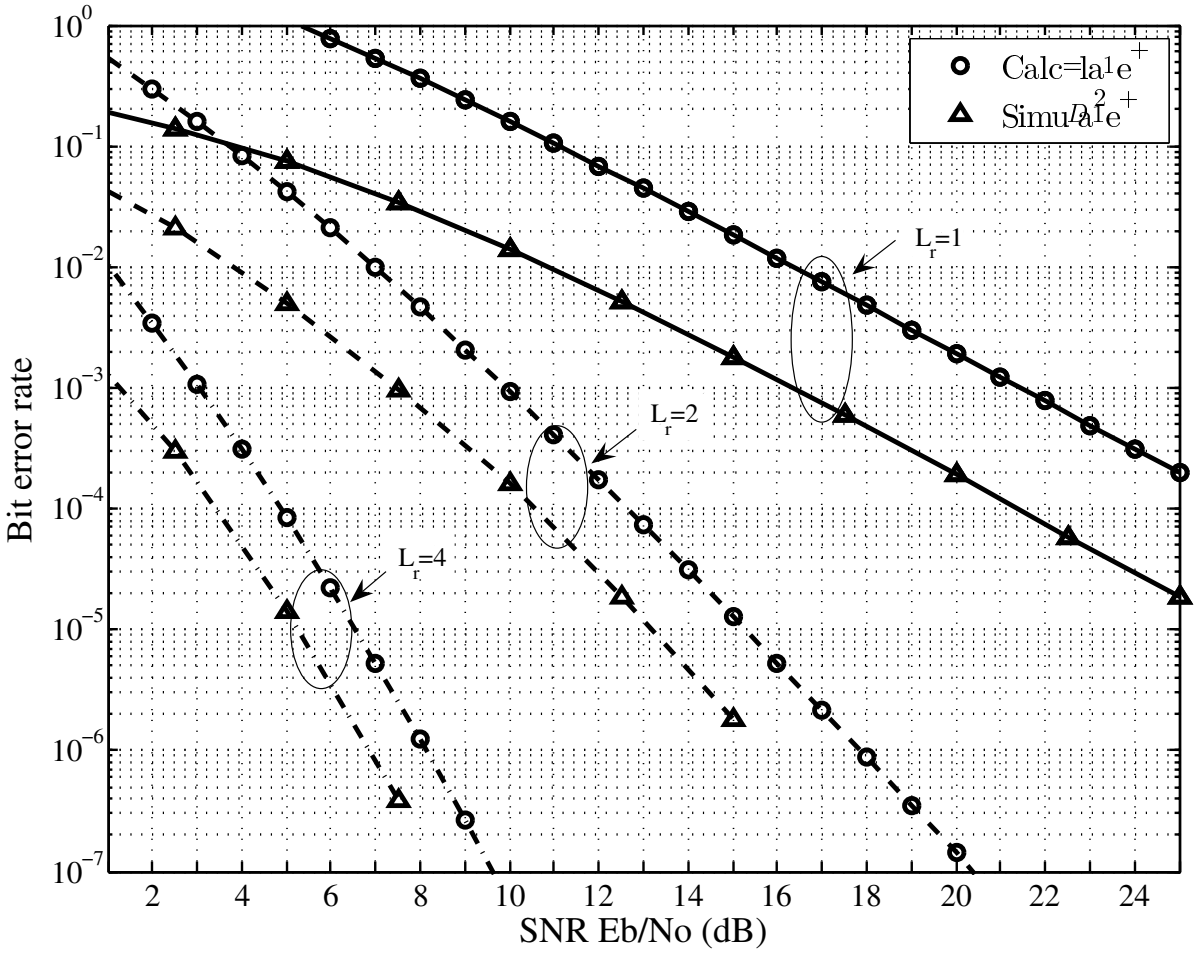

Figure 5.4: Approximate upper (3 dB) bit error rate performance bounds and simulated bit error rate performance of $\boldsymbol{G}(D) = \begin{bmatrix} 1 & \frac{2+D}{1+2D} \end{bmatrix}$ with 4-CPFSK and $L_t = 2$.

performance bounds. A PEP bound derived in [33], for linearly modulated space-time codes, is claimed to be the tightest bound for the PEP based on the product distance. This bound is derived in Appendix E and is given by

$$P(\boldsymbol{X} \to \hat{\boldsymbol{X}}) \leq \left(P\left[\frac{E_s}{4N_0} \left(\Lambda^P\right)^{\frac{1}{\rho}} \right] \right)^{\rho L_r} \sum_{i=0}^{\rho L_r - 1} \begin{pmatrix} \rho L_r - 1 + i \\ i \end{pmatrix} \left(1 - P\left[\frac{E_s}{4N_0} \left(\Lambda^P\right)^{\frac{1}{\rho}} \right] \right)^i, \tag{5.55}$$

where

$$P\left[x\right] = \frac{1}{2}\left(1 - \sqrt{\frac{x}{1+x}}\right), \quad x \geq 0. \tag{5.56}$$

We have shown that the pairwise error probability analysis of linearly modulated space-time codes may be applied to STC-CPM, if the correct distance matrix is considered. Replacing the PEP bound of Equation (5.1) with the PEP of Equation (5.55) in Equation (5.41) we obtain the

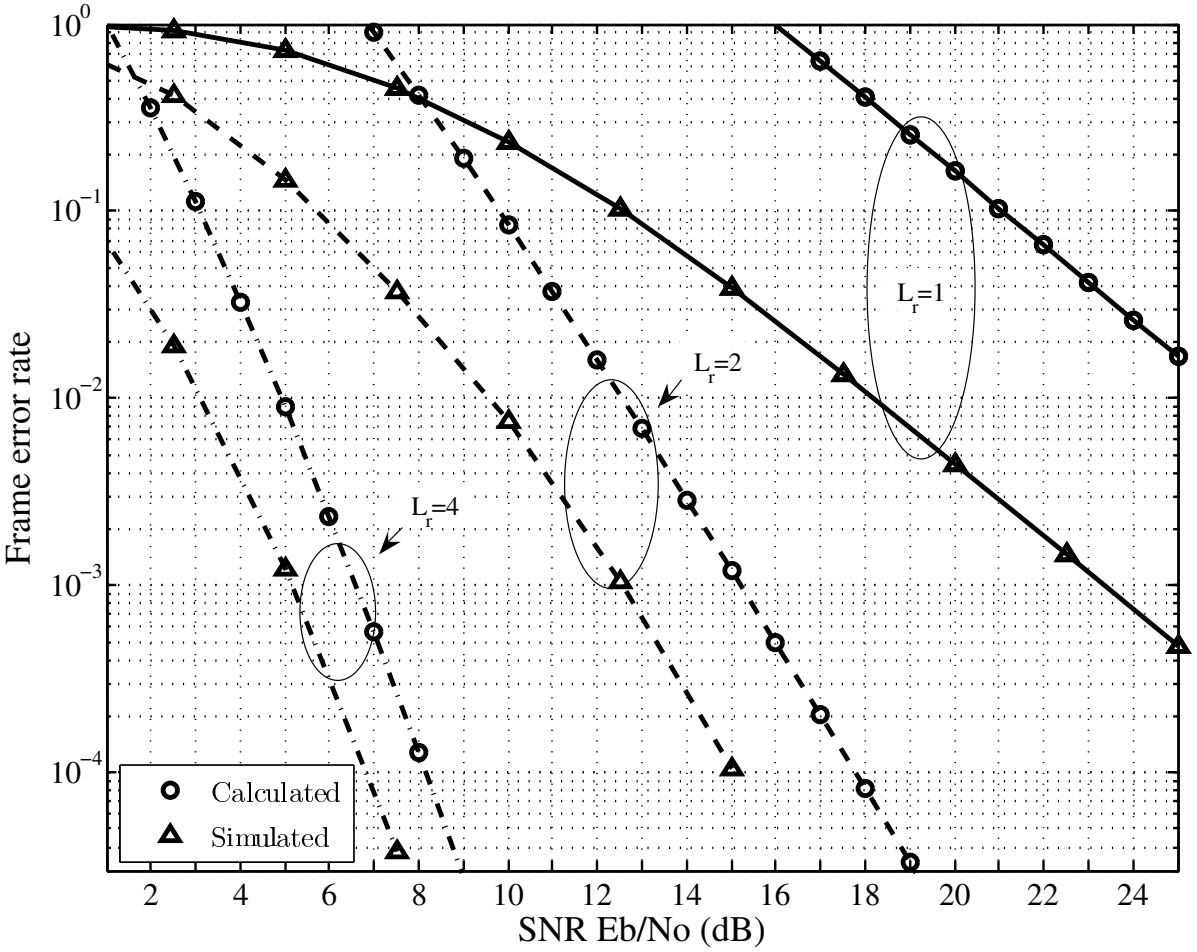

Figure 5.5: Approximate upper (3 dB) frame error rate performance bounds and simulated frame error rate performance of $\boldsymbol{G}(D) = \begin{bmatrix} 1 & \frac{2+D}{1+2D} \end{bmatrix}$ with 4-CPFSK and $L_t = 2$.

generic equation to calculate the error rate performance, using the PEP bound given in [33] as

$$P_E \leq \sum_{\Lambda^E} \sum_{\Lambda^P} \sum_{\rho} C_E(\Lambda^E, \Lambda^P, \rho) \left(P\left[\frac{E_s}{4N_0} \left(\Lambda^P\right)^{\frac{1}{\rho}} \right] \right)^{\rho L_r} \sum_{i=0}^{\rho L_r - 1} \begin{pmatrix} \rho L_r - 1 + i \\ i \end{pmatrix} \left(1 - P\left[\frac{E_s}{4N_0} \left(\Lambda^P\right)^{\frac{1}{\rho}} \right] \right)^{i}, \tag{5.57}$$

where the error coefficient $C_E(\Lambda^E, \Lambda^P, \rho)$ is equal to $C_B(\Lambda^E, \Lambda^P, \rho)$ of Equation (5.31), $C_S(\Lambda^E, \Lambda^P, \rho)$ of Equation (5.36) and $C_F(\Lambda^E, \Lambda^P, \rho)$ of Equation (5.39), for the bit, symbol and frame error probabilities, respectively. We illustrate in the following discussion that the truncated bounds calculated with Equation (5.57) are significantly tighter than the truncated bounds calculated using Equation (5.41).

The parameters in Table 5.1 are calculated using the signal distance matrix of the STC-CPM system with $\boldsymbol{G}(D) = \begin{bmatrix} 1 & \frac{2+D}{1+2D} \end{bmatrix}$. Therefore, the union bound of Equation (5.57) may

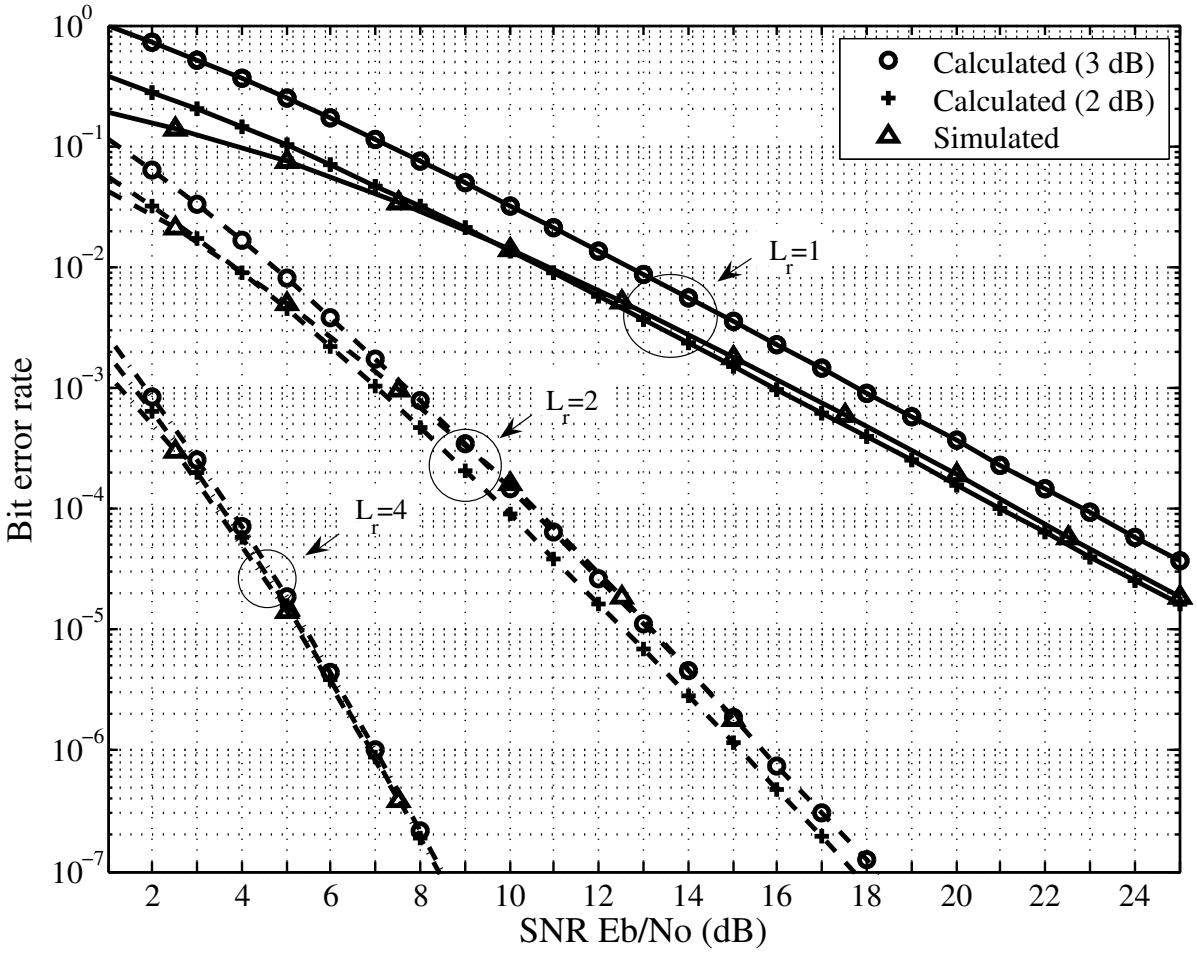

Figure 5.6: Approximate upper bit error rate performance bounds and simulated bit error rate performance of $\boldsymbol{G}(D) = \begin{bmatrix} 1 & \frac{2+D}{1+2D} \end{bmatrix}$ with 4-CPFSK and $L_t = 2$. The bounds incorporate the PEP bound proposed in [33].

be truncated to evaluate approximate bounds on the performance of this STC-CPM using the distance spectrum terms of Table 5.1. Truncated bit error rate bounds calculated using Equation (5.57) for $\boldsymbol{G}(D) = \begin{bmatrix} 1 & \frac{2+D}{1+2D} \end{bmatrix}$ with 4-CPFSK, $L_t = 2$ and 1, 2 and 4 receive antennas are shown in Figure 5.6. The 2 dB and 3 dB approximations are calculated using the distance spectrum terms as discussed in the previous examples.

The 2 dB approximations for the system with 1 and 2 receive antennas, are below the simulated performance curves. This may be because the distance spectrum terms are chosen such that the trace is below a certain threshold and therefore some terms with low product distance are not used to calculate the approximations. Hence, the approximations are slightly optimistic at high SNR. The 3 dB approximations calculated with Equation (5.57) (and all

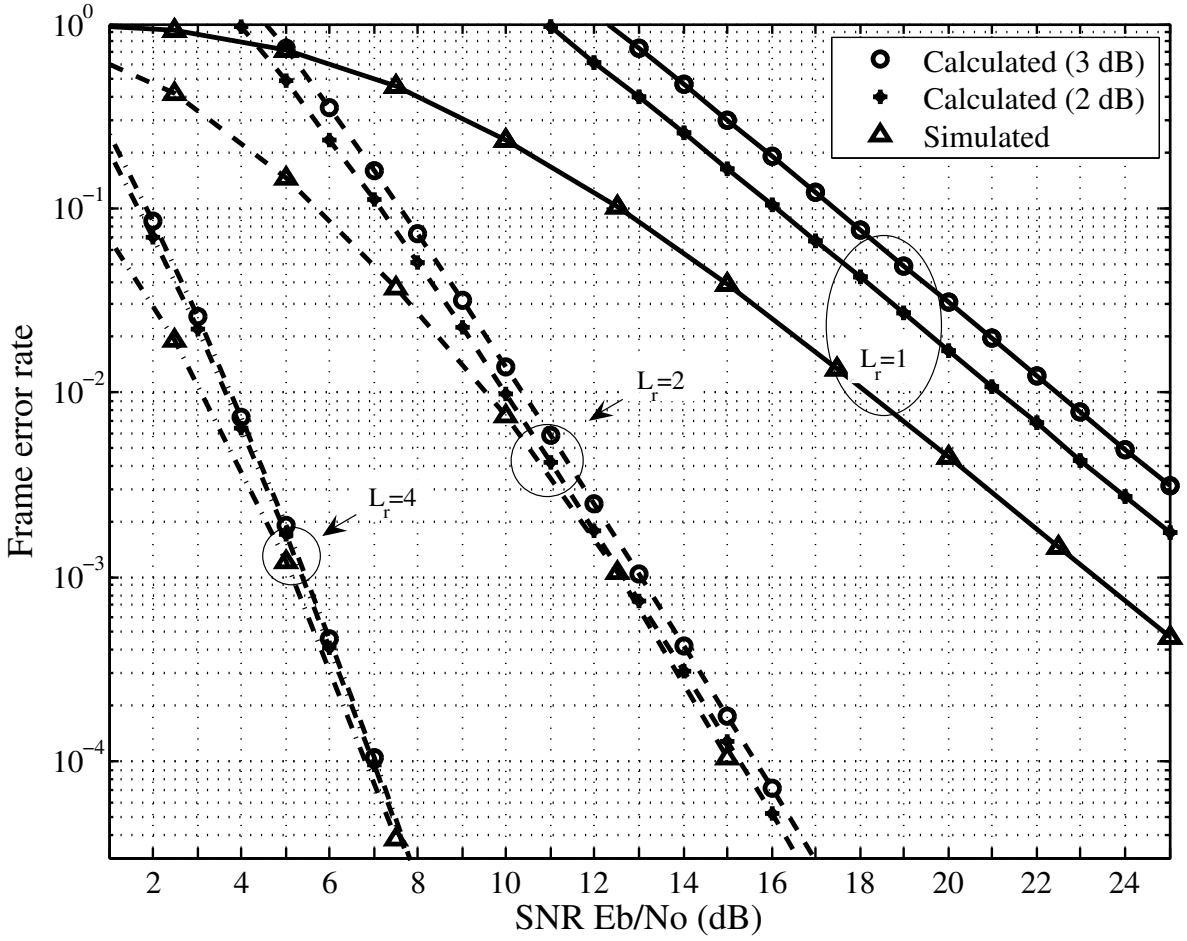

Figure 5.7: Approximate upper frame error rate performance bounds and simulated frame error rate performance of $\boldsymbol{G}(D) = \begin{bmatrix} 1 & \frac{2+D}{1+2D} \end{bmatrix}$ with 4-CPFSK and $L_t = 2$. The bounds incorporate the PEP bound proposed in [33].

1000 distance spectrum terms evaluated) are significantly tighter than the 3 dB approximations calculated using Equation (5.41) (see Figure 5.4). At a bit error rate of 10^{-3} the 3 dB approximation for the system with 1 receive antenna in Figure 5.6, is approximately 3.5 dB closer to the simulated performance than corresponding 3 dB approximation in Figure 5.4. The 3 dB approximations shown in Figure 5.6 for the system with 2 and 4 receive antennas converge to the simulated performance at low BER.

Similar behaviour is observed for the frame error rate approximations shown in Figure 5.7. The approximations calculated with Equation (5.57) are significantly tighter than the approximations shown in Figures 5.3 and 5.5. None of the frame error rate approximations are lower than the simulated performance curves.

ρ	$\mathbf{\Lambda^E}$	$\mathbf{\Lambda^P}$	$\mathbf{C_B}(\mathbf{\Lambda^E}, \mathbf{\Lambda^P}, \rho)$	$\mathbf{C_S}(\mathbf{\Lambda^E}, \mathbf{\Lambda^P}, \rho)$	$\mathbf{C_F}(\mathbf{\Lambda^E}, \mathbf{\Lambda^P}, \rho)$
1	8.000	8.000	0.50000	1.00000	130.0000
1	16.000	16.000	0.50000	1.00000	65.0000
1	24.000	24.000	0.37500	0.75000	32.5000
1	32.000	32.000	0.25000	0.50000	16.2500
1	40.000	40.000	0.15625	0.31250	8.1250
2	5.756	5.483	0.37500	0.56250	48.7500
2	5.756	5.922	0.25000	0.37500	32.5000
2	7.454	5.739	0.75000	1.12500	97.5000
2	7.454	6.692	0.62500	0.93750	81.2500
2	7.454	11.528	0.12500	0.18750	16.2500
2	8.483	12.552	0.16406	0.23438	12.1875
⋮	⋮	⋮	⋮	⋮	⋮
2	24.546	39.925	1.50000	2.62500	97.5000

Table 5.2: Partial distance spectrum for STC $\boldsymbol{G}(D) = \left[1 \;\; \frac{1}{1+2D}\right]$ with 4-CPFSK and two transmit antennas (286 terms).

5.4.2 $\rho_{\min} = 1$ Space-Time Code

We now consider the system with the space-time code $\boldsymbol{G}(D) = \left[1 \;\; \frac{1}{1+2D}\right]$, 4-CPFSK and two transmit antennas, which has $\rho_{\min} = 1$. This STC is optimal in terms of the trace criterion for $S_J = 8$ (see Table 4.2). The system has a normalized minimum squared Euclidean distance of $d^2_{\min} = 2.878$. Delay diversity with $L_t = 2$ ($\boldsymbol{G}(D) = [1 \;\; D]$) and 4-CPFSK has twice the number of states as the system with $\boldsymbol{G}(D) = \left[1 \;\; \frac{1}{1+2D}\right]$. The space-time coded system with $\boldsymbol{G}(D) = \left[1 \;\; \frac{1}{1+2D}\right]$, has superior frame error rate performance compared to delay diversity, in schemes with 2 and 4 receive antennas, below SNR $= 10$ dB. The two systems have similar frame error rate performance with 1 receive antenna, at SNR less than 8 dB.

Due to the space-time coded system with $\boldsymbol{G}(D) = \left[1 \;\; \frac{1}{1+2D}\right]$ not having full spatial diversity, we limited the search for distance spectrum terms to 500 trellis intervals. We set a threshold of $\Lambda^P_{\max} = 40$ and searched for 1000 distance spectrum terms, minimizing Λ^E. During the coefficient search, we did not discard the distance spectrum terms of incomplete error

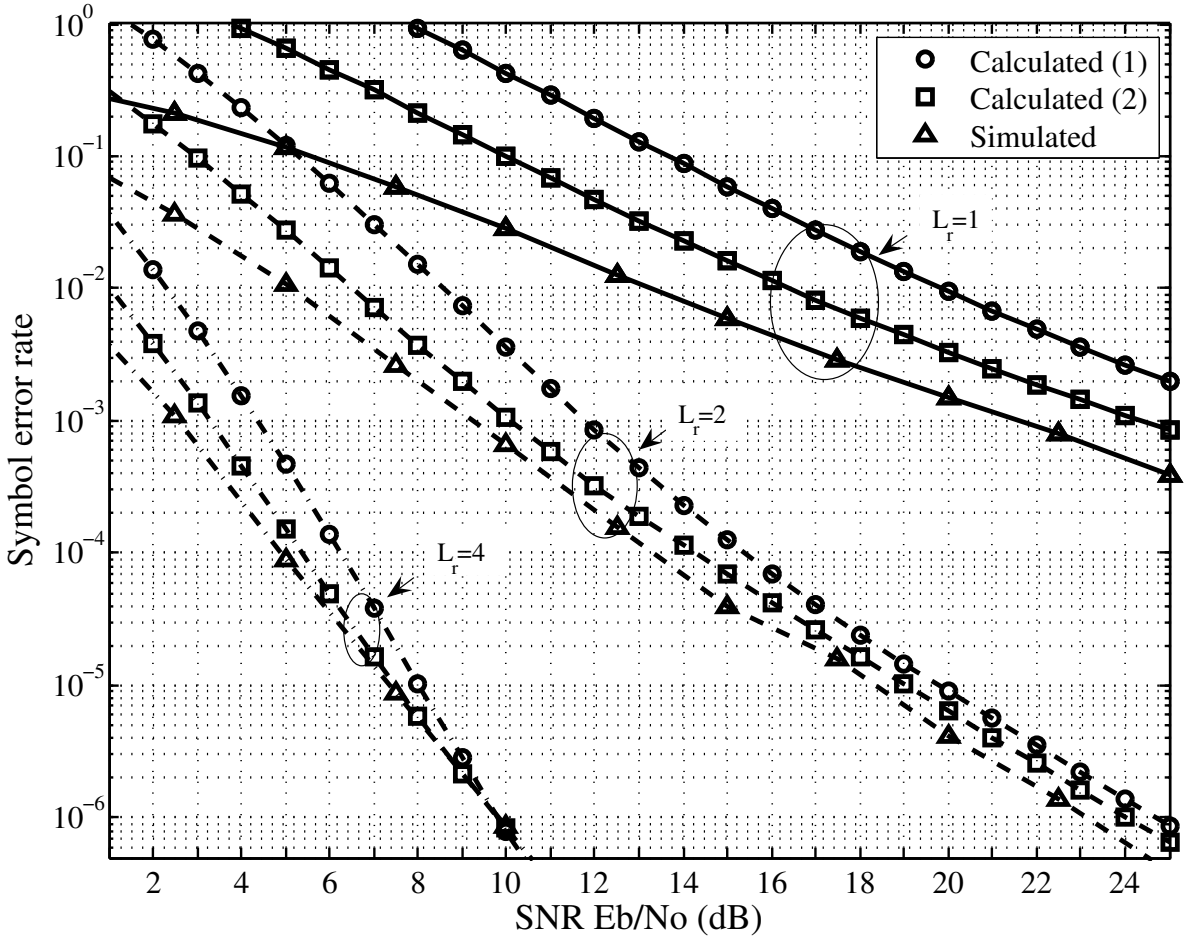

Figure 5.8: Approximate upper symbol error rate performance bounds and simulated symbol error rate performance of $\boldsymbol{G}(D) = \begin{bmatrix} 1 & \frac{1}{1+2D} \end{bmatrix}$ with 4-CPFSK and $L_t = 2$.

events that were not full rank, even if $\Lambda^P(m)$ was greater than $\Lambda^P_{\max}$.

The search for distance spectrum terms did not converge within 500 trellis intervals. This was expected because the system does not have full spatial diversity. However, the search was terminated after 500 trellis intervals in any case. We found that 286 distance spectrum terms for $\boldsymbol{G}(D) = \begin{bmatrix} 1 & \frac{1}{1+2D} \end{bmatrix}$, with $\zeta \leq 500$, have $\Lambda^P \leq 40$. We note that rank-1 error events only occurred for $\Lambda^E = \Lambda^P = \{8, 16, 24, \ldots\}$. Therefore, we assume that the product distance of the rank-1 error events that did not converge within 500 intervals, would be greater than the threshold set. That is, we assume that all error events with $\Lambda^P \leq 40$ were found. Table 5.2 displays a partial list of the 286 distance spectrum terms and their coefficients. The rank-1 error events are displayed first. The results are then sorted in ascending order, by Λ^E and then by Λ^P.

In Figure 5.8, we plot calculated truncated symbol error rate performance bounds for the

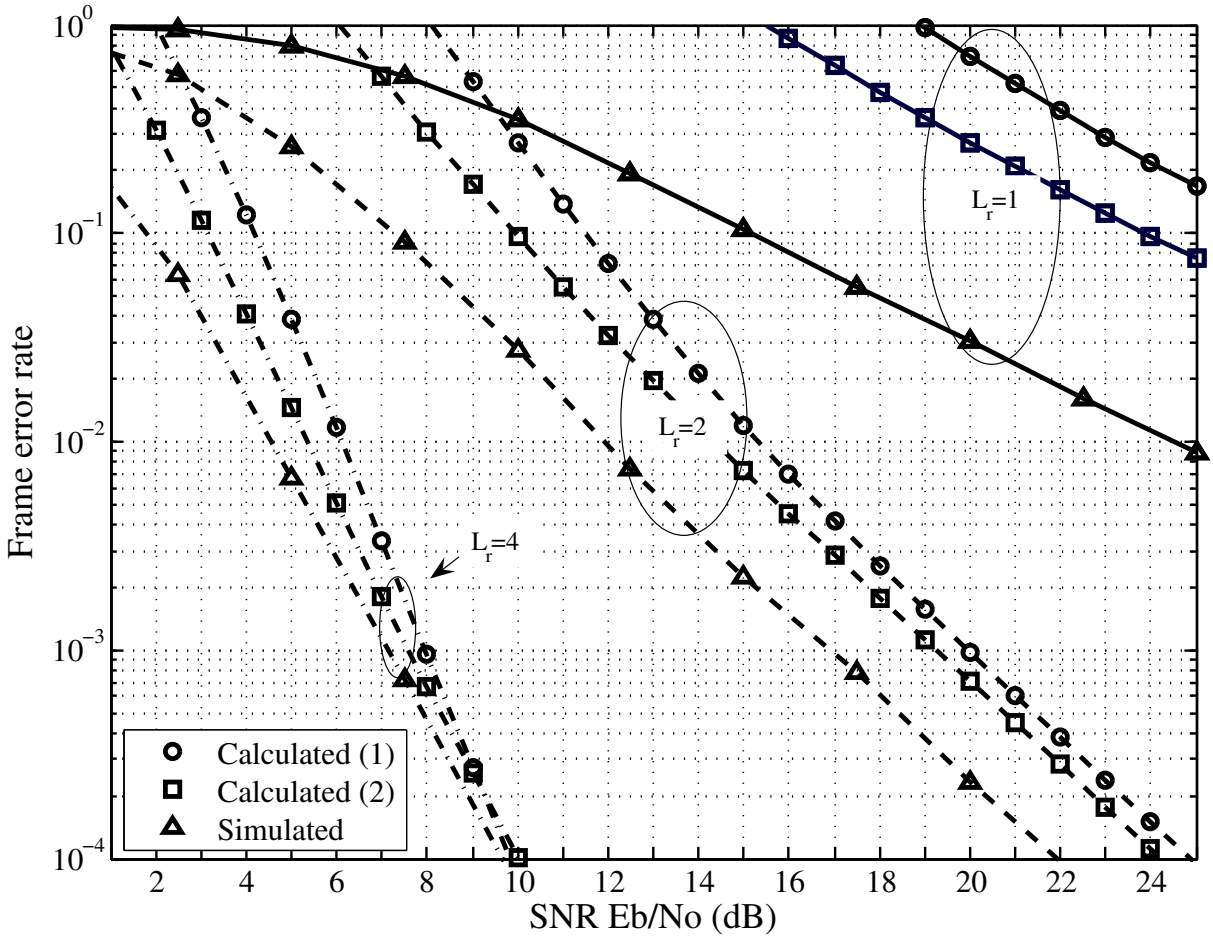

Figure 5.9: Approximate upper frame error rate performance bounds and simulated frame error rate performance of $\boldsymbol{G}(D) = \begin{bmatrix} 1 & \frac{1}{1+2D} \end{bmatrix}$ with 4-CPFSK and $L_t = 2$.

space-time code $\boldsymbol{G}(D) = \begin{bmatrix} 1 & \frac{1}{1+2D} \end{bmatrix}$, with 4-CPFSK and two transmit antennas. The truncated bounds are calculated using the 286 distance spectrum terms represented by Table 5.2. The truncated bounds labelled, *Calculated (1)*, are evaluated using Equation (5.41), and the truncated bounds labelled, *Calculated (2)*, are evaluated using Equation (5.57). We illustrate the truncated performance bounds of the system with 1, 2 and 4 receive antennas. We present the corresponding simulated results on the same plot. The truncated symbol error rate bounds become tighter, as the number of receive antennas is increased. The bounds correctly predict the curvature of the simulated performance results, at lower symbol error rates. The truncated symbol error rate bounds evaluated using Equation (5.57) are tighter than the truncated symbol error rate bounds evaluated using Equation (5.41). The two truncated bounds for the system with 4 receive antennas converge to the simulated performance at low SER.

Truncated frame error rate performance bounds calculated for the system with the space-time code $\boldsymbol{G}(D) = \begin{bmatrix} 1 & \frac{1}{1+2D} \end{bmatrix}$, 4-CPFSK and 2 transmit antennas are shown in Figure 5.9. The simulated frame error rate performance is also shown. The truncated bounds and the simulated performance curves are shown with 1, 2 and 4 receive antennas. The truncated bounds are calculated using the 286 distance spectrum terms represented by Table 5.2. The truncated bounds labelled, *Calculated (1)*, are evaluated using Equation (5.41) and the truncated bounds labelled, *Calculated (2)*, are evaluated using Equation (5.57). As we observed for the full rank space-time code, the calculated truncated frame error rate performance bounds provide upper bounds that are fairly loose, especially for $L_r = 1$. We may improve the tightness of the approximate bounds by reducing the number of distance spectrum terms used to evaluate them.

5.4.3 STC-CPM Comparison using Truncated Performance Bounds

We compare calculated approximate bit error rate performance bounds for the two optimum rate-$\frac{1}{2}$ STC for 4-CPFSK with $S_J = 16$ and 2 transmit antennas. As discussed in Chapter 4, the space-time coded system with $\boldsymbol{G}(D) = \begin{bmatrix} 1 & \frac{2+D}{1+2D} \end{bmatrix}$ has $\Lambda^P_{\min} = 6.976$ and the space-time coded system with $\boldsymbol{G}(D) = \begin{bmatrix} 1 & \frac{2+3D}{1+2D} \end{bmatrix}$ has $\Lambda^P_{\min} = 7.694$. The simulated performance of these two codes was shown to be almost identical in all cases in Figure 4.3. Similarly their approximate performance bounds, shown in Figure 5.10, are almost identical. Both truncated bounds are calculated with 1000 distance spectrum terms with $\Lambda^E \leq 16$ and Equation (5.57).

In Figure 5.11 we show approximate bounds and simulated performance of the space-time codes $\boldsymbol{G}(D) = \begin{bmatrix} 1 & \frac{1+3D+D^2}{1+D+D^2} \end{bmatrix}$ and $\boldsymbol{G}(D) = \begin{bmatrix} 1 & \frac{2+D}{1+2D} \end{bmatrix}$ with 4-CPFSK with two transmit antennas. As discussed in Chapter 4, both schemes have a minimum squared Euclidean distance of 4.000. However, the system with $\boldsymbol{G}(D) = \begin{bmatrix} 1 & \frac{1+3D+D^2}{1+D+D^2} \end{bmatrix}$ has $\rho_{\min} = 1$ and the system with $\boldsymbol{G}(D) = \begin{bmatrix} 1 & \frac{2+D}{1+2D} \end{bmatrix}$ has $\rho_{\min} = 2$.

The approximate bit error rate bounds correctly predict the relative performance of the two space-time codes. All of the truncated bounds were calculated using Equation (5.57). The truncated bound of the $\rho_{\min} = 1$ system was calculated using all 453 distance spectrum terms found with $\Lambda^P \leq 45$ (this value was selected based on the maximum product distance evaluated for the $\rho_{\min} = 2$ code). The search (initially for 1000 terms) for distance spectrum terms was terminated after 500 trellis intervals. The truncated bounds for the $\rho_{\min} = 1$ system

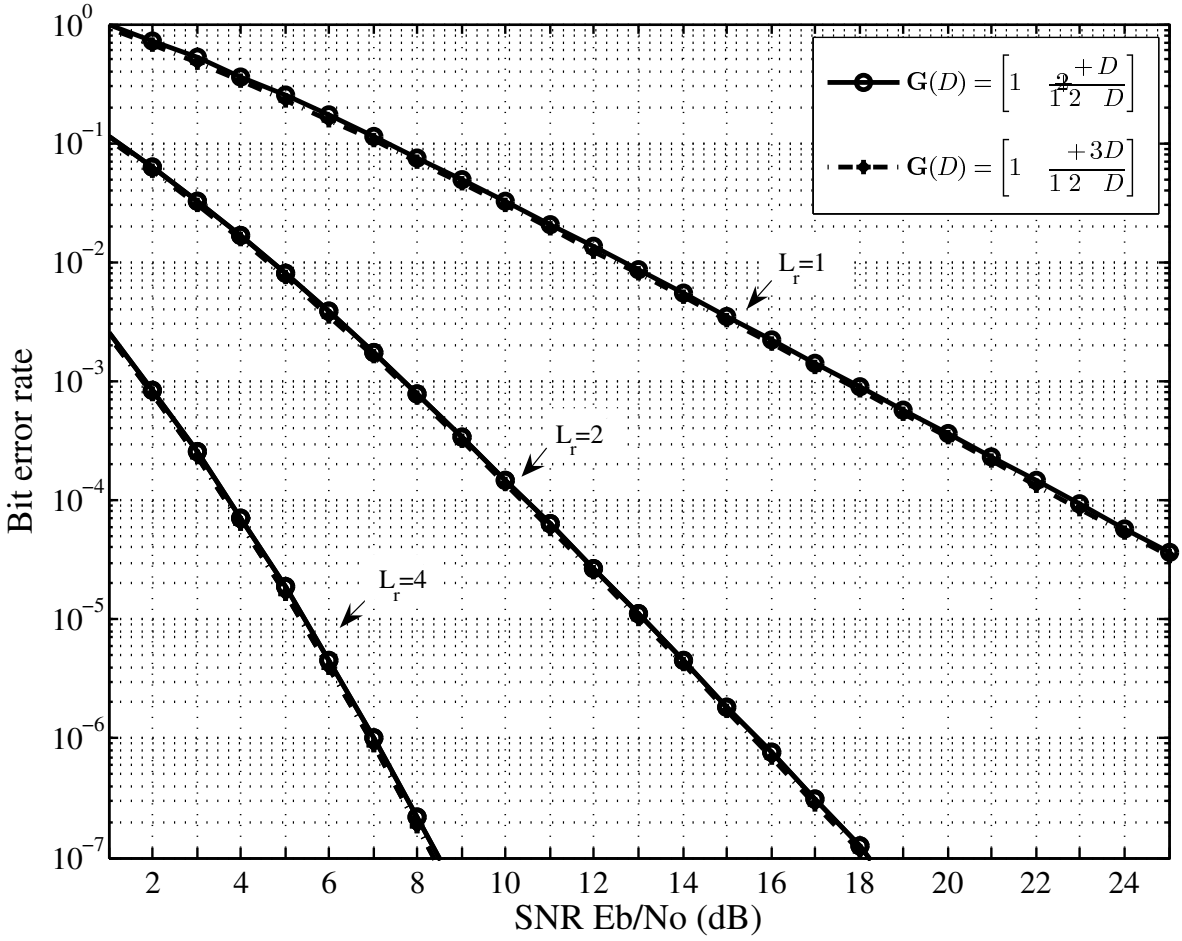

Figure 5.10: Approximate upper bit error rate performance bounds for $\boldsymbol{G}(D) = \begin{bmatrix} 1 & \frac{2+D}{1+2D} \end{bmatrix}$ and $\boldsymbol{G}(D) = \begin{bmatrix} 1 & \frac{2+3D}{1+2D} \end{bmatrix}$ with 4-CPFSK and $L_t = 2$.

are looser than the truncated bounds for the $\rho_{\min} = 2$ system, for the configurations with 1 and 2 receive antennas. This may be due to the greater weight of the distance spectrum terms for the $\rho_{\min} = 1$ system, compared to those for the $\rho_{\min} = 2$ system. We note that all distance spectrum terms with $\Lambda^P \leq 45$ were found for the $\rho_{\min} = 1$ system (assuming no further rank deficient events with $\Lambda^P \leq 45$ would be found after 500 trellis intervals). Whereas, for the $\rho_{\min} = 2$ system Λ^E was required to be less than or equal to 16. Thus, some distance spectrum terms with $\Lambda^P \leq 45$ would not have been evaluated. The truncated performance bounds for schemes with 4 receive antennas tend not to diverge when calculated with an increased number of distance spectrum terms, and therefore, this issue would not significantly affect these truncated bounds. This makes it possible to be confident in predicting the relative performance of STC-CPM systems with $L_r = 4$, using these truncated performance bounds.

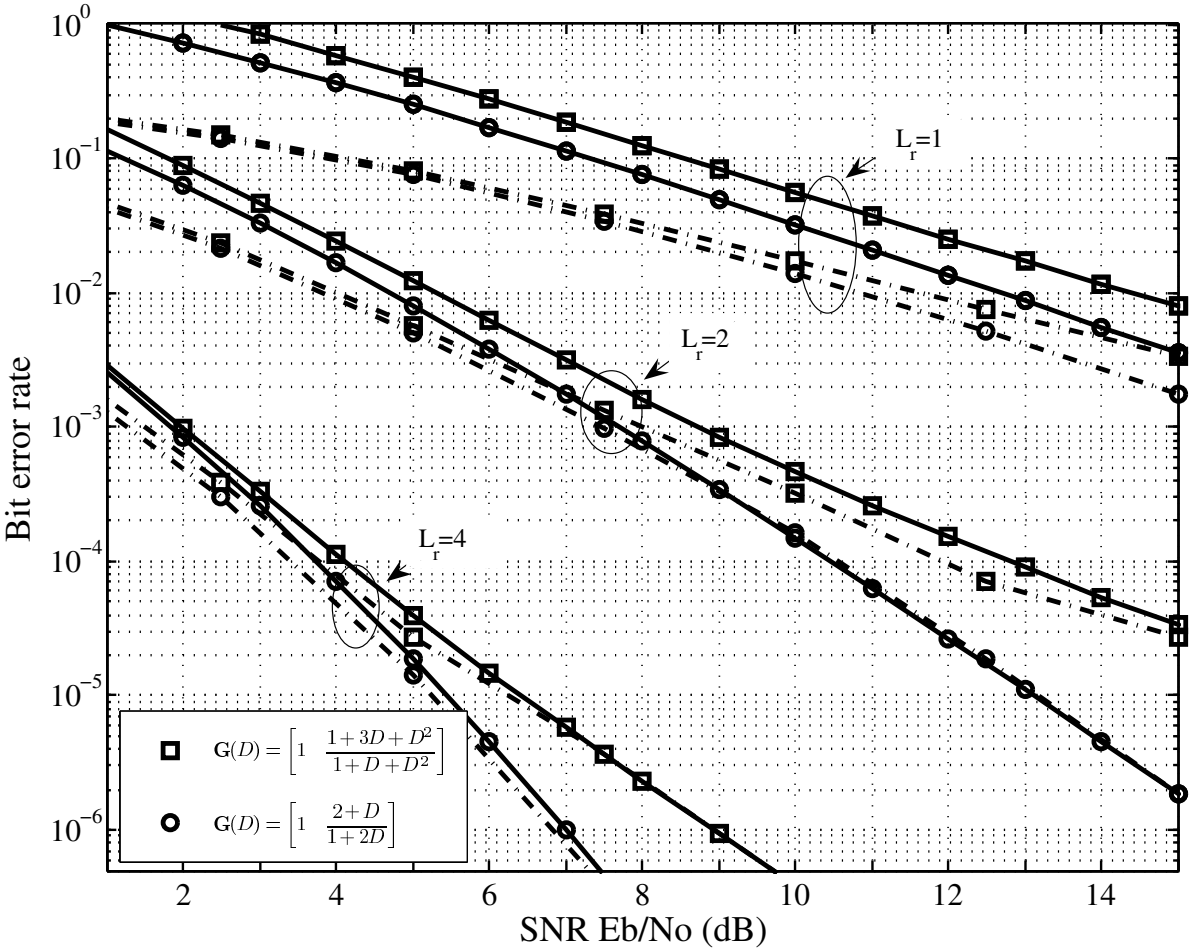

Figure 5.11: Approximate upper bit error rate performance bounds and simulated bit error rate performance of $\boldsymbol{G}(D) = \begin{bmatrix} 1 & \frac{1+3D+D^2}{1+D+D^2} \end{bmatrix}$ and $\boldsymbol{G}(D) = \begin{bmatrix} 1 & \frac{2+D}{1+2D} \end{bmatrix}$ with 4-CPFSK and $L_t = 2$ ($- \cdot -$ Simulated, —— Bound).

5.5 Complexity of Performance Bound Evaluation

To evaluate the truncated performance bounds of both Equation (5.41) and Equation (5.57), the distance spectrum and its error coefficients are required. Once this information is known the truncated bounds are simple to calculate. However, obtaining the information requires a search through a supertrellis which has ${S_J}^2$ states. During the search, at each node in the trellis there is a number of unterminated paths for which information must be retained. Thus, the computational complexity and memory requirements become prohibitively large for systems with a large number of states.

The truncated bound of Equation (5.57) does not require computation of the trace of the signal distance matrices. However, the computational requirements for the truncated bound

of Equation (5.41), which does require this information, is not significantly greater. This is because the signal distance matrices are already calculated in order to obtain their product distances. However, requiring both the product distance and the trace does increase the value of $\varpi_m(\sigma_m, \hat{\sigma}_m)$ for a given number of error events. Because error events with a given product distance may have different trace values, more memory is required to keep separate information on these events. Thus, the truncated bound of Equation (5.57) is superior to the truncated bound of Equation (5.41) in both terms of computational complexity and accuracy.

The time taken to calculate the distance spectrum terms precludes the use of the truncated performance bound as a method to comprehensively search for optimum space-time coded CPM systems. However, the computational time is significantly less than required to simulate a system's performance using the Monte Carlo method. Therefore, the truncated bounds are suited to predicting the performance of a space-time coded CPM system that has been identified using the minimum Euclidean distance criterion, as described in Chapter 4.

5.6 Summary

In this chapter, we have derived performance bounds for STC-CPM systems, based on the PEP derived in Chapter 4, using the union bound technique. We have also formed performance bounds based on the PEP bound derived in [33]. We have evaluated truncated performance bounds of various full rank and rank deficient space-time coded systems. We have found that the truncated bounds follow the curves of the simulated performance at lower error rates. In some cases, the bounds converge to the simulated error rate curves. The truncated bounds tend to be loose for systems with one receive antenna. In practice, we have found that using a smaller number of distance spectrum terms to calculate a bound approximation, leads to a tighter approximate bound. The improvement is more noticeable for the schemes with fewer receive antennas. However, if too few terms are used to evaluate a truncated bound, it can be slightly optimistic. The truncated performance bounds evaluated using the PEP bound derived in [33] were tighter than the truncated bounds calculated using the Chernoff bound on the PEP.

The truncated bounds on the bit error rate and the symbol error rate curves were found to have similar characteristics. They were tighter than the truncated bounds on the frame error rate performance. It has been predicted that using a union bound to estimate a system's performance is not feasible, because the bounds will diverge [6]. It appears that this is the case

for the schemes with one receive antenna. However, for the schemes with $L_r = 4$, there was not a significant change in the truncated bounds when the number of distance spectrum terms used to calculate the approximations was increased to include those that have a minimum squared Euclidean distance of 2 dB to 3 dB greater than the minimum squared Euclidean distance.

Chapter 6

Conclusion

In this thesis, we have developed a STC-CPM model that allows the space-time encoder and the continuous phase encoders, to be simply combined, into a single trellis encoder defined on a ring of integers. The approach of defining all code structures over the same rings, leads to minimization of the total number of states through state combining. The model makes it straightforward to calculate distance measures, which are important for code design and performance analysis. The trellis of the overall encoder is used in decoding with the Viterbi algorithm. The STC-CPM structure designed can be used as the inner code of an interleaved, iteratively decoded system.

Design criteria for STC-CPM, based on applying results for linearly modulated STC to STC-CPM, were derived. The criteria are analogous to the linear STC criteria, if the signal distance matrix introduced by Zhang and Fitz [11] is considered, in place of the codeword distance matrix. Previous work on space-time coded CPM had explicitly shown that the rank and product distance criteria may be used as design criteria. We have shown that the minimum squared Euclidean distance is a valid criterion for $\rho_{\min} L_r > 3$. We demonstrated that the squared Euclidean distance criterion is valid for a large number of systems. By first maximizing the minimum squared Euclidean distance, and then finding those amongst these systems with the best rank, well performing systems, for any number of receive antennas are identified.

We implemented a code search to find optimal space-time codes for STC CPFSK systems. We searched over systematic ring convolutional encoders. The space-time codes are optimized

for minimum squared Euclidean distance. These codes were then surveyed for spatial diversity. Significant coding gains are achieved using the space-time codes identified instead of delay diversity, for no increase in complexity.

The STC-CPM design allows high data rate systems. We searched for optimal systems with rate-$\frac{2}{3}$ space-time codes, which provide a system throughput of $2\log_2(M)$ bits/symbol period with M-CPFSK and $L_t = 3$. We presented simulation results for STC CPFSK systems with a system throughput of 4 bits/symbol period. They consist of a rate-$\frac{2}{3}$ space-time code with 4-CPFSK and transmit over three antennas. Although the systems presented with rate-$\frac{2}{3}$ space-time codes and 4-CPFSK only had transmit diversity equal to 1, the performance curves of one of these systems with a 128 state overall trellis have the same slopes as a $\rho_{\min} = 2$ system's performance curves at BER $> 10^{-4}$. Thus, at these bit error rates the system is indistinguishable from a $\rho_{\min} = 2$ system and has excellent coding gain due to its high minimum squared Euclidean distance.

We have developed performance bounds using the union bound based on the pairwise error probability. Truncated approximations of the bounds were evaluated for various full rank and rank deficient space-time coded systems. The truncated bounds calculated using the PEP based on the Chernoff bound predicted the shape of the simulated curves at low error rates. However, they tended to be offset from the simulated curves. Approximate performance bounds incorporating the PEP bound developed in [33] were also calculated. These were tighter than the approximate performance bounds formed using the Chernoff bound on the PEP and in many cases converged to the simulated performance at low error rates. For systems with a small number of receive antennas, the bounds significantly diverge as the number of distance spectrum terms used to evaluate them is increased. Due to the less divergent behaviour of the performance bounds with larger L_r, they provide an accurate measure of the relative performance of STC-CPM systems.

6.1 Future work

In this section we discuss possible areas of research that could be further pursued, based on the STC-CPM system we have developed.

- We have assumed a quasi-static Rayleigh flat fading channel, the work should be extended to investigate the effects of different fading environments.

- The integrated design could be extended to incorporate differential decoding. I have briefly investigated such a model. However, in order to decode, the receiver requires channel state information. This is due to cross signal terms that are received. Channel estimation is not desirable in a non-coherent scheme, where a simplified receiver is implemented. Therefore, either orthogonal or unitary code designs should be considered. A multi-antenna structure that achieves orthogonality by only transmitting from one antenna at a time, has been proposed in [24]. This scheme suffers from poor information rates.

- If the requirement for channel estimation is unavoidable for differential systems with good information rates, then training for channel estimates in a coherent receiver or estimator-correlator in a non-coherent receiver should be investigated. That is, find the channel and then use it as an estimate in succeeding intervals.

- The higher rate space-time coded systems require more trellis states. The trellises of the systems with large modulation alphabets also have greater complexity due to the number of transitions from each state. Hence, further reducing decoder/demodulator complexity through existing or new algorithms is of interest.

- We have alluded to the fact that the STC-CPM design we have developed could be used in a turbo or iterative decoding structure. An investigation into the performance and design of STC-CPM in a turbo structure would be of interest.

Appendix A

Simulation Procedure

The simulations in this thesis are implemented using the Monte Carlo simulation method. Information on the simulation of communications systems using the Monte Carlo method is presented in [78]. A generic Monte Carlo simulator is illustrated in Figure A.1. The total number of errors divided by the total number of trials, forms a simulated performance point.

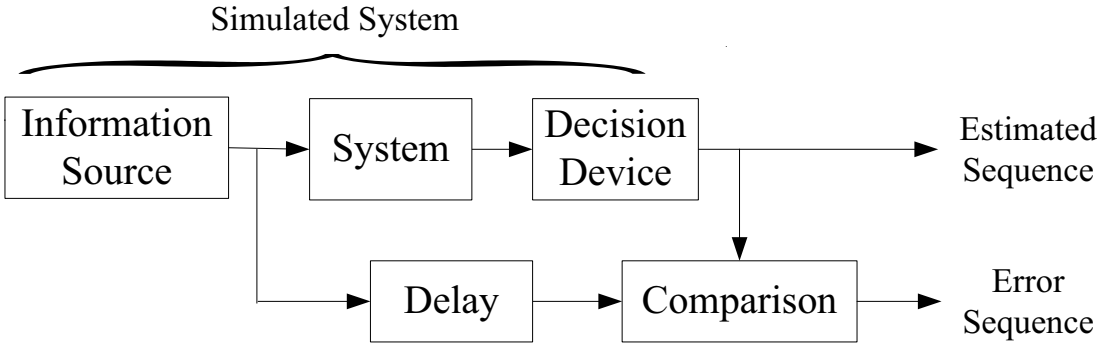

Figure A.1: Model of Monte Carlo simulator.

For simplicity, we have restricted the simulations to use the modulation continuous phase frequency shift keying (CPFSK); a full response CPM with a rectangular frequency pulse. Simulations were run using a data frame length of 130 symbols. To calculate each simulated point, a minimum of 100 frame errors and a minimum of 50 000 frames were simulated. To calculate the bit error rates natural mapping was used to map the symbols to bits.

For the simulations in this thesis, M-ary data symbols are generated and then encoded by a space-time encoder. The encoded symbols are then used generate L_t sampled CPM signals,

using the scrambled (feedback-free) continuous phase encoders. We use $n_s = 16$ samples per channel symbol interval. The fading is assumed to be quasi-static Rayleigh flat fading, such that the $L_t L_r$ fading gains are constant during a frame, but vary from frame to frame. The random fading gain between each transmit and receive antenna during a frame is modelled as an independent complex Gaussian random variable with zero mean and a variance of $\frac{1}{2}$ per dimension.

Each receive antenna receives a faded superposition of the L_t simultaneously transmitted signals corrupted by additive white Gaussian noise (AWGN). The AWGN at each receive antenna is modelled as independent samples of a zero-mean complex Gaussian random process, with power spectral density N_0. The variance of the noise or noise power is given by

$$\sigma_n^2 = N_0 f_w, \tag{A.1}$$

where f_w is the bandwidth of the noise. We let

$$f_w = \frac{n_s}{T}, \tag{A.2}$$

where T is the channel symbol interval.

The power of the signal received at each antenna is denoted P_t and is defined by Equation (3.4). The signal to noise ratio (SNR) at each receiver is given by

$$\begin{aligned} SNR &= \frac{P_t}{\sigma_n^2} \\ &= \frac{L_t \left[\left(\sqrt{\frac{2E_s}{TL_t}} \right)^2 /2 \right]}{\sigma_n^2} \\ &= \frac{\frac{E_s}{T}}{\sigma_n^2}, \end{aligned} \tag{A.3}$$

where $E_s = L_t \frac{k}{l} \log_2(M) E_b$ is the symbol energy and E_b is the energy per bit, $\frac{k}{l}$ is the STC code rate and M is the modulation alphabet size. We let the power, $P_t = \frac{E_s}{T}$, be normalized to 1, and then using Equations (A.1) to (A.3), we may write the noise variance as

$$\begin{aligned} \frac{\sigma_n^2}{1} &= \frac{N_0 f_w}{\frac{E_s}{T}} \\ \sigma_n^2 &= \frac{n_s N_0}{E_s} \\ \sigma_n^2 &= \frac{n_s}{L_t \frac{k}{l} \log_2(M) \frac{E_b}{N_0}}. \end{aligned} \tag{A.4}$$

The receiver decodes the signal on the trellis of the combined STC-CPM encoder using the Viterbi algorithm. Perfect channel state information is assumed at the receiver.

Appendix B

Linear Multi-Valued Sequential Coding Networks

Linear multi-valued sequential coding networks are described in [46], we give a brief overview here. The networks have synchronized input and output sequences of non-negative numbers that are less than some value p. The networks' output depends on past and present inputs. They have finite memory, which is stored in delay elements. A single unit delay element is denoted D. When r delay elements are serially connected there is a delay of r time units, this is denoted D^r. The networks have modulo-p adders and multipliers. Because the networks are linear, the multipliers only multiply by a constant.

Such a network can be described using the delay polynomial

$$\boldsymbol{A}(D) = a_n D^n + a_{n-1} D^{n-1} + \ldots + a_1 D + a_0 \,. \tag{B.1}$$

It is of degree n over the ring of integers modulo-p. If the input sequence is given by

$$\boldsymbol{x} = (x_0, x_1, x_2, \ldots), \tag{B.2}$$

and the output sequence is given by

$$\boldsymbol{z} = (z_0, z_1, z_2, \ldots), \tag{B.3}$$

then the output at time k is

$$z_k = [a_0 x_k + a_1 x_{k-1} + \ldots + a_n x_{k-n}] \mod p. \tag{B.4}$$

The relationship can also be written in terms of the output polynomial as

$$\boldsymbol{z}(D) = \boldsymbol{A}(D)\boldsymbol{x}(D), \tag{B.5}$$

where

$$\boldsymbol{z}(D) = z_0 + z_1 + z_2 D^2 + \ldots, \tag{B.6}$$

and

$$\boldsymbol{x}(D) = x_0 + x_1 + x_2 D^2 + \ldots. \tag{B.7}$$

Connecting two networks $\boldsymbol{A}_1(D)$ and $\boldsymbol{A}_2(D)$ in series, results in a combined network with the polynomial

$$\boldsymbol{A}(D) = \boldsymbol{A}_1(D)\boldsymbol{A}_2(D). \tag{B.8}$$

Similarly, combining the two networks in parallel results in the polynomial

$$\boldsymbol{A}(D) = \boldsymbol{A}_1(D) + \boldsymbol{A}_2(D). \tag{B.9}$$

If the output is dependent on a finite number of previous outputs, as well as current and previous inputs, then the system can be represented as a rational transfer function of the delay operator

$$\boldsymbol{A}(D) = \frac{\boldsymbol{A}_1(D)}{\boldsymbol{Q}_1(D)} = \boldsymbol{A}_1(D)\frac{1}{\boldsymbol{Q}_1(D)}. \tag{B.10}$$

The function can be realized if $\boldsymbol{Q}_1(D)$ has a non-zero constant term that is prime to the modulus p, that is, a unit of p. The condition for two encoders to be considered equivalent is

$$\frac{\boldsymbol{A}_1(D)}{\boldsymbol{Q}_1(D)} \sim \frac{\boldsymbol{A}_2(D)}{\boldsymbol{Q}_2(D)} \quad \textbf{if and only if} \quad \boldsymbol{A}_1(D)\boldsymbol{Q}_2(D) = \boldsymbol{A}_2(D)\boldsymbol{Q}_1(D). \tag{B.11}$$

When a system has more than one input or output data stream, the system can be described by a generator matrix of delay polynomials. A system with k input data streams and l output data streams, has a $(k \times l)$ dimensional generator matrix.

Appendix C

Viterbi Algorithm

A tutorial on the Viterbi algorithm by Forney can be found in [79]. A brief overview of the algorithm, as it relates the system presented in this thesis, is given here. The Viterbi algorithm is a solution for maximum a posteriori probability (MAP) state sequence estimation, for a finite-state, discrete time, Markov process that is observed in memoryless noise.

A state at time k_v is denoted σ_{k_v}, and it is from a finite set of S states, that run from time 0 to time K

$$\sigma_{k_v} \in \{0, 1, \ldots, S-1\}, \quad k_v = 0, 1, \ldots K\,. \tag{C.1}$$

It is assumed that the process starts in the zero state and finishes in the zero state. The probability of being in state σ_{k_v+1} at time $k_v + 1$ given all the previous states up to time k_v, is only dependent on the state at time k_v

$$P(\sigma_{k_v+1}|\sigma_0, \sigma_1, \ldots, \sigma_{k_v}) = P(\sigma_{k_v+1}|\sigma_{k_v})\,. \tag{C.2}$$

The state transition from σ_{k_v} to σ_{k_v+1} at time k_v is denoted ξ_{k_v}

$$\xi_{k_v} = \{\sigma_{k_v}, \sigma_{k_v+1}\}\,. \tag{C.3}$$

For transition ξ_{k_v} to be possible

$$P(\sigma_{k_v+1}|\sigma_{k_v}) \neq 0\,. \tag{C.4}$$

The set of possible transitions is denoted Ξ, and the number such transitions is denoted $|\Xi|$. The number of possible transitions is limited by

$$|\Xi| \leq S^2\,. \tag{C.5}$$

There is a one-to-one correspondence between the state sequences, $\boldsymbol{\sigma}$, and the transition sequences, $\boldsymbol{\xi}$. If the observed sequence is $\boldsymbol{z}$, then

$$P(\boldsymbol{z}|\boldsymbol{\sigma}) = P(\boldsymbol{z}|\boldsymbol{\xi}) = \prod_{k_v=0}^{K-1} P(z_{k_v}|\xi_{k_v}). \tag{C.6}$$

Given an observed sequence of a discrete-time finite-state Markov process, $\boldsymbol{z}$, the Viterbi algorithm is used to find the state sequence, $\boldsymbol{\sigma}$, that maximizes the $a\,posteriori$ probability

$$\begin{aligned} P(\boldsymbol{\sigma}, \boldsymbol{z}) &= P(\boldsymbol{\sigma})P(\boldsymbol{z}|\boldsymbol{\sigma}) \\ &= \prod_{k_v=0}^{K-1} P(\sigma_{k_v+1}|\sigma_{k_v}) \prod_{k_v=0}^{K-1} P(z_{k_v}|\sigma_{k_v+1}, \sigma_{k_v}) \\ &= \prod_{k_v=0}^{K-1} P(\sigma_{k_v+1}|\sigma_{k_v}) \prod_{k_v=0}^{K-1} P(z_{k_v}|\xi_{k_v}). \end{aligned} \tag{C.7}$$

This is equivalent to finding the transition sequence for which $P(\boldsymbol{\sigma}, \boldsymbol{\xi})$ is maximum. For the STC-CPM system, the input symbols are independent and equiprobable. Therefore,

$$P(\sigma_{k_v+1}|\sigma_{k_v}) = \frac{1}{S}, \tag{C.8}$$

for all allowable transitions. Hence, we do not need to consider the expression of Equation (C.8), when searching for the sequence that maximizes $P(\boldsymbol{\sigma}, \boldsymbol{\xi})$. The problem is reduced to finding the state sequence that maximizes the likelihood probability, $P(\boldsymbol{z}|\boldsymbol{\sigma})$ or equivalently, $P(\boldsymbol{z}|\boldsymbol{\xi})$.

State transition sequences can be represented as the paths through a trellis, where each node of the trellis is a distinct state at a given time. Each branch that connects the nodes of the trellis, is a possible transition from one state to the next, at an instant of time. For each possible state sequence, $\boldsymbol{\sigma}$, there is a unique path through the trellis. The trellis begins and ends in known states σ_0, and σ_K, respectively.

Finding the sequence for which $P(\boldsymbol{z}|\boldsymbol{\sigma})$ is maximum, is equivalent to finding the sequence for which $-\ln[P(\boldsymbol{z}|\boldsymbol{\sigma})]$ is minimum. The function can be rewritten using Equation (C.7) as

$$\begin{aligned} -\ln\left[P(\boldsymbol{z}|\boldsymbol{\sigma})\right] &= -\ln\left[\prod_{k_v=0}^{K-1} P(z_{k_v}|\xi_{k_v})\right] \\ &= \sum_{k_v=0}^{K-1} -\ln\left[P(z_{k_v}|\xi_{k_v})\right]. \end{aligned} \tag{C.9}$$

Each transition (trellis branch) is assigned with a length

$$\lambda(\xi_{k_v}) = -\ln[P(z_{k_v}|\xi_{k_v})]\,, \tag{C.10}$$

which is called the branch metric. The total length of the path through the trellis or path metric is the sum of the branch metrics. Substituting Equation (C.10) into Equation (C.9) we find the path metric

$$-\ln[P(\boldsymbol{z}|\boldsymbol{\sigma})] = \sum_{k_v=0}^{K-1} \lambda(\xi_{k_v})\,. \tag{C.11}$$

The problem now is to find the shortest path through the trellis. At any time, there will be a number of paths terminating at a given node of the trellis. A path that begins in state σ_0 and ends in state σ_{k_v} at time k_v is denoted $\boldsymbol{\sigma}_0^{k_v}$. The path metric associated with each of these paths has length

$$\lambda(\boldsymbol{\sigma}_0^{k_v}) = \sum_{i=0}^{k_v-1} \lambda(\xi_i)\,. \tag{C.12}$$

The path that has the smallest metric is called the $survivor$ path, it is denoted $\tilde{\boldsymbol{\sigma}}(\sigma_{k_v})$. There are S survivor paths for any time greater than zero, one for each node. Therefore, at any time the S survivor paths, $\tilde{\boldsymbol{\sigma}}(\sigma_{k_v})$, and their metrics $\Gamma(\sigma_{k_v}) = \lambda[\tilde{\boldsymbol{\sigma}}(\sigma_{k_v})]$ must be stored. At each time step an estimate of the state sequence is output. The length of state sequence estimate is denoted δ; it is also known as the $decision\,depth$. At time k_v a definite decision on the states up to time $k_v - \delta + 1$ must be made. δ is chosen to be large enough such that there is a large probability that all time-k_v survivor paths go through the same nodes up to time $k_v - \delta + 1$.

The algorithm starts by initializing

$$\begin{aligned}
&k_v = 0;\\
&\tilde{\boldsymbol{\sigma}}(\sigma_0) = \sigma_0; \quad \tilde{\boldsymbol{\sigma}}(s)\, arbitrary, \quad s \neq \sigma_0;\\
&\Gamma(\sigma_0) = 0; \quad\;\; \Gamma(s) = \infty, \qquad\quad s \neq \sigma_0.
\end{aligned}$$

For the recursive part of the algorithm, at each time k_v, provisional path metrics are computed for each possible transition, ξ_{k_v}, from each possible state, σ_{k_v}, using

$$\Gamma(\sigma_{k_v+1}, \sigma_{k_v}) = \Gamma(\sigma_{k_v}) + \lambda(\xi_{k_v}). \tag{C.13}$$

For each new node, σ_{k_v+1}, the minimum path metric that terminates in that node is found using

$$\Gamma(\sigma_{k_v+1}) = \min_{\sigma_{k_v}} \Gamma(\sigma_{k_v+1}, \sigma_{k_v}). \tag{C.14}$$

This is the survivor metric of the survivor path terminating in node, σ_{k_v+1}. The S survivor path metrics, $\Gamma(\sigma_{k_v+1})$, and the corresponding survivor paths, $\tilde{\boldsymbol{\sigma}}(\sigma_{k_v+1})$, are stored.

The node with the minimum value of $\Gamma(\sigma_{k_v+1})$ is found. The state at time $k_v - \delta + 1$ from the associated survivor path, $\tilde{\boldsymbol{\sigma}}(\sigma_{k_v+1})$, is output. If there are two nodes that have the minimum value of $\Gamma(\sigma_{k_v+1})$ and their survivor paths have different states for time $k_v - \delta + 1$, the output is chosen arbitrarily between the states. Then, k_v is set equal to $k_v + 1$ and the recursion is repeated until time k_v is equal to K. If k_v is large the path metrics are normalized by subtracting a constant. At time K the survivor path from the node that has the minimum survivor metric is output.

Appendix D

Code Search Results

In this appendix, we present the complete results of the space-time code searches for M-CPFSK space-time coded schemes. The results are for rate-$\frac{1}{2}$ space-time encoders, with 8-CPFSK and $L_t = 2$ transmit antennas, and rate-$\frac{2}{3}$ space-time encoders, with $M = \{2, 4, 8\}$-CPFSK and $L_t = 3$. Partial results for these systems are presented in Chapter 4. The generic systematic rate-$\frac{1}{2}$ and rate-$\frac{2}{3}$ encoders used in the code searches are given by

$$\boldsymbol{G}(D) = \left[\begin{array}{cc} 1 & \frac{f_0^1+f_1^1 D+f_2^1 D^2+...+f_{\nu_{\max}}^1 D^{\nu_{\max}}}{f_0^0+f_1^0 D+f_2^0 D^2+...+f_{\nu_{\max}}^0 D^{\nu_{\max}}} \end{array} \right] \tag{D.1}$$

and

$$\boldsymbol{G}(D) = \left[\begin{array}{ccc} 1 & 0 & \frac{f_0^1+f_1^1 D+f_2^1 D^2+...+f_{\nu_{\max}}^1 D^{\nu_{\max}}}{f_0^0+f_1^0 D+f_2^0 D^2+...+f_{\nu_{\max}}^0 D^{\nu_{\max}}} \\ 0 & 1 & \frac{f_0^2+f_1^2 D+f_2^2 D^2+...+f_{\nu_{\max}}^2 D^{\nu_{\max}}}{f_0^0+f_1^0 D+f_2^0 D^2+...+f_{\nu_{\max}}^0 D^{\nu_{\max}}} \end{array} \right], \tag{D.2}$$

respectively.

We represent the rate-$\frac{l-1}{l} = \frac{L_t-1}{L_t}$ space-time encoders with the summation

$$\boldsymbol{G}_{\boldsymbol{L_t,M,\nu_{\max}}} = \sum_{i=0}^{L_t-1} \sum_{j=0}^{\nu_{\max}} M^{(\nu_{\max}-j)+(\nu_{\max}+1)(L_t-1-i)} f_j^i, \tag{D.3}$$

for all i and j, except $(i = j = 0)$. Note that f_0^0 is set to one for all code searches. For example, if we let $\nu_{\max} = 4$, $L_t - 1 = 2$ and $M = 2$, the encoder

$$\boldsymbol{G}(D) = \left[\begin{array}{ccc} 1 & 0 & 1 \\ 0 & 1 & 1 \end{array} \right], \tag{D.4}$$

is represented by

$$\boldsymbol{G}_{\boldsymbol{3,2,4}} = 2^{(4-0)+(4+1)(3-1-1)} f_0^1 + 2^{(4-0)+(4+1)(3-1-2)} f_0^2 = 2^9 + 2^4 = 528. \tag{D.5}$$

The number of delay cells, which is denoted ν, required to implement this encoder is zero. Variable $\nu_{\max}$ denotes the maximum power of D used in the code search and is used to represent the encoder numerically using Equation (D.3).

Table D.1 presents the results of the search for rate-$\frac{1}{2}$ space-time encoders with 8-CPFSK and $\nu_{\max} = 2$. Table D.2 presents the results of the search for rate-$\frac{2}{3}$ space-time encoders with MSK and $\nu_{\max} = 4$ and $\nu_{\max} = 5$. Table D.3 presents the results of the search for rate-$\frac{2}{3}$ space-time encoders with 4-CPFSK and $\nu_{\max} = 1$ and $\nu_{\max} = 2$. Table D.4 presents the results of the search for rate-$\frac{2}{3}$ space-time encoders with 8-CPFSK and $\nu_{\max} = 1$.

ν	S_J	$\rho_{\min}$	$d^2_{\min}$	**Space-Time Codes $G_{2,8,2}$**
0	8	1	2.180	$192, 320$
1	16	1	2.374	$4272, 4496, 12432, 12720, 20656, 20880, 28816, 29104$
1	32	1	3.888	$4328, 4440, 12536, 12616, 20680, 20856, 28888, 29032$
1	64	2	4.079	$8472, 8488, 16552, 16792$
2	64	1	4.317	$1234, 1238, 1266, 1270, 1362, 1366, 1394, 1398, 3282, 3286, 3314, 3318, 3410, 3414, 3442, 3446, 9410, 9414, 9442, 9446, 9538, 9542, 9570, 9574, 11458, 11462, 11490, 11494, 11586, 11590, 11618, 11622, 17618, 17622, 17650, 17654, 17746, 17750, 17778, 17782, 19666, 19670, 19698, 19702, 19794, 19798, 19826, 19830, 25794, 25798, 25826, 25830, 25922, 25926, 25954, 25958, 27842, 27846, 27874, 27878, 27970, 27974, 28002, 28006$
2	128	1	5.087	$5871, 5977, 7915, 8029, 13005, 13053, 13131, 13179, 14031, 14201, 15049, 15097, 15183, 15231, 16075, 16253, 22223, 22393, 24267, 24445, 29405, 29421, 29531, 29547, 30447, 30553, 31449, 31465, 31583, 31599, 32491, 32605$
2	256	2	5.286	$14479, 14777, 15645, 15659, 30859, 31165, 32025, 32047$

Table D.1: Full code search results for rate-$\frac{1}{2}$ STC with 8-CPFSK and 2 transmit antennas. The spectral efficiency is 3 bits/s/Hz.

ν	S_J	$\rho_{\min}$	$d^2_{\min}$	**Space-Time Codes $G_{3,2,4}$**
0	4	1	2.667	528
1	8	1	2.667	264, 272, 280, 520, 536, 776, 784, 792, 8456, 8464, 8472, 8712, 8720, 8728, 8968, 8976
2	16	1	4.000	412, 908, 4380, 5000, 8348, 9092, 12440, 12564, 12688, 12812, 12936, 13060
2	16	2	4.000	404, 652, 664, 668, 788, 796, 916, 920, 4236, 4248, 4252, 4364, 4376, 4484, 4488, 4496, 4508, 4620, 4632, 4636, 4868, 4872, 4880, 4892, 4996, 5004, 5008, 5016, 8340, 8468, 8476, 8724, 8732, 8836, 8840, 8848, 8860, 9096, 9104, 9108, 12428, 12436, 12556, 12568, 12676, 12680, 12692, 12820, 12824, 12932, 12940, 12944, 12952, 13064, 13072, 13076
3	32	2	5.333	470, 474, 718, 730, 732, 846, 854, 860, 918, 922, 2262, 2266, 2390, 2394, 2454, 2458, 2710, 2714, 2758, 2762, 2764, 2772, 2776, 2778, 2782, 2838, 2842, 2886, 2890, 2892, 2900, 2902, 2904, 2910, 3030, 3034, 4694, 4698, 4818, 4826, 4946, 4950, 6222, 6234, 6236, 6286, 6298, 6300, 6354, 6414, 6426, 6428, 6482, 6490, 6546, 6594, 6596, 6600, 6608, 6618, 6622, 6670, 6682, 6684, 6726, 6730, 6732, 6740, 6744, 6746, 6750, 6802, 6810, 6930, 6978, 6980, 6984, 6986, 6990, 6992, 6994, 6996, 7004, 7006, 7042, 7044, 7048, 7056, 7066, 7070, 7118, 7122, 7130, 7132, 8790, 8794, 8914, 9042, 10318, 10326, 10332, 10382, 10390, 10396, 10450, 10510, 10518, 10524, 10578, 10582, 10642, 10690, 10692, 10696, 10704, 10710, 10718, 10766, 10774, 10780, 10822, 10826, 10828, 10836, 10838, 10840, 10846, 10898, 10902, 10946, 10948, 10952, 10954, 10958, 10960, 10962, 10964, 10972, 10974, 11026, 11138, 11140, 11144, 11152, 11158, 11166, 11214, 11218, 11222, 11228, 12374, 12378, 12438, 12442, 12566, 12570, 12822, 12826, 12994, 12996, 13000, 13008, 13018, 13022, 13122, 13124, 13128, 13136, 13142, 13150, 13270, 13274, 14806, 14810, 14934, 14938, 15054, 15058, 15066, 15068,

continued on next page

continued from previous page

ν	S_J	$\rho_{\min}$	$d^2_{\min}$	**Space-Time Codes $G_{3,2,4}$**
				15182, 15186, 15190, 15196, 15254, 15258
4	64	2	6.667	1267, 1273, 1395, 1397, 1401, 1459, 1461, 1465, 1491, 1497, 1639, 1643, 1645, 1646, 1654, 1658, 1660, 1661, 1663, 1707, 1709, 1718, 1722, 1723, 1727, 1747, 1749, 1753, 1785, 1791, 1831, 1835, 1837, 1838, 1846, 1847, 1850, 1852, 1855, 1875, 1877, 1881, 1909, 1919, 1939, 1945, 1971, 1983, 2035, 2037, 2039, 2041, 2043, 2045, 2685, 2809, 2815, 2871, 2995, 3007, 3063, 3069, 3255, 3313, 3389, 3415, 3439, 3441, 3454, 3505, 3537, 3563, 3574, 3575, 3623, 3627, 3629, 3630, 3638, 3642, 3644, 3645, 3647, 3677, 3735, 3771, 3773, 3791, 3793, 3806, 3813, 3818, 3823, 3828, 3833, 3837, 3838, 3895, 3901, 3921, 3957, 3965, 3985, 4009, 4017, 4018, 4021, 4023, 4025, 4027, 4031, 4043, 4054, 4055, 4081, 4093, 4727, 4851, 4863, 4925, 5049, 5055, 5111, 5117, 5489, 5499, 5553, 5563, 5623, 5629, 5675, 5677, 5686, 5690, 5691, 5695, 5755, 5757, 5841, 5851, 5871, 5881, 5883, 5886, 5943, 5947, 5969, 5979, 5995, 5997, 6001, 6003, 6006, 6007, 6009, 6010, 6013, 6015, 6063, 6067, 6075, 6078, 6103, 6109, 6129, 6139, 6643, 6707, 6709, 6713, 6767, 6769, 6782, 6833, 6843, 6961, 7029, 7123, 7347, 7359, 7481, 7487, 7507, 7519, 7667, 7669, 7737, 7743, 7769, 7775, 7781, 7786, 7791, 7796, 7801, 7805, 7806, 7827, 7839, 7855, 7865, 7867, 7870, 7977, 7985, 7986, 7987, 7989, 7995, 7997, 7999, 8053, 8057, 8115, 8121, 8147, 8149, 8165, 8169, 8170, 8177, 8178, 8180, 8185, 9405, 9457, 9527, 9565, 9585, 9647, 9649, 9662, 9681, 9709, 9722, 9725, 9767, 9771, 9773, 9774, 9782, 9783, 9786, 9788, 9791, 9815, 9847, 9853, 9885, 9911, 9915, 9937, 9961, 9969, 9970, 9971, 9973, 9979, 9981, 9983, 10063, 10065, 10078, 10101, 10103, 10129, 10149, 10154, 10159, 10163, 10164, 10167, 10174, 10189, 10202, 10205, 10225, 10231, 10745, 10803, 10805, 10809, 10865, 10929, 10939, 11055, 11057, 11070, 11125, 11225,

continued on next page

continued from previous page

ν	S_J	$\rho_{\min}$	$d^2_{\min}$	**Space-Time Codes $G_{3,2,4}$**
				11637, 11701, 11829, 11839, 11893, 11901, 11947, 11949, 11953, 11955, 11958, 11959, 11961, 11962, 11965, 11967, 11989, 12021, 12025, 12085, 12087, 12117, 12211, 12213, 12273, 12277, 12851, 12857, 12913, 13105, 13497, 13503, 13619, 13631, 13657, 13663, 13813, 13817, 13875, 13887, 13907, 13919, 13929, 13937, 13938, 13941, 13943, 13945, 13947, 13951, 13977, 13983, 13999, 14003, 14011, 14014, 14067, 14073, 14117, 14122, 14127, 14131, 14132, 14135, 14142, 14195, 14197, 14293, 14297, 14309, 14313, 14314, 14321, 14322, 14323, 14324, 14707, 14777, 14955, 14966, 14967, 15031, 15037, 15059, 15091, 15093, 15149, 15162, 15165, 15193, 15285, 15289, 15543, 15549, 15671, 15677, 15703, 15709, 15923, 15925, 15927, 15929, 15931, 15933, 15959, 15965, 15985, 15997, 16023, 16029, 16049, 16059, 16101, 16105, 16106, 16113, 16114, 16116, 16121, 16177, 16183, 16241, 16245, 16293, 16297, 16298, 16305, 16306, 16307, 16308
				Space-Time Codes $G_{3,2,5}$
5	128*	2	8.000	13029, 13553, 13565, 13657, 13663, 13671, 13673, 13679, 13682, 13687, 13691, 13693, 13694, 13733, 13909, 13925, 13929, 13930, 13937, 14293, 14313, 14314, 14331, 14667, 14678, 14681, 14700, 14705, 14706, 14711, 14769, 14781, 14805, 14826, 14933, 14937, 14943, 14954, 14961, 14962, 14971, 14974, 15001, 15007, 15015, 15017, 15023, 15026, 15031, 15035, 15037, 15038, 15089, 15095, 15141, 15221, 15317, 15338, 15345, 15357, 15443, 15449, 15461, 15462, 15465, 15467, 15471, 15474, 15477, 15479, 15483, 15485, 15509, 15525, 15529, 15530, 15537, 15725, 15729, 15829, 15845, 15850, 15851, 15857, 16085, 16095, 16105, 16106, 16113, 16126, 16211, 16213, 16230, 16234, 16239, 16241, 16277, 16297, 16298, 16315

continued on next page

continued from previous page

ν	S_J	$\rho_{\min}$	$d^2_{\min}$	**Space-Time Codes $G_{3,2,4}$**

Table D.2: Full code search results for rate-$\frac{2}{3}$ STC with 2-CPFSK and 3 transmit antennas. The spectral efficiency is 2 bits/s/Hz. *The search for codes with $S_J = 128$ is incomplete.

ν	S_J	$\rho_{\min}$	$d^2_{\min}$	**Space-Time Codes $G_{3,4,1}$**
0	16	1	1.938	$68, 72, 76, 132, 136, 140, 196, 200, 204$
1	32	1	2.667	$38, 46, 98, 104, 106, 134, 142, 166, 174, 226, 232, 234, 295, 301,$ $370, 376, 378, 391, 397, 423, 429, 466, 472, 474, 548, 556, 578,$ $584, 586, 644, 652, 676, 684, 706, 712, 714, 805, 815, 850, 856,$ $858, 901, 911, 933, 943, 1010, 1016, 1018$
1	64	1	3.756	$359, 365, 374, 377, 379, 382, 407, 413, 439, 445, 470, 473, 475,$ $478, 487, 493, 599, 605, 629, 639, 725, 735, 759, 765, 854, 857,$ $859, 862, 869, 879, 917, 927, 949, 959, 997, 1007, 1014, 1017,$ $1019, 1022$
				Space-Time Codes $G_{3,4,2}$
2	128	1	4.322	$5529, 5563, 5718, 5733, 5743, 5758, 6489, 6523, 7129, 7163,$ $7894, 7909, 7919, 7934, 8089, 8123, 13735, 13741, 14046, 14055,$ $14061, 14070, 14235, 14245, 14255, 14265, 14686, 14710, 14806,$ $14811, 14841, 14846, 15190, 15195, 15225, 15230, 15326, 15350,$ $15771, 15781, 15791, 15801, 15966, 15975, 15981, 15990, 16295,$ $16301, 17830, 17838, 18838, 18878, 19350, 19390, 20390, 20398,$ $25689, 25723, 25831, 25837, 25894, 25902, 26193, 26215, 26221,$ $26227, 27028, 27068, 27091, 27097, 27121, 27131, 27475, 27481,$ $27505, 27515, 27540, 27580, 27751, 27757, 27865, 27899, 28369,$ $28391, 28397, 28403, 28454, 28462, 37974, 37989, 37999, 38014,$ $38289, 38311, 38317, 38323, 38821, 38831, 39249, 39262, 39283,$ $39286, 39382, 39422, 39766, 39806, 39889, 39902, 39923, 39926,$

continued on next page

continued from previous page				
ν	S_J	$\rho_{\min}$	$d^2_{\min}$	**Space-Time Codes $G_{3,4,1}$**
				40150, 40165, 40175, 40190, 40357, 40367, 40849, 40871, 40877, 40883, 46302, 46311, 46317, 46326, 46995, 47025, 47571, 47601, 47955, 47985, 48222, 48231, 48237, 48246, 48531, 48561, 51108, 51116, 51486, 51510, 51998, 52022, 52644, 52652, 58587, 58597, 58607, 58617, 58981, 58991, 59091, 59121, 59172, 59180, 59676, 59700, 59731, 59737, 59761, 59771, 60188, 60212, 60371, 60377, 60401, 60411, 60507, 60517, 60527, 60537, 60708, 60716, 61011, 61041, 61157, 61167
2	256	†	5.330	30623, 30645, 30686, 30695, 30701, 30710, 31199, 31221, 31583, 31605, 32094, 32103, 32109, 32118, 32159, 32181, 58847, 58869, 59351, 59389, 60759, 60797, 61279, 61301, 62942, 62951, 62957, 62966, 63383, 63421, 63383, 63421, 63959, 63997, 64343, 64381, 64919, 64957, 65374, 65383, 65389, 65398

Table D.3: Full code search results for rate-$\frac{2}{3}$ STC with 4-CPFSK and 3 transmit antennas. The spectral efficiency is 4 bits/s/Hz. †$\rho_{\min}$ was not calculated for the 256 state systems.

ν	S_J	$\rho_{\min}$	$d^2_{\min}$	**Space-Time Codes $G_{3,8,1}$**
0	64	1	1.454	1056, 2064, 2096, 3104
1	128	1	2.181	5531, 5549, 5846, 5874, 6998, 7026, 7323, 7341, 13465, 13487, 13906, 13942, 15314, 15350, 15769, 15791, 21919, 21929, 22486, 22514, 23126, 23154, 23711, 23721, 29853, 29867, 30546, 30582, 31442, 31478, 32157, 32171
1	256*	†	2.907	1314, 1318, 2196, 2228, 2452

continued on next page

continued from previous page				
$\boldsymbol{\nu}$	$\boldsymbol{S_J}$	$\boldsymbol{\rho_{\min}}$	$\boldsymbol{d^2_{\min}}$	**Space-Time Codes $G_{3,8,1}$**

Table D.4: Full code search results for rate-$\frac{2}{3}$ STC with 8-CPFSK and 3 transmit antennas. The spectral efficiency is 6 bits/s/Hz. *The search for codes with $S_J = 256$ is incomplete. †$\rho_{\min}$ was not calculated for the 256 state systems.

Appendix E

Pairwise Error Probability Bound

An alternative method used to derive a bound on the pairwise error probability (PEP) for space time coded schemes is presented in [33]. It uses Craig's [80] representation of the Gaussian Q function,

$$Q(x) = \frac{1}{\pi}\int_0^{\frac{\pi}{2}} \exp\left(-\frac{x^2}{2\sin^2\theta}\right) d\theta, \quad x > 0. \tag{E.1}$$

With ideal channel state information the PEP may be written as [33]

$$P(\boldsymbol{X} \to \hat{\boldsymbol{X}}) = E\left[Q\left(\sqrt{\frac{\gamma_s}{2} d_m^2(\boldsymbol{X}, \hat{\boldsymbol{X}})}\right)\right], \tag{E.2}$$

where $\gamma_s = \frac{E_s}{N_0}$ is the SNR per symbol and the modified Euclidean distance $d_m^2(\boldsymbol{X}, \hat{\boldsymbol{X}}) = \sum_{j=1}^{L_r}\sum_{i=1}^{L_t} \lambda_i \left|\beta_{i,j}\right|^2$ is given by Equation (4.18). Applying Equation (E.1) to Equation (E.2) we get

$$\begin{aligned} P(\boldsymbol{X} \to \hat{\boldsymbol{X}}) &= \frac{1}{\pi}\int_0^{\frac{\pi}{2}} E\left[\exp\left(-\frac{\gamma_s d_m^2(\boldsymbol{X}, \hat{\boldsymbol{X}})}{4\sin^2\theta}\right)\right] d\theta \\ &= \frac{1}{\pi}\int_0^{\frac{\pi}{2}} \prod_{i=1}^{\rho}\prod_{j=1}^{L_r} E\left[\exp\left(-\frac{\gamma_s \lambda_i \left|\beta_{i,j}\right|^2)}{4\sin^2\theta}\right)\right] d\theta, \end{aligned} \tag{E.3}$$

where only the non-zero eigenvalues λ_i are included. The chi squared characteristics of the variables $\left|\beta_{i,j}\right|^2$ [33] are used to express the the PEP as

$$P(\boldsymbol{X} \to \hat{\boldsymbol{X}}) = \frac{1}{\pi}\int_0^{\frac{\pi}{2}} \prod_{i=1}^{\rho}\left(1 + \frac{\gamma_s \lambda_i}{4\sin^2\theta}\right)^{-L_r} d\theta. \tag{E.4}$$

The inequality

$$\prod_{i=1}^{\rho}(1 + x_i) \geq \left(1 + \left[\prod_{i=1}^{\rho} x_i\right]^{\frac{1}{\rho}}\right)^{\rho}, \quad x_i > 0 \tag{E.5}$$

is applied to Equation (E.4) to obtain the bound

$$P(\boldsymbol{X} \rightarrow \hat{\boldsymbol{X}}) \leq \frac{1}{\pi} \int_0^{\frac{\pi}{2}} \left(1 + \frac{\gamma_s (\Lambda^P)^{\frac{1}{\rho}}}{4 \sin^2 \theta} \right)^{-\rho L_r} d\theta, \tag{E.6}$$

where $\Lambda^P = \prod_{i=1}^{\rho} \lambda_i$. Finally, the bound is evaluated [33] to give

$$P(\boldsymbol{X} \rightarrow \hat{\boldsymbol{X}}) \leq \left(P\left[\frac{E_s}{4N_0} \left(\Lambda^P \right)^{\frac{1}{\rho}} \right] \right)^{\rho L_r} \sum_{i=0}^{\rho L_r - 1} \binom{\rho L_r - 1 + i}{i} \left(1 - P\left[\frac{E_s}{4N_0} \left(\Lambda^P \right)^{\frac{1}{\rho}} \right] \right)^i, \tag{E.7}$$

where

$$P[x] = \frac{1}{2} \left(1 - \sqrt{\frac{x}{1+x}} \right), \quad x \geq 0. \tag{E.8}$$

Bibliography

[1] G. Foschini and M. Gans, "On the limits of wireless communications in a fading environment when using multiple antennas," *Wireless Pers. Commun.*, vol. 6, pp. 311–335, Mar. 1998.

[2] E. Telatar, "Capacity of multi-antenna Gaussian channels," *Euro. Trans. Telecomm.*, vol. 10, pp. 585–595, Nov.-Dec. 1999.

[3] B. Vucetic and J. Yuan, *Space-time coding*. England: Wiley, 2003.

[4] V. Tarokh, N. Seshadri, and A. R. Calderbank, "Space-time codes for high data rate wireless communication: Performance analysis and code construction," *IEEE Trans. Inform. Theory*, vol. 44, no. 2, pp. 744–765, Mar. 1998.

[5] J. K. Cavers, "Space-time coding using MSK," in *Proc. Veh. Tech. Conf.*, vol. 1, Sept. 2002, pp. 401–405.

[6] ——, "Spacetime coding using MSK," *IEEE Trans. Wireless Commun.*, vol. 4, no. 1, pp. 185–191, Jan. 2005.

[7] J. B. Anderson, T. Aulin, and C.-E. W. Sundberg, *Digital Phase Modulation*. NY: Plenum, 1986.

[8] X. Zhang and M. P. Fitz, "Constant envelope space-time modems," in *Proc. Veh. Tech. Conf.*, vol. 3, Oct. 2003, pp. 1772–1776.

[9] S. Ogose, K. Murota, and K. Hirade, "A transmitter diversity for MSK with two-bit differential detection," *IEEE Trans. Veh. Technol.*, vol. 33, no. 1, pp. 37–43, Feb. 1984.

[10] X. Zhang and M. P. Fitz, "Space-time code design with CPM transmission," in *Proc. Int. Symp. Inform. Theory*, Washington, DC, June 2001, p. 327.

[11] ——, "Space-time code design with continuous phase modulation," *IEEE J. Select. Areas Commun.*, vol. 21, no. 5, pp. 783–792, June 2003.

[12] C.-C. Chen and C.-C. Lu, "Space-time code design for CPFSK modulation over frequency-nonslective fading channels," *IEEE Trans. Commun.*, vol. 53, no. 9, pp. 1477–1489, Sept. 2005.

[13] J. Sykora, "Constant envelope space-time modulation trellis code design for Rayleigh flat fading channel," in *Proc. Global Telecommun. Conf.*, vol. 2, San Antonio, USA, 2001, pp. 1113–1117.

[14] A. R. Ahmadi and R. K. Rao, "Space-time trellis code design with binary CPM," *IEE Electronics Letters*, vol. 42, no. 3, pp. 168–169, Feb. 2006.

[15] A. G. Zajić and G. L. Stüber, "Optimization of coding gain for full-response CPM space-time codes," in *Proc. Global Telecommun. Conf.*, 2006.

[16] A. Hammons, Jr. and H. E. Gamal, "On the theory of space-time codes for PSK modulation," *IEEE Trans. Inform. Theory*, vol. 46, no. 2, pp. 524–542, Mar. 2000.

[17] X. Zhang and M. P. Fitz, "Soft-output demodulator in space-time-coded continuous phase modulation," *IEEE Trans. Signal Processing*, vol. 50, no. 10, pp. 2589–2598, Oct. 2002.

[18] D. Bokolamulla and T. M. Aulin, "Performance of space-time coded continuous phase modulated signals over different fading environments," in *Proc. Int. Symp. Inform. Theory*, Sept. 2005, pp. 1048–1052.

[19] S. M. Alamouti, "A simple transmitter diversity scheme for wireless communications," *IEEE J. Select. Areas Commun.*, vol. 16, no. 8, pp. 1451–1458, Oct. 1998.

[20] G. Wang and X.-G. Xia, "Orthogonal space-time coding for CPM system with fast decoding," in *Proc. Int. Symp. Inform. Theory*, 2002, p. 107.

[21] T. Pande, H. Huh, and J. V. Krogmeier, "Non-coherent demodulation for orthogonal space-time coded CPM," in *Proc. Veh. Tech. Conf.*, vol. 2, Stockholm, Sweden, May-June 2005, pp. 1206–1209.

[22] B. M. Hochwald and W. Sweldens, "Differential unitary space-time modulation," *IEEE Trans. Commun.*, vol. 48, pp. 2041–2052, Dec. 2000.

[23] B. L. Hughes, "Differential space-time modulation," *IEEE Trans. Inform. Theory*, vol. 46, pp. 2567–2578, Nov. 2000.

[24] A.-M. Silvester, L. Lampe, and R. Schober, "Diagonal block space-time code design for continuous-phase modulation," in *Proc. Global Telecommun. Conf.*, 2006.

[25] W. Zhao and G. B. Giannakis, "Reduced complexity receivers for layered space-time CPM," *IEEE Trans. Wireless Commun.*, vol. 4, no. 2, pp. 574–582, Mar. 2005.

[26] H.-H. R. Yang, "On trellis coded continuous phase frequency shift keying," Ph.D. dissertation, McMaster University, Canada, June 1994.

[27] R. H.-H. Yang and D. P. Taylor, "Trellis-coded continuous-phase frequency-shift keying with ring convolutional codes," *IEEE Trans. Inform. Theory*, vol. 40, no. 4, pp. 1057–1067, July 1994.

[28] B. E. Rimoldi and Q. Li, "Coded continuous phase modulation using ring convolutional codes," *IEEE Trans. Commun.*, vol. 43, no. 11, pp. 2714–2720, Nov. 1995.

[29] A. Griffin, "Coding CPFSK for differential demodulation," Ph.D. dissertation, University of Canterbury, New Zealand, Feb. 2000.

[30] A. Griffin and D. P. Taylor, "Coding CPFSK for differential demodulation," *IEEE Trans. Commun.*, vol. 48, pp. 721–724, May 2000.

[31] APCO project 25 - Standards for public safety digital radio. [Online]. Available: http://www.apcointl.org/frequency/project25/information.html

[32] B. E. Rimoldi, "A decomposition approach to CPM," *IEEE Trans. Inform. Theory*, vol. 34, no. 2, pp. 260–270, Mar. 1988.

[33] M.-K. Byun and B. G. Lee, "New bounds for pairwise error probability for space-time codes in Rayleigh fading channels," in *Proc. Wireless Commun. and Networking Conf.*, Mar. 2002, pp. 89–98.

[34] T. S. Rappaport, *Wireless Communications Principles and Practice*, 2nd ed. NJ: Prentice-Hall, 2002.

[35] J. G. Proakis, *Digital communications*, 4th ed. NY: McGraw-Hill, 2001.

[36] R. H. Clarke, "A statistical theory of mobile radio reception," *Bell Sys. Tech. J*, vol. 47, no. 6, pp. 957–1000, July/Aug. 1986.

[37] W. C. Jakes, Ed., *Microwave Mobile Communications*. NY: John Wiley & Sons, 1974.

[38] J. B. Anderson and A. Svensson, *Coded modulation systems*. NY: Kluwer Academic/ Plenum Publishers, 2003.

[39] C.-P. Liang, J. Jong, W. E. Stark, and J. East, "Nonlinear amplifier effects in communications systems," *IEEE Trans. Microwave Theory Tech.*, vol. 47, no. 8, pp. 1461–1466, Aug. 1999.

[40] T. Aulin and C.-E. W. Sundberg, "Continuous phase modulation - Part I: Full response signalling," *IEEE Trans. Commun.*, vol. 29, no. 3, pp. 196–209, Mar. 1981.

[41] J. B. Anderson and C.-E. W. Sundberg, "Advances in constant envelope coded modulation," *IEEE Commun. Mag.*, pp. 36–45, Dec. 1991.

[42] J. B. Anderson and D. P. Taylor, "A bandwidth-efficient class of signal space codes," *IEEE Trans. Inform. Theory*, vol. 24, pp. 703–712, Nov. 1978.

[43] J. L. Massey and T. Mittelholzer, "Convolutional codes over rings," in *Proc. 4th Joint Swedish-USSR Workshop on Info. Th.*, Gotland, Sweden, Aug.-Sept. 1989, pp. 14–18.

[44] ——, "Systematicity and rotational invariance of convolutional codes over rings," in *Proc. 2nd Int. Workshop on Algebraic and Combinatorial Coding Th.*, Leningrad, Sept. 1990, pp. 154–159.

[45] R. Johannesson, Z.-X. Wan, and E. Wittenmark, "Some structural properties of convolutional codes over rings," *IEEE Trans. Inform. Theory*, vol. 44, no. 2, pp. 839–845, Mar. 1998.

[46] J. Hartmanis, "Linear multivalued sequential coding networks," *IRE Trans. Circuit Theory*, vol. 6, no. 1, pp. 69–74, 1959.

[47] G. Foschini, "Layered space-time architecture for wireless communication in a fading environment when using multi-element antennas," *Bell Labs. Tech. J*, pp. 41–59, Autumn 1996.

[48] N. Al-Dhahir, C. Fragouli, A. Stamoulis, W. Younis, and R. Calderbank, "Space-time processing for broadband wireless access," *IEEE Commun. Mag.*, vol. 40, no. 9, pp. 136–142, Sept. 2002.

[49] V. Tarokh, H. Jafarkhani, and A. R. Calderbank, "Space-time block codes for orthogonal designs," *IEEE Trans. Inform. Theory*, vol. 45, pp. 1456–1467, July 1999.

[50] H. Jafarkhani, "A quasi-orthogonal space-time block code," *IEEE Trans. Commun.*, vol. 49, no. 1, pp. 1–4, Jan. 2001.

[51] N. Sharma and C. B. Papadias, "Improved quasi-orthogonal codes through constellation rotation," *IEEE Trans. Commun.*, vol. 51, no. 3, pp. 332–335, Mar. 2003.

[52] W. Su and X.-G. Xia, "Signal constellations for quasi-orthogonal spacetime block codes with full diversity," *IEEE Trans. Inform. Theory*, vol. 50, no. 10, pp. 2331–2347, Oct. 2004.

[53] J.-C. Guey, M. P. Fitz, M. R. Bell, and W.-Y. Kuo, "Signal design for transmitter diversity wireless communication systems over Rayleigh fading channels," in *Proc. Veh. Tech. Conf.*, vol. 46, Atlanta, GA, 1996, pp. 136–140.

[54] A. S. Deif, *Advanced matrix theory for scientists and engineers*, 2nd ed. Abacus Press, 1991.

[55] D. Aktas and M. P. Fitz, "Computing the distance spectrum of space-time trellis codes," in *Proc. Wireless Commun. and Networking Conf.*, Chicago, IL, Sept. 2000, pp. 51–55.

[56] Z. Chen, J. Yuan, and B. Vucetic, "An improved space-time trellis coded modulation scheme on slow Rayleigh fading channels," in *Proc. Int. Conf. Commun.*, vol. 4, June 2001, pp. 1110–1116.

[57] J. Yuan, Z. Chen, B. Vucetic, and W. Firmanto, "Performance and design of space-time coding in fading channels," *IEEE Trans. Commun.*, vol. 51, no. 12, pp. 1991–1996, Dec. 2003.

[58] J. Grimm, "Transmitter diversity code design for achieving full diversity," Ph.D. dissertation, Purdue Univ., Layfette, IN, 1998.

[59] S. Baro, G. Bauch, and A. Hansmann, "Improved codes for space-time trellis coded modulation," *IEEE Commun. Lett.*, vol. 4, no. 1, Jan. 2000.

[60] M. P. Fitz, J. Grimm, and S. Siwamogsatham, "A new view of performance analysis techniques in correlated rayleigh fading," in *Proc. Wireless Commun. and Networking Conf.*, New Orleans, LA, Sept. 1999, pp. 139–144.

[61] X. Zhang and M. P. Fitz, "On the achievable rate/diversity from CPM MIMO fading channel," in *Proc. Int. Symp. Inform. Theory*, Yokohama, Japan, June 2003, p. 98.

[62] P. A. Laurent, "Exact and approximate construction of digital phase modulations by superposition of amplitude modulated pulses (AMP)," *IEEE Trans. Commun.*, vol. 34, no. 2, pp. 150–160, Feb. 1986.

[63] U. Mengali and M. Morelli, "Decomposition to M-ary CPM signals into PAM waveforms," *IEEE Trans. Inform. Theory*, vol. 41, no. 5, pp. 1265–1275, Sept. 1995.

[64] A. R. Ahmadi and R. K. Rao, "Design of space-time trellis codes with multi-h CPM signals," in *Canadian Conf. on Elec. and Comp. Eng.*, 2005, pp. 200–203.

[65] F. Morales-Moreno, W. Holubowicz, and S. Pasupathy, "Optimization of trellis coded TFM via matched codes," *IEEE Trans. Commun.*, vol. 42, no. 2/3/4, pp. 1586–1594, Feb./Mar./Apr. 1994.

[66] G. D. Forney, Jr., "Convolutional codes I: Algebraic structure," *IEEE Trans. Inform. Theory*, vol. 16, no. 6, pp. 720–738, Nov. 1970.

[67] S. Haykin and M. Moher, *Modern Wireless Communications*. NJ: Pearson Prentice Hill, 2005.

[68] S. Haykin, *Communication systems*, 4th ed. John Wiley & Sons, 2001.

[69] D. Aktas, H. E. Gamal, and M. Fitz, "On the design and maximum-likelihood decoding of space-time trellis codes," *IEEE Trans. Commun.*, vol. 51, no. 6, pp. 854–859, June 2003.

[70] B. E. Rimoldi, "Exact formula for the minimum squared Euclidean distance of CPFSK," *IEEE Trans. Commun.*, vol. 39, no. 9, pp. 1280–1282, Sept. 1991.

[71] R. L. Maw and D. P. Taylor, "High rate CPFSK space-time trellis codes," *IEEE Trans. Commun.*, (Submitted).

[72] J. L. Massey, T. Mittelholzer, T. Riedel, and M. Vollenweider, "Ring convolutional codes for phase modulation," in *Proc. Int. Symp. Inform. Theory*, Jan. 1990.

[73] G. D. Forney, Jr., "Maximum-likelihood sequence estimation of digital sequences in the presence of intersymbol interference," *IEEE Trans. Inform. Theory*, vol. 18, no. 3, pp. 363–378, May 1972.

[74] D. Aktas and M. P. Fitz, "Distance spectrum analysis of space-time trellis-coded modulations in quasi-static Rayleigh-fading channels," *IEEE Trans. Inform. Theory*, vol. 49, no. 12, pp. 3335–3344, Dec. 2003.

[75] E. Malkamäki and H. Leib, "Evaluating the performance of convolutional codes over block fading channels," *IEEE Trans. Inform. Theory*, vol. 45, no. 5, pp. 1643–1646, July 1999.

[76] G. Lindell and C.-E. W. Sundberg, "An upper bound on the bit error probability of combined convolutional coding and continuous phase modulation," *IEEE Trans. Inform. Theory*, vol. 34, no. 5, pp. 1263–1269, Sept. 1988.

[77] E. Biglieri, D. Divsalar, P. J. McLane, and M. K. Simon, *Introduction to trellis-coded modulation with applications*. NY: Maxwell Macmillan, 1991.

[78] M. C. Jeruchim, P. Balaban, and K. S. Shanmugan, *Simulation of Communications Systems: Modelling, Methodology and Techniques*, 2nd ed. NY: Kluwer Academic/ Plenum Publishers, 2000.

[79] G. D. Forney, Jr., "The Viterbi algorithm," *Proc. IEEE*, vol. 61, no. 3, pp. 268–277, Mar. 1973.

[80] J. W. Craig, "A new, simple and exact result for calculating the probability of error for two-dimensional signal constellations," in *Proc. Mil. Comm. Conf.*, Nov. 1991, pp. 571–575.